



Universiteit Gent
Faculteit Wetenschappen
Vakgroep Geologie en Bodemkunde

Definitie en modelisatie van de limieten van hoge-resolutie akoestische beeldvorming in marien milieu.

Defining and modeling the limits of high-resolution underwater acoustic imaging.

Peter Staelens

Dit werk kwam tot stand in het kader van een specialisatiebeurs van de Belgische Marine.

Promotor: Prof. Dr. Jean-Pierre Henriët
Universiteit Gent
Faculteit Wetenschappen
Vakgroep Geologie en Bodemkunde

Krijgslaan 281 S8
B-9000 Gent



Proefschrift tot het behalen van de graad van
Doctor in de Wetenschappen: Geologie
Academiejaar 2008-2009

ABSTRACT

In underwater warfare, detection of sea mines is a challenging discipline. Within the field of sea mine hunting, the detection of fully buried sea mines has always been the most difficult. In fact all objects located under water near to interfaces with high acoustic and or magnetic impedance differences and roughness are hard to detect. Today most up to date modern sea mines have a non magnetic hull and a minimum of magnetic materials on board. They preferably hide near interfaces that hinder detection. The shape often makes the modern sea mine stealth for acoustic detection instrumentation. The electronics on board of the mine also becomes increasingly smarter, smaller, lower power and more complex. Up till the time of writing this thesis, despite all the promising publications, there is no known instrument or combination of instruments capable of detecting buried sea mines within a reasonable timeframe. During the last decennia a number of instruments, methods and platforms have been thoroughly tested and evaluated. This research aimed at evaluating the applicability of very high resolution reflection seismic systems in buried object detection. The thesis basically covers 3 fields: field experiments (1), acoustic modeling and migration (2) and the evaluation of an existing acoustic 3D model and construction of a new alternative acoustic model based upon computer gaming technology (3).

(1) The tests described cover detection of objects near interfaces. With interfaces is meant: air-water and seafloor- water interface. Some of the tests were performed by NATO partners, some tests were done in cooperation with NATO partners, and some tests were performed by the Belgian Navy.

(2) Triggered by the failed processing of some field tests, 3D acoustic models were built and used for the evaluation of the processing algorithms. The research tried to interconnect field tests to existing mathematical models and focusing algorithms. The limitations of the migration algorithms and the implementations on the recording conditions were identified.

(3) Trying to push the modeling to a higher level, the NURC model BORIS 3D was used and found to be inapplicable for the testing of migration algorithms. Eventually a completely new acoustic model enabling the accurate and reliable reproduction of acoustic signals and shadows in a full 3D environment with a velocity gradient and objects was developed. In short: the model handles very complex 3D environments. Unlike many other 3D models, the signals produced by this new model can also be used to test 3D migration algorithms and does not only serve as an estimate of sonar performance.

The thesis had also some 'spin-out' results in the field of sediment dynamics. A new 4D sand dynamic model was developed to generate sand ripple fields where not only the pattern and shape of the ripples were more realistic but also parameters such as acoustic impedance and grain size distribution were made available. Based upon these results and existing swath bathymetry maps new algorithms for GIS applications to detect and vectorize sand crests are proposed.

DUTCH EXTENDED ABSTRACT

Het uitzenden van geluid en de analyse van het ontvangen signaal om objecten te localiseren werd voor het eerst op grote schaal gebruikt in militaire kringen. De detectie van duikboten en later het localiseren van zeemijnen waren twee militaire disciplines die al zeer vroeg intensief akoestische middelen gebruikten. Vandaag beperkt het onderzoeksveld van de onderwaterakoestiek zich niet meer uitsluitend tot beeldvorming en detectie van objecten. Sonar systemen zijn een onmisbaar deel gaan uitmaken van vele onderzoeksvelden binnen de onderwater technologie. Onderwaterakoestiek heeft ook zijn toepassingen in beeldvorming van petroleumvelden, visualisatie en karakterisatie van de zeebodem, peilingen, sonars om vis te localiseren, stromingsmeters, USBL en LBL systemen om bijvoorbeeld een onderwater robot te localiseren, onderwater camera, data communicatie,...

Door de veelheid aan toepassingen en ook het gebruiksgemak, snelheid van opname en meerwaarde van akoestische data heeft het gebruik van akoestische instrumenten ook zijn ingang gevonden in andere markten dan de militaire. Akoestische beeldvorming is een zeer belangrijk luik in de afstandswaarneming onder water en zodoende een belangrijk instrument in academisch en industrieel maritiem onderzoek. Ook in deze onderzoeksvelden is er een trend om steeds meer naar de limieten van de beeldinterpretatie te gaan. De druk om steeds verder te gaan met de interpretatie van de signalen zorgt er voor dat interpretaties en conclusies niet altijd met zekerheid nog extrapoleerbaar zijn buiten de geografische regio van het waarnemen of van 'fit'. De grens tussen waarnemen en 'wishful thinking' wordt dan ook altijd maar fijner. Het zijn deze onzekerheden die aanzet gegeven hebben tot dit onderzoeksproject.

In de onderwater oorlogsvoering is de detectie van zeemijnen een uitdagend onderzoeksveld. In het veld van de mijnenjacht is de detectie van de volledig begraven objecten waarschijnlijk één van de meest complexe problemen. In feite zijn alle detecties en onderscheidingen van objecten onder water, gelocaliseerd bij een interface met hoge akoestische en of magnetische impedantieverschillen en ruwheden, problematisch. De vandaag geproduceerde geplaatste zeemijnen, waaronder bijvoorbeeld de Italiaanse manta en de Zweedse rockan, zijn gebouwd uit amagnetische materialen. De vorm van de mijnen maakt ze dikwijls, gewild of ongewild onzichtbaar voor akoestische detectie apparatuur. Door hun vorm gaan ze zich daarenboven nog gaan inbedden in hun omgeving, ze worden dus één met de interface. De nieuwe generatie zeemijnen krijgt ook een veel intelligentere elektronica aan boord die toelaat schepen te herkennen en selectief aan te vallen of te negeren. Het vermogensverbruik en de grootte van de nieuwe chips leidt er toe dat steeds kleinere printplaten en batterijen kunnen gebruikt worden wat dan weer de magnetische sigantuur van de mijn gaat beperken. Tot op het moment van dit schrijven bestaat er geen enkel instrument of een combinatie van instrumenten om volledig begraven mijnen te detecteren binnen een redelijk tijdsframe.

Het onderzoek startte met veldtesten. Een praktische voeling met de problematiek en de data acquisitie is essentieel. In het tweede militair dok in Zeebrugge werd een cilindrische mijn geplaatst die zichzelf gedeeltelijk begroef en werden een reeks laag frequente seismische bronnen getest op het doelwit. Er werden sparkers, één boomer en één pinger getest. Enkel met de boomer (Seistec) werd het object ook effectief waargenomen. Belangrijker waren de resultaten naast de detectie van het object. De inversie algoritmes om het object scherp te stellen op de beelden leken niet te werken door een te slechte positionering. En het ruwe zandoppervlak begraven onder de modder waarin de mijn ingebed zat gaf dezelfde signatuur als de mijn zelf. Deze veldtest werd dan ook volledig in drie dimensies gemodelleerd. Andere veldtesten werden uitgevoerd met sidescan sonars op verschillende platformen (getrokken en zelfzwemmend), synthetic aperture sonar,

parametrische echosounder, akoestische camera en infrarood camera. Alle testen wezen een beetje in dezelfde richting: objecten nabij zones met een grote impedantievariatie is moeilijk detecteerbaar. Belangrijk is om het instrument te kiezen dat geen last heeft van de interface impedantievariaties en ruwheden. Een voorbeeld zou kunnen zijn een metallisch object detecteren nabij een zuiver geribbeld zand-water interface met een magnetometer. Maar zoals eerder gesteld zijn de meeste hedendaagse zeemijnen helemaal niet meer metallisch.

Gedurende de laatste decennia, door het véél krachtiger worden van computers, zijn er heel wat bijkomende mogelijkheden gecreëerd in de onderwater beeldvorming. Niet alleen de beeldvorming heeft zijn voordelen getrokken uit de met kracht toenemende rekeninstrumenten, maar ook het aantal en de complexiteit van de modelleringsinstrumenten is exponentieel toegenomen. Omdat modelleren dikwijls veel meer rekenkracht vraagt dan dataverwerking en omdat de verwerkingswereld toch al een viertal decennia over goede echte data beschikt loopt de modelleringswereld op dit moment een beetje achter op de verwerkingswereld. Het is zelfs zo dat men op dit moment de waarde van een model kan testen door zijn resultaten te verwerken met bestaande verwerkingsalgoritmes. In een ideaal geval zou het statement omgekeerd moeten kunnen gesteld worden: verwerkingsalgoritmes worden eerst getest op model data waarvan alle parameters gekend zijn. Door het niet krachtig genoeg zijn van het computermateriaal, of de steeds hogere verwachtingen van performantie van akoestische modellen, is er een evolutie om akoestische modellen te ontwikkelen gebaseerd op golfnummer integratie. Golfnummer integratie wordt ook gebruikt bij inversie van akoestische beelden en behoort daar inderdaad tot de snelste algoritmes. De keerzijde van de medaille is dat deze algoritmes zeer gevoelig zijn aan allerhande variaties van voorplantingssnelheden en andere inhomogeniteiten.

Een eerste grote stap vooruit was het volledig modelleren van de eerste tests in het tweede militair dok te Zeebrugge. Het model werd gebruikt om migratie algoritmes te testen. De migratietests op het model slaagden wel, en stap voor stap werd ruis op de akoestische data en positioneringsdata toegevoegd. De grote boosdoener bleek de ruis op de positionering te zijn. Dit positioneringsprobleem was al veel eerder opgedoken in het synthetic aperture onderzoeksveld, waar dan ook oplossingen voor uitgewerkt waren. Een onderzoeksstage in NURC (NATO Undersea Research Centre) bracht de modelleringsinspanning tot een veel hoger niveau. Het onderzoek spitste zich toe op het waarom van het falen van 'micronavigatie' algoritmes in de meest performante golfnummer integratie 3D akoestische modellen terwijl die algoritmes helemaal niet faalden op 'point scatterer' modellen. Dit onderzoek wees het verkeerdelijk of onvoorzichtig gebruik van deze golfnummer akoestische modellen aan als oorzaak van het falen. Bijgevoegd in deze thesis zijn een reeks testen en resultaten van het 'stressen' van het BORIS-SSA model die kunnen gebruikt worden om valse resultaten in de gemodelleerde data te herkennen en bij detectie de juiste aanpassingen te kunnen maken in het model.

Het BORIS-SSA model bleek nog veel te beperkt te zijn voor de toepassingen die onderzocht werden in dit onderzoek en een nieuw betrouwbaarder en flexibeler model werd ontworpen. Dit model, gebaseerd op computer gaming technologie, is een point scatterer model en vraagt zodoende zeer veel middelen van de rekencomputer of cluster. Het model laat toe snelheidsgradienten in de waterkolom te introduceren, multibeam echosounder grids te gebruiken als modelleringsgebied, wavelet functies te maken van de akoestische bron, objecten in de omgeving te plaatsen, alle schaduwen perfect uit te rekenen,... Het nieuw ontwikkelde model onderging dezelfde tests als de stress tests op het BORIS-SSA model en gaf geen afwijkende resultaten, het is dus niet alleen betrouwbaarder maar vooral veel flexibeler in gebruik. De keerzijde is dan weer de zeer lange rekentijden.

Naast akoestische modellen en resultaten heeft dit onderzoek misschien nog wel resultaten opgeleverd in het veld van de sedimentdynamiek. Door een gebrek aan voor akoestische modellering bruikbare 3D sedimentdynamische modellen, die niet alleen de vorm van de zandribbels beschrijven maar ook de distributie van de korrels en porositeiten, werd een model ontworpen dat wel alle, voor akoestiek nuttige parameters uitrekent. Het model start met een vlak zand oppervlak en een stromingspatroon wordt geplaatst in het model. Het zand herschikt zich daarop tot een nieuwe evenwichtstoestand. De evolutie van dit Monte Carlo model doorheen de tijd stemt in grote mate overeen met wat in de realiteit geobserveerd kan worden. Het model werd maar beperkt uitgewerkt maar kan in de toekomst een onderzoeksobject op zich worden.

Op basis van de bovenstaande beschreven sediment dynamische modellen werd ook een vectorisatie algoritme voor zandduinen op multibeam grids ontwikkeld. Origineel was het de bedoeling dit te gebruiken in een snelle uitrekening van de schaduwen maar uiteindelijk bleek dit pad niet te leiden naar een sneller algoritme en werd toch ray tracing gebruikt. Wat niet wegneemt dat een gecombineerde aanpak misschien wel tot zeer goede resultaten kan leiden.

PREFACE

'If a man does not know to what port he is sailing, no wind is favourable.'

(Seneca the Younger)

When I started this research I saw it as wind, a wind to bring me there where I wanted to be with my knowledge and skills: the crossing between geology, geophysics, signal analysis, computer graphics and last but not least embedded electronics. I saw that particular field as a field of open opportunities. After 7 years of devotedly following the favourable wind which safely navigated me through a world of opportunities and which severely broadened my knowledge and skills, it was time for the next step in my life. The next step, is one many people dream about, even more regret they never tried it, only a few do it and even less make it. This next step is patenting ideas and starting your own company. When it all started mid 2008 the wind was very favourable and the future bright, but if the wind or storm is favourable now, time will tell. One thing is sure: it has been already and it will be a unique course full of lessons again, a course I'm thrilled to follow for at least a while or forever.

It is time to focus on those who suffered most under the will to achieve too many and impossible goals. First of all I would like to thank all the people closest to me who naturally suffered most. Thanks to my parents, wife, daughter and family for staying patient and providing continuous support and motivation during the hard times. Thanks to the people who gave me the chance to do this research: Prof. Dr. Jean-Pierre Henriët and Commander Yves Dupont. Thanks to all my colleagues in the Belgian Navy, Ghent University and the Renard Centre of Marine Geology. Special thanks go to all those who made life on board of all the research vessels we worked on lighter, and who gave me the opportunity to join and learn from all of them. Thank you to every crew I ever worked together with these last 7 years. Without all the Belgica and other campaigns I would never have achieved the insights I have today. Thank you to all the NATO colleagues I cooperated with, especially to Herr Dr. Thomas Wever to convince me to finalize this document, but also to Gorm, Jens, Andrei and crew for joining me every evening on the R/V Planet (sorry to all the nice people I forgot). Thanks to Fred for the nice talks in the margins of the NATO meetings. Thank you to the whole team of Vera for giving me a lot of practical opportunities, the mwdc (Paul and Gino), the Navy divers for diving 'on the rocks' in February in the Baltic sea, thanks to JPP and tutu. Thanks to Anneleen, Lieven and Ben to keep me on track. There are simply too many people to thank and people who were decisive in this project.

I wish all the best to all those I ever collaborated with, maybe one day, a wind will bring us together again, maybe sooner, maybe later.

Peter

TABLE OF CONTENTS

Abstract.....	1
Dutch Extended Abstract.....	2
Preface.....	5
Table of contents	6
List of figures.....	10
List of abbreviations	16
1 Transducer design and implications on wavelets and wave fields.....	17
1.1 Introduction.....	17
1.2 Active and passive piezoelectric transducers	18
1.3 Point scattering and directivity patterns.....	19
1.3.1 Point scatterer	19
1.3.2 Line transducer.....	20
1.3.3 Mills Cross.....	21
1.4 Fourier transform table, an easy tool to predict directivity patterns.....	23
1.5 Side lobe suppression and beam steering.....	25
1.6 Conventional sonar	25
1.7 A special case: chirp.....	26
1.8 Near field and far field.....	29
1.9 Parametric sonar.....	29
1.10 Migration or image focusing (SAS)	32
1.10.1 Image focusing or migration concepts.....	32
1.10.1.1 Kirchhoff migration in detail	33
1.10.1.2 F-K migration in detail.....	34
1.10.2 Sonar application.....	37
1.11 Acoustic retroreflectors.....	39
2 Detecting objects, field tests.....	40
2.1 Introduction.....	40
2.2 Buried target detection, penetration of acoustic waves into the seafloor	41
2.3 Low frequency acoustic detection of a semi buried object (Zeebrugge 04)	42
2.3.1 Introduction.....	42
2.3.2 Geological and sedimentological setting	45
2.3.3 Description, difficulties and results of the tests.....	49
2.3.4 Conclusions	54
2.4 The NATO Expert System tRials (Baltic Sea 06)	54
2.4.1 Introduction.....	54

2.4.2	AUV tests, directionality of scatter	55
2.4.2.1	Theory	55
2.4.2.2	Discussion and overview of results.....	57
2.4.3	Parametric sonar tests, detection of a fully buried mine	60
2.4.4	Conclusions.....	60
2.5	Floating object detection (Zeebrugge 06).....	61
2.5.1	Introduction.....	61
2.5.2	Theory.....	61
2.5.3	Discussion and overview of results.....	62
2.5.4	Conclusions.....	66
2.6	Towed side-scan sonar versus AUV (Sigurd Faulbaums 07)	66
2.6.1	Introduction.....	66
2.6.2	Available information.....	67
2.6.3	Data acquisition and description of the recorded data.....	68
2.6.4	Discussion.....	71
2.6.5	Conclusions.....	73
2.7	General conclusions.....	73
3	Unraveling field tests trough modeling and migration	75
3.1	Introduction.....	75
3.2	3D point scatterer model first version.....	76
3.2.1	Modeling low frequency acoustic object detection (Zeebrugge 04).....	76
3.2.1.1	Introduction	76
3.2.1.2	Theory	76
3.2.1.3	Model software overview.....	78
3.2.1.4	Software flowcharts	79
3.2.1.5	Model parameters.....	82
3.2.1.6	Raw model results.....	83
3.2.1.7	Reflector coherence of non migrated acoustic data	85
3.3	Migration of a 3D modeled acoustic block.....	86
3.3.1	Introduction.....	86
3.3.2	Migration software overview	88
3.3.3	Software flowcharts	88
3.3.3.1	Total flow	88
3.3.3.2	Bin10cm.m	89
3.3.3.3	Driedmig.m	89
3.3.4	Migration parameters.....	90

3.3.5	Migration results.....	90
3.3.5.1	Overall.....	90
3.3.5.2	Inline.....	91
3.3.5.3	Cross line.....	91
3.3.5.4	Time slices.....	93
3.3.5.5	Object detection.....	96
3.3.6	Deviations on spatial sample densities and positioning affect migration performance.....	98
3.3.6.1	Introduction.....	98
3.3.6.2	Migration with exact positioning and spatial downsampling.....	98
3.4	Conclusions.....	103
4	Two mainstream approaches of acoustic modeling.....	104
4.1	BORIS 3D SSA (wavenumber integration).....	104
4.1.1	Introduction.....	104
4.1.2	Preface: 2D and 3D acoustic models.....	105
4.1.3	Mathematics of BORIS 3D in a nutshell.....	106
4.1.4	Tuning of the BORIS 3D SSA model for side-scan simulation.....	107
4.1.4.1	Goals.....	108
4.1.4.2	Implementation strategy proposal:.....	110
4.1.5	Encountered limitations of the BORIS_SSA model.....	112
4.2	3D model second edition (point-scattering model).....	114
4.2.1	Introduction.....	114
4.2.2	Specifications.....	114
4.2.3	Point scatter versus facet scatter.....	116
4.2.4	Coordinate systems.....	118
4.2.5	Computer graphics in acoustic modeling.....	120
4.2.5.1	Introduction.....	120
4.2.5.2	Representation of the grid environment.....	122
4.2.5.3	Processing and building 3D objects.....	127
4.2.5.4	Acoustic Level of Detail (ALOD).....	130
4.2.5.5	Shadows, rasterization and rendering.....	130
4.2.5.6	Conclusion.....	132
4.2.6	Building the environment.....	133
4.2.6.1	Introduction.....	133
4.2.6.2	Tiling up the environment.....	133
4.2.6.3	Generating the environment: modeling sand dynamics.....	134

4.2.6.4	Automated detection of sand dune crests	140
4.2.6.5	Roughness and acoustic impedances.....	149
4.2.6.6	Multiple Z coordinates on one XY coordinate.....	151
4.2.7	Processing the environment: Refraction and ray tracing.....	151
4.2.7.1	Ray tracing vertex points.....	153
4.2.7.2	Raytracing facets.....	153
4.2.7.3	Ray tracing scatters	153
4.2.7.4	Ray tracing shadows	153
4.2.7.5	Retriangulation and edge equations.....	154
4.2.7.6	Tiling of the shadow rasters.....	155
4.2.8	Monostatic and multistatic approach.....	155
4.2.9	Acoustic response and impulse response	156
4.2.10	Discretisation of send and receive array versus array functions	157
4.2.11	Practical modeling workflow.....	158
4.2.12	Conclusions.....	162
5	Conclusions and outlook	163
5.1	Overall conclusions.....	163
5.2	Field tests.....	163
5.2.1	Low frequency bottom penetrating tests (<15 kHz).....	163
5.2.2	High frequency underwater acoustic tests (>15 kHz).....	164
5.3	The models.....	165
5.4	Migration.....	165
5.5	Outlook.....	166
6	References.....	167
7	Appendix.....	178

LIST OF FIGURES

FIGURE 1-1: RESONANCE CURVE OF A PIEZOELECTRIC MINERAL. f_1 TO f_2 IS A LINEAR ZONE USED BY SENSORS, WHILE ACTUATORS ARE GENERALLY USED IN THE RESONANCE PEAK AT f_3 . WHEN THE TRANSMITTED FREQUENCY BAND IS VERY NARROW, SENSORS MIGHT BE USED AT f_3	19
FIGURE 1-2: A SPHERICAL UNIT VIBRATES AND CREATES A SPHERICAL WAVE FIELD, THE FREQUENCY OF THE VIBRATION DEFINES THE WAVELENGTH OF THE WAVES. THE FIGURE SLICES THE SPHERICAL WAVEFIELD THROUGH THE SCATTERER. ALONG THE Z AXIS THE POWER INTENSITY IS PLOTTED. X AND Y AXIS ARE SPATIAL.	19
FIGURE 1-3: A LINE OF 100 POINTS VIBRATING IN PHASE. THE WAVE FRONTS ARE SPHERICAL BUT THE ENERGY INTENSITY WITHIN EACH WAVE FRONT VARIES. Z,Y,X AXIS IS TAKEN AS IN FIGURE 1-2.	21
FIGURE 1-4: RADIATION PATTERNS FROM SOME ACOUSTIC LINE ARRAYS. ALL ARRAYS ARE CONSIDERED ONE DIMENSIONAL (INFINITELY THIN). THE LENGTH OF THE ARRAY AND THE WAVELENGTH OF THE ACOUSTIC WAVES PRODUCED BY THE ARRAY DEFINE THE BEAM PATTERN. THE LENGTH OF AN ARRAY IS DEFINED IN A NUMBER OF WAVELENGTHS (HERE 1, 4 AND 10 LAMBDA). WITH INCREASING LENGTH OF THE ARRAY THERE IS A DECREASING APERTURE. ADAPTED FROM: 39 TH MULTIBEAM SONAR TRAINING COURSE (CHRISTIAN DE MOUSTIER) (CLARKE, DE MOUSTIER ET AL. 2005).....	22
FIGURE 1-5: TWO LINE ARRAYS HAVE THEIR OWN DIRECTIVITY PATTERN, WHEN THESE TWO ARRAYS ARE CROSSED, A NEW DIRECTIVITY PATTERN EMERGES. COPIED FROM 39TH MULTIBEAM SONAR TRAINING COURSE, OCEAN MAPPING GROUP (CLARKE, DE MOUSTIER ET AL. 2005)	23
FIGURE 1-6: THIS TABLE OF BASIC FOURIER TRANSFORMS CAN BE USED TO ESTIMATE THE DIRECTIONALITY OF THE WAVE FIELD PRODUCED BY AN ENVELOPED LINE TRANSDUCER. CONSIDER ON THE LEFT SIDE A LINE TRANSDUCER ALONG THE TIME AXIS (CHANGE TIME TO SPACE). THEN THE RIGHT SIDE OF THE IMAGE DEPICTS THE AMPLITUDE VARIATIONS VERSUS THE ANGLE OF INCIDENCE (CHANGE Ω TO Φ). REFERENCE: HTTP://WEBHOST.ETC.TUIASI.RO/CIN/DOWNLOADS/FOURIER/TABLE2.GIF	24
FIGURE 1-7: SIDE LOBES ARE NOT ONLY A PROBLEM IN TRANSDUCER DESIGN, THEY ARE ALSO PROBLEMATIC IN FILTER DESIGN (SPECTRAL LEAKAGE). THE HANNING WINDOW IS IN THIS CASE THE BEST OPTION TO REDUCE THE SIDE LOBES. COPIED FROM: MATLAB [®] RECIPES FOR EARTH SCIENCES (TRAUTH, GEBBERS ET AL. 2007).....	25
FIGURE 1-8: COPIED FROM MATLAB [®] , SIGNAL PROCESSING TOOLBOX, CHIRP HELP FILE. THIS FIGURE SHOWS HOW THE FREQUENCY CHANGES IN FUNCTION OF TIME FOR A LINEAR CHIRP. BASICALLY IT IS THE FOURIER TRANSFORM TAKEN IN A WINDOW RUNNING OVER THE SWEEP.	26
FIGURE 1-9: SUBBOTTOM CHIRP PROCESSING IN PRACTICE. FROM TOP TO BOTTOM: TOP: THE LINEAR CHIRP SWEEP, CENTRAL: THE AUTOCORRELATION OF THE CHIRP OR KLAUDER WAVELET AND AT THE BOTTOM THE ABSOLUTE VALUE OF THE HILBERT TRANSFORM OF THE KLAUDER WAVELET. THE TERM AUTO-CORRELATION IS USED WHEN A CROSS-CORRELATION IS DONE FROM A SIGNAL WITH ITSELF.....	27
FIGURE 1-10: IMAGE 1 DISPLAYS A RECORD OF CHIRP SWEEPS (2 KHz TO 12 KHz, 50 MS, LINEAR CHIRP: DIMENSIONS 6 BY 60 CM) RECORDED IN THE FAR FIELD OF THE LINEAR ARRAY, STARTING IN THE CENTRE OF THE ARRAY AT A DISTANCE OF 100 METER. THE GEOMETRY OF THE RECORDING IS DISPLAYED IN IMAGE 2. AT EVERY PING THE POSITION OF THE RECORDER IS DISPLACED 20CM OUT OF THE CENTRE, ON A LINE PARALLEL WITH THE LINE ARRAY. THE IMAGE DISPLAYS A CLEAR FILTERING EFFECT IN THE HIGHER FREQUENCY AMPLITUDES WITH INCREASING PING NUMBER. IMAGE 3 AND 4 DISPLAY TWO PROCESSED IMAGES. IMAGE 2 SHOWS AN AUTOCORRELATION FUNCTION OF EVERY RECORDED SWEEP. IMAGE 4 SHOWS A CROSS CORRELATION FUNCTION OF THE RECORDED TRACE WITH THE SWEEP THAT HAS BEEN SENT TO THE TRANSDUCER ELECTRONICS (STANDARD SUBBOTTOM SONAR PROCESSING). IMAGE 4 SHOWS HOW A REFLECTOR BECOMES DOUBLE AND GETS A TIME SHIFT THROUGHOUT THE APERTURE. THIS EFFECT WILL GENERATE UNDERMIGRATED PROFILES WHEN MIGRATION IS APPLIED WITH CORRECT VELOCITY INFORMATION FED INTO THE ALGORITHM.	28
FIGURE 1-11: MEASURING THE PATH DIFFERENCE FOR A LINE TRANSDUCER.....	29
FIGURE 1-12: NEAR FIELD AND FAR FIELD OF A PARAMETRIC SONAR	31
FIGURE 1-13: LEFT: A POINT SOURCE P EMITS A SPHERICAL WAVE RECORDED AT A, B, C AND D IN THE X-Z PLANE. RIGHT THE OBSERVATIONS IN A,B,C AND D PLOTTED IN FUNCTION OF TIME RESULTS IN A HYPERBOLIC FUNCTION IN THE X-T PLANE. THE STEEPNESS OF THE HYPERBOLA IS A FUNCTION OF THE WAVE PROPAGATION SPEED.....	33
FIGURE 1-14: UP: A SYNTHETIC ACOUSTIC PROFILE WITH THREE SCATTERERS IN A MEDIUM WITH A VELOCITY GRADIENT AND BELOW THE MIGRATION RESULTS. LEFT FIGURE ARE SPACE-TIME PROFILES, THE OTHER SIX ARE SPACE-SPACE SECTIONS OR TIME SLICES. COPIED FROM SEISMIC DATA ANALYSIS (YILMAZ 2001)	33
FIGURE 1-15: THE F-K ALGORITHM, LEFT THE ORIGINAL DATA B IN THE F-K DOMAIN, RIGHT THE REMAPPING OF THE DATA TO B' IN THE K_x - K_z DOMAIN.	36

FIGURE 1-16: A HIGH FREQUENCY SAS SYSTEM PROCESSING RESULTS. COPIED FROM: SYMPOSIUM: "BURIED SEA MINES - THREAT TO THE SECURITY OF THE BALTIC REGION" RIGA 27-28 OCTOBER 2005, PRESENTATION DR. MARC PINTO (NATO UNDERSEA RESEARCH CENTRE)	37
FIGURE 1-17: A LOW FREQUENCY SAS IMAGE, AN EXPERIMENT TO DETECT BURIED OBJECTS USING A RAIL MOUNTED SAS SYSTEM. COPIED FROM: SYMPOSIUM: "BURIED SEA MINES - THREAT TO THE SECURITY OF THE BALTIC REGION" RIGA 27-28 OCTOBER 2005, PRESENTATION DR. MARC PINTO (NATO UNDERSEA RESEARCH CENTRE).....	38
FIGURE 1-18: LEFT AN ACOUSTIC RETROREFLECTOR IN 2D THEORY AND RIGHT A REAL 3D EXAMPLE. THE RED AND THE GREEN RAYS ARE RAY PATHS PERPENDICULAR TO INCOMING AND OUTGOING THE WAVE FRONT. A RETROREFLECTOR IS AN APPLICATION OF MULTI PATH. WHEN A WAVE HITS A RETROREFLECTOR IT IS REFLECTED BACK TO THE SOURCE.	39
FIGURE 2-1: THE PULSE SHAPES GENERATED BY A BOOMER SPARKER AND GEOPULSE PINGER	43
FIGURE 2-2: THE 3D VHRS SYSTEM OF THE RCMG, UGENT (MISSIAEN 2005)	44
FIGURE 2-3: LOCALISATION.....	45
FIGURE 2-4: INTERPRETATION OF STRATIGRAPHY OF THE TEST SITE (BACCAERT AND BAETEMAN 1980)	46
FIGURE 2-5: SMALL SAND RIPPLES ON THE BEACH OF NIEUWPOORT, BELGIUM. NOTE HOW THE COARSE PARTICLES, BOTH ORGANIC (BLACK) AND SHELL FRAGMENTS (WHITE) CONCENTRATE BETWEEN THE RIPPLES. THE DISTRIBUTION OF PARTICLES IS CLEARLY HAS A PATTERN.	47
FIGURE 2-6: PRACTICAL EXAMPLES OF SAND BEDFORMS AND RIPPLES ON THE BEACH NORTH OF AUDRESELLES IN FRANCE. ON THE LEFT, TWO EXAMPLES OF MARINE JURASSIC DEPOSITS, ON THE RIGHT SIDE TWO RELATIVELY RECENT AEOLIAN DEPOSITS.	49
FIGURE 2-7: SEISTEC BOOMER SOURCE. RAW, SINGLE CHANNEL DATA AND INTERPRETATION, TOP TWO FIGURES ARE THE INLINE AND CROSS LINE SECTIONS ON TOP OF THE SEMI BURIED SEA MINE. THE BOTTOM FIGURE SHOWS THE ENERGY DISTRIBUTION WITHIN THE IMAGE. CLEAR IS THAT THE WATER-MUD INTERFACE REFLECTS A LOT OF ENERGY, WHILE IN THE MUD LAYER THERE IS ALMOST NO ENERGY REFLECTED AND THE MUD-SAND INTERFACE PLUS THE SAND VOLUME REFLECT ALL THE AVAILABLE ENERGY.	53
FIGURE 2-8: THE REMUS 100 AUV IS A PROGRAMMABLE AUTONOMOUSLY SWIMMING VEHICLE MOUNTED WITH A MARINE SONIC SIDE-SCAN SONAR, TWO ADCP'S, A GPS, A CTD AND AN OPTICAL BACKSCATTER UNIT. ON THE RIGHT HAND SITE THERE IS THE SAILING PATTERN PROGRAMMED INTO THE AUV.	55
FIGURE 2-9: THIS SIDE-SCAN SONAR IMAGE HAS BEEN TAKEN WITH THE REMUS 100 AUV WITH THE DIDSON UNDERWATER ACOUSTIC CAMERA MOUNTED ON THE HEAD. THE SHAPE OF THE SONAR DESTABILIZES THE AUV AND THAT HAS A SIGNIFICANT REPERCUSSION ON THE SIDE-SCAN SONAR IMAGE.	56
FIGURE 2-10: INTERPRETATION OF A SIDE-SCAN IMAGE. LEFT TOP: THE ACOUSTIC IMAGE OF A SEMI BURIED CYLINDRICAL MINE TAKEN WITH A 900 KHZ SONAR MOUNTED ON A REMUS AUV. RIGHT TOP: THE INTERPRETATION OF THE IMAGE. BOTTOM: FRONTAL VIEW, EXPLANATION OF THE SHADOWING.....	57
FIGURE 2-11: FIVE RAW ACOUSTIC RESPONSES FROM A CYLINDRICAL MINE. THE RECORDING HAS BEEN DONE WITH THE MARINE SONIC 900 KHZ SIDE SCAN SONAR MOUNTED ON THE REMUS 100 AUV. ALL RESPONSES MORE OR LESS LOOK THE SAME. THE MAJOR VARIATIONS IN BACKSCATTER ARE TO BE SEEN IN THE MUD LAYER WHERE THE SEA MINE IS LAYING IN. THE METER SCALE IS GIVEN ON TOP OF EVERY FIGURE. THE SCALE ON TOP OF EVERY IMAGE IS METER. THE HORIZONTAL AND VERTICAL SCALE ARE IDENTICAL.....	58
FIGURE 2-12: ELEVEN RAW SIDE-SCAN SONAR IMAGES FROM THE SAME MINE, ALL WITH DIFFERENT ANGLES OF INCIDENCE. THE RECORDING HAS BEEN DONE WITH THE MARINE SONIC 900 KHZ SIDE SCAN SONAR MOUNTED ON THE REMUS 100 AUV. THE AUV IS SAILING 3M ABOVE THE SEAFLOOR. THE REFLECTOR PROPERTIES OF THE LED BRIDGES ARE THE REASON WHY THE BACKSCATTERED FIELD FROM THE SEA MINE IS MORE OR LESS EQUAL IN EVERY IMAGE. IMPORTANT TO NOTE ARE THE DIFFERENCES IN BACKSCATTER PATTERNS FROM THE MUD LAYER THE MINE IS RESTING IN. THE BACKSCATTER OF THE ROPE SHOWS THAT LINEAR FEATURES PARALLEL TO THE LINE OF SAILING ARE MORE VISIBLE THAN OTHERS. THE METER SCALE IS GIVEN ON TOP OF EVERY FIGURE. THE SCALE ON TOP OF EVERY IMAGE IS METER. THE HORIZONTAL AND VERTICAL SCALE ARE IDENTICAL.	59
FIGURE 2-13: A RAW PARAMETRIC ECHO SOUNDING RECORDING. THIS PROFILE HAS BEEN TAKEN UNDER A 13° ANGLE (ANGLE OF INCIDENCE IS 77°). THE OBJECT WAS BURIED A YEAR BEFORE. THE SEDIMENT IS SAND. NOTE THAT THE OBJECT COULD NOT BE DETECTED UNDER VERTICAL INCIDENCE. THAT FACT DEMONSTRATES THE AMOUNT OF LUCK NEEDED TO FIND A BURIED OBJECT, BECAUSE VERTICAL INCIDENCE SHOULD BE THE EASIEST ANGLE TO WORK UNDER TO FIND THE OBJECT BACK. THE SMALL FOOTPRINT OF THE PARAMETRIC ECHO SOUNDER IMPLICATES THAT A LOT OF PINGS AND A HIGH POSITION ACCURACY IS NEEDED IN ORDER TO FULLY COVER THE SEAFLOOR.....	60
FIGURE 2-14: ACOUSTIC DIRECTIONALITY PLOTS OF SIDE-SCAN SONARS: LEFT AND RIGHT ARE FRONT VIEWS, THE CENTRE IS A VIEW ON TOP OF THE SONAR. ON THE LEFT THE EXPECTED PATTERN OF THE MARINE SONIC 900 KHZ SIDE-SCAN SONAR MOUNTED ON	

THE REMUS 100 IS PLOTTED. ON THE RIGHT THE EXPECTED PATTERN OF THE KLEIN 3000 SIDE-SCAN SONAR IS PLOTTED (100-500 kHz).	61
FIGURE 2-15: LEFT THE OIL BARREL, RIGHT THE ACOUSTIC REFLECTOR USED DURING THE TESTS. THE DIMENSIONS OF THE REFLECTOR ARE 20x20x20 CM, THE OIL BARREL IS APPROXIMATELY 50 CM HIGH.	63
FIGURE 2-16: A SONAR IMAGE NEAR A QUAY, 1) IS THE DISTANCE BETWEEN THE SONAR AND THE SEAFLOOR, 2) IS THE CLOSEST DISTANCE TO THE QUAY, 3) IS THE DISTANCE TO THE FOOT OF THE QUAY, R) REFLECTOR RESPONSE. GREEN: DETECTION POSSIBLE, RED: NO DETECTION POSSIBLE, BLUE: REDUCED IMAGE QUALITY DUE TO CONVOLUTION AND MULTIPATH LEAVE OBJECTS UNDETECTED	63
FIGURE 2-17: LEFT RAW 500 KHZ RECORDINGS OF A FLOATING OBJECT. RIGHT THE RAW 100 KHZ COUNTERPART. THE PURPLE LINES ARE THE 10 M RANGE LINES. THE BRIGHT SPOT IS THE ACOUSTIC RETROREFLECTOR. THE SONAR WAS TOWED 1 METER BELOW THE WATER SURFACE IN LINES PARALLEL TO THE TWO OBJECTS, STARTING AT JUST A COUPLE OF METERS TO 40 METER.	64
FIGURE 2-18: SOME RAW SNAPSHOTS FROM DETECTIONS OF THE BARREL (HAS A LONG TAIL IN THE ACOUSTIC IMAGE) AND THE REFLECTOR (HAS NO TAIL IN THE ACOUSTIC IMAGE). ALL SONAR IMAGES ARE TAKEN WITHIN A 10 METER DISTANCE RANGE. THE METER SCALE IS GIVEN ON TOP OF EVERY FIGURE.	65
FIGURE 2-19: AN EM3002D SWATH BATHYMETRY MAP OF THE SIGURD FAULBAUMS WRECK. THE SWATH BATHYMETRY MAP SUGGESTS THAT MOST OF THE WRECK IS COVERED BY SAND. DATA FROM VLAAMSE HYDROGRAFIE, AFDELING KUST (VLAAMSE HYDROGRAFIE 2007)	68
FIGURE 2-20: A PAIR OF SIDE-SCAN IMAGES FROM THE WRECK AND THE REGION AROUND. THE KLEIN 3000 SIDE-SCAN IMAGES HAVE ALMOST NO SHADOWS BECAUSE THE SONAR WAS TOWED 10 METER ABOVE THE SEAFLOOR, WHILE THE REMUS 100 SAILED 5 METER ABOVE THE SEAFLOOR.	68
FIGURE 2-21: THE IXSEA SHADOWS IMAGE OF THE SIGURD FAULBAUMS.	70
FIGURE 2-22: IMAGE TAKEN WITH A KLEIN 3000 SIDESCAN SONAR TOWED FROM A STABLE PLATFORM.	71
FIGURE 2-23: LEFT A REMUS 100 IMAGE OF TWO TARGETS, RIGHT THE KLEIN 3000 COUNTERPART. LEFT ALSO A METER SCALE HAS BEEN ADDED TO THE FIGURE.	72
FIGURE 2-24: DEBRIS FROM THE SIGURD FAULBAUMS NEAR THE WRECK SITE. THE SAND WAVES ARE CLEARLY VISIBLE AND ALSO THE MULTI-PATH RETURN AT 20 METER (DEPTH OF THE AUV) IS STILL PRESENT.	73
FIGURE 3-2: FLOWCHART OF SERVER SOFTWARE	79
FIGURE 3-3: DRIEDBLOK.M FLOWCHART, MAIN SOFTWARE RUNNING ON THE WORKSTATIONS, CALLS FUNCTIONS PPCSLAVE.M AND SIMUL3D.M	80
FIGURE 3-4: SIMUL3D FLOWCHART: THE FUNCTION IS CALLED BY DRIEDBLOK AND GENERATES ACOUSTIC PROFILES	81
FIGURE 3-5: FLOWCHART OF PPCSLAVE, THIS FUNCTION CONTROLS THE CONNECTIONS BETWEEN THE WORKSTATIONS AND THE SERVER. THE SLAVE CONTINUOUSLY CHECKS THE CONNECTION.	82
FIGURE 3-6: RIPPLE FIELD ENTERED IN THE MODEL	83
FIGURE 3-7: INLINE, CROSSLINE AND TIMESLICE PRINCIPLE	84
FIGURE 3-8: A MODELED PROFILE SECTION. THIS SECTION IS TAKEN PARALLEL WITH THE TWO LOWEST FREQUENCY BEDFORM STRUCTURES, TROUGH ONE OF THE SANDBANKS. THE ACOUSTIC RESPONSE IN THIS IMAGE IS SURFACE COMPONENT ONLY, NO VOLUME CONTRIBUTIONS ARE ADDED TO THE SIGNAL	84
FIGURE 3-9: SIMULATED TIME SLICES, THE FOUR TIME SLICES ARE TAKEN IN EQUAL TIME STEPS IN A NON MIGRATED ACOUSTIC VOLUME. THE FIRST SLICE IS LEFT TOP, SECOND: RIGHT TOP, THIRD: LEFT BOTTOM, FOURTH: RIGHT BOTTOM. THE NEXT TIME SLICES WILL BE DISPLAYED IN THE JET COLOUR SCALE, JET COLOUR SCALE REVEALS MORE DETAIL	85
FIGURE 3-10: FOUR DETAILS OF TIME SLICES IN THE RAW ACOUSTIC DATA VOLUME PRESENTED BEFORE EACH WITH A LARGER BIN SIZE. UPPER LEFT IS THE HIGHEST RESOLUTION IMAGE WITH A VALUE EVERY 5 CM BOTH IN X AND Y DIRECTION. THE OTHER THREE IMAGES UP LEFT AND RIGHT AND LEFT DOWN ARE SPATIALLY UNDERSAMPLED. THE UPPER RIGHT IMAGE IS ONLY SLIGHTLY UNDERSAMPLED AND SIGNIFICANT IMAGE DEGRADATION IS NOT VISIBLE.	86
FIGURE 3-11: THE APERTURE CHANGES TROUGHOUT MIGRATION. LEFT: THE SURFACE CONTRIBUTIONS TO AN UNMIGRATED SIGNAL, CENTRE: THE SURFACE CONTRIBUTIONS TO A 2D MIGRATED SIGNAL, RIGHT: THE SURFACE CONTRIBUTIONS OF A SIGNAL AFTER TWO PERPENDICULAR MIGRATIONS OR 3D MIGRATION.	87
FIGURE 3-12: 3D MIGRATION FLOW	88
FIGURE 3-13: STACKING BINS AND STORING THE RESULT IN A 3D ARRAY	89
FIGURE 3-14: A 3D CONSTANT VELOCITY F-K MIGRATION OF AN ACOUSTIC VOLUME LOADED IN THE RAM MEMORY	90
FIGURE 3-15: INLINE SECTIONS OF THE 3D VOLUME. THE TOP FIGURE IS THE RAW DATA, THE CENTRE FIGURE IS THE SAME PROFILE 2D MIGRATED IN THE DIRECTION OF THE PROFILE. THE PROFILE ON THE BOTTOM IS THE SAME SECTION AS THE TWO PROFILES ABOVE IT, TAKEN IN THE 3D MIGRATED VOLUME.	91

FIGURE 3-16: CROSS LINE SECTIONS OF THE 3D VOLUME. THE TOP FIGURE IS THE RAW DATA, THE CENTRE FIGURE IS THE SAME PROFILE 2D MIGRATED PERPENDICULAR TO THE DIRECTION OF THE PROFILE. THE PROFILE ON THE BOTTOM IS THE SAME SECTION AS THE TWO PROFILES ABOVE IT, TAKEN IN THE 3D MIGRATED VOLUME	92
FIGURE 3-17: THE TOP IMAGE IS THE TOPOGRAPHY USED TO SIMULATE THE ACOUSTIC DATA VOLUME. THE MATRIX OF NINE FIGURES ARE TIME SLICES THROUGH A RAW ACOUSTIC DATA VOLUME (LEFT), A 2D MIGRATED VOLUME IN THE UP DOWN DIRECTION (MIDDLE) AND A 3D PROCESSED VOLUME (RIGHT). THE SLICES ARE TAKEN WITH A STEP OF 0.23 MS STARTING AT 13.2 MS....	94
FIGURE 3-18: THE TOP IMAGE IS THE TOPOGRAPHY USED TO SIMULATE THE ACOUSTIC DATA VOLUME. THE MATRIX OF NINE FIGURES ARE TIME SLICES THROUGH A RAW ACOUSTIC DATA VOLUME (LEFT), A 2D MIGRATED VOLUME IN THE UP DOWN DIRECTION (MIDDLE) AND A 3D PROCESSED VOLUME (RIGHT). THE SLICES ARE TAKEN WITH A STEP OF 0.23 MS STARTING AT 13.9 MS....	95
FIGURE 3-19: A ZOOM IN ON THE SEMI BURIED CYLINDRICAL MINE IN THE DATASET	96
FIGURE 3-20: A VOLUME IS TAKEN OF 10 BY 10 BY 1.4 METER AND THEN HORIZONTALLY SLICED EVERY 3 CM, IN THE CENTRE OF THE VOLUME THERE IS THE OBJECT. TIME SLICES TAKEN IN THE ZONE WITH THE OBJECT AND TILED UP IN A FIGURE. SLICE 351 IS IN THE UPPER LEFT CORNER, SLICE 400 IS IN THE LOWER RIGHT CORNER OF EACH INDIVIDUAL FIGURE. THE TOP FIGURE ARE 50 TIME SLICES IN THE RAW DATA BLOCK, THE MIDDLE FIGURE IS THE COLLECTION OF TIME SLICES IN THE 2D MIGRATED BLOCK AND THE LOWER FIGURE IS THE COLLECTION OF TIME SLICES IN THE 3D MIGRATED BLOCK. EACH FIGURE CONTAINS 50 SECTIONS OF 10 BY 10 METER, THE FIRST TEN SECTIONS ARE IN THE FIRST ROW, THE NEXT TEN IN THE SECOND ROW AND SO ON. IMPORTANT TO NOTICE BESIDES THE OBJECT IS THAT IN LAST SEVEN TIME SLICES OF THE 3D MIGRATED DATA THE REVERBERATION IS GONE AND THE OBJECT IS CLEAR. FURTHER ON, THE FOOTPRINT OF THE OBJECT IN THE LOWEST ROW OF FIGURES IN THE 3D MIGRATED DATA IS DISAPPEARED	97
FIGURE 3-21: A DETAILED SECTION OF A 3D MIGRATED TIME SLICE AND THE EFFECT OF SPATIAL UNDER SAMPLING	99
FIGURE 3-22: A DETAIL FROM A 2D HIGH RESOLUTION IMAGE BEFORE SWELL FILTERING (LEFT) AND AFTER SWELL FILTERING (RIGHT)	100
FIGURE 3-23: TIME SLICES IN A 3D MIGRATED ACOUSTIC DATASET. WHITE NOISE HAS BEEN ADDED TO THE POSITIONING. THE TOP FIGURE IS A 3D MIGRATED DATASET WITH EXACT POSITIONING OF EVERY SEISMIC TRACE. THE FOUR IMAGES IN THE CENTRE AND BOTTOM HAVE UNIFORMLY DISTRIBUTED WHITE NOISE ADDED TO THE POSITION COORDINATES OF EVERY TRACE WITH A DISTRIBUTION RANGING FROM 1 CM TO 4 CM.	101
FIGURE 3-24: A VOLUME IS TAKEN OF 10 BY 10 BY 1.4 METER AND THEN HORIZONTALLY SLICED EVERY 3 CM, IN THE CENTRE OF THE VOLUME THERE IS THE OBJECT. TIME SLICES TAKEN IN THE ZONE WITH THE OBJECT AND TILED UP IN A FIGURE. SLICE 351 IS IN THE UPPER LEFT CORNER, SLICE 400 IS IN THE LOWER RIGHT CORNER OF EACH SEPARATE FIGURE. THE TOP FIGURE ARE TIME SLICES IN THE 3D MIGRATION OF THE ORIGINAL DATA, THE MIDDLE FIGURE ARE TIME SLICES ARE TAKEN FROM A BLOCK THAT HAS BEEN 3D MIGRATED WITH MAX 2 CM RANDOM VARIATION ON THE POSITION OF EACH TRACE AND THE LOWER FIGURE ARE TIME SLICES IN THE 3D MIGRATED BLOCK WITH MAX 4 CM RANDOM VARIATION ON THE POSITION OF EACH TRACE. EACH FIGURE CONTAINS 50 SECTIONS OF 10 BY 10 METER, THE FIRST TEN SECTIONS ARE IN THE FIRST ROW, THE NEXT TEN IN THE SECOND ROW AND SO ON.	102
4-1: THE SOURCE RECEIVER PAIR DIRECTED TO THE SEAFLOOR UNDER NON VERTICAL AND VERTICAL ANGLE OF INCIDENCE. VERTICAL ANGLE OF INCIDENCE WOULD CREATE A REFLECTION, NON VERTICAL ANGLE OF INCIDENCE AS SHOWN IN THE FIGURE, DIRECTS THE OUTGOING PING AWAY FROM THE SOURCE RECEIVER PAIR. THE BLACK BEAMS ARE THE INCOMING PINGS, THE RED, THE OUTGOING.	107
FIGURE 4-2: PURE YAW IS A ROTATION AROUND THE Z AXIS OF THE SONAR FACE. THE GRAZING ANGLE OF THE CENTRE OF THE BEAM IS 60°, THE SONAR IS POSITIONED 5 METER ABOVE THE SEAFLOOR.....	108
FIGURE 4-3: LEFT THE APPLIED SEAFLOOR TILE (BATHYMETRY) AND RIGHT THE BEAM PATTERN, THE COLOUR SCALE IS ALSO A METER SCALE RANGING FROM -0.15 TO +0.15	108
FIGURE 4-4: EVERY 0.5 DEGREES A PING IS SENT AND RECEIVED FROM THE SEAFLOOR. THESE PINGS ARE LINED UP IN THIS FIGURE. A PING TO PING RELATION IS CLEARLY VISIBLE (HORIZONTAL LINES IN THE IMAGE)	109
FIGURE 4-5: THE PATTERN OF THE CORRELATION IS SIMILAR TO THE BEAM PATTERN.....	110
FIGURE 4-6: EVERY PING IS CORRELATED WITH ITSELF AND ALL THE OTHER PINGS IN THE SCAN. THE AUTOCORRELATION SHOWS UP IN THE DIAGONAL PATTERN (DARK RED LINE). THE COLOUR SCALE INDICATES FULL CORRELATION OR THE SIGNALS ARE EQUAL (DARK RED) TILL BLUE WHERE BLUE INDICATES THAT THE SIGNALS ARE COMPLETELY DIFFERENT AND THERE IS NO CORRELATION BETWEEN THE TWO SIGNALS.....	110
FIGURE 4-7: LEFT: THE STANDARD IMPLEMENTATION OF CARTESIAN TO SPHERICAL COORDINATE TRANSFORMATION IN MATLAB®. RIGHT: THE TRANSFORMATION USED IN THE ACOUSTIC MODEL. ADAPTED FROM THE MATLAB® HELP FILES.....	119

FIGURE 4-8: ADAPTED FROM THE MATLAB(R) HELP FILES. THIS FIGURE DEPICTS THE COORDINATE SYSTEM USED IN THE CARTESIAN – CYLINDRICAL TRANSFORMATION. THE CART2POL TRANSFORMATION IS USED IN THE ROTATION ALGORITHMS FOR THE OBJECTS.	120
FIGURE 4-9: A PHOTOREALISTIC RENDERED IMAGE CREATED BY USING POV-RAY. THIS IMAGE WAS CONSTRUCTED USING A 3D TRIANGULARIZED MODEL, A VIEWPOINT, TEXTURE, LIGHTING AND SHADING INFORMATION BEFORE BEING RENDERED. SOURCE: (WIKIPEDIA 2007).....	122
FIGURE 4-10: LEFT A REGULAR TERRAIN REPRESENTATION AS INITIALLY USED BY THE ACOUSTIC MODEL, AND RIGHT A TIN REPRESENTATION (GARLAND AND HECKBERT 1995). COPYRIGHT © 1995 CARNEGIE MELON UNIVERSITY.	123
FIGURE 4-11: REDUCING THE NUMBER OF VERTICES OF A 1D SURFACE (DUCHAIANEAU, WOLINSKY ET AL. 1997). COPYRIGHT © 1997 IEEE.....	124
FIGURE 4-12: A HYBRID DTM, THE ORIGINAL DEM IS VISIBLE BUT THE SPATIAL SAMPLING IS NO LONGER UNIFORM. THIS IS AN EXAMPLE USED IN THE MODEL TESTING. THE SURFACE HAS BEEN GENERATED WITH THE MODEL PROPOSED IN 4.3.6.3.....	125
FIGURE 4-13: PRINCIPLE SKETCH OF THE POINT-SCATTERER POSITION ALGORITHM. LEFT: A TILE WITH ON TOP THE SCATTERERS (THE SCATTERER POSITION ALGORITHM HAS BEEN FED WITH THE SHADOW MATRIX, SO THE SCATTERERS ARE ONLY GENERATED IN THE, FOR THE SOURCE/RECEIVER, VISIBLE ZONES). RIGHT: A ZOOM IN ON ONE OF THE MEGA RIPPLES AND THE CORRESPONDING POINT SCATTERER MATRIX. THE FACETSIZE VERSUS SCATTERDENSITY IS TOO SMALL, DIRECTIONALITIES CAN BE OBSERVED.	126
FIGURE 4-14: A CLOSER VIEW ON THE 3D IMAGE OF FIGURE 4-13. THE SAME DIRECTIONALITY PROBLEM IN THE POINT-SCATTERER MATRIX DUE A TOO LOW DENSITY CAN BE OBSERVED. THE FACET MATRIX IS VISUALIZED BY THE NEAR TO VERTICAL WHITE LINES RUNNING TROUGH THE IMAGE. A HIGHER DENSITY OF SCATTERERS REDUCES AND EVENTUALLY REMOVES THESE LINES.	127
FIGURE 4-15: FOUR SHAPES OF OBJECTS. THESE SHAPES CAN BE GENERATED USING THE MINETYPE.M FILE DELIVERED WITH THE MODELING PACKAGE. TOP: MANTA (LEFT), SPHERE (RIGHT), BOTTOM: CYLINDER (LEFT), TUBE (RIGHT).....	128
FIGURE 4-16: A PARTLY BURIED CONE SHAPED AS MANTA-LIKE OBJECT. THE BLUE FACET LINES ARE A SECTION OF THE SEAFLOOR AND THE OBJECT FACETS. THE RED DOTS ARE SOME RAY TRACED POINT SCATTERERS OF THE OBJECT, THE SOURCE TRANSDUCER COORDINATES ARE NOT MADE VISIBLE.....	129
FIGURE 4-17: SHADOWS ON A TILE FROM A CYLINDER (LEFT) AND A SEMI BURIED MANTA MINE (CENTRE RIGHT) SEEN FROM A SOURCE S. THE CYLINDER IS CLOSE TO THE SOURCE AND THEREFORE HAS A HUGE SHADOW. THE RIPPLED SURFACE DETERMINES THE SHADOW SHAPE. THIS MATRIX IS FED INTO THE POINT SCATTERER MODELS. THE POINT OF VIEW IS IN THE CENTRE OF THE TILE.	129
FIGURE 4-18: EDGE WALKING ALGORITHM VISUALIZED. DRAW THE EDGES VERTICALLY AND FILL IN HORIZONTAL SPANS FOR EACH SCAN LINE. ADAPTED FROM LUEBKE, 1998.	131
FIGURE 4-19: EDGE EQUATION ALGORITHM VISUALIZED. ADAPTED FROM LUEBKE, 1998.	132
FIGURE 4-20: FIVE HIGH RESOLUTION SEAFLOOR TILES TILED UP. THIS FIGURE DEMONSTRATES THAT THE TILES LEAVE NO HOLES OPEN IN THE DEM, A PROPERTY REQUIRED FOR ACOUSTIC MODELING.....	134
FIGURE 4-21: COMPLETELY PROCESSED TILES. BUMP MAPPING OF 2 SAND RIPPLE TILES ON A DUNE FIELD. THE BUMP MAPPING IS NOT DONE WITH A PICTURE AS IN COMPUTER GRAPHICS APPLICATIONS BUT WITH THE MICRO BATHYMETRY TILES DISPLAYED IN FIGURE 4-20.	134
FIGURE 4-22: A 3D MODELED RIPPLE ON DUNE PATTERN (BUMP MAPPING AND TILING METHOD) WITH THE TWO STABILITY ANGLES THAT PLAY A ROLE IN 2D MODELING.....	136
FIGURE 4-23: 2D SCHEMATIC REPRESENTATION OF A SAND RIPPLE WITH A VORTEX.....	137
FIGURE 4-24: LEFT TOP: PHASE 3 OF THE RIPPLE FIELD EVOLUTION. RIGHT TOP: PHASE 8 OF THE RIPPLE FIELD EVOLUTION. LEFT CENTRE: PHASE 13 OF THE RIPPLE FIELD EVOLUTION. RIGHT CENTRE: PHASE 50 OF THE RIPPLE FIELD EVOLUTION. LEFT BOTTOM: PHASE 500 OF THE RIPPLE FIELD EVOLUTION BUMP MAPPED WITH THE GRAIN SIZE MATRIX. RIGHT BOTTOM: PHASE 500 OF THE RIPPLE FIELD EVOLUTION BUMP MAPPED WITH A VERSION OF THE GRAIN SIZE MATRIX PROCESSED WITH A MOVING AVERAGE FILTER OF 3 BY 3 BINS, GIVING EVERY BIN THE AVERAGE VALUE OF THE NEIGHBOURING BINS AND THE BIN ITSELF. IMPORTANT TO NOTICE ARE THE CONCENTRATIONS OF LARGER GRAINS (RED AND YELLOW SPOTS) IN THE RIPPLE TROUGHS.	139
FIGURE 4-25: IMPEDANCE MAP PLOTTED ON TOP OF A TOPOGRAPHY TILE, THE HIGHEST IMPEDANCES CAN BE FOUND IN BETWEEN THE RIPPLES AND ON THE SIDE OF THE RIPPLES WHERE EROSION OCCURS.....	140
FIGURE 4-26: THE SEAFLOOR TILE USED IN THE ALGORITHM TESTING.....	141
FIGURE 4-27: THE OUTPUT FROM THE CREST.M AND CRESTDIAG.M METHOD. A AND B DISPLAYS THE RESULT OF THE METHOD AFTER TAKING THE SECOND DERIVATIVE, TAKEN PERPENDICULAR TO THE SAND WAVES. C AND D: PARALLEL, E, F, G AND H: DIAGONAL. RED ARE THE DETECTIONS OF THE CRESTLINES. NOTE THAT HERE THE CRESTLINES HAVE NOT YET BEEN VECTORIZED.	143

FIGURE 4-28: COMBINED OPTIMUM SOLUTIONS USED IN THE STATISTICS AND VECTOR CALCULATIONS. THE CREST LINES BECOME VISIBLE WITH DIFFERENT INTENSITIES. THIS MATRIX WILL BE USED TO CONNECT VECTORS BASED UPON THE DETECTIONS SHOWN AT FIGURE 4-27.....	145
FIGURE 4-29: A SUMMARY OF THE RASTER OPERATIONS DONE AS A PREPARATION FOR THE VECTORISATION.....	145
FIGURE 4-30: THE VECTORISATION FLOWCHART. FOR MORE INFORMATION SEE THE SOFTWARE BOOK. THE PROCEDURE THAT INTERCONNECTS VECTORS USING THE STATISTICS MATRIX IS A COMPLEX NON DIRECTIONAL PROCEDURE BASED UPON THE 'SEARCH A CREST' LOOP.	146
FIGURE 4-31: LEFT THE DIGITAL TERRAIN MODEL WITH THE VECTOR DETECTIONS (MAGENTA LINES) AND RIGHT THE ELEVEN CREST LINE VECTORS PLOTTED IN 2D.....	147
FIGURE 4-32: A PROCESSED SECTION OF A BATHYMETRY RASTER.....	147
FIGURE 4-33: A DETECTION ALGORITHM AND THE STATISTICS MATRIX CALCULATED FROM THE OTHER DETECTION MATRICES.....	148
FIGURE 4-34: THE VECTORS DERIVED FROM THE CREST LINE MATRIX AND THE STATISTICS MATRIX.....	148
FIGURE 4-35: IMPEDANCE MAP PLOTTED ON TOP OF A TOPOGRAPHY TILE, THE HIGHEST IMPEDANCES CAN BE FOUND IN BETWEEN THE RIPPLES AND ON THE SIDE OF THE RIPPLES WHERE EROSION OCCURS.....	150
FIGURE 4-36: THE GRAIN SIZE DISTRIBUTION PLOTTED ON TOP OF THE BATHYMETRY TILE. THE DARKER HOMOGENEOUS REGIONS ARE LOCATED ON TOP OF THE CRESTS, WHILE THE PLACES WITH A HIGHER VARIATION IN GRAIN SIZES ARE LOCATED IN BETWEEN THE RIPPLE STRUCTURES. THIS PHENOMENON BECOMES MORE AND MORE APPARENT WITH DEVELOPMENT MATURITY OF THE SEAFLOOR (MORE CYCLES). ALSO SEE FIGURE 4-24 FOR A SIMILAR VERSION OF THIS FIGURE THAT HAS BEEN PROCESSED USING A 3x3 MOVING AVERAGE FILTER.....	150
FIGURE 4-37: RAY BENDING IN A WATER COLUMN OF 20 METER CAUSED BY AN EXTREME ACOUSTIC VELOCITY GRADIENT. THE LEFT FIGURE DISPLAYS THE VELOCITY GRADIENT, THE RIGHT FIGURE DISPLAYS THE ACOUSTIC RAY PATHS TROUGH THE WATER COLUMN.	152
FIGURE 4-38: RELATIVE SURFACE DEFORMATION CAUSED BY THE RE-PROJECTING OF THE SURFACE IN AN ISO-VELOCITY MEDIUM. THE RED CURVE IS THE ORIGINAL SURFACE: A HORIZONTAL SURFACE AT 20 METRE OF FIGURE 4-37. AFTER PROJECTING THE ACOUSTIC TRAVEL DISTANCES IN A MEDIUM WITH A UNIFORM SOUND SPEED THE BLUE SURFACE APPEARS.	152
FIGURE 4-39: THE TOP TWO FIGURES DISPLAY THE PRINCIPLE OF RAY BENDING DUE TO A VELOCITY GRADIENT AND THE EFFECT ON THE SHADOW (BLUE). THE EQUIVALENT IN THE MODEL SAND DUNE FIELD IS A TRANSDUCER HELD APPROXIMATELY 10 METER ABOVE A SAND DUNE FIELD. LEFT THE WATER COLUMN HAS AN INCREASING LINEAR SOUND VELOCITY GRADIENT AND RIGHT WITH A LINEAR DECREASING SOUND VELOCITY GRADIENT. THE RESULTING SHADOW CALCULATION IS DISPLAYED (SHADOW = BLUE). .	154
FIGURE 4-40: A MULTISTATIC APPROACH IS A COMBINATION OF BISTATIC APPROACHES. AND EVERY BISTATIC SET-UP IS A COMBINATION OF TWO MONOSTATIC APPROACHES. MULTIPLYING BOTH MONOSTATIC MATRICES (LEFT) GIVES THE BISTATIC MATRIX (RIGHT). SHADOW IS EQUAL TO ZERO, WHILE VISIBLE IS EQUAL TO ONE. NOW INTRODUCING BEAM PATTERNS ENABLES FAST CALCULATION OF THE ACOUSTIC RESPONSE.	156
FIGURE 4-41: SHADOW MATRICES AND COMBINATION OF BOTH RECEIVER AND SOURCE MATRIX. THE GREEN AND BLUE DOTS ARE THE RECEIVER AND SEND ARRAY. THE GREEN CIRCLES ARE THREE OBJECTS INTRODUCED IN THE MODEL.....	159
FIGURE 4-42: THE FINAL RESULT OF A MODELING CYCLE. THE TOP FIGURE IS THE IMPULSE RESPONSE OF THE ENVIRONMENT, THE CENTRE FIGURE IS A BURST USED IN THE CONVOLUTION (CONVOLUTION HAS BEEN TAKEN TO SIMPLIFY THE CALCULATION, NOTE THAT HERE ANY KIND OF ALGORITHM CAN BE USED.). THE BOTTOM FIGURE SHOWS THE RESULT OF A BISTATIC ACOUSTIC TEST, WHERE BOTH SOURCE AND RECEIVER HAVE A SPHERICAL POWER PATTERN.....	160
FIGURE 4-43: FLOWCHART OF THE COMPLETE MODELING FLOW. SHADOW CALCULATIONS ARE AN IMPORTANT PART IN IT AND ARE SPLIT UP IN THREE UNITS: OBJECTS, RECEIVE AND SEND ARRAY. AFTER CALCULATING THE SHADOWS, THE POINT SCATTERERS ARE GENERATED WITH FED PSEUDORANDOM ALGORITHMS. AFTER GENERATING THE SCATTER POSITIONS, THEY ARE RAY TRACED FROM BOTH THE SEND AND RECEIVE ARRAY AFTER WHICH THE BEAM PATTERNS AND WAVELETS CAN BE APPLIED.....	161

LIST OF ABBREVIATIONS

2D:	two dimensional
3D:	three dimensional
ADCP:	acoustic Doppler current profiler
ALOD:	acoustic level of detail
ASW:	anti submarine warfare
AUV:	autonomous underwater vehicle
BRM:	burial registration mine
CTD:	conductivity, temperature and depth probe
DEM:	digital elevation model
DGPS:	differential global positioning system
DTM:	digital terrain model
ECUA:	European Conference on Underwater Acoustics
FFT:	fast fourier transform
GPS:	global positioning system
HRS:	high resolution seismics
IFFT:	inverse fast fourier transform
ISAR:	inverse synthetic aperture radar
LBL:	long baseline positioning system
LOD:	level of detail
MCM:	mine counter measures
NEST:	NATO Expert System Trials
NRL:	Naval Research Laboratories
NURC:	NATO Undersea Research Centre
R/V:	research vessel
RCMG:	Renard Centre of Marine Geology
RMS:	root mean square
SAR:	synthetic aperture radar
SAS:	synthetic aperture sonar
SMBES:	Sea Mine Burial Expert System
SSA:	small slope approximation
ST-SMBES:	Specialist team on the Sea Mine Burial Expert System
TAW:	Tweede Algemene Waterpassing (geographic reference level used in Belgium)
TCP/IP:	internet protocol suite
TIN:	triangular irregular network
UDP:	user datagram protocol
USBL:	ultra short baseline positioning system
VHRS:	very high resolution seismics
VIOE:	Vlaams Instituut voor het Onroerend Erfgoed (Flemish Archaeological Institute)
VLIZ:	Vlaams Instituut voor de Zee (Flemish Institute for the Sea)

1 TRANSDUCER DESIGN AND IMPLICATIONS ON WAVELETS AND WAVE FIELDS

Today acoustic tools, acoustic transducers or sonar systems are commonly used tools in the fields of marine geology and marine biology. Transducers are used for visualizing the seafloor (reflection/refraction seismics and subbottom profilers), for visualization of the surface (sidescan sonar), for recording the bathymetry (multibeam echosounder), measuring currents (ADCP), finding fish (fish finding sonar), locating objects and for underwater navigation (LBL and USBL), detailed site investigation (underwater camera), data communication (acoustic modems),... Often scientists using acoustic means for measurements push the interpretations of the data to the very limits and sometimes even beyond. It is the need to push to the limits and to avoid pushing beyond the capability limits of a sonar system that triggered this research.

This thesis provides tools for better understanding acoustic systems and evaluations of existing tools. It does not only provide tools to have an idea about the performance of a sonar system, but it also provides tools to generate reliable sonar signals in 3D environments that can be used to test performance of processing algorithms.

Before analyzing and processing digital signals it is important to fully understand the system that produced the signal. In the cycle of transmitting and receiving signals five sections can be recognized: (1) the digital control system, (2) digital circuitry + the analog to digital and digital to analog converters, (3) analog signal treatment (low and high voltage), (4) transducers (passive and active) and (5) the environment.

All five sections are understood and documented up to a certain level of complexity. This chapter will focus on some basic knowledge about the transducers. First of all it will explain how transducers are used, secondly some special cases such as regular sonar systems, chirp and parametric sonar will be highlighted. The three examples will demonstrate why it is important to start with understanding transducers before moving on to processing and modeling. It will also demonstrate why beam pattern theory cannot be applied to broadband system modeling in conventional models.

1.1 INTRODUCTION

Transducers are the core of most acoustic systems. Understanding how a transducer is made, what frequency response it has, how it reacts on environmental changes is essential to understand the recorded signal. The definition of a transducer according to the Wikipedia is : “A transducer is a device, usually electrical, electronic, electro-mechanical, electromagnetic, photonic, or photovoltaic that converts one type of energy to another for various purposes including measurement or information transfer (for example, pressure sensors). **In a broader sense, a transducer is sometimes defined as any device that converts a signal from one form to another.**”

In this chapter a brief conceptual explanation about sonar theory will be given. This introduction enables understanding of the theory in the next chapters. For readers who would like to have a more detailed explanation about sonar theory, the following literature is suggested:

Basic introduction:

- Sound Propagation in the Sea (Urick 1982)
- An Introduction to Underwater Acoustics (Lurton 2002)
- Principles of Underwater Sound 3rd Edition (Urick 1983)
- Coastal Multibeam Sonar Training Course (Clarke, de Moustier et al. 2005)

Advanced with some very basic chapters:

- Underwater Acoustic System Analysis (Burdic 1991)
- High-Frequency Seafloor Acoustics (Jackson and Richardson 2007)

For those who want to go a lot deeper into transducer properties:

- Introduction to the Theory and Design of Sonar Transducers (Wilson 1988)

The colour scales used in the seismic images are the genuine grayscale (min = white, max = black) and the MATLAB® standard jet colour scale (blue=min, light blue, green=average, yellow, red=max). In sidescan sonar images, the copper colour scale (black=min, yellow=max) is used. The colour bars used are each time chosen in function of displaying the maximum detail. In vertical seismic profiling that often is the grayscale, in time slicing it often is the jet colour scale.

1.2 ACTIVE AND PASSIVE PIEZOELECTRIC TRANSDUCERS

Most transducers, both active and passive, used in underwater acoustics are piezoelectric elements. Piezoelectric elements can be cut out of minerals such as quartz, topaz, Rochelle salt,... or man-made crystals, ceramics or polymers (ex: lead zirconate titanate is the most common piezoelectric ceramic used today). Active elements are actuators or projectors, passive elements are known as sensors or hydrophones in the case of underwater acoustics. A piezoelectric element is an element that transforms pressure changes to electric charge, or the other way round: transferring electric charges to changes in dimensions of the piezoelectric element. The transformation from pressure to electricity is a function of the crystal cut and environmental conditions. Every transducer has a certain efficiency, sensitivity, frequency response and directivity. Efficiency and sensitivity are material properties and will not be covered. Frequency response will be briefly covered. Most of the attention will go to directivity patterns.

Figure 1-1 shows a conceptual sketch of how the amplitude of electric charge (Q) of a piezoelectric crystal varies with imposed frequency at a fixed temperature and pressure. If a frequency sweep is used by the acoustic system, then a sensor and actuator are built from different materials and the sensor uses a different zone in the frequency spectrum of the crystal.

Sensors preferably have a flat frequency response within the selected frequency range of use, while actuators are used there where the imposed frequency gives the maximum changes in amplitude of dimension (same as maximum in charge).

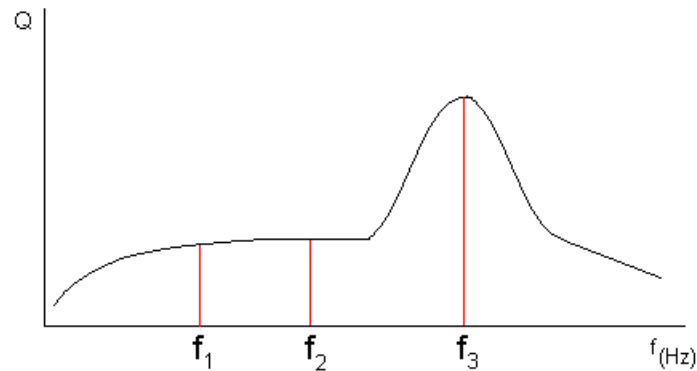


FIGURE 1-1: RESONANCE CURVE OF A PIEZOELECTRIC MINERAL. f_1 TO f_2 IS A LINEAR ZONE USED BY SENSORS, WHILE ACTUATORS ARE GENERALLY USED IN THE RESONANCE PEAK AT f_3 . WHEN THE TRANSMITTED FREQUENCY BAND IS VERY NARROW, SENSORS MIGHT BE USED AT f_3 .

1.3 POINT SCATTERING AND DIRECTIVITY PATTERNS

1.3.1 Point scatterer

Consider a compressing and expanding spherical unit in a uniform medium. Figure 1-2 depicts a two dimensional slice through that medium with in the centre the vibrating spherical unit and plotting the intensity or power in the direction of the Z axis. The compressional waves' energy decays with increasing distance from the source and spreads spherically.

An object can be decomposed into elementary spherical units, also known as scatter points.

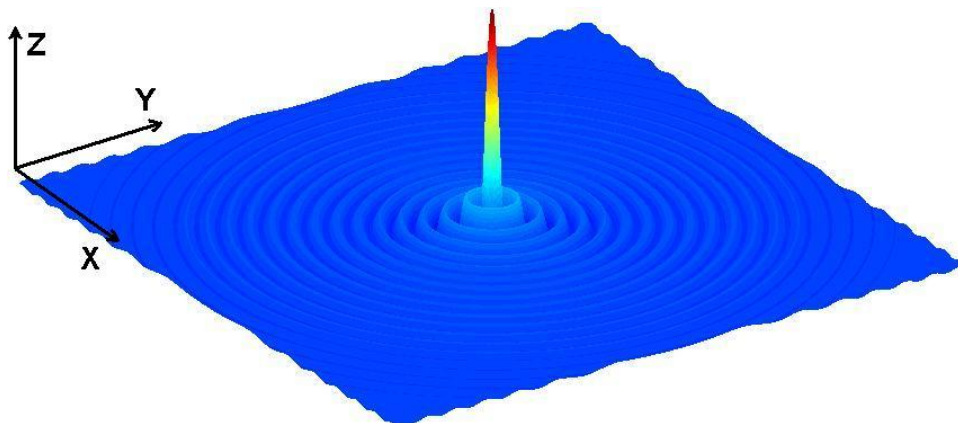


FIGURE 1-2: A SPHERICAL UNIT VIBRATES AND CREATES A SPHERICAL WAVE FIELD, THE FREQUENCY OF THE VIBRATION DEFINES THE WAVELENGTH OF THE WAVES. THE FIGURE SLICES THE SPHERICAL WAVEFIELD THROUGH THE SCATTERER. ALONG THE Z AXIS THE POWER INTENSITY IS PLOTTED. X AND Y AXIS ARE SPATIAL.

1.3.2 Line transducer

One vibrating point generates spherical waves. A line of points vibrating in phase at a fixed frequency with equal amplitude also generates spherical waves but the energy intensity within each wave front varies. The changing energy distribution can be used to focus or concentrate energy into a certain direction. Figure 1-3 demonstrates that when this focusing technique is used, side lobes appear. A full 3D representation of the wave fields can be found in Figure 1-4. Also in Figure 1-4 the connection between wavelength and array length is made clear.

Mathematically, the array emission pattern can be expressed as (Burdic 1991):

$$g(x) = \frac{1}{L} \text{RECT}\left(\frac{x}{L}\right)$$

With RECT a function that is 0 at $[-\infty, -x[$ and $]x, +\infty]$, 1 at $[-x, +x]$ (Figure 1-6, upper left function). The corresponding lobe pattern is (Fourier transform):

$$G(u) = \frac{1}{L} \int_{-\infty}^{+\infty} \text{RECT}\left(\frac{x}{L}\right) \exp(-j2\pi xu) dx = \text{SINC}(uL).$$

In the case of beam forming interpretation, the spatial frequency u can be interpreted as an angle. The angular width ψ_B of the main lobe is given by $u=1/L$ or if $L \gg \lambda$

$$\psi_B = \frac{\lambda}{L}$$

L is the length of the array, u is related to the spatial angle and λ is the wavelength of the transmitted waves. In Figure 1-4 the effect of increasing the array length L on the angular width of the main lobe or aperture is demonstrated. λ is a chosen wavelength. Since λ is used to define the lobe pattern, estimating the lobe pattern properties using this approximation can only be done for narrow band systems. Broadband systems are to be approached in a completely different way.

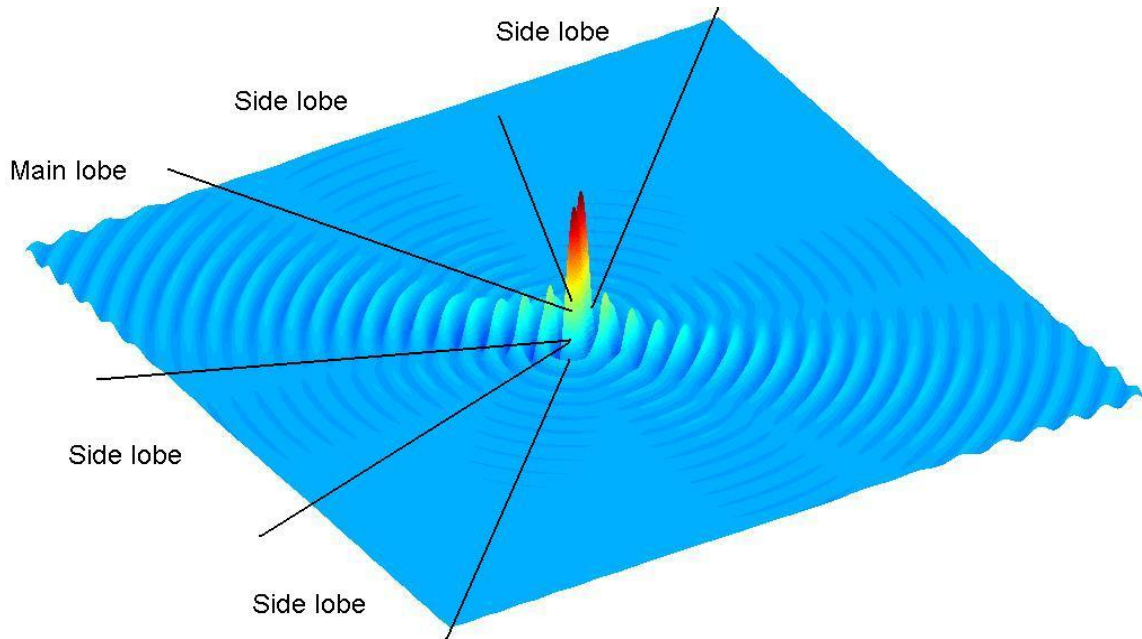


FIGURE 1-3: A LINE OF 100 POINTS VIBRATING IN PHASE. THE WAVE FRONTS ARE SPHERICAL BUT THE ENERGY INTENSITY WITHIN EACH WAVE FRONT VARIES. Z,Y,X AXIS IS TAKEN AS IN FIGURE 1-2.

1.3.3 Mills Cross

In 1.3.2, a line transducer was described in function of acoustic wavelength λ , a corresponding 3D acoustic pattern is visualized in Figure 1-4. The 2D section aligned with the line transducer has a pattern with certain energy concentrations, while the section perpendicular to the line array has uniform wave field and energy properties in every direction in the plane. When two perpendicular line arrays are transmitting or receiving in phase, three dimensional energy variations in the wave field are generated. In the literature, two perpendicular line arrays are referred to as Mills Cross. Mills Cross set-ups can be found back in any kind of acoustic equipment that aims to use narrow beams. The design of a mine hunting sonar, parametric sonar and a multibeam sonar are based upon this principle. Figure 1-5 visualizes the beam patterns in 3D.

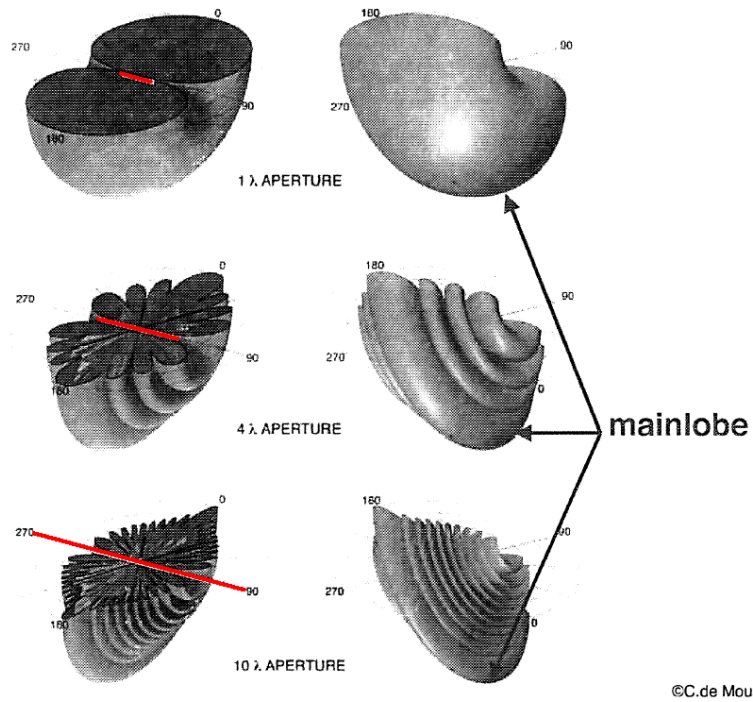


FIGURE 1-4: RADIATION PATTERNS FROM SOME ACOUSTIC LINE ARRAYS. ALL ARRAYS ARE CONSIDERED ONE DIMENSIONAL (INFINITELY THIN). THE LENGTH OF THE ARRAY AND THE WAVELENGTH OF THE ACOUSTIC WAVES PRODUCED BY THE ARRAY DEFINE THE BEAM PATTERN. THE LENGTH OF AN ARRAY IS DEFINED IN A NUMBER OF WAVELENGTHS (HERE 1, 4 AND 10 LAMBDA). WITH INCREASING LENGTH OF THE ARRAY THERE IS A DECREASING APERTURE. ADAPTED FROM: 39TH MULTIBEAM SONAR TRAINING COURSE (CHRISTIAN DE MOUSTIER) (CLARKE, DE MOUSTIER ET AL. 2005)

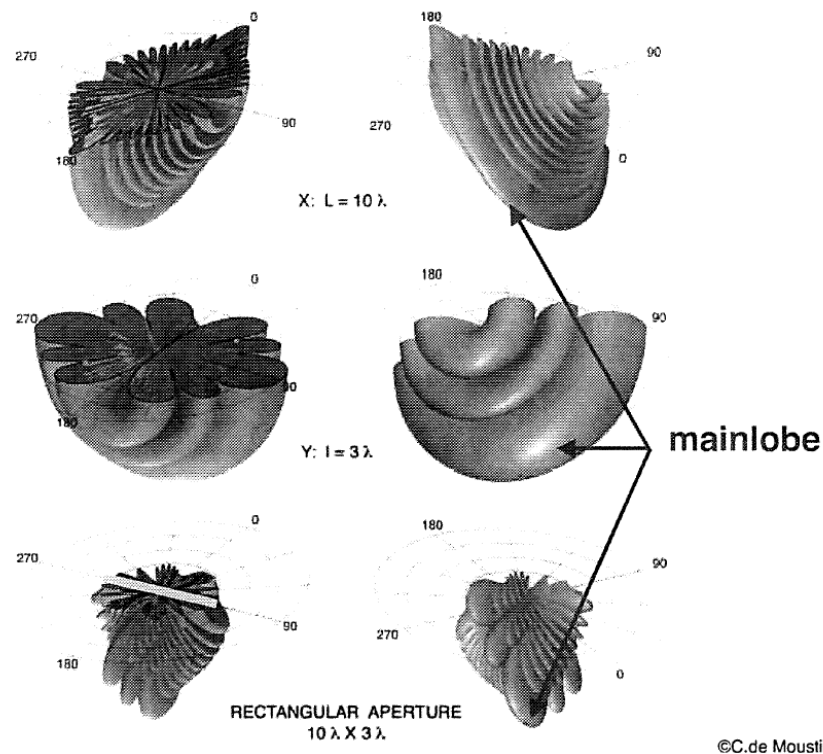


FIGURE 1-5: TWO LINE ARRAYS HAVE THEIR OWN DIRECTIVITY PATTERN, WHEN THESE TWO ARRAYS ARE CROSSED, A NEW DIRECTIVITY PATTERN EMERGES. COPIED FROM 39TH MULTIBEAM SONAR TRAINING COURSE, OCEAN MAPPING GROUP (CLARKE, DE MOUSTIER ET AL. 2005)

1.4 FOURIER TRANSFORM TABLE, AN EASY TOOL TO PREDICT DIRECTIVITY PATTERNS

As stated in 1.3.2, the Fourier transformation of the amplitude versus space results in the amplitude versus angle of incidence or directivity pattern of a line transducer. In the case of a *RECT* function the Fourier transform is a *SINC*. The power spectrum of a *SINC* function implies the existence of side lobes. Side lobes are in many acoustic systems undesired because they might restrict the performance in shallow water severely. The table of Fourier transforms shows that other functions might not have side lobes in their transformed counterpart. Windowing or enveloping reduces the power emitted by the outer transducers following a certain function. Figure 1-6 shows a table of Fourier transforms, on the left the power distribution along a line transducer is depicted, on the right the resulting spectrum (square the spectrum for a power spectrum) versus angle of incidence.

Examples of Fourier transforms

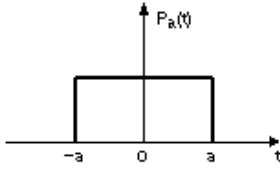

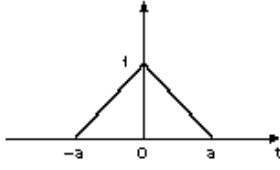
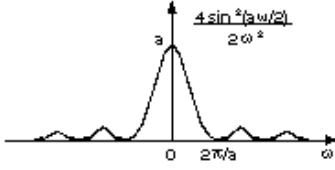
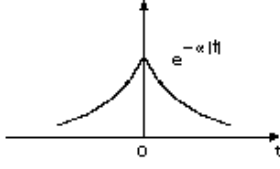
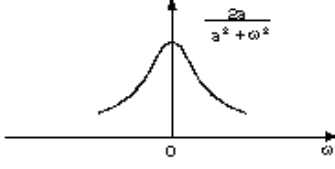
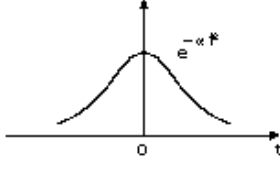
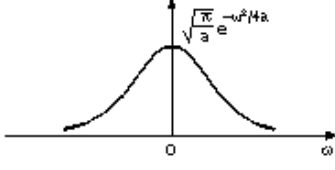
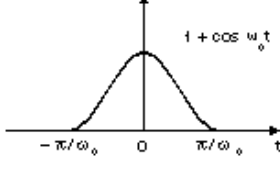
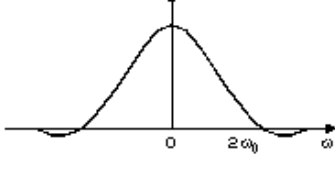
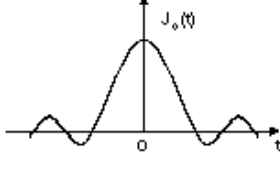
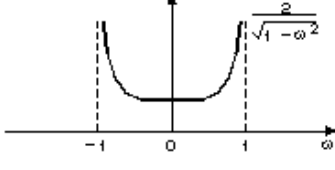
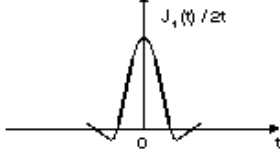
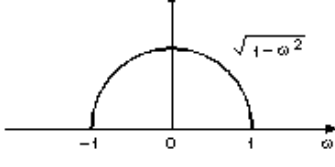
$f(t) = \frac{1}{2\pi} \int_{-\infty}^{\infty} F(\omega) e^{j\omega t} d\omega$	$F(t) = \int_{-\infty}^{\infty} f(t) e^{-j\omega t} dt$
	
	
	
	
	
	
	

FIGURE 1-6: THIS TABLE OF BASIC FOURIER TRANSFORMS CAN BE USED TO ESTIMATE THE DIRECTIONALITY OF THE WAVE FIELD PRODUCED BY AN ENVELOPED LINE TRANSDUCER. CONSIDER ON THE LEFT SIDE A LINE TRANSDUCER ALONG THE TIME AXIS (CHANGE TIME TO SPACE). THEN THE RIGHT SIDE OF THE IMAGE DEPICTS THE AMPLITUDE VARIATIONS VERSUS THE ANGLE OF INCIDENCE (CHANGE Ω TO Φ). REFERENCE: [HTTP://WEBHOST.ETC.TUIASI.RO/CIN/DOWNLOADS/FOURIER/TABLE2.GIF](http://webhost.etc.tuiasi.ro/cin/downloads/fourier/table2.gif)

1.5 SIDE LOBE SUPPRESSION AND BEAM STEERING

Figure 1-6 provides insight in side lobe suppression; certain windows in the space domain along the line transducer, such as the Hanning window, have smaller side lobes in their transformed counterparts (Figure 1-7). The downside of side lobe suppression is a wider main lobe and the loss of energy due to the fact that only the centre transducer elements emit the maximum energy. This phenomenon is also known in filter design, where energy lost in the side lobes is described as spectral leakage. Other window functions with low spectral leakage are: Hamming, Blackman, Blackman-Harris, Blackman-Nuttall, Gauss,... (Cohen 1995; Oppenheim, Schaffer et al. 1999; Mitra 2006; Trauth, Gebbers et al. 2007).

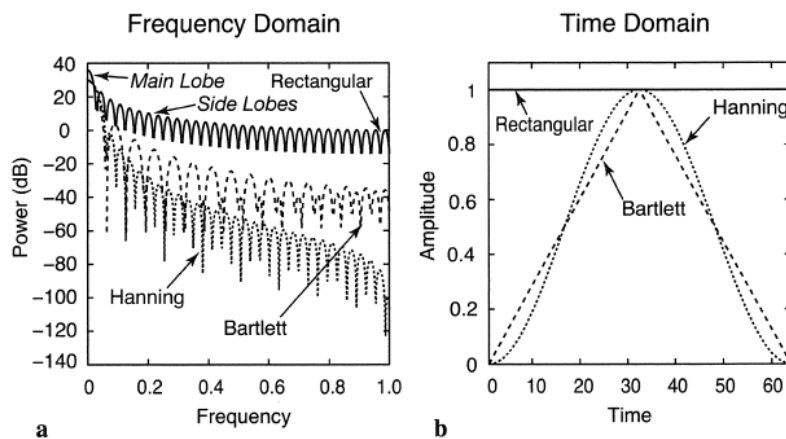


FIGURE 1-7: SIDE LOBES ARE NOT ONLY A PROBLEM IN TRANSDUCER DESIGN, THEY ARE ALSO PROBLEMATIC IN FILTER DESIGN (SPECTRAL LEAKAGE). THE HANNING WINDOW IS IN THIS CASE THE BEST OPTION TO REDUCE THE SIDE LOBES. COPIED FROM: MATLAB® RECIPES FOR EARTH SCIENCES (TRAUTH, GEBBERS ET AL. 2007).

Beam steering has, at first sight, nothing to do with power spectra but all with phase spectra. Beam steering can be done in two ways: by adding to every discrete transducer element a ping to ping delay or by physically turning the array. Adding a delay or phase to the discrete elements of a transducer can be done both in an active and in a passive system. Active beam steering is frequently applied in the field of parametric sonars. Passive beam steering is by far the easiest, most flexible to apply and the most commonly used in underwater acoustics. Passive beam steering needs no extra electronic steering circuitry (ex: multibeam sonar), the steering is done by software or firmware. Beam steering is limited by the side lobes formed. The more phase is added to an array, the larger some of the side lobes become. A combination of physically turning the array and software beam steering is sometimes applied in multibeam sonars such as the Kongsberg EM1002.

1.6 CONVENTIONAL SONAR

Conventional sonars, sometimes referred to as pingers, usually produce in the time domain an enveloped sine-like burst. In the frequency domain, the spectrum of the burst looks like a narrow Gauss curve. Due to the narrow band, the directionality pattern of the pinger does not change significantly throughout the burst and the burst itself does not change significantly

throughout the directionality pattern. The beam pattern approximation usually applies to this type of acoustic sources.

1.7 A SPECIAL CASE: CHIRP

A Chirp source is a broadband source where both the frequency spectrum and the phase spectrum are controlled and steered during emission time of the pulse (Figure 1-8). The term burst should be replaced by the more appropriate term: frequency sweep or shorter: sweep. As a consequence of the manipulation of the spectra, not only the directionality pattern changes during the sweep but also the sweep itself becomes an angular function. The beam pattern theory applies to every single frequency in the system but cannot be applied to approximate the beam pattern of the system itself. Here the beam pattern should be replaced by wavelet pattern (Figure 1-10).

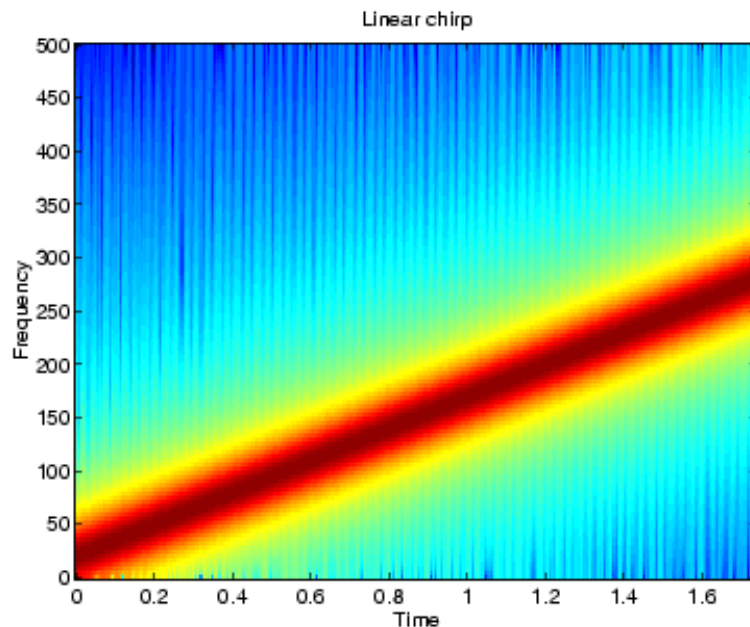


FIGURE 1-8: COPIED FROM MATLAB®, SIGNAL PROCESSING TOOLBOX, CHIRP HELP FILE. THIS FIGURE SHOWS HOW THE FREQUENCY CHANGES IN FUNCTION OF TIME FOR A LINEAR CHIRP. BASICALLY IT IS THE FOURIER TRANSFORM TAKEN IN A WINDOW RUNNING OVER THE SWEEP.

The standard processing of a received subbottom echosounder chirp signal to extract the subbottom image, Figure 1-9, is done by taking the absolute value of the Hilbert transform of the cross correlation of the received signal with the chirp signal sent to the transducers.

For standard sub-bottom imaging the elementary processing technique described before can be applied without any problem. When migration is to be applied, sound velocity information is needed. The migration algorithm focuses all contributions of each scatter point in each scatter point respectively. According to Figure 1-10, the sound velocity entered in the migration algorithm will have to be over estimated. Each contributing signal trace should be correlated with the correct sweep in order to find the contributions of a wave field within the aperture. Figure 1-10-3 displays the correlation of every contribution in the aperture with the real sweep the scatter point received. Figure 1-10-4 displays a standard processing; cross correlation of the

contributions of one scatter point with the original linear chirp sweep is done. Figure 1-10-4 shows how, with decreasing angle of incidence, the correlation makes a time shift and eventually splits up into two reflectors. This effect, when not taken into account, changes the steepness of the hyperbola or in other words the sound velocity. This effect can have a significant influence on migration algorithms.

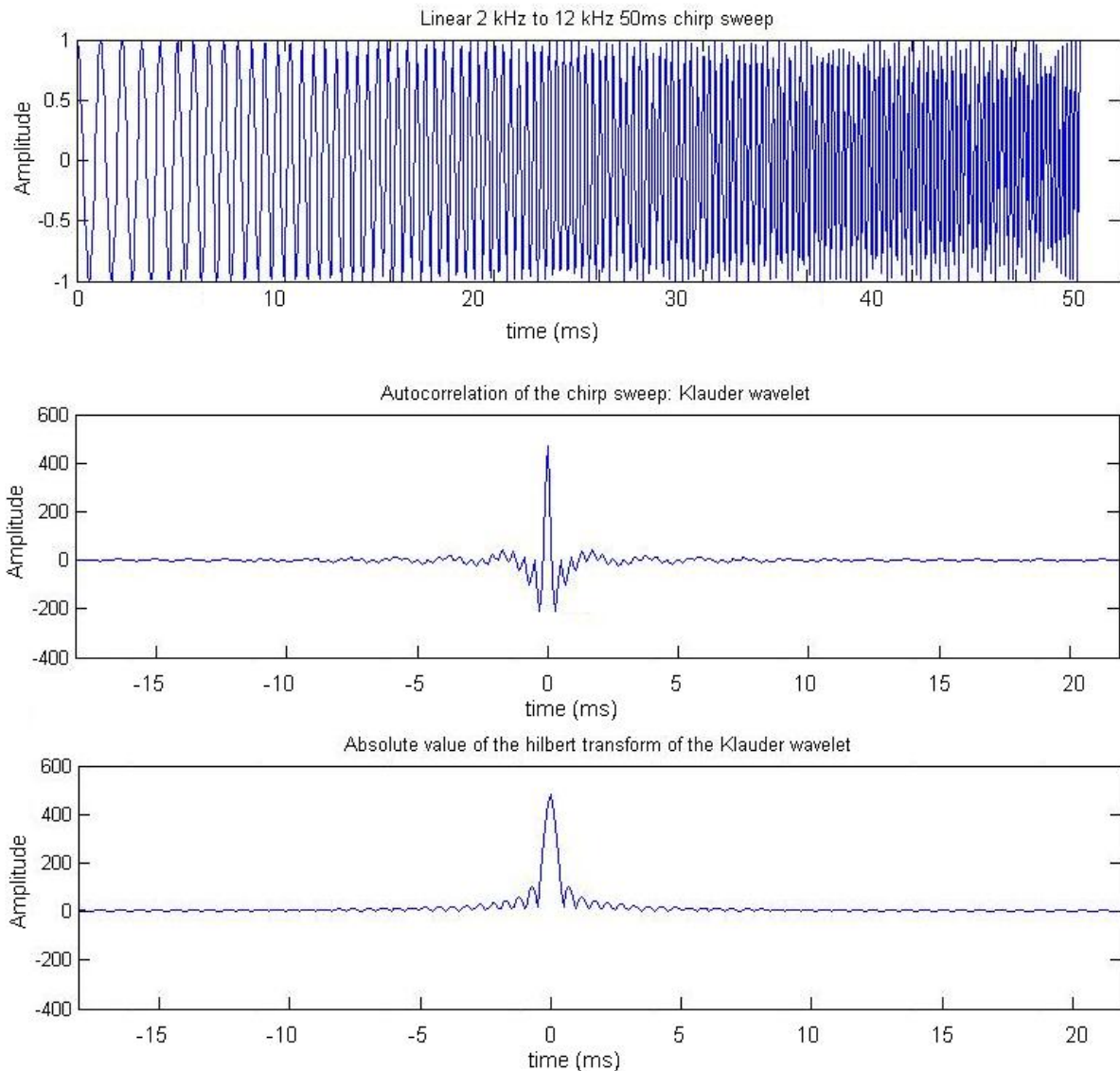


FIGURE 1-9: SUBBOTTOM CHIRP PROCESSING IN PRACTICE. FROM TOP TO BOTTOM: TOP: THE LINEAR CHIRP SWEEP, CENTRAL: THE AUTOCORRELATION OF THE CHIRP OR KLAUDER WAVELET AND AT THE BOTTOM THE ABSOLUTE VALUE OF THE HILBERT TRANSFORM OF THE KLAUDER WAVELET. THE TERM AUTO-CORRELATION IS USED WHEN A CROSS-CORRELATION IS DONE FROM A SIGNAL WITH ITSELF.

Windowing the chirp array signal in both space and time or repeating all the correlations in every aperture with the correct wavelet can help to generate correlated signals that can be used in migration algorithms.

The signals in Figure 1-10 were generated using the MATLAB® script: `initburst.m`, `vblock.m` and `discretetransd.m` (described in the software book). Figure 1-10-1 demonstrates that the beam

pattern theory becomes useless with this type of broadband sources and a wavelet pattern should be used in acoustic models and migrations.

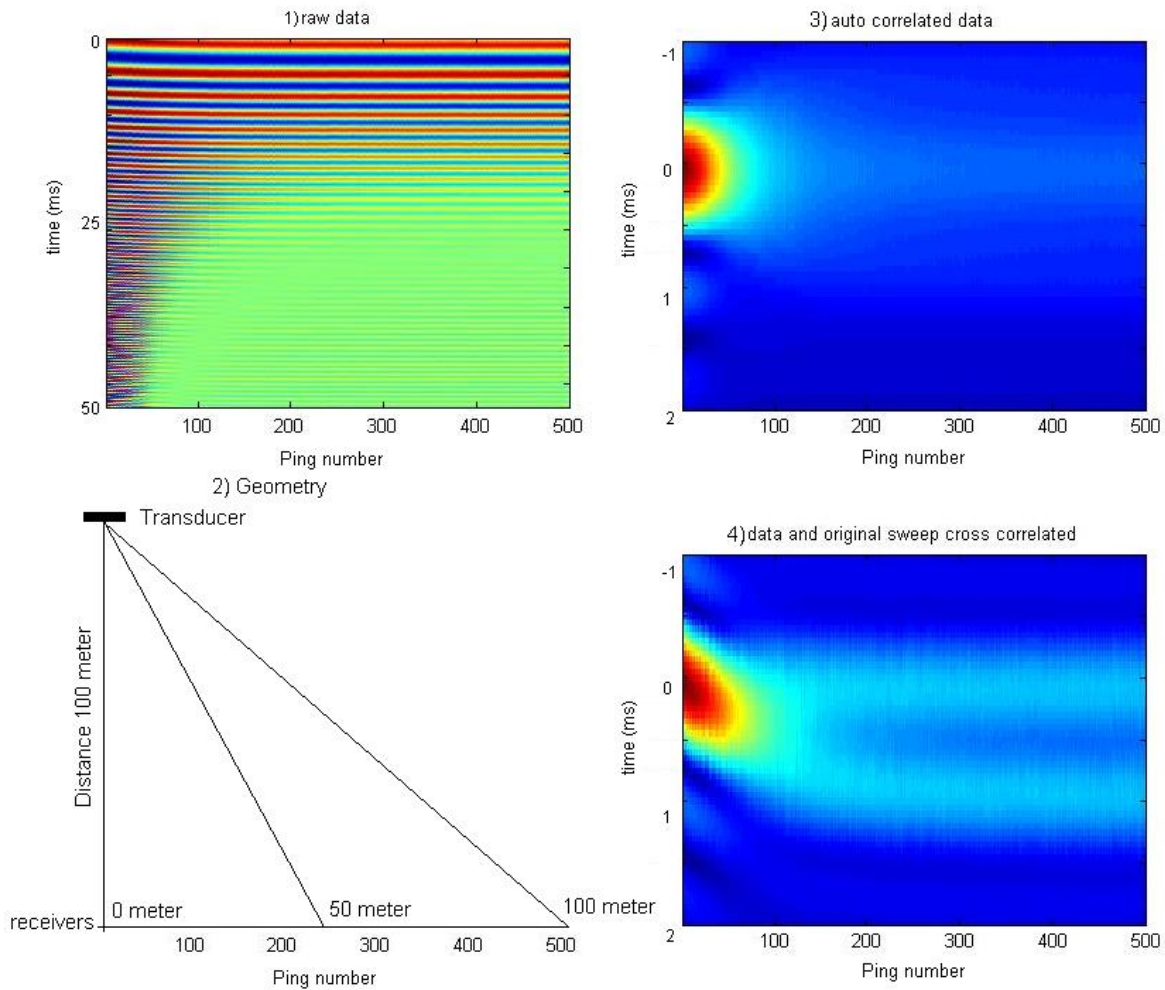


FIGURE 1-10: IMAGE 1 DISPLAYS A RECORD OF CHIRP SWEEPS (2 KHZ TO 12 KHZ, 50 MS, LINEAR CHIRP: DIMENSIONS 6 BY 60 CM) RECORDED IN THE FAR FIELD OF THE LINEAR ARRAY, STARTING IN THE CENTRE OF THE ARRAY AT A DISTANCE OF 100 METER. THE GEOMETRY OF THE RECORDING IS DISPLAYED IN IMAGE 2. AT EVERY PING THE POSITION OF THE RECORDER IS DISPLACED 20CM OUT OF THE CENTRE, ON A LINE PARALLEL WITH THE LINE ARRAY. THE IMAGE DISPLAYS A CLEAR FILTERING EFFECT IN THE HIGHER FREQUENCY AMPLITUDES WITH INCREASING PING NUMBER. IMAGE 3 AND 4 DISPLAY TWO PROCESSED IMAGES. IMAGE 3 SHOWS AN AUTOCORRELATION FUNCTION OF EVERY RECORDED SWEEP. IMAGE 4 SHOWS A CROSS CORRELATION FUNCTION OF THE RECORDED TRACE WITH THE SWEEP THAT HAS BEEN SENT TO THE TRANSDUCER ELECTRONICS (STANDARD SUBBOTTOM SONAR PROCESSING). IMAGE 4 SHOWS HOW A REFLECTOR BECOMES DOUBLE AND GETS A TIME SHIFT THROUGHOUT THE APERTURE. THIS EFFECT WILL GENERATE UNDERMIGRATED PROFILES WHEN MIGRATION IS APPLIED WITH CORRECT VELOCITY INFORMATION FED INTO THE ALGORITHM.

1.8 NEAR FIELD AND FAR FIELD

The recording of the radiation of a transducer can be decomposed in near field and far field regions in space (Lurton 2002). The near field or Fresnel zone refers to the region close to the transducer face. The signal recorded in the near field oscillates with the distance. The signal contributions of the different point scatterers describing the transducer face are strongly out of phase in the near field. Also the average amplitude decreases more rapidly than spherical ($1/R^2$). R is the distance between the transducer and the recording point. The far field or Fraunhofer zone refers to the region where the signal contributions from each point scatterer describing the transducer face are no longer strongly out of phase. In this region spherical spreading of the energy appears and the amplitude decays with a rate of $1/R$.

Figure 1-11 shows a line transducer of length L , radiating a signal of wavelength λ and a recording point at distance x . A signal oscillates as long as the path difference of the signal emitted from the contributing point scatterers is at least equal to $\lambda/2$. δR is the path difference and can be calculated.

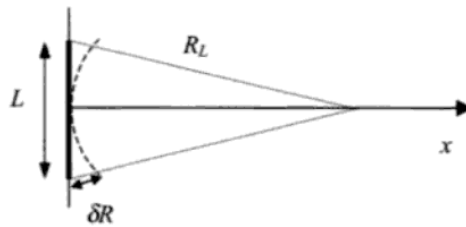


FIGURE 1-11: MEASURING THE PATH DIFFERENCE FOR A LINE TRANSDUCER

$$\delta R = R_L - x = \sqrt{x^2 + \left(\frac{L}{2}\right)^2} - x \approx \frac{L^2}{8x}$$

The Fresnel zone has a limit called the Fresnel distance D_F :

$$\frac{L^2}{8x} \geq \frac{\lambda}{2} \Leftrightarrow x \leq \frac{L^2}{4\lambda} \Rightarrow D_F = \frac{L^2}{4\lambda}$$

Beyond the Fresnel distance the field cannot oscillate anymore. The radiating regime of the far field is reached at 4 times the Fresnel distance (amplitude decrease at $1/R$) or L^2/λ .

1.9 PARAMETRIC SONAR

The research of non linear acoustics was the base of the development of the parametric sonar. The method manipulates spectra by combining a high frequency signal (spectrum f_1) into another very narrow band high frequency signal (spectrum f_2). Two new secondary frequencies emerge: f_1+f_2 and f_1-f_2 . The secondary frequencies generated are more than 10 dB lower compared to the primary frequencies. Therefore filters play an important role in extracting the secondary frequencies.

In a radio application a similar technique is used. An antenna receives a high frequency signal f_1 (around 100 MHz), containing for example audio data. The receiver, through an oscillator and mixer, injects in the amplified received signal a narrow band frequency f_2 . As a result the

received signal f_1 is projected into the audio region f_1 - f_2 . The other components of the signal (f_1 , f_2 , f_1+f_2 , and some higher order inter modulation products) are suppressed by an analog filter (mostly Chebychev filters).

Since the early sixties of the twentieth century the research field of non linear acoustics has been expanding rapidly. Recent publications cover both the history as the mathematics in this field (Beyer 1997; Hamilton and Blackstock 1998). The publications referred to in the introduction do not cover this type of sonars. Parametric sonar was used only once during this research. Going into the complex mathematics of the system was not part of the research, but still a number of milestones should be mentioned. The history of non linear acoustics goes back to 1766 when Euler derived an equation for non linear acoustic plane waves in air. A century later Earnshaw (1860) found the correct law of propagation of progressive waves. Lagrange (1761) and Poisson (1808) contributed by solving non linear wave equations. Airy (1849) contributed by presenting the theory of nonlinear plane waves in a lossless fluid. Another contributor to the field was Stokes who showed waveform distortion caused by the dependence of propagation speed on particle velocity. The effect essential for the parametric sonar was first described: nonlinearities in wave propagation. Other contributors were Lord Rayleigh, Hugoniot, Fay, Bateman, Burgers and Taylor. In the second half of the twentieth century, theory was put into practice and experiments. According to Fried (Fried 1992), in the late fifties and early sixties of the twentieth century, the theory for this sound source was developed by P.J. Westervelt, he called it: a parametric acoustic array. Lighthill developed the theory of nonlinear interaction. At his turn Westervelt formulated the theory of scattering of sound by sound. Their work was later expanded mainly by Muir and Bjorno. This eventually led to the classical theory for the parametric acoustic array. (Lighthill 1952; Lighthill 1952; Westervelt 1957; Westervelt 1957; Beyer 1960; Westervelt 1963; Muir and Willette 1972; Konrad 1974; Bjorno 1977; Moffett and Mellen 1977; Bjorno, Folsberg et al. 1979) Beyer defined by experiment the nonlinearity parameter of the medium water $B/A = 5$ (Beyer 1960).

$$\beta = 1 + \frac{1}{2} \frac{B}{A}$$

The acoustic wave speed at a particular point in a sound wave varies with the particle velocity at that particular point.

$$\frac{dx}{dt} = C_0 + \beta \frac{du}{dt} = C_0 + \beta \frac{p}{\rho C_0}$$

where dx/dt is the acoustic wave speed at a certain point in the sound wave. It is the summation of the sound speed (C_0) and the nonlinearity parameter (β) defined by Beyer multiplied with the particle velocity (du/dt) at the specified point in the sound wave. The particle velocity can be rewritten in function of the density (ρ) of the medium, the sound speed (C_0) and the acoustic pressure (p). This equation explains why a sinusoidal wave will evolve to a sawtooth wave and eventually become a shockwave.

Kuznetsov contributed by defining the Kuznetsov equation. Eventually the Khokhlov-Zabolotskaya-Kuznetsov or KZK equation was defined (Zabolotskaya and Khokhlov 1969;

Kuznetsov 1971), an equation still used today. The KZK equation below describes the combined effects of diffraction, nonlinearity and absorption in directional sound beams.

$$\frac{\partial^2 p}{\partial z \partial \tau} = \frac{C_0}{2} \nabla_{\perp}^2 p + \frac{\delta}{2C_0^2} \frac{\partial^3 p}{\partial \tau^3} + \frac{\beta}{2\rho C_0^3} \frac{\partial^2 p^2}{\partial \tau^2} \quad (= \text{diffraction} + \text{absorption} + \text{nonlinearity})$$

And $\tau = t - \frac{z}{C_0}$

The parameter δ is the sound diffusivity, τ the retarded time and Z is the nominal axis of the beam pattern pointing in the direction of the wave propagation, with z a point on that axis.

During the seventies of the twentieth century, the path to constructing hydrographic equipment was opened, the TOPS projector is just one example (Konrad 1974). These developments triggered extensive research in sub bottom acoustic imaging, in the extraction of sedimentological parameters and in the seafloor characterization, derived from the acoustic response of the seafloor. Recent projects dealing with more advanced parametric sonars and buried waste detection is for example the SITAR project (Blondel, Pace et al. 2007).

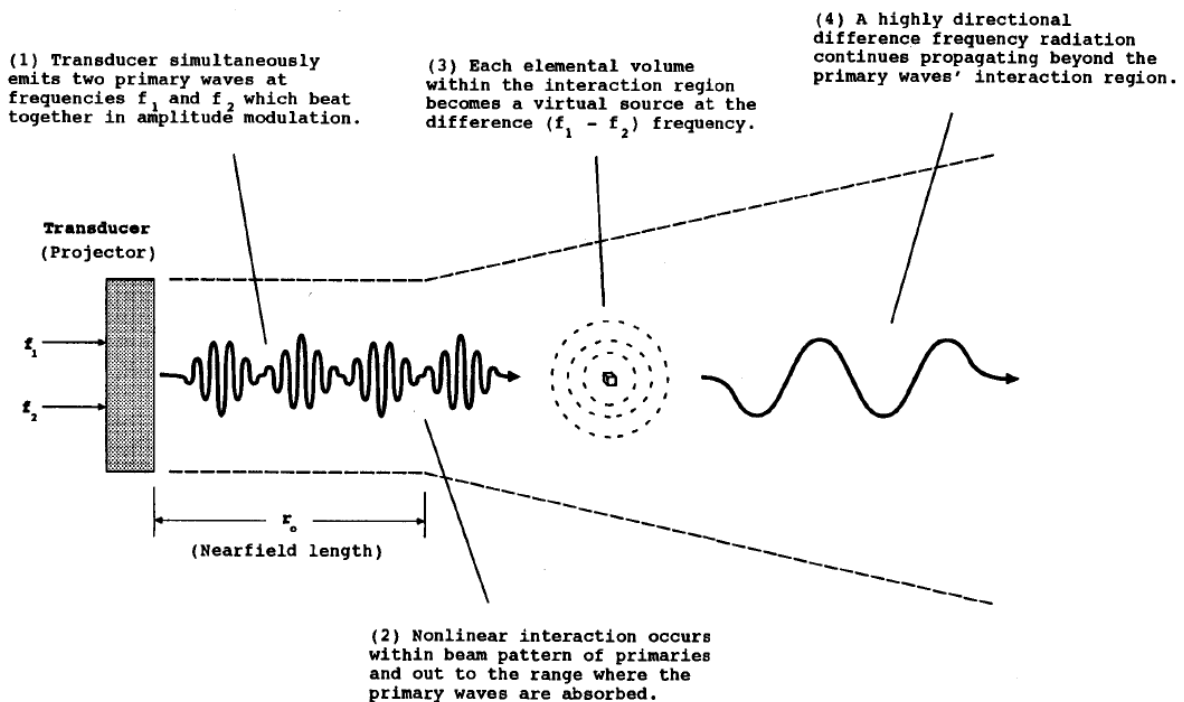


FIGURE 1-12: NEAR FIELD AND FAR FIELD OF A PARAMETRIC SONAR

The parametric sonar has some advantages, a standard bottom penetrating acoustic source does not have. The first one is the beam pattern. The pencil beam pattern or very narrow beam is derived from the two relatively high frequency transducer arrays are used to generate the sound. If that pencil beam has to be formed with conventional transducers, a much bigger transducer plate should have been needed. A second advantage is the side lobe suppression. With a conventional transducer plate there are side lobes. In the case of the parametric sonar,

the side lobes are often suppressed. A third advantage of the system is that the near field is related to the primary frequencies used and not to the secondary frequency. The near field of a standard sonar is bigger than the near field of a parametric sonar. The parametric sonar can as such be used closer to the seafloor. A fourth advantage is that the signal sent to the seafloor is much more under control than the signal from a seismic source, enabling extraction of sedimentological parameters. The major disadvantage is the low energy efficiency.

1.10 MIGRATION OR IMAGE FOCUSING (SAS)

1.10.1 Image focusing or migration concepts

In the previous chapters, properties of sonar systems were described. There are no sonars with an infinitely narrow beam. All sonars have a certain beam width or opening angle, also called aperture. In practice that means that the received signal always is a convolution of the source signal, amplitude and shape related to the beam pattern (see section 1.7) with the impulse response of many scatter points or areas. Digital signal processing will be the only option to focus the image. Synonyms for a focusing algorithm are migration or synthetic aperture. A good reference about migration algorithms is *Seismic Data Analysis* (Yilmaz 2001) and *Numerical Methods of Exploration Seismology with algorithms in Matlab®* (Margrave 2001; Margrave 2003). Some migration algorithms are: Kirchhoff migration, f-k migration, Stolt migration, phase shift migration, finite difference migration and reverse time migration. The most known or commonly used are the Kirchhoff migration (time space domain), phase shift migration (frequency space domain) and f-k migration (frequency wavenumber domain). Phase shift migration is not discussed or used in this thesis, Kirchhoff and f-k migrations are used in chapter 3 and discussed in the following sections.

Figure 1-13 and Figure 1-14 displays the basics of migration algorithms. Three point scatterers are located on top of each other in different stratigraphic layers. A zero offset acoustic transceiver approaches the scatterers from the left to the right. The resulting acoustic profile is shown as the upper left image of Figure 1-14 and the right image in Figure 1-13. The other upper images in Figure 1-14 are time slices at the apex of each hyperbola. The simplest migration to understand is the Kirchhoff migration or Kirchhoff summation. Using the velocity information, a summation of data is done along a hyperbolic path. Summing data or stacking data requires, for an optimum result and maximum noise cancellation, a high spatial data density. If that spatial density within the aperture taken is too low, image degradation might occur.

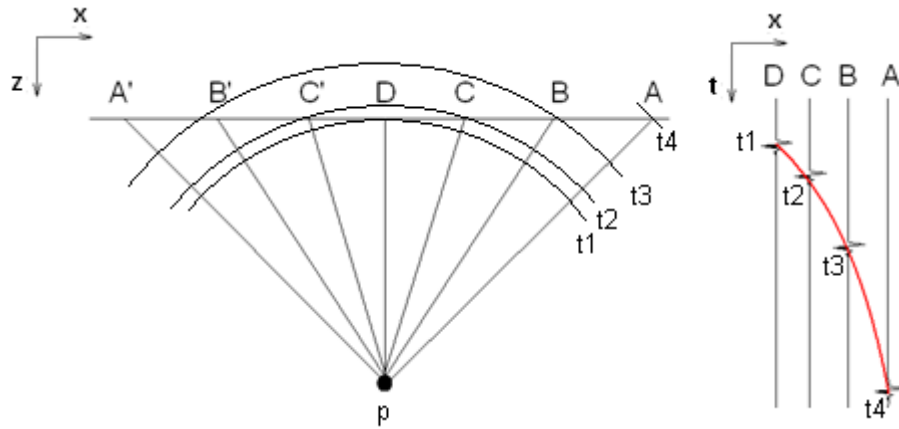


FIGURE 1-13: LEFT: A POINT SOURCE P EMITS A SPHERICAL WAVE RECORDED AT A, B, C AND D IN THE X-Z PLANE. RIGHT: THE OBSERVATIONS IN A,B,C AND D PLOTTED IN FUNCTION OF TIME RESULTS IN A HYPERBOLIC FUNCTION IN THE X-T PLANE. THE STEEPNESS OF THE HYPERBOLA IS A FUNCTION OF THE WAVE PROPAGATION SPEED.

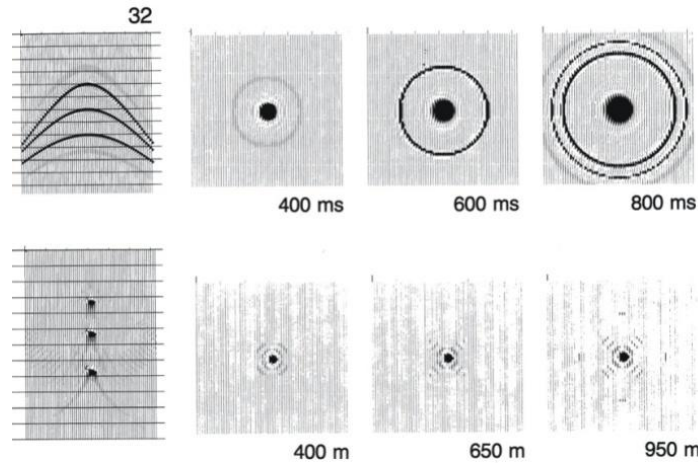


FIGURE 1-14: UP: A SYNTHETIC ACOUSTIC PROFILE WITH THREE SCATTERERS IN A MEDIUM WITH A VELOCITY GRADIENT AND BELOW THE MIGRATION RESULTS. LEFT FIGURE ARE SPACE-TIME PROFILES, THE OTHER SIX ARE SPACE-SPACE SECTIONS OR TIME SLICES. COPIED FROM SEISMIC DATA ANALYSIS (YILMAZ 2001)

1.10.1.1 KIRCHHOFF MIGRATION IN DETAIL

Kirchhoff migration or diffraction summation was the first computer implementation of a migration. Figure 1-13 displays a point p acting as a Huygens' secondary source. A zero offset recording is performed at points A, B, C and D. In the x - z plane the spherical wave is a semi circle. While in the x - t plane the corresponding wave arrival is expressed by a hyperbola. A seismic section consists of many secondary sources p . Consider now the single secondary source p in Figure 1-13. Kirchhoff migration sums along a hyperbolic path all the contributions of secondary source p (in A, B, C and D) and plots the result in a new x - z plane, where p will again be a point.

Time t_1 is the two way travel time of D to p in a medium with propagation velocity v . Time t_2 , t_3 and t_4 are the two way travel times of receivers A, B and C to p . The relation of t in function of the distance between the different receivers on the X axis can be described as:

$$t^2 = t_1^2 + \frac{4x^2}{v^2}$$

This gives the travelttime trajectory for a hyperbola with the apex at two way travel time t_1 . In the migration process the summing will take place in the x-t plane along this travelttime trajectory. Now amplitude and phase changes along the hyperbolic path have to be introduced. Three major factors play a role: the obliquity factor of the sound source (previously described as beam pattern), spherical spreading and wavelet shaping. A sound source never emits a perfectly spherical wave, as previously demonstrated it has a certain power pattern. When p is insonified from an oblique angle of the sound source in A, B or C, it will be insonified with lower power. The power pattern has to be introduced in the equation, in migration algorithms this may be referred to as the cosine taper (Margrave 2001; Margrave 2003). Spherical spreading of the wave will result in amplitude changes. Wave energy decays as $1/r^2$, with r the distance between p and the receiver, while the amplitude decays as $1/r$. The amplitude must be scaled with a factor $1/r$ as a result. When many point scatterers p are close together, amplitude cancellation along the hyperbolic path may occur. The resulting summation must be restored in both phase and amplitude. Neglecting near field terms the equation for $P_{out}(x_0, z=vr/2, t=0)$ at a location (x_0, z) computed from the 2D zero offset wavefield $P_{in}(x, z=0, t)$ measured over the aperture at the surface ($z=0$) becomes:

$$P_{out} = \frac{\Delta x}{2\pi} \sum_x \left[\frac{\cos \theta}{\sqrt{vr}} \rho(t) * P_{in} \right]$$

$$r = \sqrt{(x - x_0)^2 + z^2}$$

Where r is the distance between the input $(x, z=0)$ and the output (x_0, z) . The rho filter $\rho(t)$ is convolved with the input wavefield P_{in} .

1.10.1.2 F-K MIGRATION IN DETAIL

Fast fourier transforms (FFT, IFFT) are very powerful and computing time efficient algorithms. Kirchhoff migration may have been the first migration implemented on a computer. It was not the fastest. The need for optimization of algorithms at the very beginning of the existence of the computer was imminent. In the late seventies of the twentieth century the f-k migration was proposed (Stolt 1978; Chun and Jacewitz 1981). The f-k migration fourier transforms the data both along the time and space axis to the frequency (f) and wavenumber (k) domain.

We consider a 2D wavefield $P(x, z, t)$ passing through a medium with a constant density and a variable acoustic sound velocity $v(x, z)$.

$$\left(\frac{\partial^2}{\partial x^2} + \frac{\partial^2}{\partial z^2} - \frac{1}{v^2} \frac{\partial^2}{\partial t^2} \right) P(x, z, t) = 0 \quad (1)$$

With x: horizontal axis, z: downgoing vertical axis and t: time. The goal is to record the wavefield at the water surface $P(x, z=0, t)$ and to focus it to the point where it was reflected $P(x, z, t=0)$ (Figure 1-13). Note that $t=0$ is not the time when the source pings but the time when the specific point scatterer starts reflecting the pulse. The wavefield can always be Fourier transformed over t, when no lateral velocity gradients are present ($\partial v / \partial x = 0$) it can also be Fourier transformed over x.

$$P(k_x, z, \omega) = \iint P(x, z, t) e^{(ik_x - i\omega t)} dx dt \quad (2.1)$$

And inverse:

$$P(x, z, t) = \iint P(k_x, z, \omega) e^{(-ik_x + i\omega t)} dk_x d\omega \quad (2.2)$$

When we apply now the operator (1) on equation (2.2)

$$\frac{\partial^2}{\partial z^2} P(k_x, z, \omega) + \left(\frac{\omega^2}{v^2} - k_x^2 \right) P(k_x, z, \omega) = 0$$

This equation has two solutions: an upcoming and down going wave. We are only interested in the upcoming wave.

$$P(k_x, z, \omega) a^2 + P(k_x, z, \omega) \left(\frac{\omega^2}{v^2} - k_x^2 \right) = 0$$

$$D = -4P(k_x, z, \omega)^2 \left(\frac{\omega^2}{v^2} - k_x^2 \right)$$

$$\text{Solution: } a_{1,2} = \pm i \sqrt{\frac{\omega^2}{v^2} - k_x^2}$$

$$\text{For the upcoming wave: } P(k_x, z, \omega) = P(k_x, z=0, \omega) e^{\left(-i \sqrt{\frac{\omega^2}{v^2} - k_x^2} z \right)} \quad (3)$$

The vertical wavenumber is defined as:

$$k_z = \sqrt{\frac{\omega^2}{v^2} - k_x^2} = \frac{\omega}{v} \sqrt{1 - \left(\frac{vk_x}{\omega} \right)^2} \quad (4)$$

This equation is called the dispersion relation of the one-way scalar wave equation. Substituting (4) into (3) provides us with a simpler equation:

$$P(k_x, z, \omega) = P(k_x, z=0, \omega) e^{(-ik_z z)} \quad (5)$$

This is the solution for the wave equation in case of zero-offset recording.

We now consider there are no horizontal velocity gradients in the medium. There can be vertical velocity gradients in the data (based on a stratified earth model). Applying the inverse Fourier transform on equation (5):

$$P(x, z, t) = \iint P(k_x, z=0, \omega) e^{(-ik_z z)} e^{(-ik_x x + i\omega t)} dk_x d\omega \quad (6)$$

k_z is defined in (4) and v is substituted by $v/2$ because the recording records two way traveltimes.

$$k_z = \frac{2\omega}{v} \sqrt{1 - \left(\frac{vk_x}{2\omega}\right)^2} \tag{7}$$

Now $t=0$ is applied in order to get the migrated section $P(x,z,t=0)$:

$$P(x, z, t = 0) = \iint P(k_x, 0, \omega) e^{(-ik_x x - ik_z z)} dk_x d\omega \tag{8}$$

This equation is also used in phase shift migration.

Rewriting equation (7) in the special case where no vertical velocity gradients are present:

$$\omega = \frac{v}{2} \sqrt{k_x^2 + k_z^2} \tag{9}$$

If the horizontal wavenumber k_x is kept constant and ω is differentiated:

$$d\omega = \frac{v}{2} \frac{k_z}{\sqrt{k_x^2 + k_z^2}} dk_z \tag{10}$$

Substitution of (10) and (9) in (8) lends to:

$$P(x, z, t = 0) = \iint \left(\frac{v}{2} \frac{k_z}{\sqrt{k_x^2 + k_z^2}} \right) P\left(k_x, 0, \frac{v}{2} \sqrt{k_x^2 + k_z^2}\right) e^{(-ik_x x - ik_z z)} dk_x dk_z$$

This equation expresses two actions: the first term is adjusts the amplitude (see obliquity factor in the Kirchhoff migration) and the second term maps ω on k_z . The remapping is demonstrated in Figure 1-15. This constant velocity migration is called the Stolt migration (Stolt 1978).

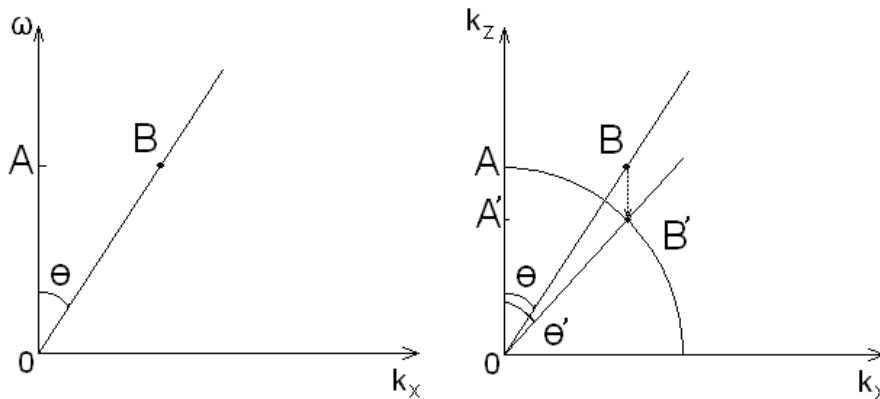


FIGURE 1-15: THE F-K ALGORITHM, LEFT THE ORIGINAL DATA B IN THE F-K DOMAIN, RIGHT THE REMAPPING OF THE DATA TO B' IN THE k_x - k_z DOMAIN.

Applications of migrations follow in chapter 3.

1.10.2 Sonar application

One of the more recent advances in the acoustic world is the Synthetic Aperture Sonar (SAS). The SAS finds its roots in the Synthetic Aperture Radar (SAR). SAR finds its roots in 2D and 3D reflection seismics. High and low frequency SAS systems were developed in a number of research centres to focus, detect and recognize small semi buried objects on the seafloor. Figure 1-16 shows a processed image of a 120 kHz to 180 kHz SAS system. A rock, a bicycle, a manta mine and a rockan mine were deployed and scanned. The recording was position corrected, binned, signal processed and migrated. In side scan sonar and high frequency SAS the volume interaction in the water column is assumed to be zero, and the volume component from the sediments is assumed to be nonexistent, that scales the problem down from a full 3D volume to a 3D surface that can be described in a function $z=f(x,y)$ (a grid).

The differences between conventional side-scan sonar and the SAS are: 1) the SAS often uses a shorter line transducer, while the side scan sonar uses a long line transducer, 2) the SAS often but not always uses multi channel recordings instead of the single channel transceiver recordings of the conventional side scan sonar, 3) the SAS stores the phase information of the signal and not only the amplitude information as a conventional sidescan sonar does. The step from the side scan sonar to the SAS system can be compared to a step from single channel seismic recordings to multi channel 2D recordings. In principle the SAS systems should be able to map a seafloor without any gaps in the coverage, large shadows not taken into account. The SAS or migration algorithm should also focus the image to a much higher resolution. The success of the focusing algorithm is extremely dependent upon the relative movement of the platform the SAS is mounted on (see 3.3.6). The only stable platforms at the moment that gave extremely successful images were rails and towers (Bellettini and Pinto 2002; Pinto, Bellettini et al. 2004). A platform with a high potential because of high stability is an AUV (see 2.6).

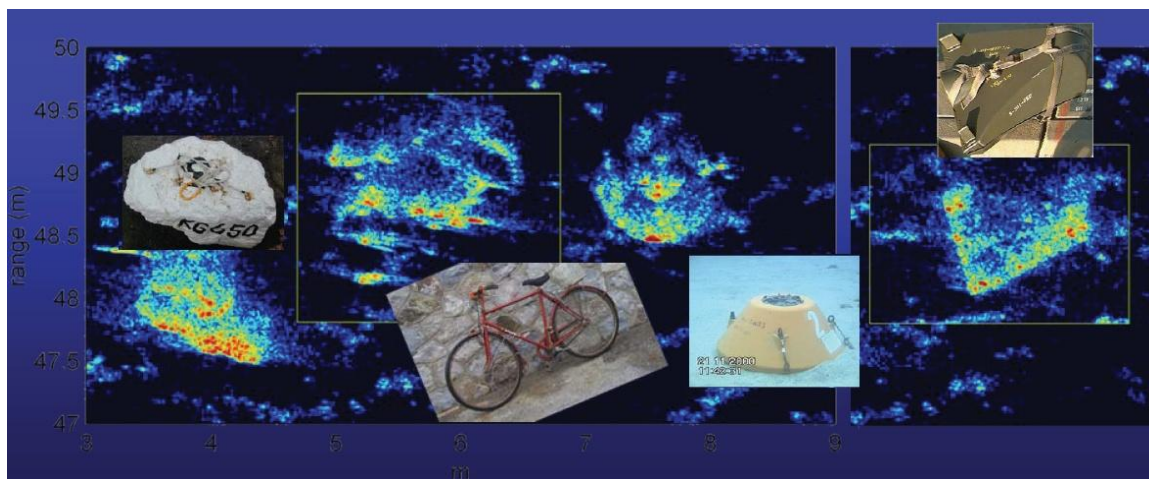


FIGURE 1-16: A HIGH FREQUENCY SAS SYSTEM PROCESSING RESULTS. COPIED FROM: SYMPOSIUM: "BURIED SEA MINES - THREAT TO THE SECURITY OF THE BALTIC REGION" RIGA 27-28 OCTOBER 2005, PRESENTATION DR. MARC PINTO (NATO UNDERSEA RESEARCH CENTRE)

The move to bottom penetrating SAS systems, based upon the side scan principle, aimed at detecting buried mines in sand, probably is a bridge too far. Figure 1-17 is a detection of buried objects with a rail mounted bottom penetrating SAS system. The high amplitude reflections, where no objects can be found, are known as reverberation. The current design will not achieve

optimum results because the recording approach is based on a one dimensional array and movement along the same axis, where it should be two dimensional when imaging a volume (Yilmaz 2001; Margrave 2003). The system does not aim to image a volume but gives all information on a predefined grid, resulting in a projection of contributions from different origins in the volume on one 2D image. Even with an interferometric SAS which is probably a logical first step to the 3D SAS, a full 3D migration is impossible. The volume component contributed by the sediment is significant, when low acoustic frequencies are used (<15 kHz), even in the case of homogeneous sediments. A significant volume component brings the problem back to a full 3D problem instead of a grid or surface problem, which was solvable with interferometry.

Using a huge 2D array instead of one or two 1D line transducers was the logic step taken in the seismic world, also the SAR field moved to 2D arrays. Maybe the SAS field will also follow that path. The step from SAS to 3D SAS will not be that easy. 1 week of SAS survey gives already terabytes of data, a square 2D array for a 3D SAS would only increase the amount of data to store and generate large datastreams that cannot be handled by one single data acquisition computer. Online processing in AUVs and embedded geophysics will probably be the path to follow.

In general there can be expected that using the low frequency SAS system as it is designed so far (interferometric SAS systems included) will probably not allow detection of buried mines in inhomogeneous sediments where an acoustic volume component does play a role. Inhomogeneous media include mixed sediments, but also sediments with preserved bedforms, layering or fluid mud on top of any other sediment as regularly found in port environments.

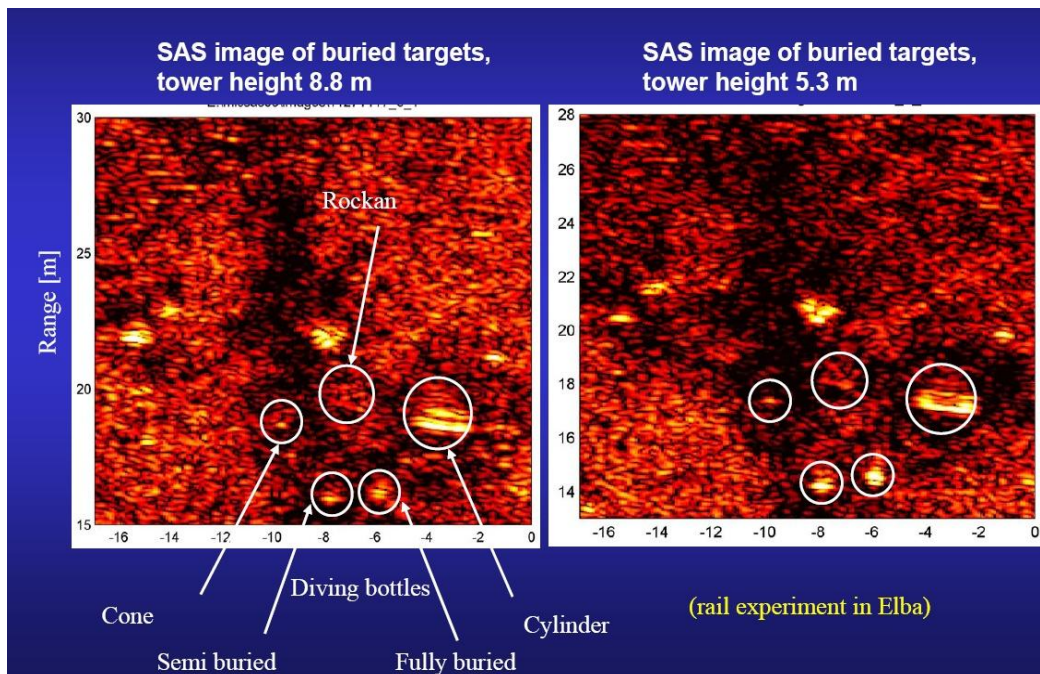


FIGURE 1-17: A LOW FREQUENCY SAS IMAGE, AN EXPERIMENT TO DETECT BURIED OBJECTS USING A RAIL MOUNTED SAS SYSTEM. COPIED FROM: SYMPOSIUM: "BURIED SEA MINES - THREAT TO THE SECURITY OF THE BALTIC REGION" RIGA 27-28 OCTOBER 2005, PRESENTATION DR. MARC PINTO (NATO UNDERSEA RESEARCH CENTRE)

1.11 ACOUSTIC RETROREFLECTORS

The physics of acoustics and light or electromagnetism have much in common. However, some aspects should be kept in mind while drawing parallels between both sciences. Major differences between visible light and acoustics are the propagation velocity, the nature of the waves and the frequency band of the signal. Directly connected to speed and frequency of the transmitted wave is the wavelength. And directly connected to the nature of waves is the nature of the building material of the reflector. The wavelengths of the sound pulses are in the electromagnetic spectrum equivalent to microwaves (millimetres and centimetres) and radio waves (decimetres and meters) and that is far above the wavelengths of visible light (nanometres). The construction materials of the acoustic reflector will not be mirrors or crystals but they will be constructed from hard materials or air filled spheres (Malme 1994).

The response received from an acoustic retroreflector (Figure 1-18) is a function of the size of the reflector, the distance towards the reflector, the medium and the elementary reflector target strength. Literature on acoustic reflectors used in underwater acoustics is very hard to find or extremely old (Whaley and Adler 1970). Literature originating in medical sciences and optical or electromagnetic sciences appear to be not very helpful either. Unclassified literature in general on this topic appears to be very hard to find. There are some traces leading towards military research programmes (Blair 2006). Knowing what level of roughness a material can have plays a role in backscatter and is of extreme importance when building stealth devices and materials.

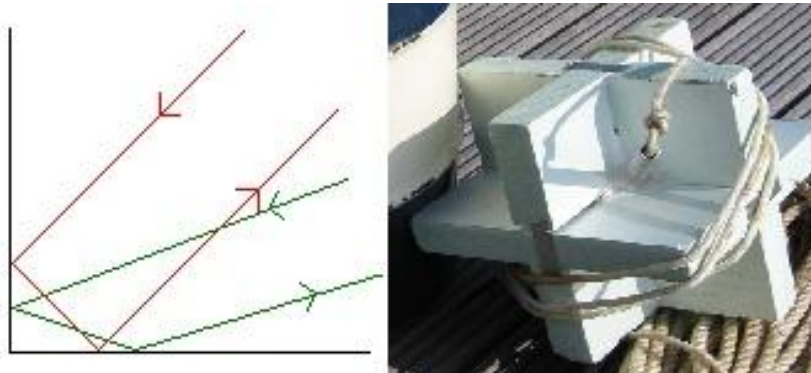


FIGURE 1-18: LEFT AN ACOUSTIC RETROREFLECTOR IN 2D THEORY AND RIGHT A REAL 3D EXAMPLE. THE RED AND THE GREEN RAYS ARE RAY PATHS PERPENDICULAR TO INCOMING AND OUTGOING THE WAVE FRONT. A RETROREFLECTOR IS AN APPLICATION OF MULTI PATH. WHEN A WAVE HITS A RETROREFLECTOR IT IS REFLECTED BACK TO THE SOURCE.

An important question is: how are the facet sizes of the reflector connected to the wavelengths it can reflect? Or in other words: what type of surfaces and what type of roughness can still act as a reflector and will have a high backscatter? Research on what type of roughness (grains or bedforms) actually contribute most to the reverberation and how to split them up might answer many questions surrounding the methods of seafloor and target classification.

Another important question for the acoustic modeling science is: from what level of roughness, and mainly micro roughness, multipath should be taken into account?

2 DETECTING OBJECTS, FIELD TESTS

Since the Second World War efficient underwater object detection became imminent. Anti submarine warfare was one of the first users of acoustic detection techniques. Shortly after the war the sea mine hunting became an intensive user field of underwater acoustic imaging. Today hydrography, underwater positioning, underwater data communication, petroleum exploration,... all use acoustics. Together with the increasing abilities of acoustic instruments to image the seafloor, the water column and the sediment itself, the sophistication of the sea mines increased. Currently a sea mine is no longer designed to be sitting and waiting in the water column, but to be actively listening to potential targets while hiding near or in the sediment-water boundary. Also the sea mines of today are either stealth, transparent or made to look like the environment. Boundaries and interfaces are the toughest challenge in acoustic imaging because of the reverberation problem. This chapter covers detections of buried and semi buried objects in, on or near boundaries or interfaces, with systems using frequencies of 500 Hz, 3.5 kHz, 7kHz and carrier frequencies of 100 kHz, 500 kHz, 900kHz and 1.8 MHz. The chapter does not only cover the detection but also an effort has been made to understand the limiting factors during a detection operation. The first successful tests were performed in a controlled environment: the second military dock at the harbour of Zeebrugge. These tests aimed at the detection of a cylindrical mine embedded in the mud. One seismic source, a boomer, gave a positive detection result. Other seismic sources failed to visualize the object. Other instrumentation used during tests in controlled and real life conditions were sidescan sonars, synthetic aperture sonar, acoustic camera, multibeam echosounder and infrared camera.

2.1 INTRODUCTION

Initially, the goal of this research was to find an acoustic detection method for buried sea mines in shallow water. Sea mines buried up to a meter depth have the same destructive power as a mine sitting on the seafloor, but they are invisible for conventional detection sonars. The acoustic system had to be able to detect an object with the size and volume of an oil barrel in sandy and muddy sediment. The object itself can have a metal or a plastic hull and can contain solid or fluid explosives. Several acoustic methods were available or in prototyping when the research started. Three real options were open: the parametric sonar, the low frequency synthetic aperture sonar (SAS) and a very high resolution 3D seismic system or a combination of the three. All three systems use a bandwidth between 1 Hz and 15 kHz.

In a later stadium, the research diverted to object detection near interfaces in general. With interfaces is meant: the sediment water boundary and the air water boundary. Interfaces are troublesome due to their roughness. When a single acoustic wave hits a rough interface and a recording device records the return, the return will no longer be a single wave; it will be a wave train or reverberation. Reverberation often masks the return of the object.

In object detection two - usually combined - methods are used. The first method is very problematic because of directionality problems: it aims to detect the acoustic return of the

object. The second one is often used in side-scan imaging and directionality is less crucial: it aims to detect the shadow of the object in acoustic echo.

The following chapters will cover field tests performed in function of object detection. Both boundaries and both detection methods will be discussed in detail. For the completeness of the text, chapter 2.2 has been added, though not strictly related to the field tests. It is a short literature study about mainly NATO field tests on penetration of acoustic waves into sediments.

2.2 BURIED TARGET DETECTION, PENETRATION OF ACOUSTIC WAVES INTO THE SEAFLOOR

In order to penetrate, with an acoustic wave, the sediment deep enough to do acoustic imaging of objects, the acoustic frequency has to be low (lower than 15 kHz in sand, lower than 50 kHz in fluid mud) (Lambert, Kalcic et al. 2002; Lyons and Pouliquen 2004). When a good image is required the rule is that higher frequencies give higher resolution images (Yilmaz 2001). The transmission loss of a signal in sand is roughly -1 dB per wavelength (Pouliquen, Lyons et al. 1998; Lyons 2005). These properties are two contradicting givens where a designer has to balance between.

Considering the acoustic image is a summation of both volume and surface scatter (Pouliquen, Lyons et al. 1998; Pouliquen and Lyons 2002), then the surface reverberation and the transmission loss can play a very significant role in the possibility of detecting an object. Usually an acoustic problem including two half-spaces is split into three problems: volume (2 half-spaces) and surface (boundary) contributions to the signal. One half-space (the water column) is neglected. Volume contributions refer to contributions coming from within the volume of one of the two half spaces, while surface contribution refers to the signal scattered by the boundary between both half spaces. The transmission loss in the sediment half space or volume component of the sediment and a definition of a root mean square (RMS) roughness of the surface to calculate the surface reverberation was presented by Eric Pouliquen (Pouliquen, Lyons et al. 1998). The RMS of the surface roughness is a measure of how rough a surface is. Roughness will be the most important factor influencing the detection. Given a fixed RMS value, the backscatter strength can easily vary 10dB. On top of that a one way transmission loss of -10dB is already measured at 60 cm depth, with frequency 7.5 kHz and grazing angle of 30° (Pouliquen, Lyons et al. 1998). It is clear that object detection should be done under circumstances where the reverberation is at a minimum and the travel distance through the sediment is at a minimum. Three options are open if reduction of the reverberation has to be done: near to vertical incidence, detection with a narrow beam, migrating the acoustic data. All methods reduce the footprint of the sonar either by using a pencil beam or by software algorithms narrowing the aperture to a pencil beam. In order to minimize the travel distance (in wavelengths) versus the depth only vertical incidence recordings and lower frequencies are an option.

An object cannot be detected with one sonar ping only, a number of succeeding pings makes an image and multiple-coverage makes an image even better. Also migration algorithms need as much data as possible about one scatter point for optimum performance (Yilmaz 2001; Margrave 2003). Here again there are two options available: one option is to make the profile under vertical incidence or with a small swath (2.4 The NATO Expert System tRials (Baltic Sea

06)), the other one is making a profile with a tilted sonar or with a large swath (Fioravanti, Magueur et al. 1997).

The advantage of a vertical incidence recording is that the sound wave penetrates the sediment to the deepest possible point. Vertical imaging is very clear and surface scatter or reverberation from the environment is, in theory, relatively small and simple to remove. A parametric sonar recording where, due to the pencil beam, the swath on the seafloor is some meters in diameter and the reverberation is almost zero solves the problem in the hardware. The disadvantage of the parametric sonar is that the swath of the sonar is at its minimum. A small swath means that slow and accurate operational conditions are required in order to avoid spatial aliasing.

In sea mine hunting a complete coverage of an area is required, and a surface has to be covered in a minimum of time and during the worst weather conditions. The advantage of using tilted sonar is the dramatic increase of swath size. The disadvantage is that all over the raw acoustic profile the surface reverberation jams the volume component of the signal. Processing is needed to focus the image or volume. The BORIS 3D SSA model demonstrates that surface reverberation is easily 10 dB higher in amplitude than the volume component and also states that the model over-estimates the volume contributions (Canepa, Bergem et al. 1997).

Conclusion: the ideal would be a low frequency tilted sonar with a large swath, a high density of receivers and a large spatial distribution which give the possibility to focus the data. The data should be a volume rather than a 2D recording. Practically that means that the receiver antenna needs to be two- dimensional and as big as possible.

2.3 LOW FREQUENCY ACOUSTIC DETECTION OF A SEMI BURIED OBJECT (ZEEBRUGGE 04)

2.3.1 Introduction

Acoustic experiments and models focusing on detection of buried objects revealed some problems related to granular non cohesive sediments such as sand (George and Bahl 1995; Pace, Pouliquen et al. 1997; Fawcett 1998; Fox and Magueur 1998; Palmese and Trucco 2006). Next to the high acoustic reflectivity coefficient (high density and high sound speed) and the high acoustic absorption coefficient of sand (Urlick 1983; Pouliquen, Lyons et al. 1998), there is also the superficial and internal structure of the bedforms. All of the parameters listed are very variable. The variability of these factors depends upon the actual and the palaeo-sedimentation environment. Over a geologically small time span the dynamic sedimentation environment in coastal areas may easily deliver a very wide spread in the grain size, grain shape, compaction and type of bedform. Acoustic buried object detection testing was done in a dock which has today a low energy sedimentation environment. The palaeoenvironment however was very variable. The acoustic sources used were a boomer ($f_c = 3.5$ kHz), multitemp sparker ($f_c = 1.2$ kHz) and a 3.5 kHz pinger (Figure 2-1). Data from drillholes showed a thick layer of fine sand intercalated by thin layers of silt or loam. The sand is covered by recent muddy sediments (0.5 - 1 meter thick). The acoustic data showed stratification between the mud-sand reflectors and chaotic acoustic facies under the sand reflector.

The Renard Centre of Marine Geology (RCMG) has a prototype of a very high resolution 3D seismic system (3D VHRS). At first sight that system had the correct set-up, the research was started using the 3D VHRS system.

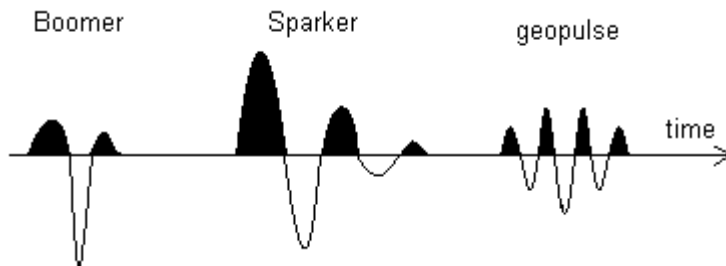


FIGURE 2-1: THE PULSE SHAPES GENERATED BY A BOOMER SPARKER AND GEOPULSE PINGER

The 3D VHRS system of the RCMG is a receiver array of 2x8 channels with 2 meter spacing between every channel and a source towed or pushed near to the array. All specifications concerning the design can be found in (Missiaen 2005). A processing after a test of the system on Lac Pavin (France) posed a first problem: the data could be binned but not be stacked (Moreaux 2003). Previous recordings could be binned and stacked but not migrated. The fact that the recording was taken on a slope visualized the problem that must have been there before as well. Previous recordings were done on a flat seafloor resulting in first breaks that were always at the correct depth. The problem was revealed after the automatic first break picking: the signals on the slope did not line up in each bin. The exact positioning of the receivers was the origin of the problem. What is the positioning accuracy needed in the processing, and what positioning accuracy is available were the main questions (Bull, Gutowski et al. 2005). In the next sub chapters these questions will be thoroughly discussed. The approach of the 3D VHRS system is bi-static. Bi-static means that the send and receive antenna are not at the same position and not necessarily near to each other. That makes the system fundamentally different from the pseudo-mono-static parametric sonar and SAS.

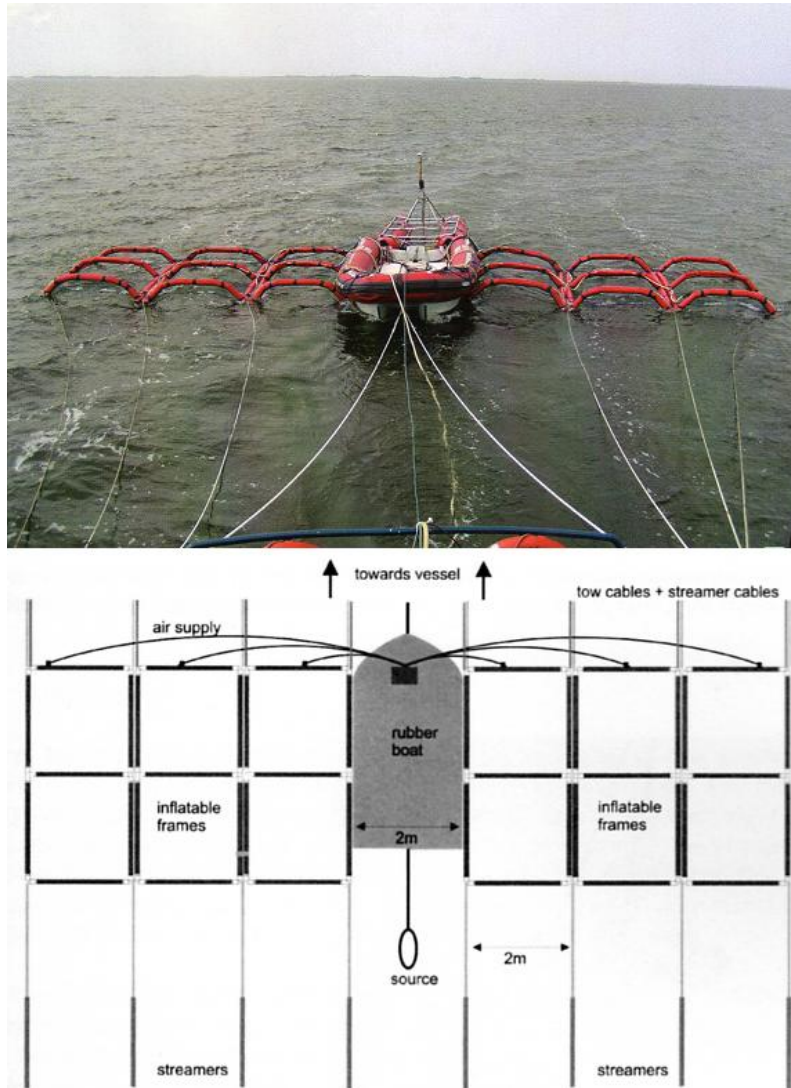


FIGURE 2-2: THE 3D VHRS SYSTEM OF THE RCMG, UGENT (MISSIAEN 2005)

Binning the data of the 3D VHRS prototype demonstrated that the mechanical flexibility of the systems' inflatable frames disabled the possibility to recalculate the exact position of the receivers. A mathematical description of what accuracies were needed was to be investigated and will be discussed in the following chapters. New simplified tests designed to fully understand what happens with the acoustic wave sent towards the seafloor were needed. Special attention went to the positioning. The tests were performed first in an uncontrolled environment, with unsuccessful results, and later in a controlled environment with better results (second military dock at Zeebrugge harbour).

During the first weeks of March 2004, seismic tests were performed in the second military dock in the harbour of Zeebrugge. The aim of the study was to investigate the possibility of detection of small semi buried and buried objects, using high resolution seismic sources and receivers, in shallow water environments (depending on the tide the dock has 8 to 12 meter water depth). A Seistec boomer ($f_c = 3.5$ kHz) (Simpkin and Davis 1993), a 3.5kHz pinger and a high resolution sparker ($f_c = 1200$ Hz) were used. Detailed information about the sediment in the dock was available from 11 drill cores (Figure 2-3, green dots) and numerous depth probes (Figure 2-3, yellow dots) made before the construction of the dock. The chosen target was a dummy mine, a

heavy metal cylinder of 1.5 meter length and about 0.5 meter diameter with 7-8 holes of 10 cm diameter. The cylinder was filled trough the holes with sediment and sank in the mud. There was concluded, that the mine rested upon the sand in the mud. The mud covered about 75 % of the volume of the mine.

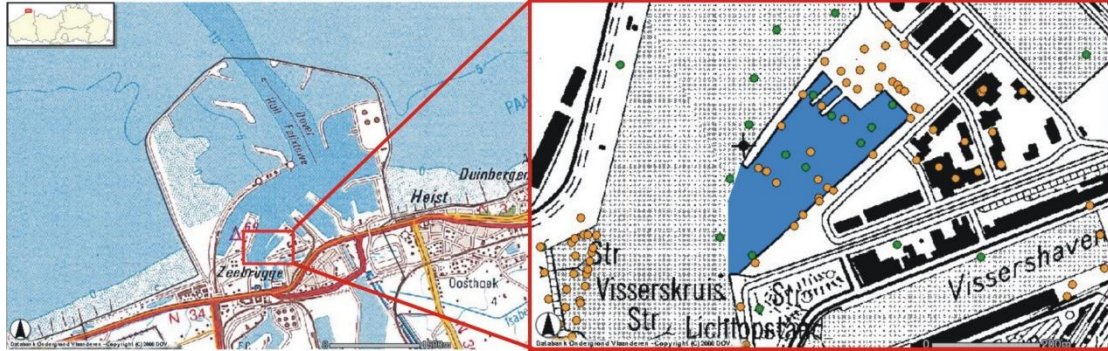


FIGURE 2-3: LOCALISATION

2.3.2 Geological and sedimentological setting

Palaeogeographic research in adjacent areas (Ebbing and Labban 1996) describe an environment with dunes and a coastline following the contours of the eroded Tertiary sediment, alluvial input, shoals, tidal sedimentation, swamps behind barriers of dunes. Cores were taken in the harbour of Zeebrugge before the construction of the docks. Analysis of the cores supports this hypothesis.

All cores described a thick layer of fine quaternary sands intercalated with fine layers of silt or loam. More recent sediments, such as mud and fluid mud, cover the sand. The cover has a thickness of 0.5 to 1 meter. Although there is a tidal difference of over 4 meter, the dock can be seen as a calm sedimentation environment where silt and clay particles can accumulate. Dredging and other construction activities have seriously turbated the top of the sand layer. Some seismic profiles showed dredging marks covered by the mud layer, during later tests (Zeebrugge, 2006) similar dredging marks at the same location were visualized using side-scan sonar. The Quaternary sand layer itself in this region (dated as Würm and Eemian) consists in the Würm part out of aeolian or alluvial reworked marine sands (shell fragments) and aeolian deposited loam (Baccaert and Baeteman 1980). The Eemian deposits are marine reworked Tertiary sands with a mixture of Tertiary and Eemian shells (Baccaert and Baeteman 1980). No matter how sand has been reworked, the deposition of sand happens in an energetic environment. The internal structure of a sand deposit, whether it is sub aqueous or aeolian, consists of dunes, ripples and sand waves with extremely variable shapes and sizes. Shapes and sizes of these bedforms depend very much upon the sedimentation environment (Gail 1990; Soulsby 1997).

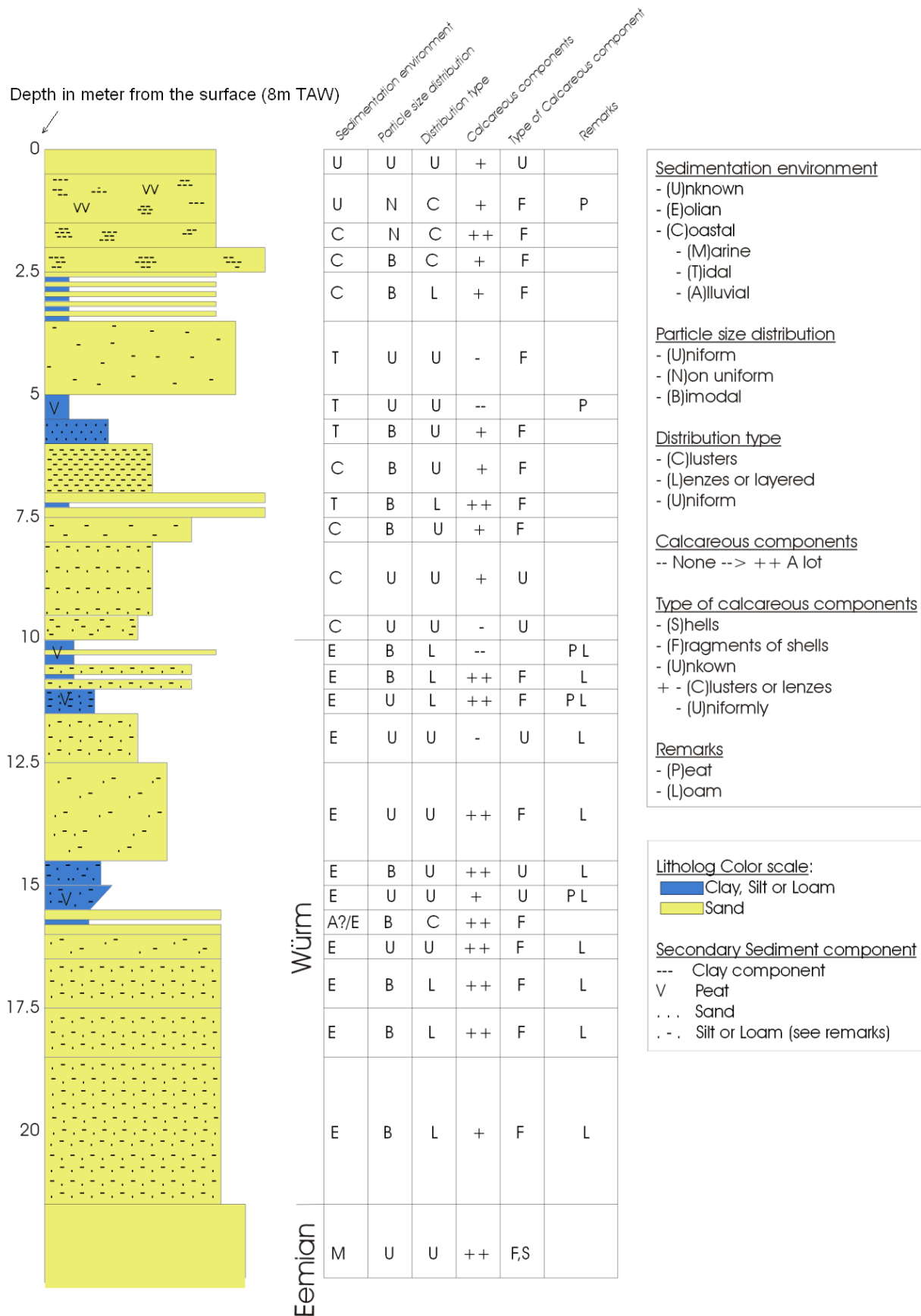


FIGURE 2-4: INTERPRETATION OF STRATIGRAPHY OF THE TEST SITE (BACCAERT AND BAETEMAN 1980)

The deposition of sand does not only create a visible layering and its typical internal structures. Sands have varying packings (loose or tight), sortings, shell fragments can be concentrated in regions, organic material can concentrate in regions, biologic activity can turbate the sand,... (Figure 2-5). Figure 2-5 displays a ripple field, with shell fragments (white) and organic material (black) in between the ripples.



FIGURE 2-5: SMALL SAND RIPPLES ON THE BEACH OF NIEUWPOORT, BELGIUM. NOTE HOW THE COARSE PARTICLES, BOTH ORGANIC (BLACK) AND SHELL FRAGMENTS (WHITE) CONCENTRATE BETWEEN THE RIPPLES. THE DISTRIBUTION OF PARTICLES IS CLEARLY HAS A PATTERN.

Aeolian sands, behave in a similar way. The variations described also create a variation of acoustic impedance Z . The acoustic impedance Z is dependent on V , its P-wave velocity, and ρ , its bulk density, where

$$Z = V\rho$$

The reflected portion of the P-wave, R , is defined as:

$$R = \frac{Z_2 - Z_1}{Z_2 + Z_1}$$

with 1 and 2 defined as adjacent media with different acoustic impedance Z_1 and Z_2 . In reflection seismic recordings a unit of sand will scatter strongly and in a chaotic way (high and variable ρ). Other evidence for the high variability of the acoustic impedance and the reflection coefficient of these sands can be found in (Liu, Hsueh et al. 2002; Pouliquen, Canepa et al. 2004).

Ripples, dunes or any type of bedforms are generated when sediment migrates or moves. Bedforms appear to have a random pattern, just as fingerprints have. A unilateral current over a flat sandy area causing enough stress to move sand grains might flatten the area or give rise to bedforms. Considering sand migration in a closed system and all sand grains have the same size and perfectly spherical shape, the compaction of the grains would be the only parameter affecting acoustic impedances. The compaction of sand grains is far from homogeneous in any bedform. A linear bedform pattern, for example ripples, indicates the direction of the current (perpendicular to the linearity). Asymmetrical bedforms are generated in unilateral currents. The ripple has a gentle sloping side on the slope facing the impact of the current: it is called the stoss side (Soulsby 1997). The steep sloping side in the direction where the current points to is the lee side (Soulsby 1997). The sand grains on the gentle sloping side are eroded. The eroded sand first underwent a coverage by sand. The earlier coverage by sand may create compaction. When a sand grain is released it slowly runs up the bedform to the top, where it rolls off (no compaction or decompaction). It is very probable that the bedform will have a loose compaction in the shadow of the current and a tighter compaction on the erosive side in the direction of the current. No specific literature has been found on this topic. The bedform will move in the direction of the current.

Nice examples and a practical evidence of the variability in shapes of both aeolian and tidal sands can be found on the northern beach of Audreselles (France), Figure 2-6. The Jurassic sandstones on the beach show a variation of fossilized marine ripple structures and other related deposits (Figure 2-6 left side). The most interesting feature is not only that the ripples are visible, but that the layers of ripples preferentially break up along the palaeo seabed. This indicates that during the fossilization process the inhomogeneous character of the sediment is preserved. In general the inhomogeneities are preserved in the sediment after the sand has been covered by other sands of the same kind. Even after compaction and cementation inhomogeneities are preserved. An indication for that is the fact that the rocks on the beach break up easily along the bedform plane and very difficultly perpendicular to that plane. Other interesting features in the fossilized deposits in Audreselles are small clay patches in and on the ripples (also in different layers) and large deposits of shells.

The dunes in Audreselles have some vertical sections showing, thanks to a variation of iron holding minerals and clay minerals, how aeolian sedimentation works. The fact that the remains of aeolian bedforms can be found back in the vertical sections, indicates that they as well remain partly preserved in the sediment.

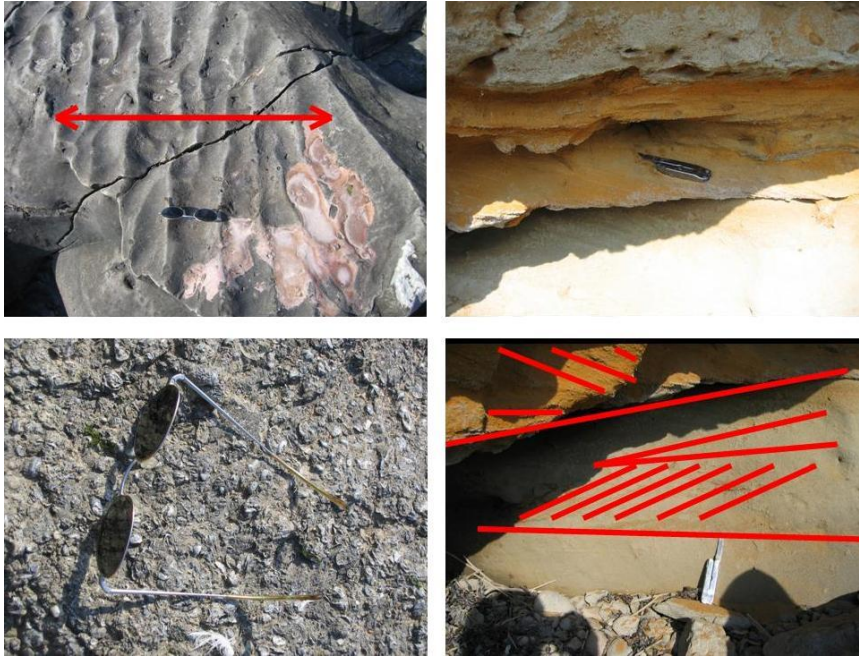


FIGURE 2-6: PRACTICAL EXAMPLES OF SAND BEDFORMS AND RIPPLES ON THE BEACH NORTH OF AUDRESELLES IN FRANCE. ON THE LEFT, TWO EXAMPLES OF MARINE JURASSIC DEPOSITS, ON THE RIGHT SIDE TWO RELATIVELY RECENT AEOLIAN DEPOSITS.

There can be concluded that bedforms have very variable internal structures and shapes, and that each internal structure is connected to: the environment through grain size, grain shape, secondary minerals deposition and sedimentary flux in general. These variations, properties and the typically high acoustic impedances in sand make it very hard to use acoustic techniques for detailed visualization needed in object detection. The effect of porosity and density in granular media on the sound velocity (and acoustic impedance) has been described in Jackson (Jackson and Richardson 2007).

2.3.3 Description, difficulties and results of the tests.

All seismic sources used, were floating sources towed by a rib. Each emission was directed vertically, perpendicular to the dock floor. The rib sailed tracks along and on top of the mine. There was little or no swell, the tests were done in optimal circumstances. Three different acoustic source-receiver configurations were used plus a reference receiver. For positioning, a DGPS with an accuracy of approximately 0.5 meter was installed. Due to technical problems a spare GPS with low accuracy was used, leaving no other option than to measure on a 0.5m grid.

The three seismic systems used were:

GeoPulse 3.5 kHz transducer (array used to send and receive)

Seistec boomer, receiver: parabolic antenna (Simpkin and Davis 1993)

Centipede sparker, receiver: single channel streamer with an array of 13 hydrophones

All systems were used in varying set-ups. The set-ups included changes of power spectrum and changes in the transducer array (four send, four receive and two send, two others receive). All source wavelets were recorded using the Bruel and Kjaer 8103 reference hydrophone.

The 'best' results were achieved using the Seistec boomer with its parabolic antenna (Simpkin and Davis 1993). These 'best' results revealed some problems. The raw results were interpreted and the interpretation fed back into a model. The interpretation as such was verified. The model gave better but similar results. The same problem appeared in the model. Figure 2-7 shows raw data of the Seistec boomer.

The 'worst' results came from the sparker. The sparker produced a signal that was too high in energy and too low in frequency. The results from the GeoPulse 3.5kHz transducer were not good. The Geopulse has a relatively long and symmetric wavelet (mixed phase). The GeoPulse also has some system-inherent problems with high power cross talk. The source gives good results in relatively deep water with muddy sediments. The cross talk decays in time, deeper images are better. Attempts were made to process the cross talk out but the processing generates ringing. Previous and further tests in Klaipeda, Lithuania, also showed that the source is not suited to investigate sands.

First the stratigraphy of the dock has been investigated. The depth of the dock is about -8 meter TAW. The sandy sediment in the dock is probably the lower layer of the Würm sedimentation. Other wells in a radius of 200 meter, if well interpreted, show the basis of the Würm on -7 meter TAW. This indicates an irregular surface of the Eemian sediments, or at a smaller scale erosion structure such as channels. Both sedimentation environments deposited reworked sands in marine or aeolian conditions. The sediments are intercalated with small layers of silt, loam, clay or patches of shells and shell fragments. The small scale sediment layers cannot be correlated from one core to another. The larger stratigraphic units however can be correlated, but on basis of depositional environment and typical sediments and minerals deposited during that period (ex.: presence of silt or loam).

A closer look at the acoustic properties of some sediment types should be taken. An extensive summary of research in this field has recently been published by (Jackson and Richardson 2007). A layer of shells has a very high attenuation and a P-wave velocity higher than 2400 m/s (Best, Tuffin et al. 2004), which is much higher than sand (up to 2400 m/s) or clay (ranging from 1600 m/s to approximately 1900 m/s). Sand has a high attenuation and clay without gas has a low attenuation. Note that these velocities were measured on cores using a high frequency source. The actual seismic P-wave velocity is much lower but changes in this order of magnitude for this range of sediments. Shells or shell fragments can be found scattered or in patches in tidal zones. In all cores taken, these patches were observed but cannot be correlated. A layer of sand does not only have bedforms and internal structures, which create different acoustic impedances. A sand layer can also contain shell- and clay-patches (Figure 2-6), which create changes in acoustic impedance. And last but not least there might be gas, creating a low P-wave velocity in the sediment.

The recorded reflection seismic profiles give an expected chaotic acoustic facies (Figure 2-7). Sediments contain patches with both high and low P-wave velocities. Very irregular internal structures, and bedforms of centimetre to metre scale were expected. The expected acoustic response results from a convolution of source wavelet and the impulse response of the seafloor.

The impulse response of the seafloor is composed of surface and volume component. The final result, knowing that the lateral distribution of the sediments is highly variable, is a chaotic acoustic facies (Pouliquen, Lyons et al. 1998). In such an unprocessed image it is very likely a buried object will remain undetected. The interpretation of the image is done using both the image and the knowledge about the environment. Figure 2-7 shows the resulting acoustic image and the interpretation. The upper layer is mud, under the mud there is an irregular sand surface. The irregularities of that surface are caused by dredging works. The upper layer of sand has also been turbated during the dredging works and under the turbated layer there is the original undisturbed stratigraphy.

The main question now is: will processing enhance the image? 2D constant velocity Kirchhoff migration and different kinds of deconvolutions were applied without any result or increase of image quality. The migration and deconvolution actually severely degraded the image. The answer is that with this kind of recordings and accuracy of DGPS used, any kind of migration will simply degrade the image. Deconvolution on a boomer image is not necessary. The very poor positioning, spatial aliasing and the relatively low spatial sample resolution of the signal make processing impossible. The types of tests performed in the dock were not performed to process and optimize images, it was testing to see and understand what the acoustic responses are of several systems and several recording geometries. The semi buried object is visible on the boomer image. No other source used visualized the object. If the object had been buried, it probably would have been invisible in raw single channel data, using the boomer as source.

The main problem in buried object detection appeared to be the seafloor and its reverberation. The chaos of reverberations may hide the buried object completely. The option to simulate was taken to get a better feeling in the time and space dimensions with the reverberation effect. The simulation was not only used to support the hypothesis. The simulation was also used to know how close the hydrophones had to be placed, how big the maximum source receiver offset could be, the effect of positioning inaccuracies, how dense the spatial sampling has to be, and to get an idea about the effect of high frequency ripples on relatively low frequency sources.

Modeling and migration is covered in the next chapter. In what follows brief results and observations are given. See section **3.2 3D point scatterer model first version** for the complete coverage of modeling and migration.

Downsampling the spatial component of real data or simulated data makes the reflector less coherent and the simulated image will start to look like Figure 2-7. Reflector coherence is *"Measures of similarity among more than two functions. For example, seismic reflection events are coherent in a linear way with respect to dip, in a hyperbolic way with respect to normal moveout,..."* (Sheriff 1984).

The seismic resolution of an image is defined as (Yilmaz 2001):

Vertical: $R_v = \frac{v}{4f}$ with v the seismic velocity and f the central frequency of the source

Horizontal: - Without migration: $R_h = \frac{v}{2} \sqrt{\frac{2t}{f}}$ with t the two way travel time

- After migration: $R_h = \frac{v}{4f}$

Note that the migrated horizontal resolution is equal to the vertical resolution after a successful deconvolution and a successful migration. In order to have a clear image it is necessary to have bin sizes of a maximum size of $R_h \times R_h$. In the case of a central frequency of 3.5kHz and a velocity of 1500 m/s, that means approximately 12 by 12 centimeter (Bull, Gutowski et al. 2005). Having that or a denser spatial sampling will enable to migrate correctly and get an optimal image. The performed tests do not have such a high spatial sampling and the DGPS used did not deliver coordinates with a high accuracy needed for the migration algorithm.

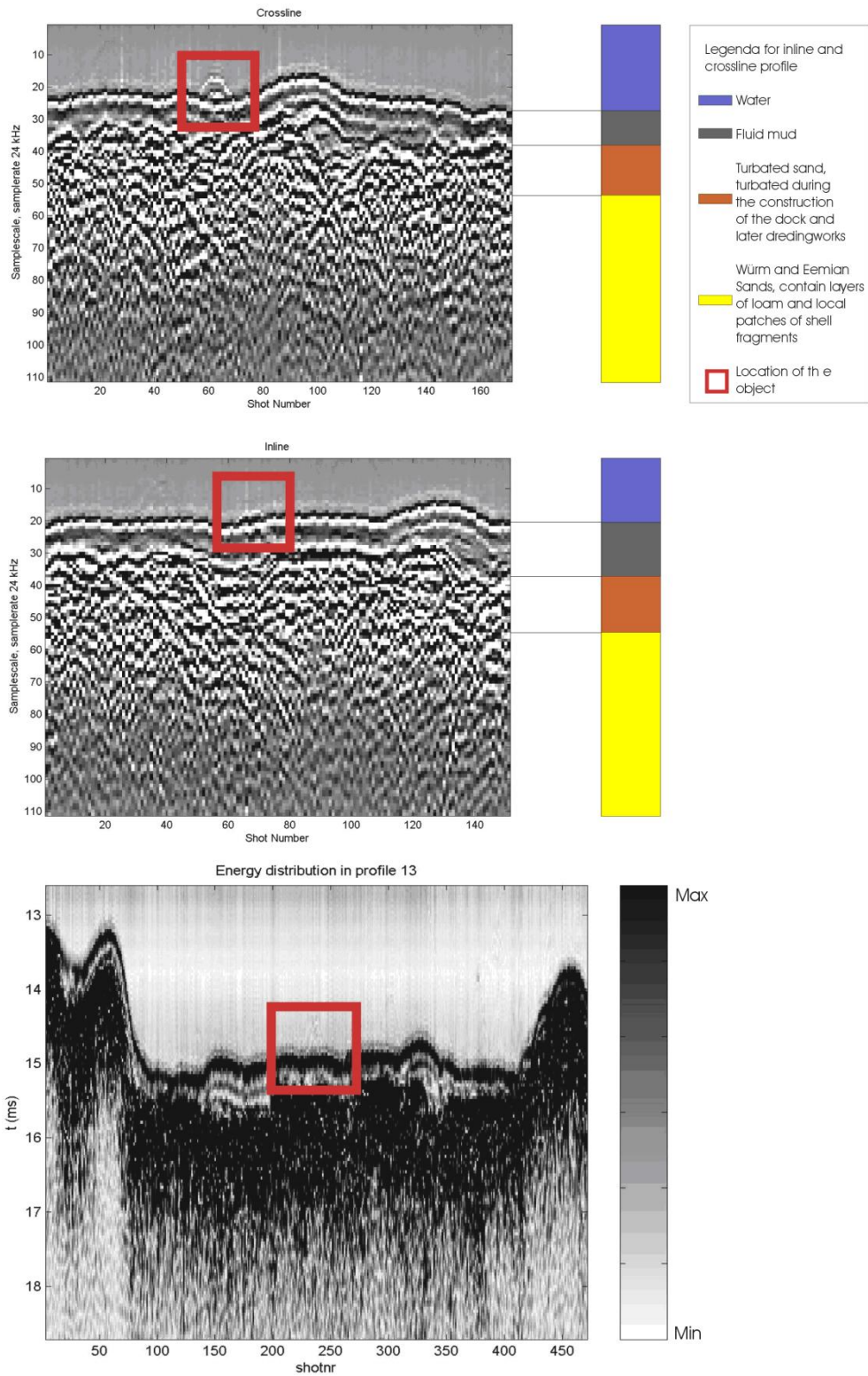


FIGURE 2-7: SEISTEC BOOMER SOURCE. RAW, SINGLE CHANNEL DATA AND INTERPRETATION, TOP TWO FIGURES ARE THE INLINE AND CROSS LINE SECTIONS ON TOP OF THE SEMI BURIED SEA MINE. THE BOTTOM FIGURE SHOWS THE ENERGY DISTRIBUTION WITHIN THE IMAGE. CLEAR IS THAT THE WATER-MUD INTERFACE REFLECTS A LOT OF ENERGY, WHILE IN THE MUD LAYER THERE IS ALMOST NO ENERGY REFLECTED AND THE MUD-SAND INTERFACE PLUS THE SAND VOLUME REFLECT ALL THE AVAILABLE ENERGY.

2.3.4 Conclusions

Whether a buried object is detectable, depends upon a number of variables. The most important variable is the distance between the sonar and the target. Long distance will create large footprints while short distances will create smaller footprints. Large footprints reduce the survey time by increasing the swath. Focusing or migrating the image might bring a solution to artificially reduce the footprint. The second important parameter is the sediment. Changes in environmental conditions may create changes in sedimentation. Some environments can have rapid and very local changes. Tidal, alluvial, aeolian and shallow marine environments typically change rapidly and therefore the sediments deposited in these environments will have extremely variable properties.

In order to get an optimal acoustic image, migration methods should be used. In order to get a nicely migrated section a full downscaling of the industrial methods has to be done. Full downscaling means that the geometric approach of previous high-resolution 3D seismic blocks has to be changed, bin sizes and positioning accuracy need to be in the range of centimeters, not in the range of decimeters. Mechanically flexible receiver arrays were not the good approach in small buried object imaging.

Detection based upon shadowing is in an unmigrated acoustic block impossible due to the volume contributions. In a migrated acoustic block detection heavily depends upon position accuracy, since it will define the level of performance of the migration. If an object or a reflector with a high impedance difference is large enough in size, a shadow can be observed, also after migration.

2.4 THE NATO EXPERT SYSTEM TRIALS (BALTIC SEA 06)

2.4.1 Introduction

Early March 2006 the NATO Specialist Team for the Sea Mine Burial Expert System (ST-SMBES) organized tests to validate a section of the burial prediction model in the Baltic Sea. That opportunity was taken to perform some other tests concerning detection of semi buried and buried sea mines. The semi buried objects were detected from 6 different angles using side-scan sonar mounted on an autonomous underwater vehicle (AUV). A very strong angle of incidence dependency was observed. A known fully buried object was detected with a parametric echo sounder.

That any scatter function has time, frequency and angle of incidence as important variables was known already for a while. For decades backscatter has been used to classify sediment types and sediment properties. Practical world examples and NATO publications however suggested that enormous variations in backscatter (up to 10dB variation) (Pouliquen, Canepa et al. 2004) can occur between day and night in shallow water (photo zone) on the same spot due to biological activity. Also tests and modeling on directionalities of backscatter were performed and demonstrate the very strong angular dependency of backscatter; a seafloor covered with sand ripples can have the ripples visualized if a side-scan sonar is sailing parallel to the ripples and the ripples will not or barely be visible when the side-scan is sailing perpendicular to the pattern. What about objects sitting in or on the seafloor? In March 2006 the NATO specialist

team on the sea mine burial expert system performed tests in the Baltic Sea. The Belgian Navy provided an AUV and divers and took the opportunity to sort out if objects also have different responses in function of directionality.

2.4.2 AUV tests, directionality of scatter

2.4.2.1 THEORY

An Autonomous Underwater Vehicle or AUV is a programmable vehicle equipped with underwater instruments (Figure 2-8, left). In the programming, software transponder positions, sailing path, height to sail above the seafloor and targets are entered (Figure 2-8, right). Most of the navigation is done using a long base line set up (LBL), in some cases an ultra short base line (USBL) approach is used during recovery. LBL means that two or more transponders are fixed on accurately known positions with some hundreds of meter spacing in between the transponders. The line formed by the coordinates of 2 LBL buoys is called the baseline. These transponders are then used to triangulate the position of the AUV. An internal computer calculates that position and corrects the sailing track if necessary. The AUV may not cross the baseline used to determine its position. A USBL system works in a similar way but has 1 transponder and 4 receivers very close to each other (decimeter scale). Other sensors such as the GPS, the ADCP (Doppler log) and the motion sensor increase the navigation accuracy. The most important instrument on board of the REMUS 100 is the side-scan sonar. A DIDSON 1.8 MHz acoustic underwater camera was also mounted during some surveys. The use of the DIDSON on this platform is not the proper way to operate the camera. The platform is not only too fast to make proper high resolution images, the shape of the camera makes the platform instable and the REMUS starts to roll. The instable platform is the origin of a strongly degraded side-scan image (Figure 2-9).

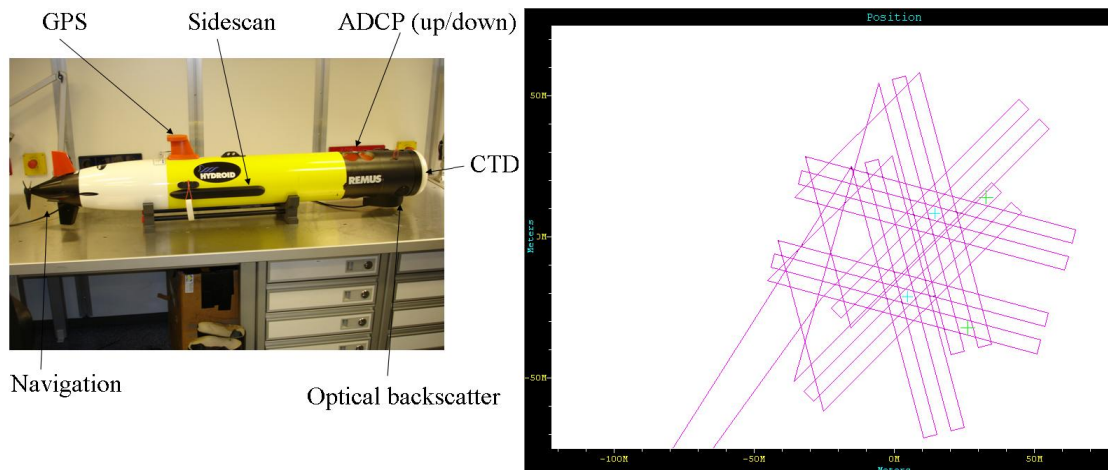


FIGURE 2-8: THE REMUS 100 AUV IS A PROGRAMMABLE AUTONOMOUSLY SWIMMING VEHICLE MOUNTED WITH A MARINE SONIC SIDE-SCAN SONAR, TWO ADCP'S, A GPS, A CTD AND AN OPTICAL BACKSCATTER UNIT. ON THE RIGHT HAND SITE THERE IS THE SAILING PATTERN PROGRAMMED INTO THE AUV.

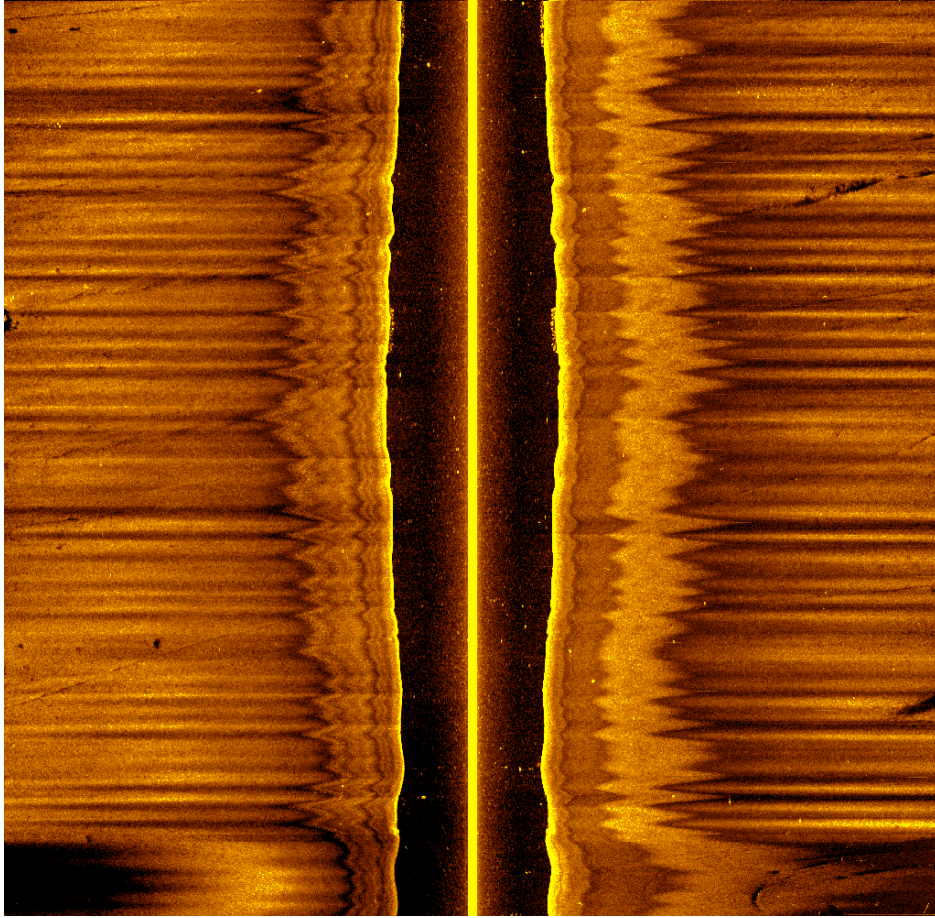


FIGURE 2-9: THIS SIDE-SCAN SONAR IMAGE HAS BEEN TAKEN WITH THE REMUS 100 AUV WITH THE DIDSON UNDERWATER ACOUSTIC CAMERA MOUNTED ON THE HEAD. THE SHAPE OF THE SONAR DESTABILIZES THE AUV AND THAT HAS A SIGNIFICANT REPERCUSSION ON THE SIDE-SCAN SONAR IMAGE.

A side-scan sonar sends and receives a signal on the same sonar array, making the main lobe of the sonar very narrow. The lobe has a big opening angle perpendicular to the line array. This results in a very long but narrow footprint on the seafloor. Chapter 1.3.2 explained the beam pattern of a line array. The REMUS 100 AUV platform sails a raster and the Marine Sonic 900 kHz side-scan sonar pings equidistantly. The fact that the REMUS 100 keeps track of its position and height, means that it can estimate the distance between every ping. This algorithm results in very good raw data images. Depicting every received signal next to the previous signals builds the acoustic image.

Figure 2-10 shows how a raw side-scan sonar recording should be interpreted. The image shows the acoustic response of a two meter long and 0.5 meter diameter mine impacted in muddy sediment.

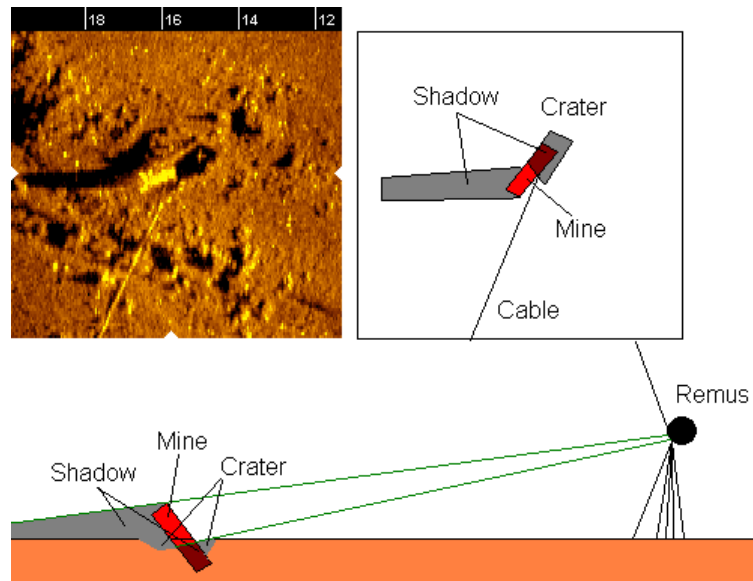


FIGURE 2-10: INTERPRETATION OF A SIDE-SCAN IMAGE. LEFT TOP: THE ACOUSTIC IMAGE OF A SEMI BURIED CYLINDRICAL MINE TAKEN WITH A 900 KHZ SONAR MOUNTED ON A REMUS AUV. RIGHT TOP: THE INTERPRETATION OF THE IMAGE. BOTTOM: FRONTAL VIEW, EXPLANATION OF THE SHADOWING.

2.4.2.2 DISCUSSION AND OVERVIEW OF RESULTS

Two types of instrumented mines were deployed during the sea trials. The 1.100 kg heavy NRL mine (Figure 2-11) (Abelev, Valent et al. 2003) and the 500 kg FWG burial registration mine with optical sensors (BRM: Figure 2-12) (Richardson, Bower et al. 2003; Wever 2004). Figure 2-11 shows the acoustic responses of the NRL instrumented mine which impacted after a free fall. The mine rests in a crater and is visible from several angles. A more interesting thing to see is the acoustic response of the seafloor and the acoustic response of the rope used to recover the mines. Each time the rope is laying in a perpendicular way to the line of sailing it is not visible, when it is laying in any other direction it is visible. The reason why it is visible while laying parallel or near to parallel to the line of sailing is because it makes a 90° angle with the seafloor and as such it acts as a retro reflector. An important conclusion can be taken about this phenomenon: when observing small or thin objects the acoustic properties and the retroreflections play a significant role in the potential detection. This conclusion is supported by the observations in Figure 2-12. Figure 2-12 shows how a mine, instrumented with optical sensors mounted in small blocks on the hull of the mine acoustically responds. The mine has numerous straight angles or acoustic retro reflectors. Whether the straight angles are truly going to act as a reflector depends upon the size of them versus the wavelength. In this case the wavelength is of millimeter scale so virtually any straight angle will be an acoustic reflector. That is why the images are so high in detail. On Figure 2-12 other linear features parallel to the longest axis of the mine and also the rope demonstrate how linear features on the seabed are filtered out of the acoustic image just by using another angle of incidence or sailing track for the acoustic imaging. It is clear that seafloors with natural linear features, such as sand ripples may only be recognized if the sailing track is not in the direction of or against the current. When talking about roughness and seafloor classification, the existence of linear features can be a significant source of misinterpretation if the side-scan images are not taken in several sailing directions.

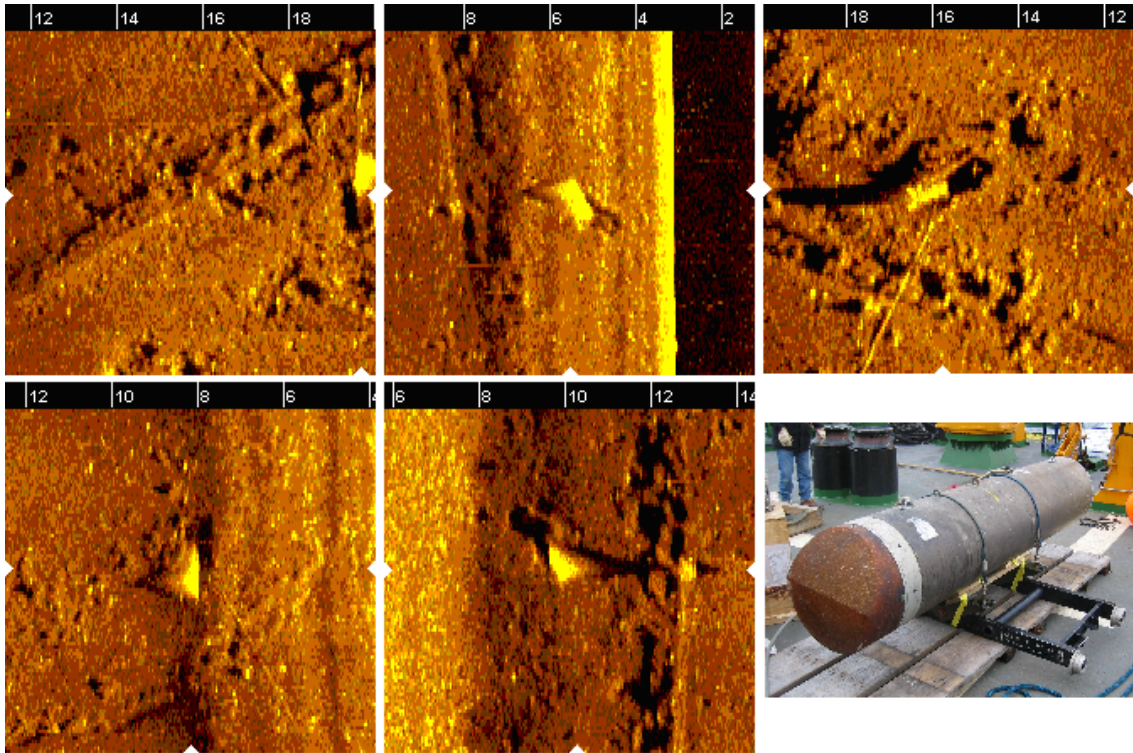


FIGURE 2-11: FIVE RAW ACOUSTIC RESPONSES FROM A CYLINDRICAL MINE. THE RECORDING HAS BEEN DONE WITH THE MARINE SONIC 900 KHZ SIDE SCAN SONAR MOUNTED ON THE REMUS 100 AUV. ALL RESPONSES MORE OR LESS LOOK THE SAME. THE MAJOR VARIATIONS IN BACKSCATTER ARE TO BE SEEN IN THE MUD LAYER WHERE THE SEA MINE IS LAYING IN. THE METER SCALE IS GIVEN ON TOP OF EVERY FIGURE. THE SCALE ON TOP OF EVERY IMAGE IS METER. THE HORIZONTAL AND VERTICAL SCALE ARE IDENTICAL.

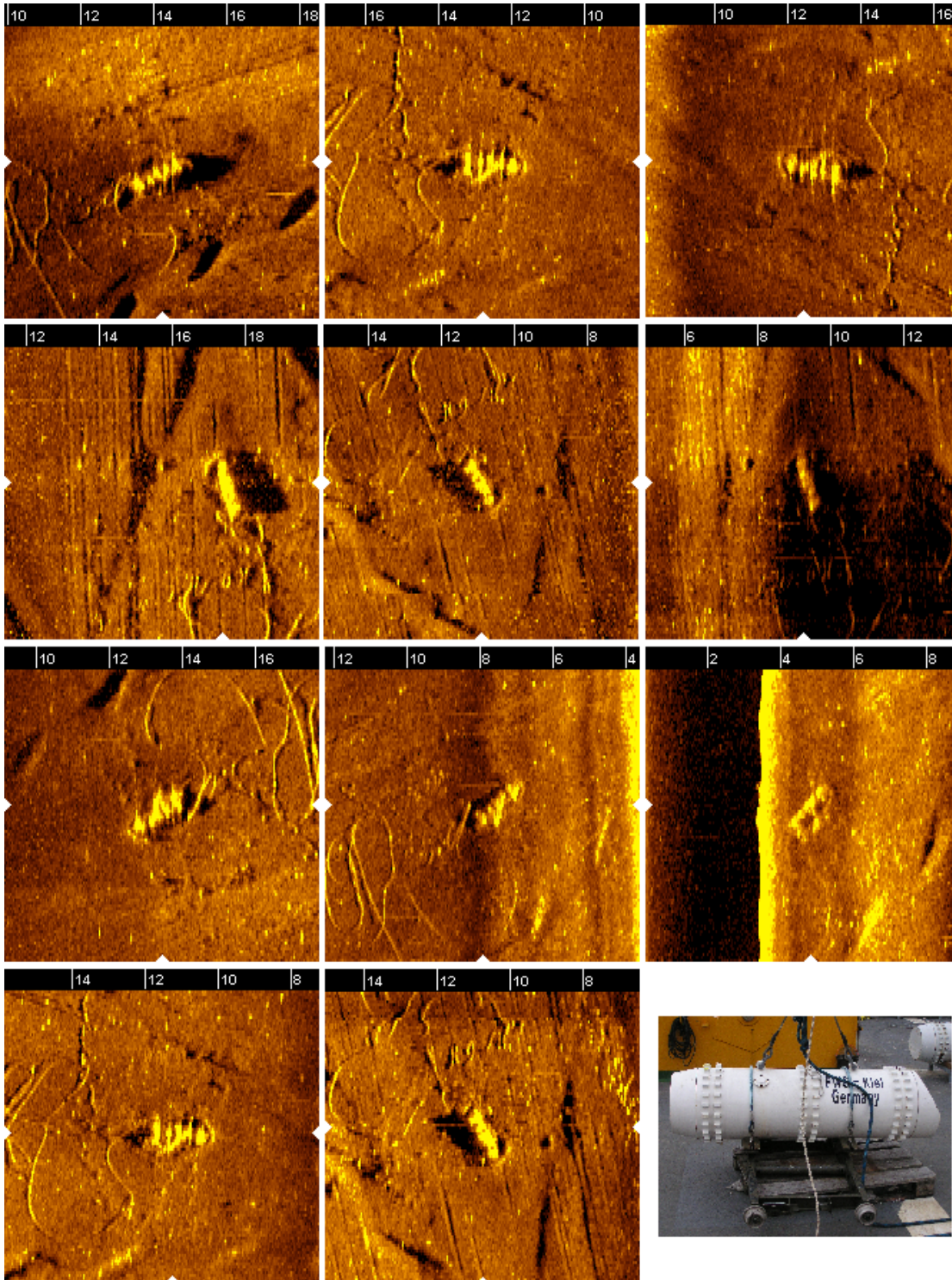


FIGURE 2-12: ELEVEN RAW SIDE-SCAN SONAR IMAGES FROM THE SAME MINE, ALL WITH DIFFERENT ANGLES OF INCIDENCE. THE RECORDING HAS BEEN DONE WITH THE MARINE SONIC 900 KHZ SIDE SCAN SONAR MOUNTED ON THE REMUS 100 AUV. THE AUV IS SAILING 3M ABOVE THE SEAFLOOR. THE REFLECTOR PROPERTIES OF THE LED BRIDGES ARE THE REASON WHY THE BACKSCATTERED FIELD FROM THE SEA MINE IS MORE OR LESS EQUAL IN EVERY IMAGE. IMPORTANT TO NOTE ARE THE DIFFERENCES IN BACKSCATTER PATTERNS FROM THE MUD LAYER THE MINE IS RESTING IN. THE BACKSCATTER OF THE ROPE SHOWS THAT LINEAR FEATURES PARALLEL TO THE LINE OF SAILING ARE MORE VISIBLE THAN OTHERS. THE METER SCALE IS GIVEN ON TOP OF EVERY FIGURE. THE SCALE ON TOP OF EVERY IMAGE IS METER. THE HORIZONTAL AND VERTICAL SCALE ARE IDENTICAL.

2.4.3 Parametric sonar tests, detection of a fully buried mine

Also during the NEST 06 tests, the parametric sonar sailed near to a known buried sea mine in a sandy area. The sonar was mounted on a huge platform (R/V Planet) that had no rotation movement around any axis, the only movement was a perfectly controlled translation movement. The recording was very similar to a recording done with rail mounted sonar from which we know that up till now they have been reasonably successful. After sailing some very dense sailing lines the object was detected. This demonstrates the possibility to detect a buried mine acoustically but as previously stated, the acoustic properties of the sea mine are crucial in detection and it is not hard to adapt them in such a way that a mine is stealth. The use of parametric sonar on a manned platform in object detection is an academic concept that cannot be used in conflict situations or any real life situation where the object position is not known with a very high accuracy.

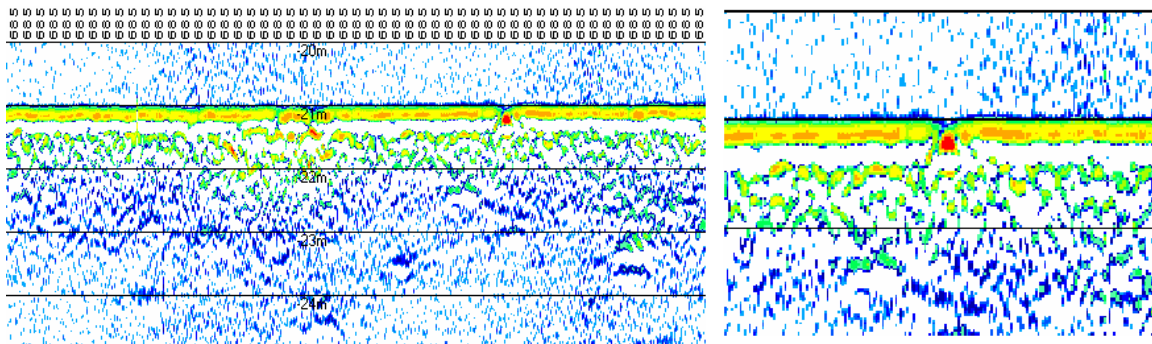


FIGURE 2-13: A RAW PARAMETRIC ECHO SOUNDING RECORDING. THIS PROFILE HAS BEEN TAKEN UNDER A 13° ANGLE (ANGLE OF INCIDENCE IS 77°). THE OBJECT WAS BURIED A YEAR BEFORE. THE SEDIMENT IS SAND. NOTE THAT THE OBJECT COULD NOT BE DETECTED UNDER VERTICAL INCIDENCE. THAT FACT DEMONSTRATES THE AMOUNT OF LUCK NEEDED TO FIND A BURIED OBJECT, BECAUSE VERTICAL INCIDENCE SHOULD BE THE EASIEST ANGLE TO WORK UNDER TO FIND THE OBJECT BACK. THE SMALL FOOTPRINT OF THE PARAMETRIC ECHO SOUNDER IMPLICATES THAT A LOT OF PINGS AND A HIGH POSITION ACCURACY IS NEEDED IN ORDER TO FULLY COVER THE SEAFLOOR.

2.4.4 Conclusions

- Semi buried and buried sea mines can be detected.
- The detection of buried sea mines is possible with parametric sonars, but the concept is inapplicable in real life situations with small platforms. Hunting mines with platforms like the R/V Planet is out of the question. The use of AUVs might be an option in the future.
- Semi buried mines can be detected with conventional AUV mounted side-scan sonar.
- The very strong directionality of scatter has been demonstrated.
- Sea mines not designed to be hidden, have a similar scatter patterns in all directions.
- Mines exploiting the directionality of scatter such as Rockan might be sometimes stealth when sonar images are not taken from multiple angles.

2.5 FLOATING OBJECT DETECTION (ZEEBRUGGE 06)

2.5.1 Introduction

The tests conducted in October 2006 in the second military dock at the harbour of Zeebrugge were material and detection tests. The aim was to detect two floating objects: an oil barrel ($d = 30\text{-}40\text{ cm}$, $h = 50\text{ cm}$) and an acoustic reflector ($20 \times 20 \times 20\text{ cm}$) with an infrared camera and with a range of sonar frequencies. The hypothesis was that when trying to detect objects on a boundary between two half spaces (water-air), the chance of detection significantly increases when detection operations are performed on both sides of that boundary. The sensors used were an infrared camera, a Klein 3000 side-scan sonar and a Marine Sonic 900 kHz sonar mounted on a REMUS 100. Detections were successful with all sonars and carrier frequencies when the objects were both floating and submerged. Only the floating objects were detected with the infrared camera.

A discussion with Cdr. Yves Dupont about multipath and the position of the two sideward looking Marine Sonic sonars on the REMUS 100 were the origin of the hypothesis that small floating objects might not only be detectable from above the water but also from the water, with off the shelf equipment. Conventional side-scan sonars have their sonars directed to the seafloor (ex.: Klein 3000), nevertheless a portion of the beam is directed towards the water surface. The side-scan sonar on the REMUS 100 has its sonars positioned without a preferential direction and as such the burst is sent in equal amounts to the sea floor and sea surface. In order to see the influence of frequency on the detection ranges a Klein 3000 was introduced in the tests. The use of the Klein and the Marine Sonic sonar enabled us to scan at a carrier frequency of 100 kHz, 500 kHz and 900 kHz.

2.5.2 Theory

The beam pattern of standard side-scan sonars without array discretisation (enveloping) and phase manipulation is a function of the dimensions of the sonar array, the frequency transmitted by the array and the sound velocity in the water near the sonar. Figure 2-14 shows the estimated acoustic lobe pattern of the two types of side-scan sonars used during the tests. The lobe patterns were derived from the dimensions and frequencies of the sonars and adapted with information derived from the images.

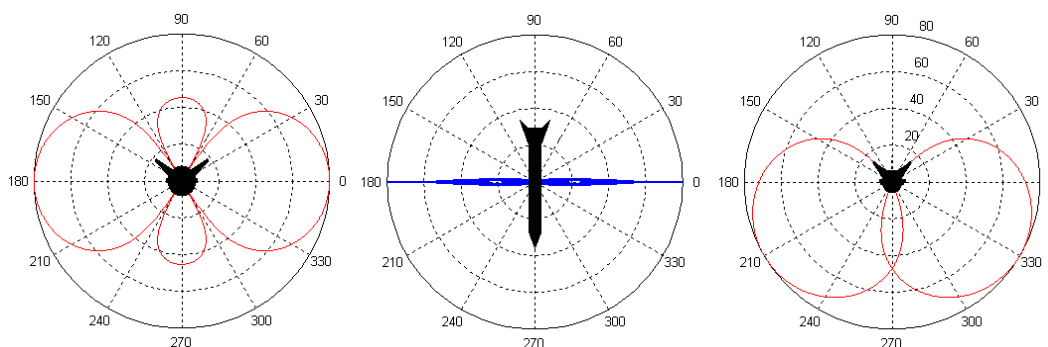


FIGURE 2-14: ACOUSTIC DIRECTIONALITY PLOTS OF SIDE-SCAN SONARS: LEFT AND RIGHT ARE FRONT VIEWS, THE CENTRE IS A VIEW ON TOP OF THE SONAR. ON THE LEFT THE EXPECTED PATTERN OF THE

MARINE SONIC 900 KHZ SIDE-SCAN SONAR MOUNTED ON THE REMUS 100 IS PLOTTED. ON THE RIGHT THE EXPECTED PATTERN OF THE KLEIN 3000 SIDE-SCAN SONAR IS PLOTTED (100-500 KHZ).

Figure 2-14 left is the estimated pattern for the 900 kHz Marine Sonic sonar mounted on a REMUS 100 platform. The hypothesis of the two sidelobes pointing up and down was originally based on the fact that all sonar images recorded with the 900 kHz Marine Sonic sonar have very hard multipath returns from the water-air interface. Figure 2-14 right is what is expected to be the type of pattern of a Klein 3000 sonar (500 kHz and also 100 kHz). Important to understand is that both sonars do not only emit energy to the seafloor but they also emit a portion of the energy towards the sea surface, also important to notice is that the width of the Klein 3000 sonar is probably exactly chosen not to have side-lobes.

The energy sent and scattered from the water-air interface is what was used during the tests. It was expected that since this equipment is not optimized to scan the sea surface, the scatter from the seafloor would be a major noise factor. Nevertheless the tests demonstrate the potentiality of the applied techniques.

2.5.3 Discussion and overview of results

Figure 2-15 shows the objects used as targets: a small oil barrel and an acoustic reflector or decoy.

The test done with the REMUS 100 was: sail two lines with a different distance to the object and then go deeper and do the same. Figure 2-18 shows some of the recorded detections. All images show a very clear detection and a difference in signature of detection between the barrel (top left and bottom right) and the acoustic retroreflector. The barrel usually has a long tail in the reflection while the reflector is a relatively short reflection in function of time.

Figure 2-16 shows a raw 500 kHz sonar image with an object within less than 10 meters range of the sonar. Figure 2-16 also shows a blind spot (red and blue zones): objects placed near the foot or against the quay might be harder to detect. In most cases they are not detectable at all using this type of sonars. Interesting to note is the hyperbola on the place where the object can be found. The presence of a hyperbola indicates that the contribution of the vertical side lobes (Figure 2-14 centre) to the total sonar image is significant, SAS processing is not possible because only amplitude and no phase information is stored by the sonars.



FIGURE 2-15: LEFT THE OIL BARREL, RIGHT THE ACOUSTIC REFLECTOR USED DURING THE TESTS. THE DIMENSIONS OF THE REFLECTOR ARE 20X20X20 CM, THE OIL BARREL IS APPROXIMATELY 50 CM HIGH.

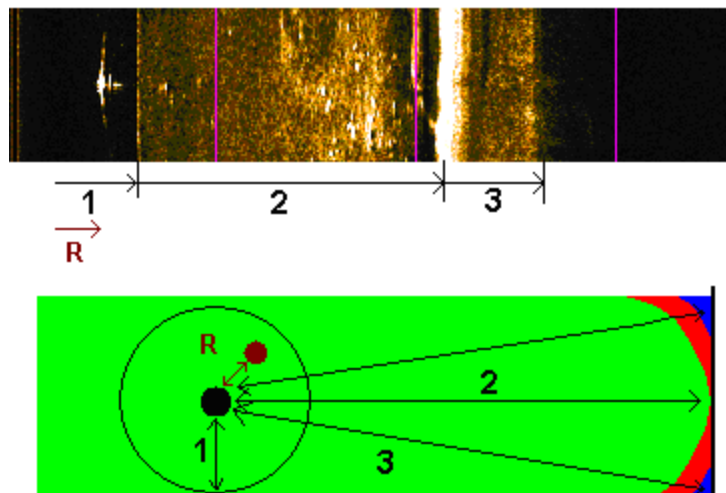


FIGURE 2-16: A SONAR IMAGE NEAR A QUAY, 1) IS THE DISTANCE BETWEEN THE SONAR AND THE SEAFLOOR, 2) IS THE CLOSEST DISTANCE TO THE QUAY, 3) IS THE DISTANCE TO THE FOOT OF THE QUAY, R) REFLECTOR RESPONSE. GREEN: DETECTION POSSIBLE, RED: NO DETECTION POSSIBLE, BLUE: REDUCED IMAGE QUALITY DUE TO CONVOLUTION AND MULTIPATH LEAVE OBJECTS UNDETECTED

As previously stated, sonar tests were performed using three carrier frequencies: 100, 500 and 900 kHz, about the beam pattern of every sonar connected to each frequency there is no accurate knowledge. Analyzing the images of the Klein versus the Marine Sonic indicate that some serious differences can be expected (Figure 2-14). Analyzing the two Klein datasets on 100 and 500 kHz, we presume that these beam patterns have similarities but are not identical, with the 100 kHz having more outspoken side-lobes and a wider main lobe than the 500 kHz.

All carrier frequencies proved to be useful in object detection, but they seem to have a range where an object can be more easily detected: 900 kHz 1 to 10 meter, 500 kHz 15 to 40 (or more) meter, 100 kHz: 25 to at least 40 meter.

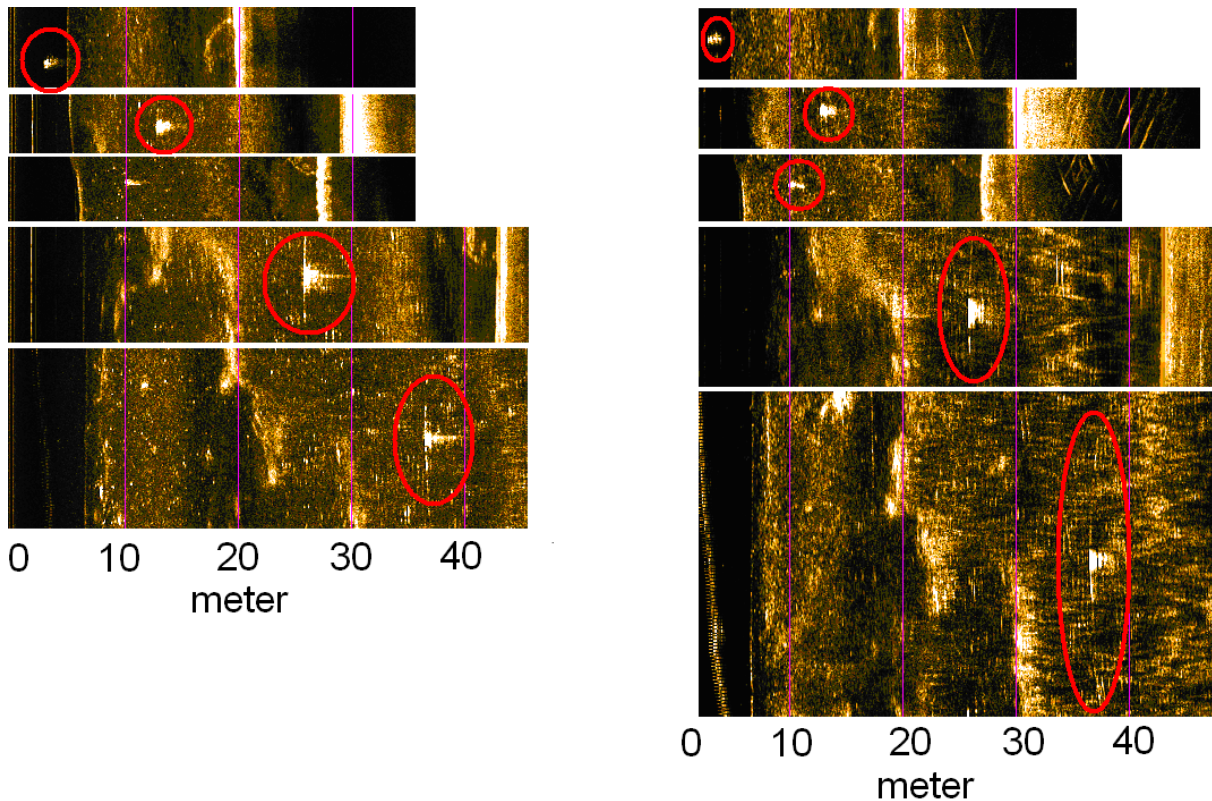


FIGURE 2-17: LEFT RAW 500 KHZ RECORDINGS OF A FLOATING OBJECT. RIGHT THE RAW 100 KHZ COUNTERPART. THE PURPLE LINES ARE THE 10 M RANGE LINES. THE BRIGHT SPOT IS THE ACOUSTIC RETROREFLECTOR. THE SONAR WAS TOWED 1 METER BELOW THE WATER SURFACE IN LINES PARALLEL TO THE TWO OBJECTS, STARTING AT JUST A COUPLE OF METERS TO 40 METER.

Full details about the sonar observations can be found in the technical report for DGMR/SYS N-1 (Staelens and Borghraef 2006).

Comparing Figure 2-17 and Figure 2-18 it is obvious that there are some significant differences between the images of the Klein 3000 sonar and the REMUS 100. Most remarkable are the yellow lines running through the images, these are echoes related to a very big side-lobe directed both up and down the sonar. Tilting the sonars will not help because that does not remove the side-lobe. A redesign of that side-scan sonar should be considered.

Another argument pointing in the direction of side-lobes is visible on the Figure 2-18 snapshots at 2 meter: there is a much darker zone of one meter wide. That indicates that that position is recorded between the main lobe and the first side-lobe. In comparison the Klein, on 500 kHz: these effects are only exceptionally visible or not present. On 100 kHz: these effects are sometimes visible but there is no dark zone, so imaging is done with only one lobe.

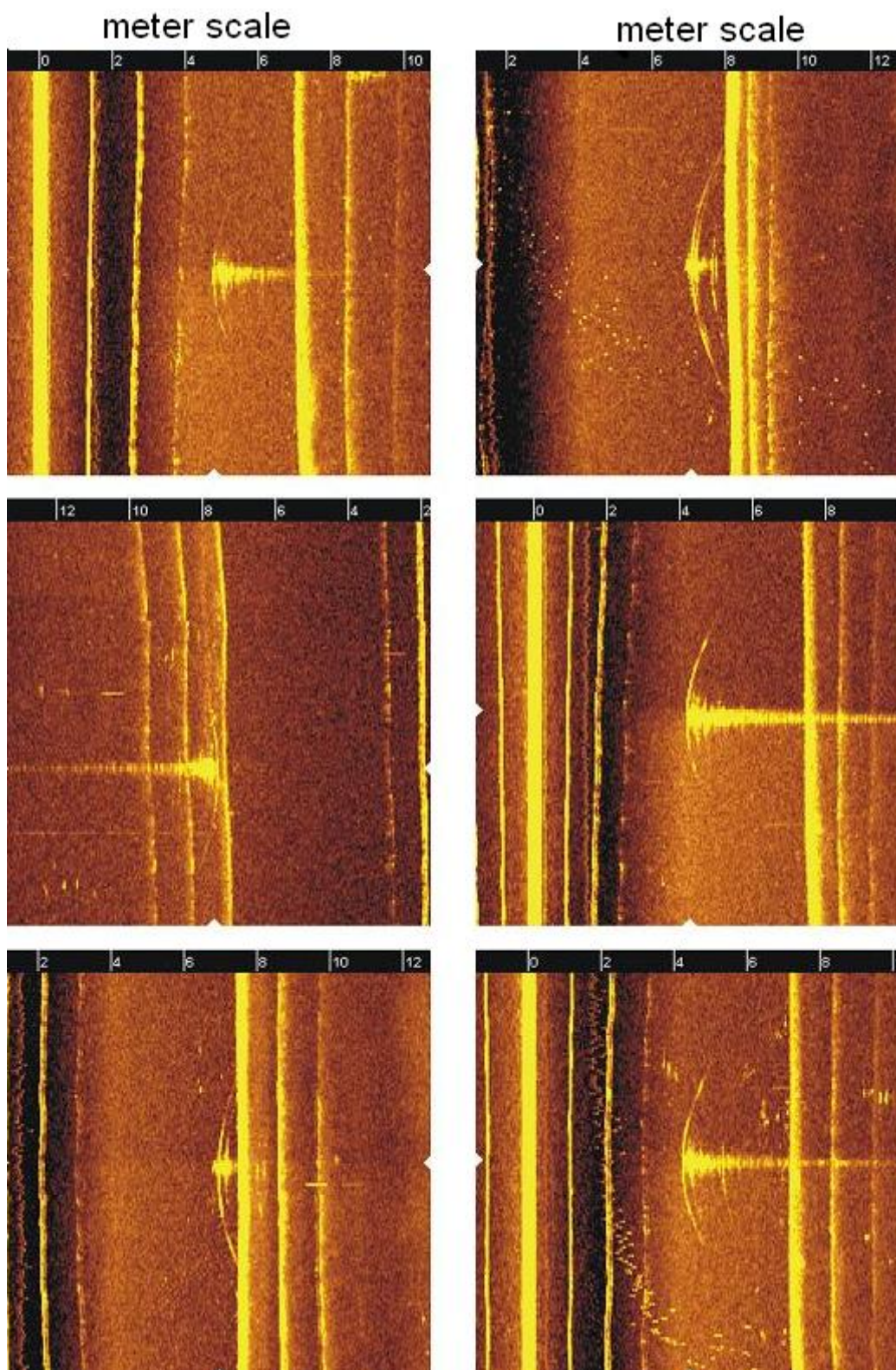


FIGURE 2-18: SOME RAW SNAPSHOTS FROM DETECTIONS OF THE BARREL (HAS A LONG TAIL IN THE ACOUSTIC IMAGE) AND THE REFLECTOR (HAS NO TAIL IN THE ACOUSTIC IMAGE). ALL SONAR IMAGES ARE TAKEN WITHIN A 10 METER DISTANCE RANGE. THE METER SCALE IS GIVEN ON TOP OF EVERY FIGURE.

2.5.4 Conclusions

- The submerged objects were detected using side-scan sonar towed one meter or deeper under the water-air interface with the arrays directed away from the interface.
- Side-scan recordings were made on 100-500-900 kHz, all frequencies proved to be useful in object detection.
- Every frequency has its optimal detection range: 900 kHz from 1 to 10 meter, 500 kHz from 15 to 40 (or more) meter and 100 kHz from 25 to at least 40 meter.
- The side-scan sonar potentially detects floating objects and has different but more noise sources than an infrared camera, data fusion with infrared and high frequency (short range) radars might make detections easier and more conclusive.
- Objects dumped from the quay or placed on the bottom next to the quay are likely to be invisible for the type of sonars used in this test. The objects might not hide in the blind spot when the side-scan sonar sails closer to the seafloor.
- SAS processing might make the detection of objects more conclusive, when phase measurements would have been recorded as well.
- The Klein 3000 sonar is more suited to be used in very shallow water than the Marine Sonic sonar because it has almost no side-lobe interference in the image and it uses no side-lobes to image.

2.6 TOWED SIDE-SCAN SONAR VERSUS AUV (SIGURD FAULBAUMS 07)

2.6.1 Introduction

At the end of March 2007 a side-scan sonar test near the wreck of the Sigurd Faulbaums was conducted in cooperation with the RCMG, Ministry of Defense, Vlaamse Hydrografie and the VLIZ. Other interested groups who used the data were Mariene Biologie Ugent and VIOE. The aim of the test, for this PhD, was to compare 3 different side-scan sonar systems. A towed Klein 3000 side-scan sonar, Marine Sonic side-scan sonar mounted on a REMUS 100 AUV and a towed Shadows SAS were compared. AUV platforms are very stable in terms of movement and can be manoeuvred closer to the seafloor and objects than conventional towed side-scan sonars. They appear to be the optimal side-scan imaging platform.

During the NEST 06 tests there already was an opportunity to compare side-scan sonar images taken with the REMUS 100 AUV with side-scan sonar images made with a towed Klein 2000 side-scan sonar. Due to organizational reasons the comparison could not take place. Three months later the comparison was done during a NEST 06 extension program on the R/V Kronsort. A target defined for years as a 'huge underwater gas bubble', frequently visited with conventional towed side-scan sonar and never identified was visited with the REMUS 100. After scanning, the 'huge underwater gas bubble', appeared to be a forgotten wreck loaded with disintegrating tree-trunks. The target was identified for the first time, it was clear that the

REMUS 100 side-scan image gives an image enabling conclusive classification of objects. In order to know how accurate the REMUS 100 could image and what the difference is with the Klein 3000 side-scan sonar, and the Shadows SAS, an area with a lot of known big and small objects was needed. That area was available on the Belgian Continental Shelf: the wreck of the Sigurd Faulbaums.

2.6.2 Available information

The Sigurd Faulbaums was a 103 meter long, 14 meter wide steamship built in 1913 and torpedoed at 23 May 1940 by the German submarine U9 under the command of one of Nazi Germany's most notorious and most decorated U-boat commanders: Wolfgang Lüth¹. After the Second World War the cargo of lead and zinc was partly recovered and major parts of the ship were cleared away, creating some debris around the wreck. The position of the remains of the wreck is: WGS84 Lat: 51°20.093'N Long: 2°36.895'E.

More recently, the department Mariene Biologie, Ghent University, installed in cooperation with the VLIZ near the wreck a number of big cages for experimental purposes. Some of the cages had been dragged away by trawlers and had to be found back, while others were in the process of being covered by sand. Object burial and the related processes are a topic of interest in the NATO, and as such the sonar tests could serve some more purposes.

The technical information available before the tests started was historical side-scan information and a very recent swath bathymetry map (Vlaamse Hydrografie 2007). The swath bathymetry map was recorded with the Kongsberg shallow water multibeam echo sounder EM3002D installed on the R/V Ter Streep. The side-scan sonar information was of very poor quality and appeared to be not very useful. From the multibeam echo sounder map the position and the height above the seafloor of the wreck could be determined. Most of the wreck appeared to have been covered by sand. All information needed for an AUV planning was available.

¹ KTZ Wolfgang Lüth (°1913 and +1945) was personally responsible for sinking in total 46 ships (225.204 tons), only Otto Kretschmer (°1912 and +1998), who after the war became Flotillenadmiral and Chief of Staff of the NATO Command COMNAVBTAP in May 1965, had a higher score with also 46 ships sunk (273.043 tons). For more information: <http://uboat.net/men/aces/top.htm> Guðmundur, H. (2007). "Uboat.net." from <http://uboat.net/men/aces/top.htm>.

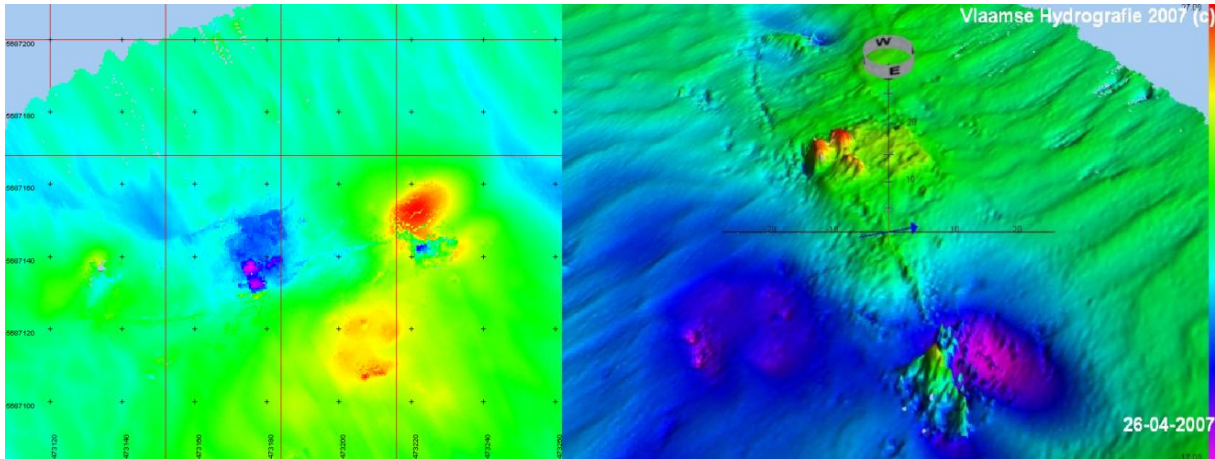


FIGURE 2-19: AN EM3002D SWATH BATHYMETRY MAP OF THE SIGURD FAULBAUMS WRECK. THE SWATH BATHYMETRY MAP SUGGESTS THAT MOST OF THE WRECK IS COVERED BY SAND. DATA FROM VLAAMSE HYDROGRAFIE, AFDELING KUST (VLAAMSE HYDROGRAFIE 2007)

2.6.3 Data acquisition and description of the recorded data

With all the necessary information available and having an exceptionally good sea state, the Klein 3000 side-scan sonar was deployed from the R/V Zeeleeuw (VLIZ) in the vicinity of the wreck. Height above the seafloor was initially chosen at 5 meter and later, due to navigational problems pulled up for safety reasons to about 10 meters. Images from all sides of the wreck were taken. Figure 2-20 shows the best result of the Klein 3000 side-scan sonar recordings next to the REMUS 100 side-scan sonar recordings. Because the Klein 3000 side-scan sonar was towed high above the seafloor, the shadows of the objects and sand dunes on the seafloor were minimized. Shadows are an essential part of imaging, the loss of the shadows makes the distinction and classification of objects much harder.

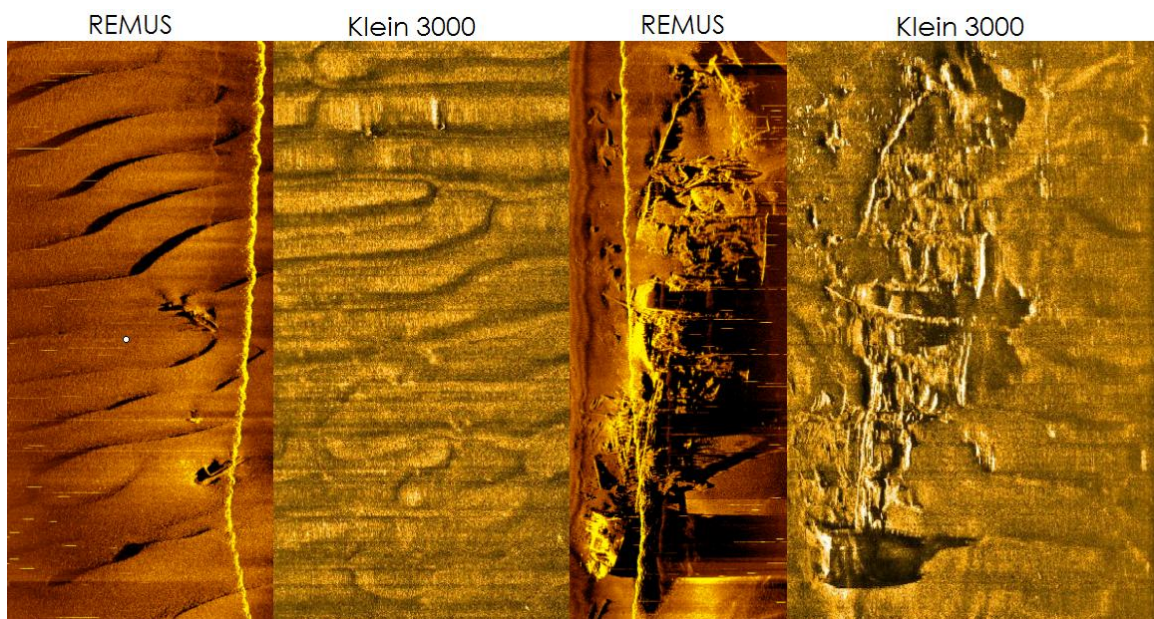


FIGURE 2-20: A PAIR OF SIDE-SCAN IMAGES FROM THE WRECK AND THE REGION AROUND. THE KLEIN 3000 SIDE-SCAN IMAGES HAVE ALMOST NO SHADOWS BECAUSE THE SONAR WAS TOWED 10 METER ABOVE THE SEAFLOOR, WHILE THE REMUS 100 SAILED 5 METER ABOVE THE SEAFLOOR.

One week later the REMUS 100 was deployed from the R/V Zeeleeuw. The sea state was not as perfect as during the Klein 3000 recordings, but because the AUV sails under the wave base, no significant influence of the sea state was expected and observed. Since a REMUS 100 is deployed and recovered from a rigid inflatable boat, the sea state can only be problematic during recovery of the AUV. It is the ability of recovery that limits the deployment of the REMUS 100.

Two missions were planned, only the first one was carried out. The first mission usually is a reconnaissance mission, while the second mission focuses on the objects found during the first mission and images them from closer by from six or eight different angles. Due to malfunctioning of the REMUS 100, only the reconnaissance survey could be done. A side-scan sonar image from one single angle of incidence was taken of all objects and the wreck.

The sailing plan included a scan of the wreck and a visit to two possible cages found and located the week before with the Klein 3000 side-scan sonar. All recordings were taken with a sailing path 5 meter above the seafloor and a side-scan sonar swath of 50 meter on both sides of the AUV.

The accurate knowledge of the position of the AUV by the AUV itself is used in the ping per meter calculations in the AUV. Because the REMUS 100 side-scan sonar pings every number of decimetres instead of every number of milliseconds the image itself and the image quality is much better. This approach also makes rastering and georeferencing of the image easier. In the past the sailing speed of the sonar had to be reduced in order to have a good spatial density of the data because a number of pings per second were recorded. With the pings per meter approach no spatial over sampling has to be done anymore and the sailing speed of the platform can be maximized. This ping per meter approach is also available in some digital side-scan sonars like the Klein 3000.

In the REMUS 100 side-scan sonar images bit-errors are visible, indicating that there is a problem with buffer overflow or parity/checksum in the electronics of the Marine Sonic side-scan sonar. The REMUS 100 clearly recorded higher quality side-scan sonar images than the towed Klein 3000 side-scan sonar.

And one year later 22/04/2008 the recordings with the IXSEA Shadows synthetic aperture sonar was done (Figure 2-21). Meanwhile other Klein 3000 sonar images from the Vlaamse Hydrografie showed up (Figure 2-22).

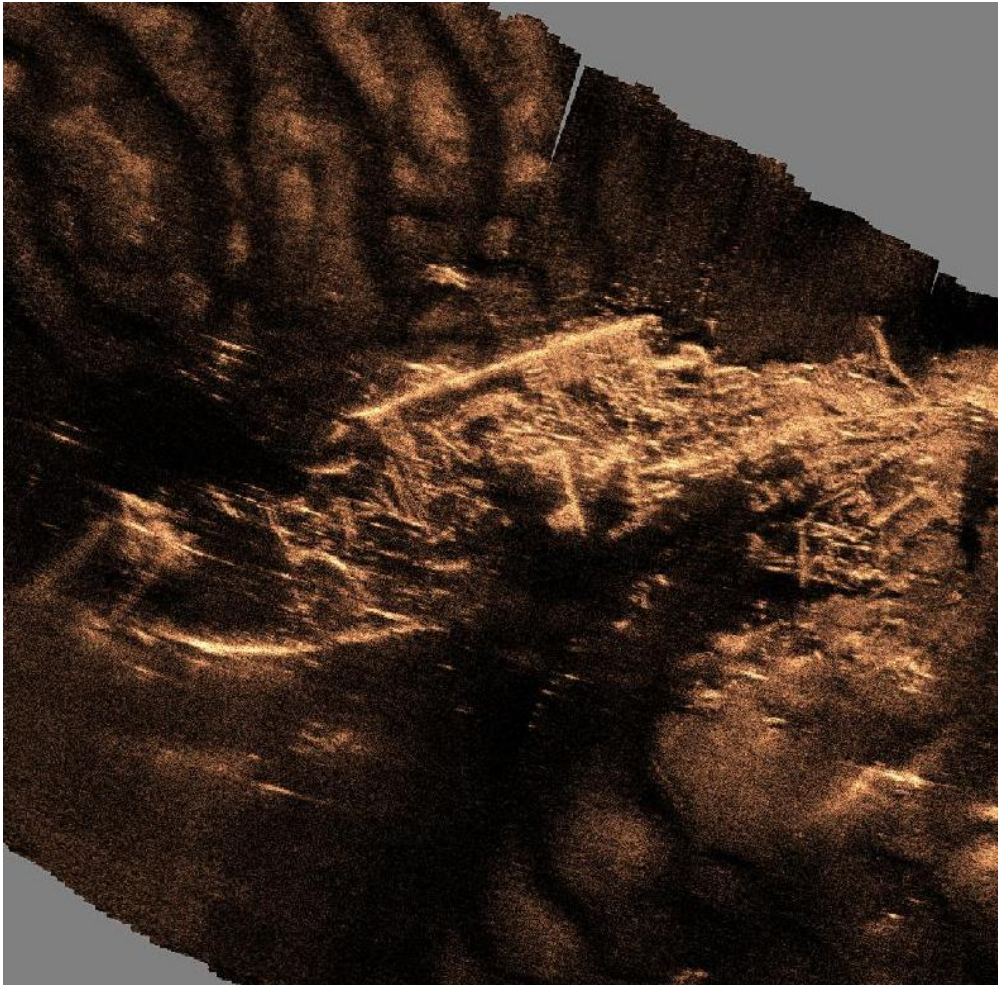


FIGURE 2-21: THE IXSEA SHADOWS IMAGE OF THE SIGURD FAULBAUMS.

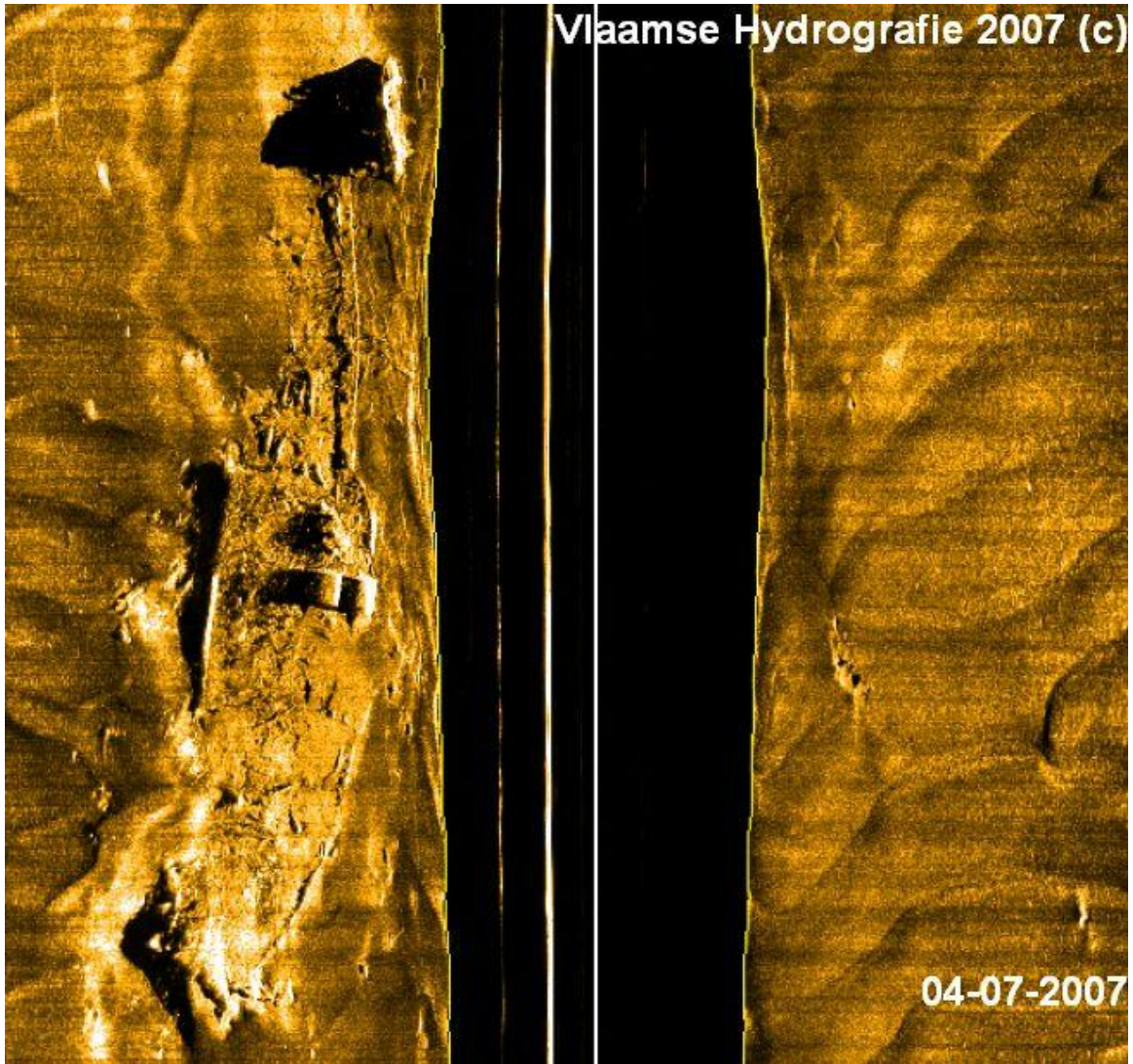


FIGURE 2-22: IMAGE TAKEN WITH A KLEIN 3000 SIDESCAN SONAR TOWED FROM A STABLE PLATFORM.

2.6.4 Discussion

Figure 2-23 demonstrates the superior side-scan sonar imaging of the seafloor by the REMUS 100 system. Two objects with their scour pit are clearly recognizable in the REMUS 100 side-scan sonar image (left), while the same image taken with the Klein 3000 towed side-scan sonar (right) just indicates that there might be an object.

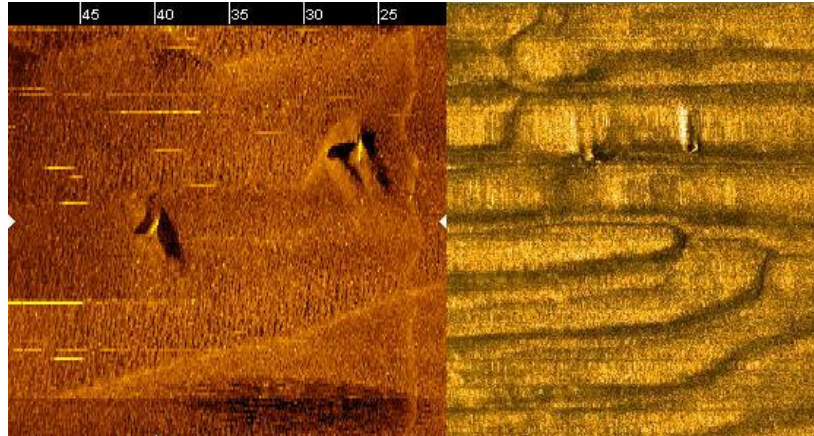


FIGURE 2-23: LEFT A REMUS 100 IMAGE OF TWO TARGETS, RIGHT THE KLEIN 3000 COUNTERPART. LEFT ALSO A METER SCALE HAS BEEN ADDED TO THE FIGURE.

Also the side-scan sonar images taken from the wreck demonstrate the higher image quality. The fact that the REMUS 100 can sail accurately both near to objects and can be accurately positioned at a fixed height above the seafloor combined with the imaging system embedded in the system (pings per meter, based on a combination of inertial and LBL positioning of the AUV, instead of pings per second) enables the AUV to make a much higher quality side-scan sonar image.

In Figure 2-23 it is the scour pit and the shadowing that make an object detectable, more than the scatter of the object itself. Other objects such as in Figure 2-24 are detected by a combination of object scatter and shadowing. Also visible on the image taken by the REMUS 100 with a 100 meter swath are horizontal lines. These lines indicate buffer overloads in the electronics of the system. These buffer overloads do not occur with a 60 meter swath.

The hard multi-path return (yellow line in the REMUS 100 side-scan sonar images) is visible in every image and can hide an object.

The Shadows SAS from IXSEA so far does not make images superior to any conventional sidescan sonar. On the contrary it appears that all objects around the bow of the wreck are properly focused (Figure 2-24). The current version of the algorithm is not sufficient to be used in mine warfare, further research is required.

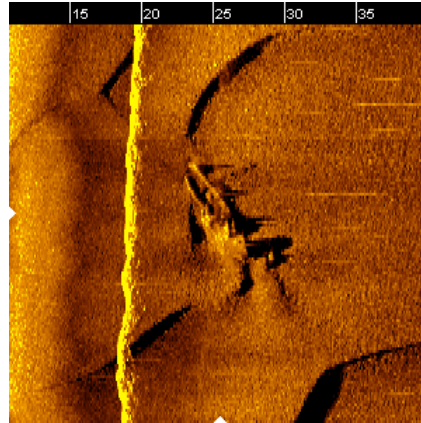


FIGURE 2-24: DEBRIS FROM THE SIGURD FAULBAUMS NEAR THE WRECK SITE. THE SAND WAVES ARE CLEARLY VISIBLE AND ALSO THE MULTI-PATH RETURN AT 20 METER (DEPTH OF THE AUV) IS STILL PRESENT.

2.6.5 Conclusions

- Stability of the recording platform is crucial for side-scan sonar imaging.
- A image that needs no stretching, rotation and compression anymore in the processing can be taken with an AUV because the ping per meter principle can be fully applied.
- With a 50 meter swath, there appears to be a problem with the buffers in the Marine Sonic side-scan sonar electronics. The problem does not show up when recording with the standard 30 meter swath.
- The multi-path return from the Marine Sonic sidescan sonar is also here visible, it only appears once; this indicates that the optimal operating depth of the REMUS 100 is somewhere between 30 and 100 meter.
- The Shadows SAS algorithms do not properly image the objects around the bow of the wreck. Raw data recorded with conventional sonars appears to have a higher image quality.

2.7 GENERAL CONCLUSIONS

A range of acoustic systems and methods have been used to evaluate their potential in object detection. Systems used ranged from 1 kHz seismic sources to an acoustic camera with a carrier wave of 1.8 MHz. In the range of the bottom penetrating sonars and seismic sources most problems are encountered. Because of the relatively low frequencies the transducers have to be larger and migration algorithms have to be used to focus the image. The migration algorithms require matrices of hydrophones, huge data storage and extreme platform stability plus extreme positioning accuracy. The positioning accuracy has to be higher than the platform stability needed by conventional side-scan sonar imaging. Another option is to use a low frequency pencil beam or a parametric system, but the footprint is so small that full coverage of an area and positioning accuracy and stability of the platform are beyond the limits of what can be achieved in the practical world with a floating manned platform. Semi buried mines can easily

be detected using side-scan sonar systems. Side-scan sonar systems produce the best image on a perfectly stable platform with equidistant pinging rate. The best performing side-scan sonar is the Klein 3000 side-scan sonar, the best image comes from the Marine Sonic 900 kHz side-scan sonar mounted on the REMUS 100 platform. In mud fully buried mines were detected, but they appeared not to be covered by mud. A floating mine can also be detected using a sonar- radar-infrared combination. In general the experience gathered demonstrates that mines on the soil-water interface and water-air interface can easily be detected with a range of sonar types. Fully buried objects pose a problem. Detection of fully buried objects will be time consuming, therefore it is highly necessary to define the geographical areas where full mine burial can occur. Very good knowledge of the environment should have a very high priority in the buried object detection field. Understanding the burial cycles will enable to hunt the periodically buried mines using the fast conventional techniques rather than the slow buried mine detection techniques. The environmental information can also be used to avoid the passing of seaways in areas with high mine burial risk. When a high risk area should be passed, sweeping and jamming techniques should be considered for a while, until the mine batteries are empty rather than hunting. The disadvantage of a buried mine is the need for sensors to activate. Over saturating the sensors and electronics of the mine probably is the easiest and fastest way to neutralize the mine. Over saturating the electronics of the mine may also prevent the core electronics of the mine to go into sleep and energy saving mode, resulting in a much higher than planned energy consumption and eventually an early deactivation. Maybe the installation of semi-permanent jamming stations recharging batteries on tidal and wave energy might be an option.

Phenomena interfering with acoustic object detection have been described; modeling will quantify the phenomena and enable to specifically design migration algorithms and hardware for object detection.

3 UNRAVELING FIELD TESTS THROUGH MODELING AND MIGRATION

The second, and first successful, test done was the low frequency test in 2004 at Zeebrugge. The aim was to detect a semi buried mine in the mud. The mine was detected on the raw image and migration of the data did not deliver a better image. There was no conclusive explanation on the failure. Also visible were hyperbola at every level of the sand body that could potentially hide a buried sea mine. The mine would have been hidden because the hyperboloids in the sand volume were of higher amplitude than the hyperboloid caused by the mine. Migrating only in 2D cannot solve this problem as will be demonstrated further in this chapter. A full 3D modeling and migration cycle was built. The aim was to find possible problems with the migration algorithm, find out the effects of roughness, position accuracy, sampling frequency,... on a number of 3D processing algorithms including 3D migration algorithms.

3.1 INTRODUCTION

The 3D VHRS experiments on Lac Pavin, the Schelde and St.Austell bay delivered data that could not be migrated properly (Marsset, Missiaen et al. 1998; Missiaen 2005; Missiaen, Wardell et al. 2005; Missiaen 2008). The Lac Pavin data could even not be stacked in each bin (Moreaux 2003). The 3D VHRS imaging was of lower quality than 2D sections. Most high resolution seismic data is 2D and is never migrated because it does not give better results. That contrasts with the SAS research, where migration on similar frequencies is possible (Bruce 1992; Pinto, Bellettini et al. 2004). A model was built to find out why in one field migration works and in a parallel field it does not. The model was an expansion based on the very early seismic models used in the literature of the sixties to early eighties of the twentieth century in reflection seismic processing (French 1974; Gardner, French et al. 1974; French 1975; Schneider 1978; Stolt 1978; Judson, Lin et al. 1979; Schultz and Sherwood 1979; Chun and Jacewitz 1981; Larner, Hatton et al. 1981; Herman, Anania et al. 1982; Kosloff and Baysal 1983; McMechan 1983; Gardner 1985). These models were crucial and very successful in the early development stages of 2D and 3D migration algorithms.

Initially one extremely simple model was built. Despite the simplicity and naivety of the model, it appeared to generate valuable synthetic data for testing processing algorithms. The model results were first migrated with all acoustic input parameters fully known, the results showed perfectly focused images. Then the data was manipulated with errors in the position matrixes and migrated again. Increasing the error interval showed a serious degradation of the focused image and this led to an estimate of maximum error on the positioning in function of frequency. Essential features such as beam patterns could not be entered in the model and the data has to be raster data. Raster data does not have enough samples on steep flanks of a terrain model and as such underestimates the acoustic contributions of for example objects. These properties are important to understand and test as well. As a result existing acoustic models were tested and three other models were built, from which two designs were abandoned and only one became a

fully working acoustic model. More information about the last complete model built can be found back in chapter 4.3.

3.2 3D POINT SCATTERER MODEL FIRST VERSION

3.2.1 Modeling low frequency acoustic object detection (Zeebrugge 04)

3.2.1.1 INTRODUCTION

The model applied is very basic, it has a lot of similarities with the 3D model used by French (French 1974) who refers to Trorey and Gardner et al. as key authors (Trorey 1970; Gardner, French et al. 1973). Point scatterer models are simple and fast, all fundamentals of seismic migration theory have been developed using these models, therefore they are the ideal tools for some deeper evaluation of the migration algorithm performance. The model described by French (1974) was expanded over a 100 times in surface elements. A matrix of point scatterers was used to describe the seafloor surface with objects. The distance from the transceiver was measured to every point scatterer. Using the measured distance of every point scatterer as an index, the impulse response matrix $L[d]$ was then incremented with one on the specified distance d resulting in an impulse response. Spherical spreading was applied on the impulse response. The impulse response was then convolved with a source wavelet (Burns 1968; Webster 1978; Yilmaz 2001; Margrave 2003).

A 60 days processing was reduced to three full days using 6 networked calculation computers and one server (early generation of pentium IV computers). A full 3D zero offset seismic block was generated. The goal of this modeling was to find out how accurate the 3D VHRS measurements had to be (Marsset, Missiaen et al. 1998; Gutowski, Bull et al. 2002; Bull, Gutowski et al. 2005; Missiaen 2005; Missiaen 2008). Field tests demonstrated that measurement accuracy both in the space as time domain might be very important if the acoustic data is to be migrated.

This chapter also includes the networking module implemented. The implementation of the networking module can be copied into the implementation of the latest extremely calculation intensive acoustic model. The final results of the simulations were extensively used in evaluating 3D migration algorithms.

In the thesis no code will appear. Codes have been replaced by flowcharts. The code itself is added in the software book, allowing the reader to compare the code with the flowcharts. Flowcharts are easy to read schematic representations of software. Not all software described in the software book will be put in flowcharts.

3.2.1.2 THEORY

A full 3D modeling approach was chosen after a combination of 2D models and migrations showed some inevitable restrictions such as the absence of sideswipes and blind structures (French 1974). The model used focused on the acoustic scattering of the seafloor. The model is based upon the model used in the early stages of migration research (French 1974; Gardner,

French et al. 1974; French 1975; Schneider 1978; Stolt 1978; Judson, Lin et al. 1979; Schultz and Sherwood 1979; Chun and Jacewitz 1981; Larner, Hatton et al. 1981; Herman, Anania et al. 1982; Kosloff and Baysal 1983; McMechan 1983; Gardner 1985). The model has the following principle. Discrete point scatterers placed in a grid, build the surface S . The size of S is a matrix of 1000×1000 elements. Every point in the matrix represents a height of the surface. The distance d to every point describing the surface to the transceiver t is measured and multiplied by 2 (two way travel time). A line array L is made and subdivided in centimeter increments. The distances between the transceiver and every point scatterer is given in centimeter and used as index in the line array $L[d]$. The position $L[d]$ is then incremented. Following this procedure for every point scatterer in S gives the impulse response of the surface. The impulse response L can now be adjusted, using spherical spreading. Following the convolution rule in reflection seismics, convolving the impulse response of the environment with the acoustic signal delivers the acoustic trace (Burns 1968; Webster 1978; Yilmaz 2001; Margrave 2003). The generated acoustic trace is stored in an acoustic profile. The position of the transceiver is changed to the next position and the calculation starts again. This procedure with the changing position of the transceiver following a line gives an acoustic profile. In order to generate a volume, several parallel lines have to be sailed resulting in a grid of acoustic responses, or an acoustic data volume (Schneider 1978). The position grid of the transceiver counts 1000 by 1000 coordinates. The X and Y coordinates are identical to the X and Y coordinates chosen for S . The disadvantage of applying this approach 1000×1000 times is the calculation time. In order to reduce the calculation time cluster processing has been introduced. Computers on a network contribute to the calculations and distribute the jobs. No formula such as ray tracing formula or any formula derived from acoustic experiments were used, the reflectivity coefficient in the given example was set to 1. The P -wave velocity in the water is assumed to be constant and set at 1500 m/s . No secondary echoes caused by P -wave multipath in between the sand waves were brought into calculation. No shadow effects were taken into account. The sources used were bottom penetrating, but due to the complexity of the sub-bottom to simulate, no bottom penetrating acoustics was modeled. In order to decrease the calculation time, the model is designed to be used in parallel on multiple computers in a network. One slow computer is set up as server, commanding workstations what and where to simulate. The server can also collect the simulated sections and writes them in a 3D seismic block (SEG-Y format). The code for the data collecting has not been added. Storing the seafloor and transducer beams in mathematical formulas reduces the use of the ram memory and makes it suitable to run the software completely in the background.

The implementation of the theory was done using MATLAB® in combination with the pnet TCP/UDP/IP Toolbox 2.0.5 (Rydesäter 2003). The communication consisted of some handshaking and passing data using UDP. The final result looks like a downsized non-connection oriented TCP/IP.

3.2.1.3 MODEL SOFTWARE OVERVIEW

TABLE 1: OVERVIEW OF PROGRAMMES USED FOR THE ACOUSTIC MODEL IMPLEMENTATION

Filename	page	Type	Description
server.m		Program	main software running on the server
multiPPcontrol.m		Program	old version of server.m
ppcslave.m		Function	communication module running on workstations
topogenerator.m		Program	generates a rippled topography
Bandpasszf.m		Function	zero phase bandpass filter
drieDblok.m		Program	main software running on the workstations
simul3D		Function	the acoustic model

3.2.1.4 SOFTWARE FLOWCHARTS

3.2.1.4.1 THE SERVER SET UP (SERVER.M)

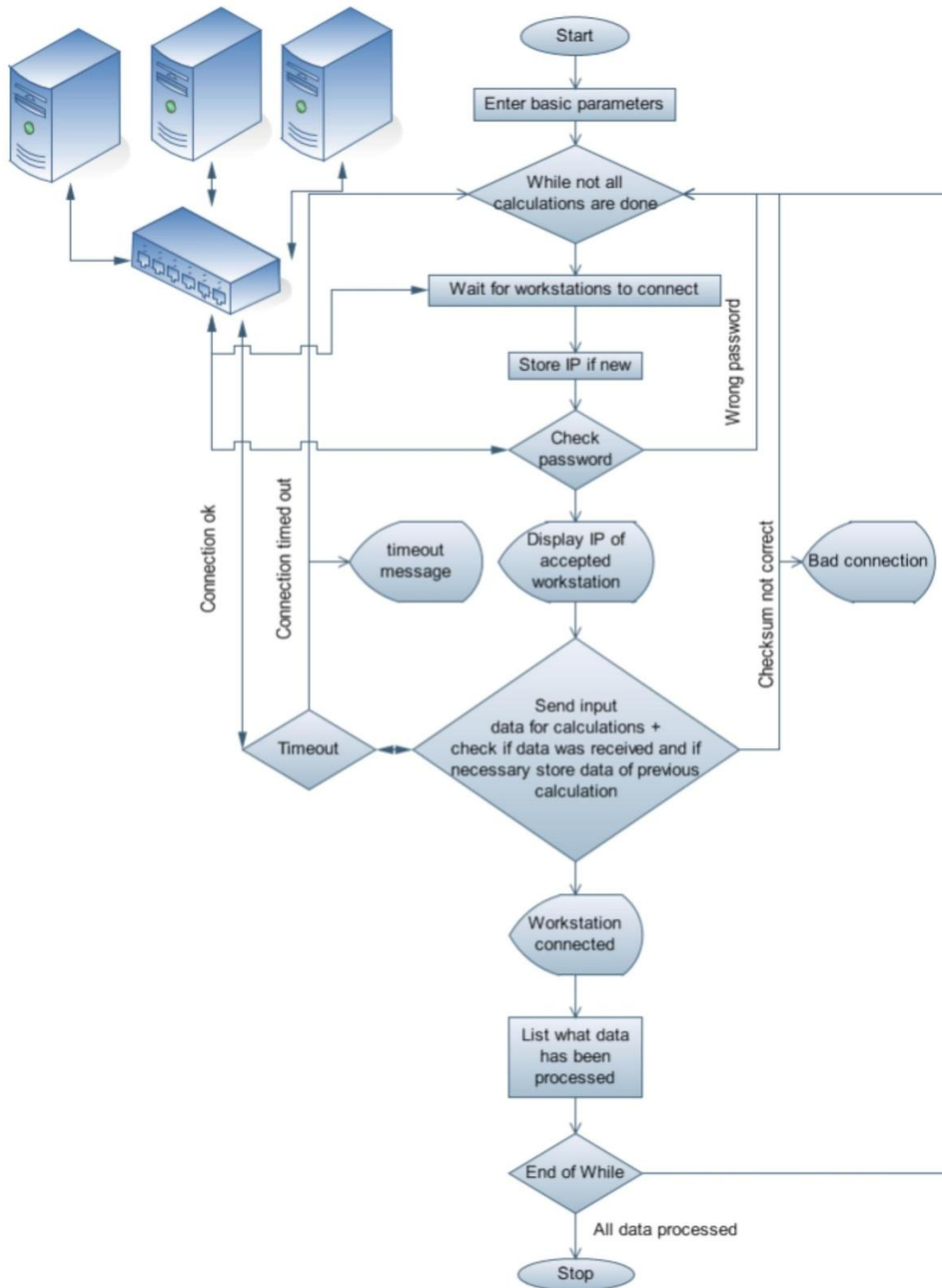


FIGURE 3-1: FLOWCHART OF SERVER SOFTWARE

3.2.1.4.2 THE WORKSTATION SET UP (TOPOGENERATOR.M AND DRIEDBLOK.M)

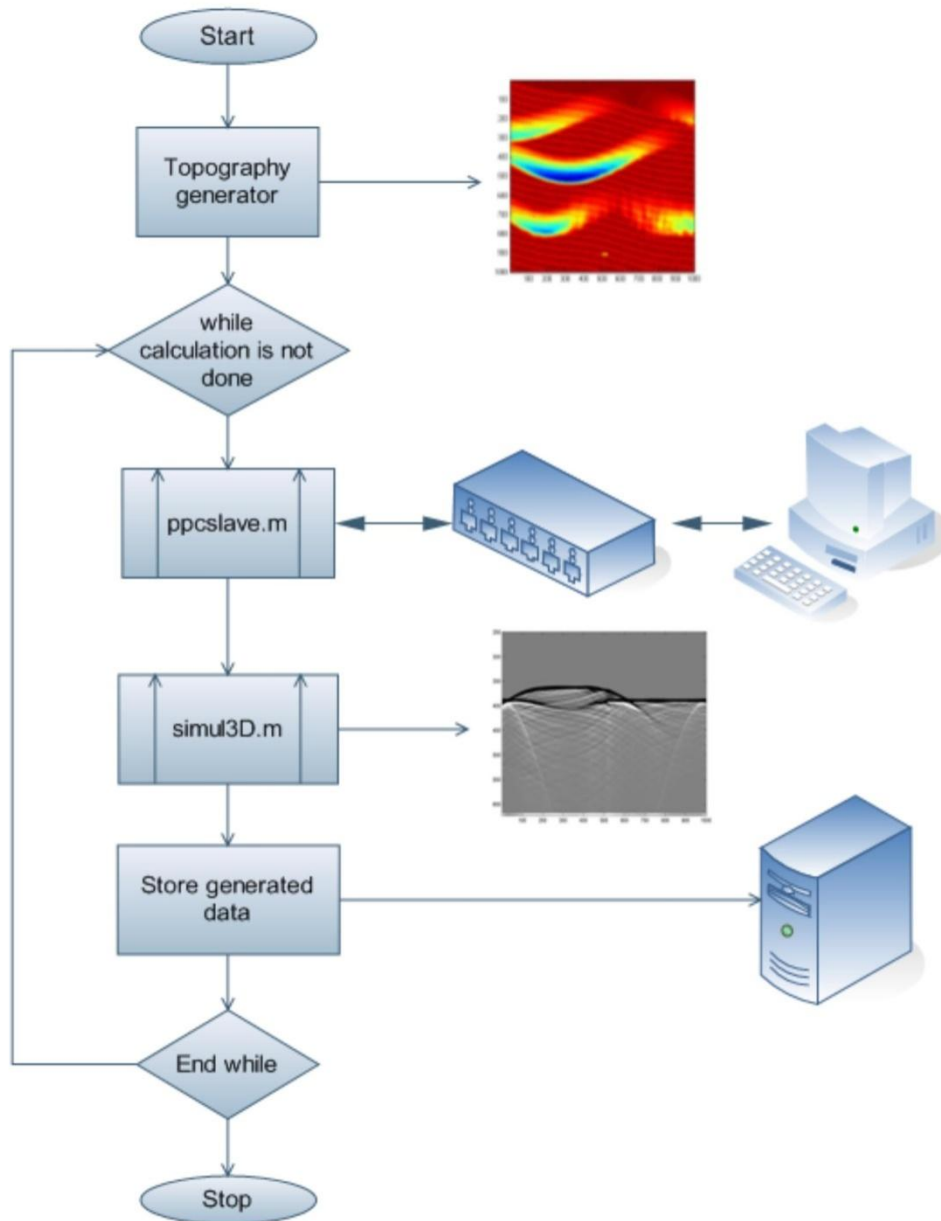


FIGURE 3-2: DRIEDBLOK.M FLOWCHART, MAIN SOFTWARE RUNNING ON THE WORKSTATIONS, CALLS FUNCTIONS PPCSLAVE.M AND SIMUL3D.M

3.2.1.4.3 SIMUL3D, THE ACTUAL MODEL

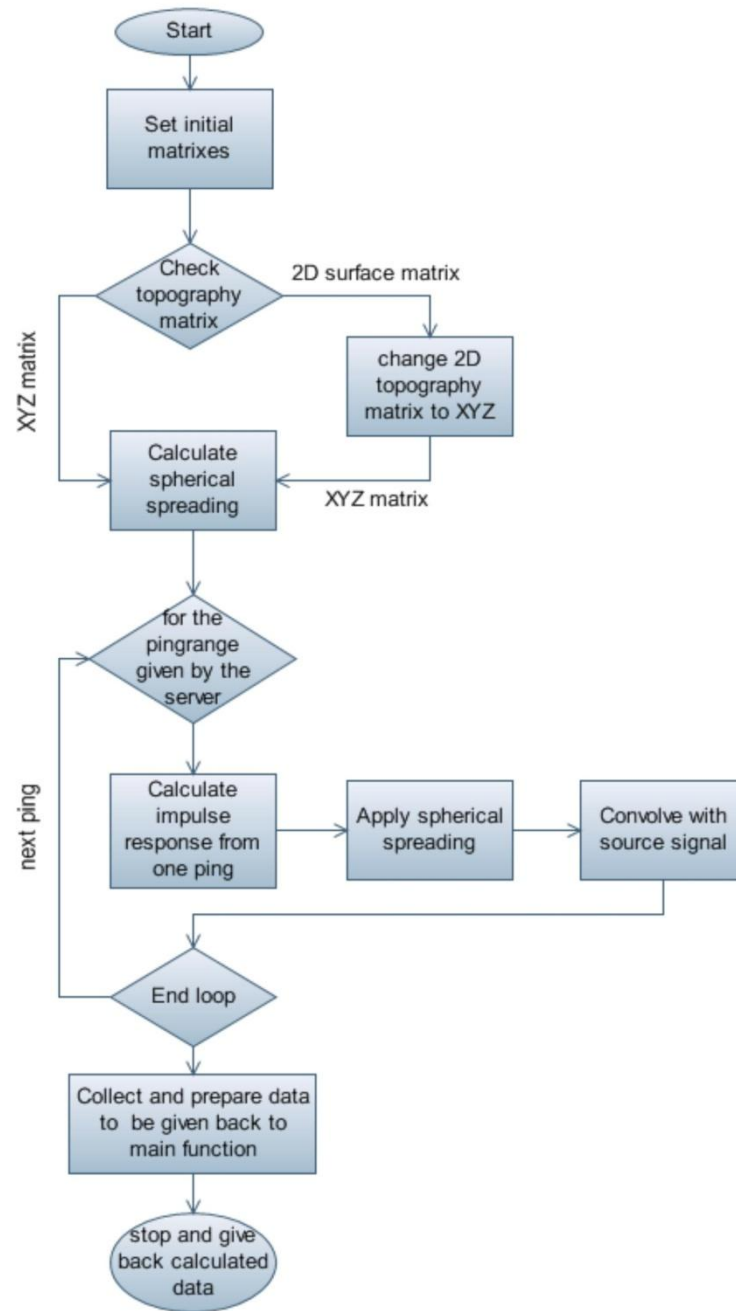


FIGURE 3-3: SIMUL3D FLOWCHART: THE FUNCTION IS CALLED BY DRIEDBLOK AND GENERATES ACOUSTIC PROFILES

3.2.1.4.4 PPCSLAVE.M; UDP BASED COMMUNICATION CONTROL (WORKSTATIONS)

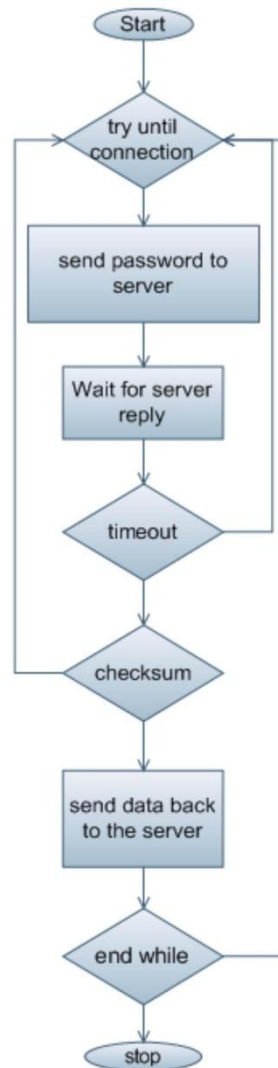


FIGURE 3-4: FLOWCHART OF PPCSLAVE, THIS FUNCTION CONTROLS THE CONNECTIONS BETWEEN THE WORKSTATIONS AND THE SERVER. THE SLAVE CONTINUOUSLY CHECKS THE CONNECTION.

3.2.1.5 MODEL PARAMETERS

Parameters entered in the topographic model were: a 3D topography generated with a mathematical function. Figure 3-5 displays the generated surface with a fixed spacing between the pixels or point scatterers (in general 1 or 5 cm). In this case 5 cm grid interval was chosen. Other input for the workstations are: a source signature, radiation pattern and central frequency of the source, the sound velocity in the water and the places where to sail a synthetic seismic line or to calculate a synthetic 3D block. Acoustic traces have a final sampling frequency of 28 kHz. The model was set to record single channel zero offset data (mono-static) as implemented by French (French 1974). The resulting data volume is equivalent to the most optimal post stack 3D seismic block. This approach avoids normal moveout corrections, binning and stacking algorithms. As a result only the constant velocity post stack migration algorithms have to be applied to get the focused volume. We also consider ourselves working with a source with a

spherical pattern. Migration of the model was done, using existing 2D and 3D f-k and Kirchhoff migrations available for academic use and made available on the internet (Margrave 2003). The surface used is depicted in Figure 3-5.

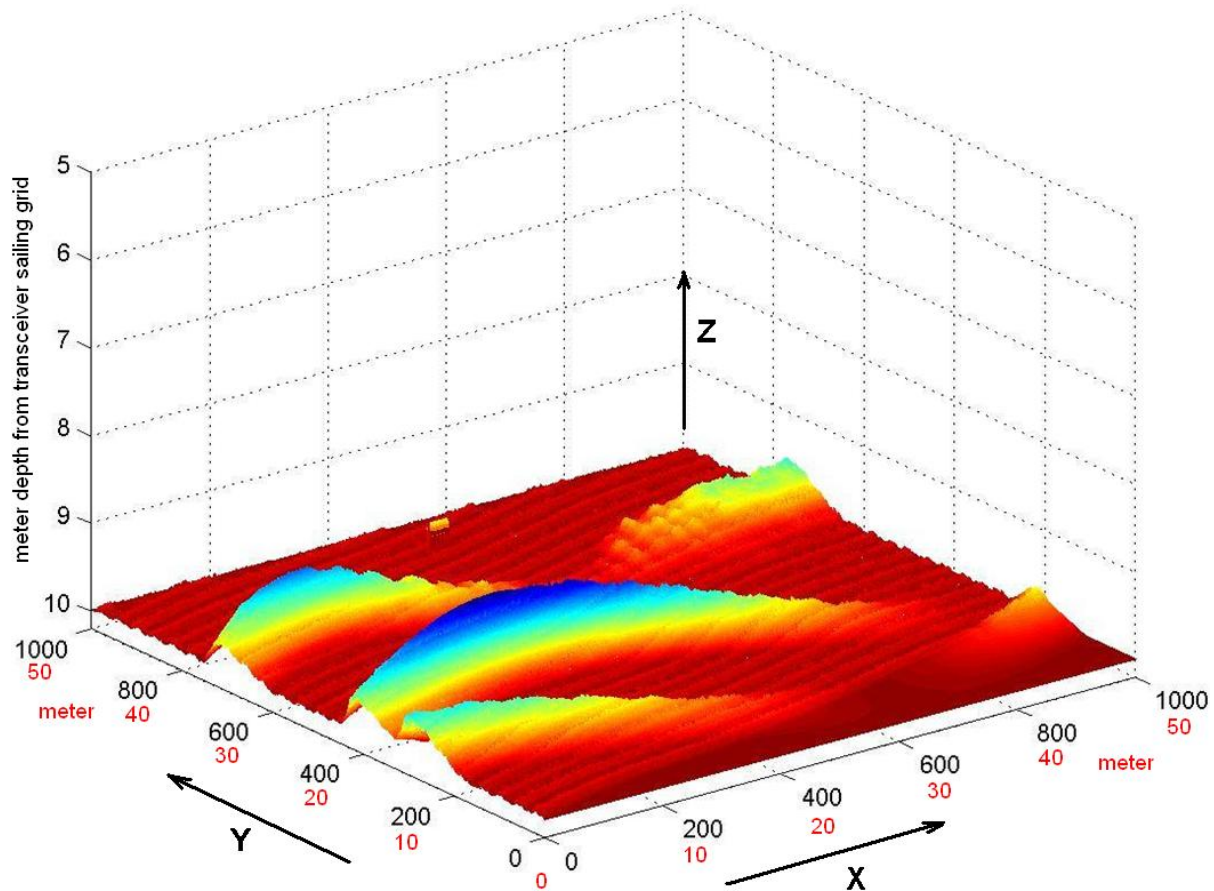


FIGURE 3-5: RIPPLE FIELD ENTERED IN THE MODEL.

A number of bedform like features were simulated and combined, an example of such a combination of bedforms is given in Figure 3-5. Three ripple frequencies were introduced; two of them are clearly visible, the two types of 'low frequency ripples'. There is one high frequency ripple field not visible on the figure, however it is asymmetric and has been introduced perpendicular to the other bedforms. A semi buried cylindrical mine can be found on (500,900). Around coordinate (700,800) dredging marks can be found on the ripple. The acoustic simulation uses a 3.5 kHz sine wavelet, a spherical point source and zero offset acquisition.

3.2.1.6 RAW MODEL RESULTS

Acoustic profiles from a 3D acoustic volume are generally taken inline, crossline and in timeslices. Figure 3-6 shows the relations between the slices and the coordinate system. The Z axis usually is the time axis, therefore slicing the Z axis is called timeslicing.

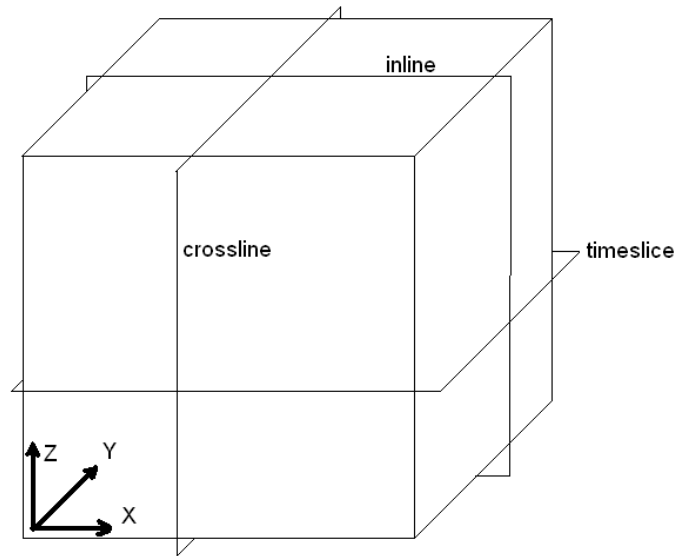


FIGURE 3-6: INLINE, CROSSLINE AND TIMESLICE PRINCIPLE

The acoustic profile (Figure 3-7) shows how the reverberation of one reflector affects a whole profile. The profile taken is taken inline $Y=500$, with $X=0$ to 1000 . Migrating in the X direction will reduce some of the reverberation but will not remove it as will be demonstrated further on and has been demonstrated in the literature (French 1974; French 1975). Migrating both in Y and X direction requires a data volume and will generate a 3D migrated dataset. 3D migration should remove most of the reverberation.

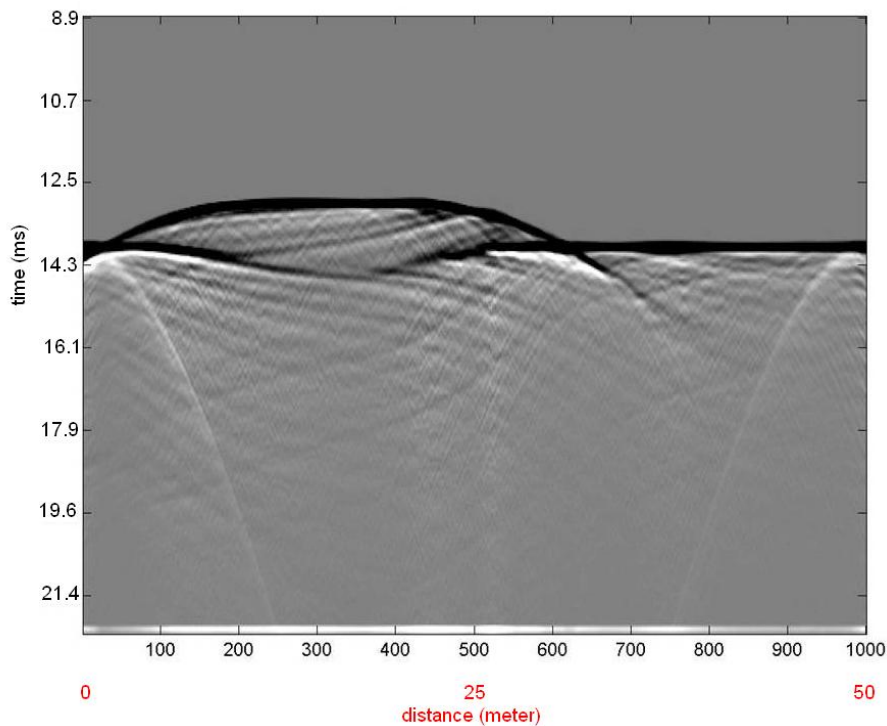


FIGURE 3-7: A MODELED PROFILE SECTION. THIS SECTION IS TAKEN PARALLEL WITH THE TWO LOWEST FREQUENCY BEDFORM STRUCTURES, TROUGH ONE OF THE SANDBANKS. THE ACOUSTIC RESPONSE IN THIS IMAGE IS SURFACE COMPONENT ONLY, NO VOLUME CONTRIBUTIONS ARE ADDED TO THE SIGNAL.

The time slices in Figure 3-8 are taken in equal time steps starting at 13.5 ms with a step of 0.5 ms. They show that also in the time slices the reverberation is very much visible. The signature of a mine, a hyperboloid, can be seen at coordinate 500,900. The two largest ripple types are clear in the slices. The third, smaller asymmetric ripples with a crest line running from top to bottom of the slices, instead of the left right direction, might be seen at the left hand side of the slices. They appear to create some kind of a higher amplitude backscatter.

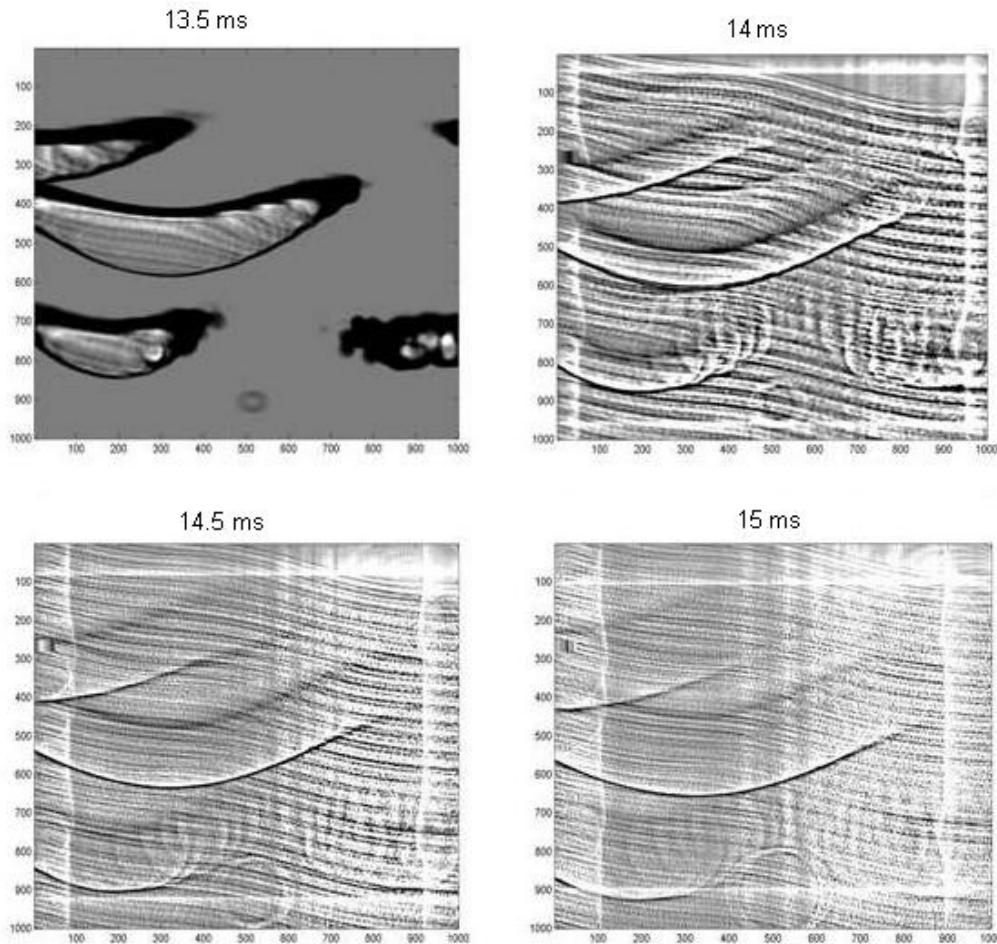


FIGURE 3-8: SIMULATED TIME SLICES, THE FOUR TIME SLICES ARE TAKEN IN EQUAL TIME STEPS IN A NON MIGRATED ACOUSTIC VOLUME. THE FIRST SLICE IS LEFT TOP, SECOND: RIGHT TOP, THIRD: LEFT BOTTOM, FOURTH: RIGHT BOTTOM. THE NEXT TIME SLICES WILL BE DISPLAYED IN THE JET COLOUR SCALE, JET COLOUR SCALE REVEALS MORE DETAIL

3.2.1.7 REFLECTOR COHERENCE OF NON MIGRATED ACOUSTIC DATA

The coherence of a reflector, defines the visibility of an event in a raw acoustic image (Sheriff 1984). Very often in VHRS the only processing done is band pass filtering, with sometimes a deconvolution and a reflector coherence enhancing filter such as a swell filter (Missiaen 2005; Missiaen 2008). Migration is, because of bad performance on real VHRS data, often not applied. Why migration does not perform well on VHRS data will be discussed in 3.3.6.

That aliasing is a source of bad signal quality is very well known. What about spatial aliasing? And in case of spatial aliasing, how dense does the sampling have to be to get an optimal image? The most logic answer would be for a to-be-migrated volume: smaller than the resolution that

can be achieved by migrating that volume (Bull, Gutowski et al. 2005). The highest resolution in a migrated volume is one fourth of the wavelength of the signal used (Yilmaz 2001). In this case, when a transducer of 3.5 kHz is used and the sound velocity in water is 1500 m/s, the spatial sampling should be at least 12 centimetre. The acoustic sections where the effects of spatial undersampling can optimally be observed are time slices: they are sections with two spatial dimensions (the X and Y axis). Figure 3-9 shows four equal sections in a time slice in the same acoustic volume we used before. The 5x5 cm bin size slice has a very clear image. Downsampling the image gives with every down sampling a worse result. Downsampling from a 5x5 cm grid to a 15x15 cm grid is done by taking from the 5x5 cm grid a trace on position (1,1), (1,4), (4,1), (4,4), (1,7),... A visual check of Figure 3-9 learns that for an unprocessed data volume more or less the same rules as for a migrated volume apply.

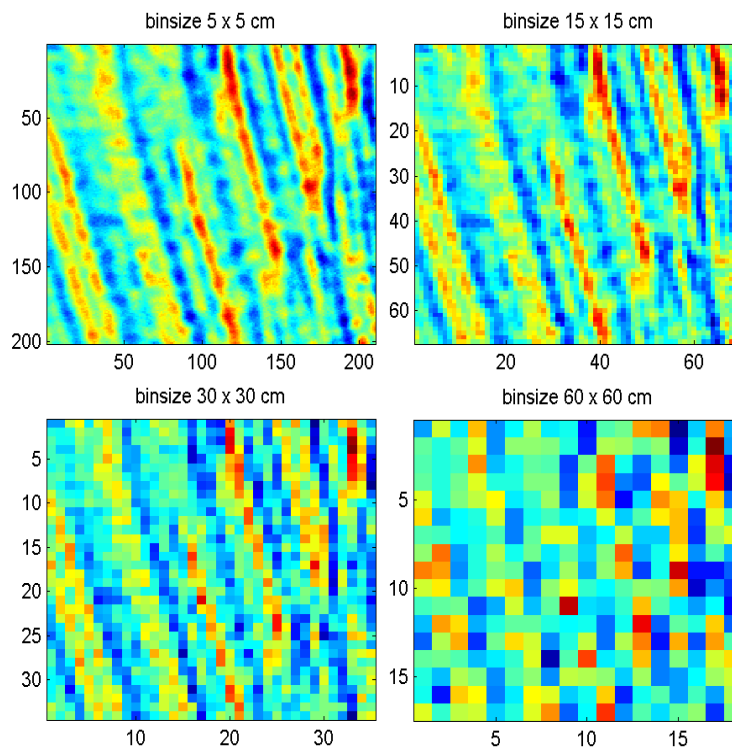


FIGURE 3-9: FOUR DETAILS OF TIME SLICES IN THE RAW ACOUSTIC DATA VOLUME PRESENTED BEFORE EACH WITH A LARGER BIN SIZE. UPPER LEFT IS THE HIGHEST RESOLUTION IMAGE WITH A VALUE EVERY 5 CM BOTH IN X AND Y DIRECTION. THE OTHER THREE IMAGES UP LEFT AND RIGHT AND LEFT DOWN ARE SPATIALLY UNDERSAMPLED. THE UPPER RIGHT IMAGE IS ONLY SLIGHTLY UNDERSAMPLED AND SIGNIFICANT IMAGE DEGRADATION IS NOT VISIBLE.

3.3 MIGRATION OF A 3D MODELED ACOUSTIC BLOCK

3.3.1 Introduction

Migration is one of the most important algorithms used in acoustic processing. Migration focuses an acoustic image. Migration algorithms have limitations. Investigating these limitations, mainly on positioning accuracy, is the goal of this chapter. Bin sizes also have an influence on the imaging, as will be demonstrated.

Migration algorithms are often customized to a dataset. Small customizations can be done by setting parameters of the migration algorithm implementation. Migration methods can work in a combination of different domains (time, space, spatial frequency, frequency) (Gardner 1985; Yilmaz 2001; Margrave 2003). All migration methods aim at focusing the wave field emitted by every point scatterer in the data volume back to that respective point. Remember that a surface can be described using a 2D point scatter matrix. In a 2D time-space representation of a wave field scattered by one single scatter point, the wave field looks like a hyperbola (Figure 1-14). Summing the contributions of the hyperbola in the apex of the hyperbola is called 2D migration. 2D acoustic wave fields do not exist in nature but 3D wave fields do. A 3D wave field in reflection seismic or in a time-space-space domain is recorded as a hyperboloid. Luckily, in this model, a 2D migrated hyperboloid results in a hyperbola perpendicular to the direction of the 2D migration, Figure 3-10. That means that in a homogeneous medium, applying another 2D migration perpendicular to the previous 2D migration will focus a hyperboloid into the apex. A good reference on migration methods is (Yilmaz 2001).

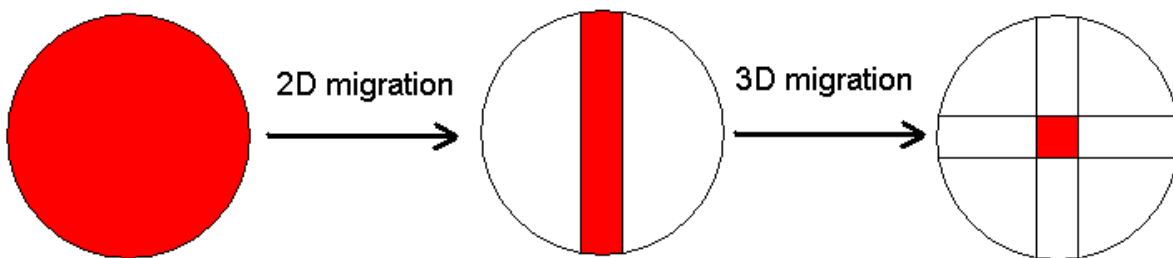


FIGURE 3-10: THE APERTURE CHANGES THROUGHOUT MIGRATION. LEFT: THE SURFACE CONTRIBUTIONS TO AN UNMIGRATED SIGNAL, CENTRE: THE SURFACE CONTRIBUTIONS TO A 2D MIGRATED SIGNAL, RIGHT: THE SURFACE CONTRIBUTIONS OF A SIGNAL AFTER TWO PERPENDICULAR MIGRATIONS OR 3D MIGRATION.

Three migration options were open: Kirchhoff migration, phase shift migration and f-k migration. Kirchhoff migration is by far the most flexible algorithm since it works in the space time domain and as such it allows implementation of for example ray tracing algorithms in a relatively simple way. Kirchhoff migration might, for that reason, become the only option in high resolution seismic migration. Kirchhoff migration is also the most used algorithm in the focusing of complex data sets with lateral acoustic velocity changes. Phase shift migration is the slowest method and transforms between the time domain to the frequency domain, it is mostly used in focusing acoustic data near very steep reflectors. The f-k or Stolt migration transforms both between space-spatial frequency and time-frequency, it is the most rigid and mathematically complex algorithm but by far the fastest (Stolt 1978).

As previously described the simplest 3D migration algorithm is composed of two 2D migrations. Thanks to the CREWES project (Margrave 2003), these 2D algorithms originally available in Seismic Unix (Dix 2006) are now available in MATLAB® and can be found for free for non commercial use on the internet. In the following migration two constant velocity f-k migrations were applied.

3.3.2 Migration software overview

The migration software consists of a number of independent programs. Memory shortage or memory allocation is always a problem when dealing with 3D acoustic volumes. The first step a processor or interpreter does is generating a set of inlines, cross lines and time slices. Like that an organized dataset is made allowing efficient swapping between the harddisk and the RAM memory. The complete dataset, more than 2GB in size could not be loaded in the RAM memory at the time of implementation (2004). In order to load the dataset in the ram, the binsizes were increased and the water column removed, resulting in a dataset of approximately 300 MB.

The second group of programs organizes the migration flow.

Filename	Page	Type	Description
drieDsegy.m		Program	write inlines into a 3D SEG-Y volume
timeslice.m		Program	Slow method to generate time slices
Timesliceblock.m		Function	Fast time slice generator
Inline3		Program	Make cross lines from an inline volume or the other way around
bin10cm.m		Program	Stack bins from 5 to 10 cm
driedmig.m		Program	Post stack constant velocity 3D migration

3.3.3 Software flowcharts

3.3.3.1 TOTAL FLOW

The volume is binned to 10 cm bins instead of 5 cm bins, the water column is removed and the resulting dataset migrated.

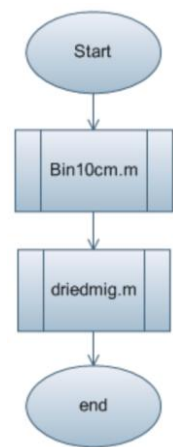


FIGURE 3-11: 3D MIGRATION FLOW

3.3.3.2 BIN10CM.M

Binning in 10 cm bins reduces the data volume four times by stacking four bins into one. The data volume is further reduced by removing the water column data from the dataset and compensated by entering a time delay in the migration algorithm.

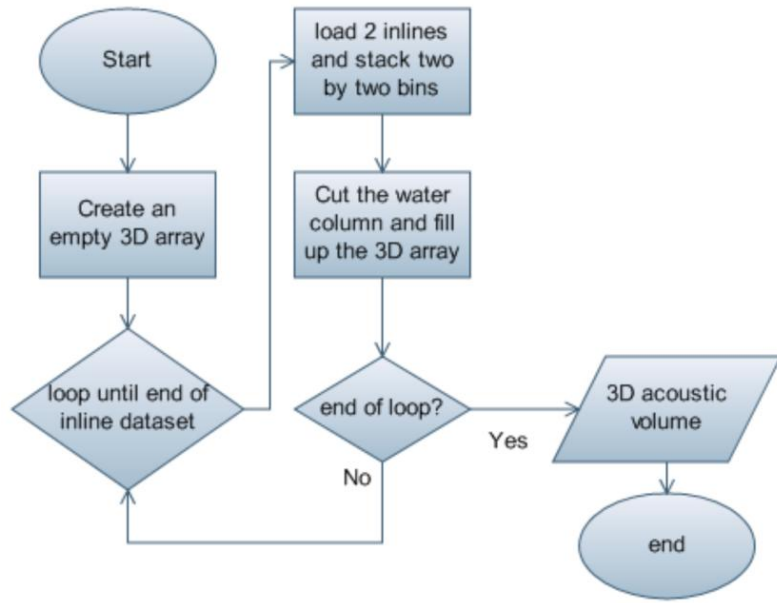


FIGURE 3-12: STACKING BINS AND STORING THE RESULT IN A 3D ARRAY

3.3.3.3 DRIEDMIG.M

This routine performs an f-k migration both in inline and in cross line direction. Adding noise to the position coordinates is possible. Keep in mind that creating too much position noise may generate errors in the migration algorithm.

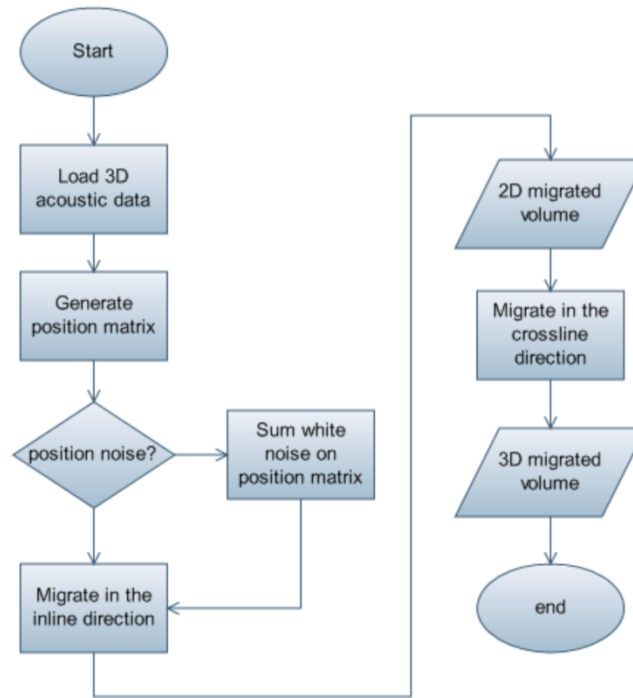


FIGURE 3-13: A 3D CONSTANT VELOCITY F-K MIGRATION OF AN ACOUSTIC VOLUME LOADED IN THE RAM MEMORY

3.3.4 Migration parameters

The migration parameters are:

- Type of migration: f-k
- seismic section (1000 sections in both X and Y direction in the case of 5x5 cm bins, 500 sections in both X and Y direction in the case of 10x10 cm bins)
- time delay introduced by removing the water column (12.5 ms)
- velocity of the acoustic wave in the water column (1500 m/s)
- position matrix (0 to 50 meter with a step of the binsize, position noise can be added to each position)
- sampling frequency (28000 Hz)
- other parameters related to the implementation of the algorithm (tapers, aperture, interpolation methods and so on) were the standard parameters in that f-k migration algorithm. The default parameters of the f-k migration are taken from (Margrave 2003).

3.3.5 Migration results

3.3.5.1 OVERALL

The reverberation visible on the profiles (real: Figure 2-7, modeled: Figure 3-7) might mask an object if buried. Applying the default algorithm focuses the hyperboloids into the apices. The algorithm clearly demonstrates the potential in reverberation focusing. The 2D applications of the migration do not remove reverberation at all (French 1975). Note that the data shown here is the complete dataset and not the reduced 10x10 cm bin set.

3.3.5.2 INLINE

The three inline sections shown are taken on row Y=500 of the data volume. Figure 3-14 shows the three stadia in the processing displayed in Figure 3-10. The top is the raw acoustic data section, the middle are the 2D migrated version (migrated in the direction of the profile) and the bottom are the 3D migrated profile. The 2D migration clearly does not suppress the reverberation, although it might have been slightly reduced. That a migration algorithm has been applied, is visible on the sides of the figure (two hyperbolae of the side effects upside down).

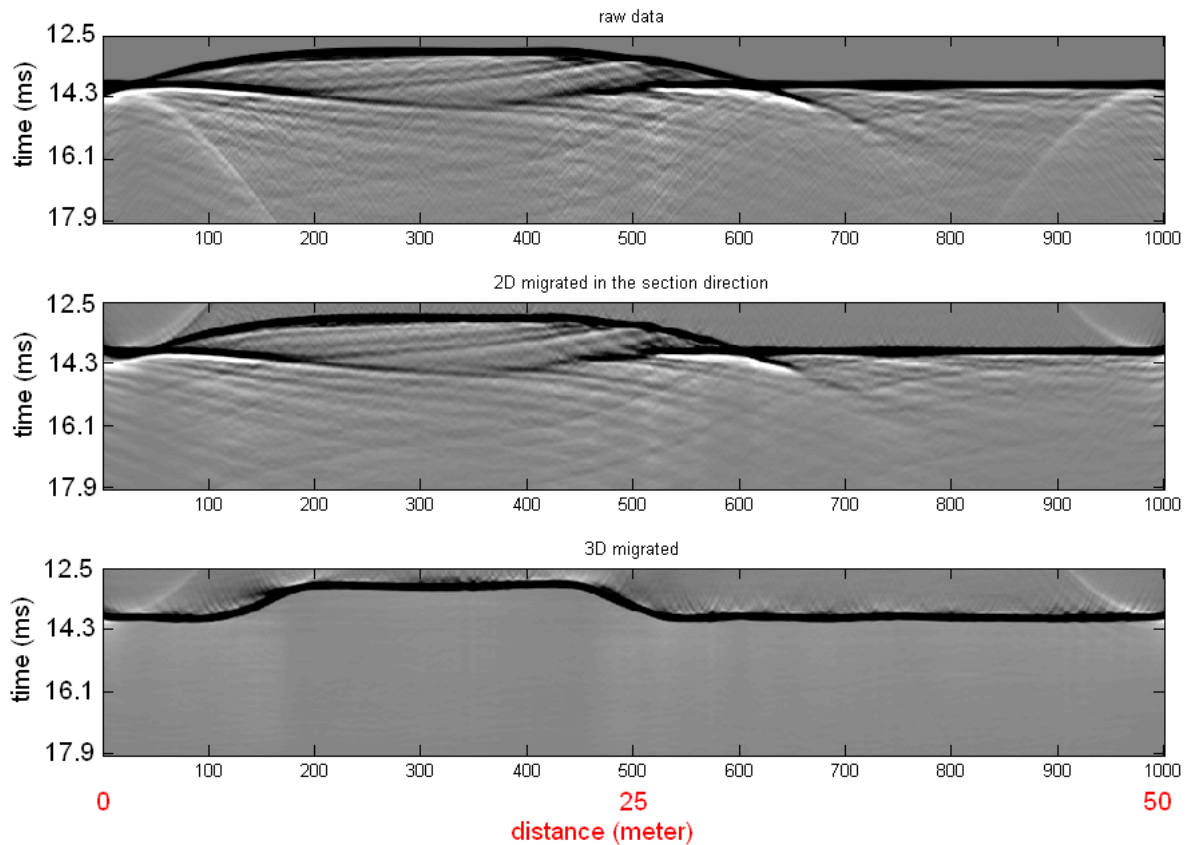


FIGURE 3-14: INLINE SECTIONS OF THE 3D VOLUME. THE TOP FIGURE IS THE RAW DATA, THE CENTRE FIGURE IS THE SAME PROFILE 2D MIGRATED IN THE DIRECTION OF THE PROFILE. THE PROFILE ON THE BOTTOM IS THE SAME SECTION AS THE TWO PROFILES ABOVE IT, TAKEN IN THE 3D MIGRATED VOLUME.

3.3.5.3 CROSS LINE

Observations in the cross lines (X=500) are similar to the inlines: 2D migration does not remove the reverberation, 3D migration does. 2D migration might have slightly reduced the reverberation.

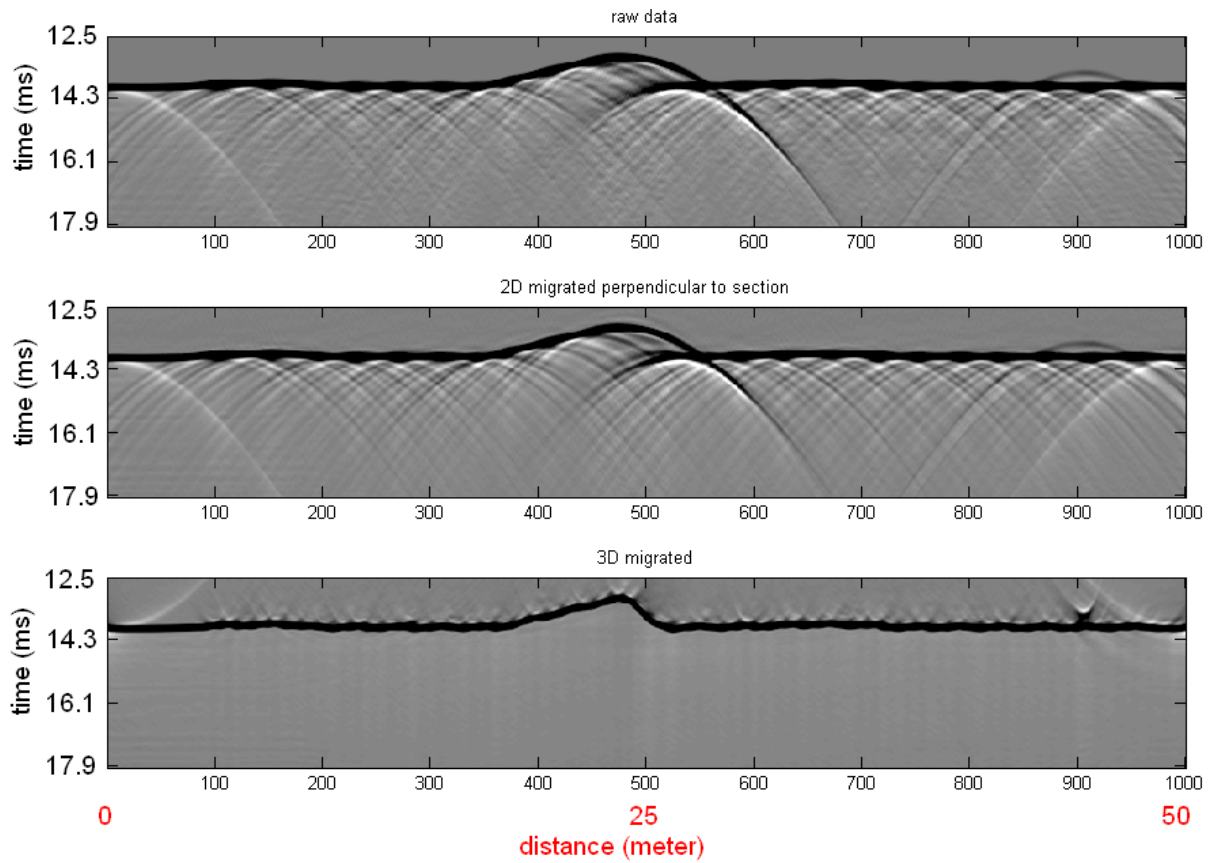


FIGURE 3-15: CROSS LINE SECTIONS OF THE 3D VOLUME. THE TOP FIGURE IS THE RAW DATA, THE CENTRE FIGURE IS THE SAME PROFILE 2D MIGRATED PERPENDICULAR TO THE DIRECTION OF THE PROFILE. THE PROFILE ON THE BOTTOM IS THE SAME SECTION AS THE TWO PROFILES ABOVE IT, TAKEN IN THE 3D MIGRATED VOLUME

3.3.5.4 TIME SLICES

Figure 3-16 and Figure 3-17 show progressively deeper time slices through a raw dataset (left), a 2D processed dataset (middle) and a 3D dataset (right). The steps are taken with a step of 0.3 ms starting at 13.2 ms. An important observation is that the reverberation in the sand waves is gone in the 3D migrated image. Also the object becomes focused.

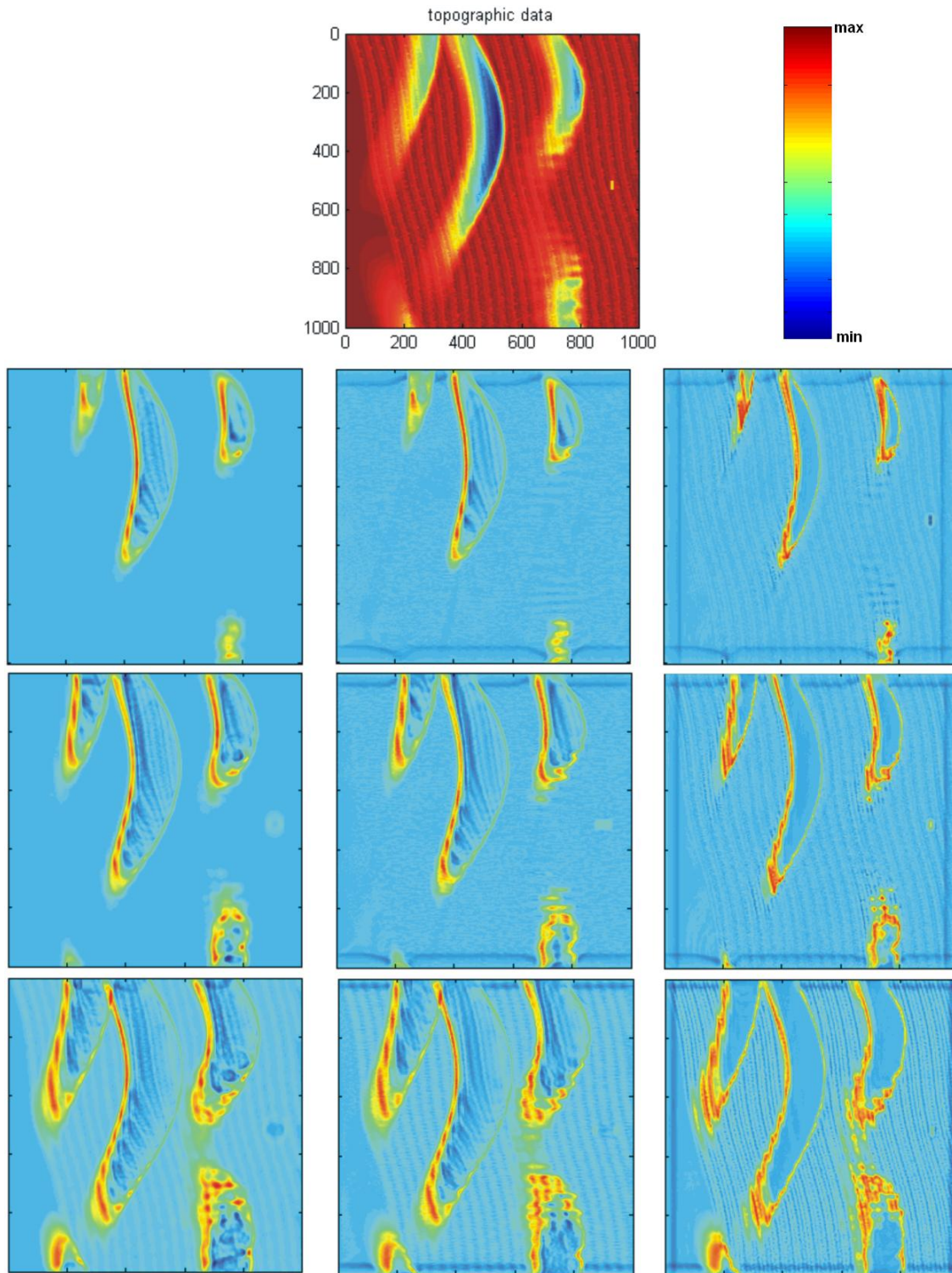


FIGURE 3-16: THE TOP IMAGE IS THE TOPOGRAPHY USED TO SIMULATE THE ACOUSTIC DATA VOLUME. THE MATRIX OF NINE FIGURES ARE TIME SLICES THROUGH A RAW ACOUSTIC DATA VOLUME (LEFT), A 2D MIGRATED VOLUME IN THE UP DOWN DIRECTION (MIDDLE) AND A 3D PROCESSED VOLUME (RIGHT). THE SLICES ARE TAKEN WITH A STEP OF 0.23 MS STARTING AT 13.2 MS

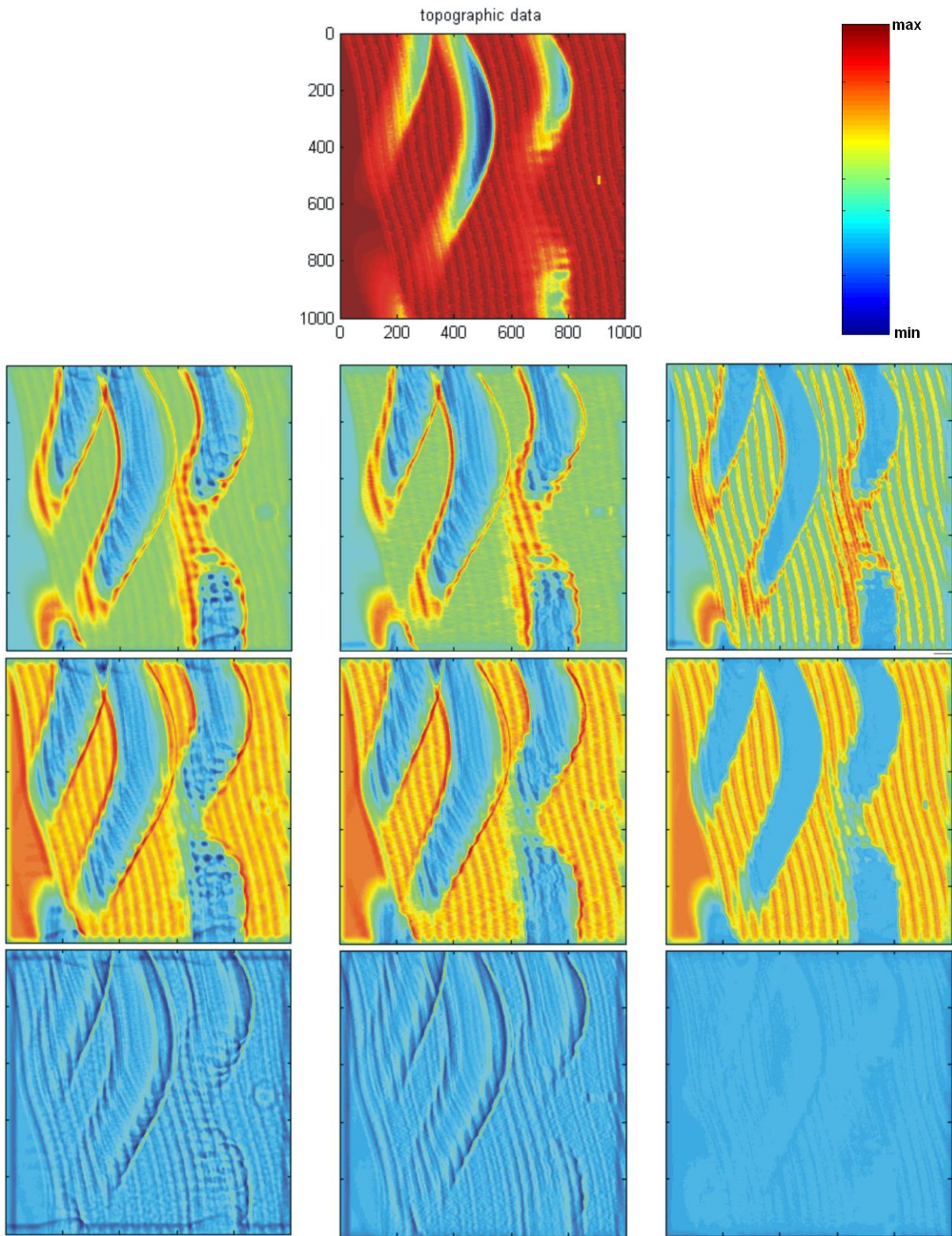


FIGURE 3-17: THE TOP IMAGE IS THE TOPOGRAPHY USED TO SIMULATE THE ACOUSTIC DATA VOLUME. THE MATRIX OF NINE FIGURES ARE TIME SLICES THROUGH A RAW ACOUSTIC DATA VOLUME (LEFT), A 2D MIGRATED VOLUME IN THE UP DOWN DIRECTION (MIDDLE) AND A 3D PROCESSED VOLUME (RIGHT). THE SLICES ARE TAKEN WITH A STEP OF 0.23 MS STARTING AT 13.9 MS

3.3.5.5 OBJECT DETECTION

In a flat ripple field in the topographic data, a semi buried cylindrical mine shape was introduced. Focusing the object appeared to work. Figure 3-18 depicts how the object was embedded in the environment. Figure 3-19 is a detail of the timeslices above, trough and under the object in high detail. 50 time slices above trough and under the object are taken and placed in a matrix. Figure 3-19 clearly demonstrates how the migration algorithm works and the effect on the imaging of the object. 3D migration allows visualizing the shape of the object clearly.

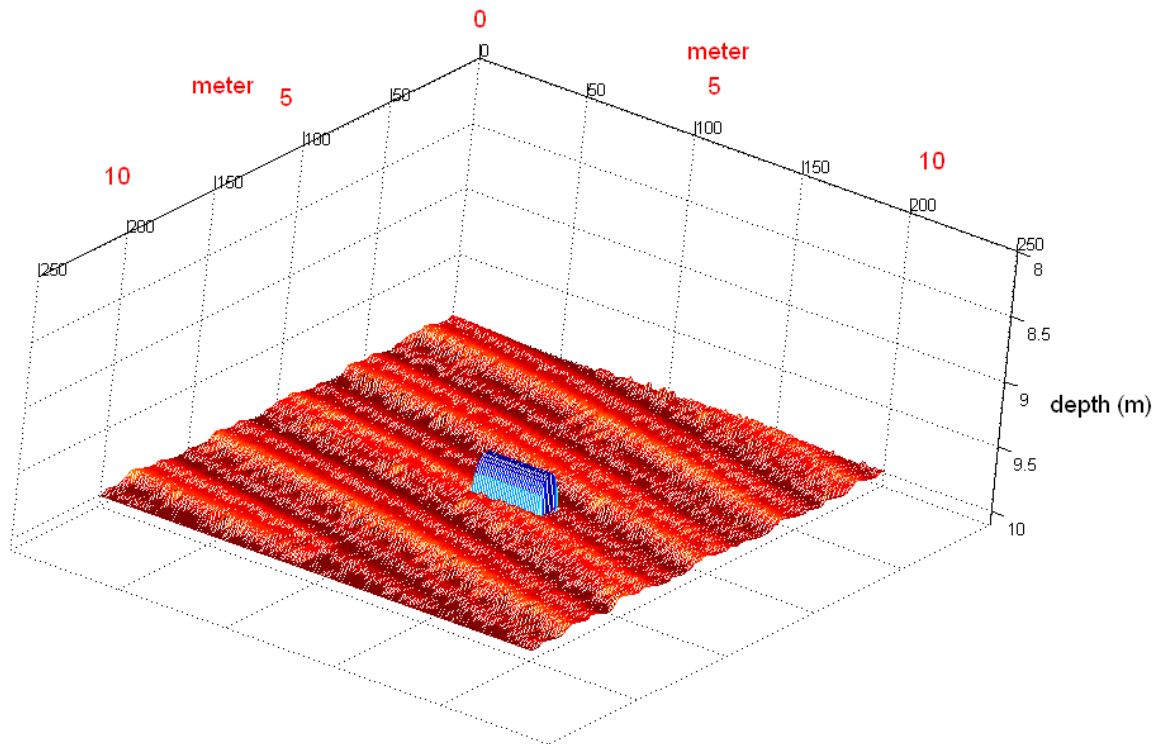


FIGURE 3-18: A ZOOM IN ON THE SEMI BURIED CYLINDRICAL MINE IN THE DATASET

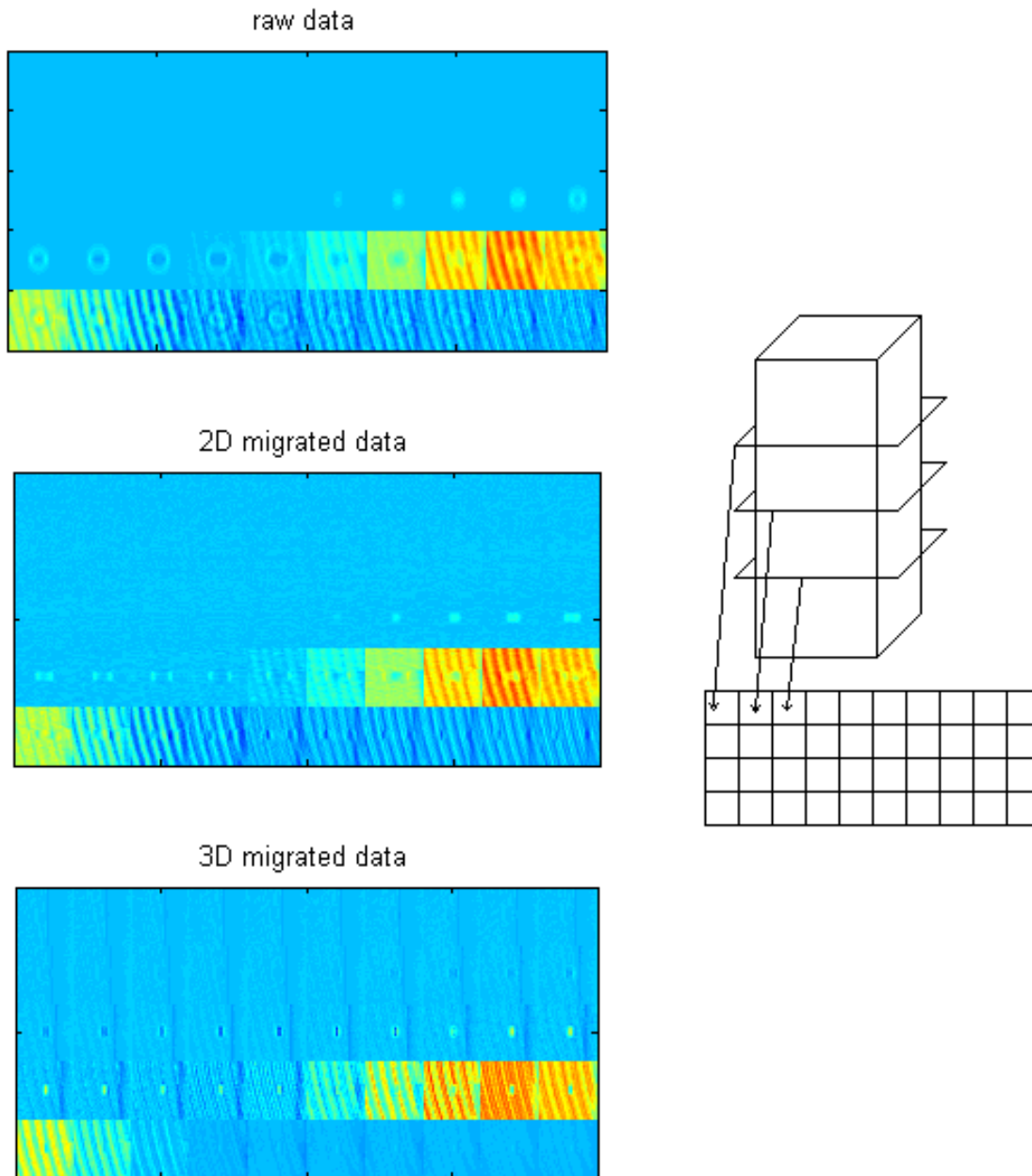


FIGURE 3-19: A VOLUME IS TAKEN OF 10 BY 10 BY 1.4 METER AND THEN HORIZONTALLY SLICED EVERY 3 CM, IN THE CENTRE OF THE VOLUME THERE IS THE OBJECT. TIME SLICES TAKEN IN THE ZONE WITH THE OBJECT AND TILED UP IN A FIGURE. SLICE 351 IS IN THE UPPER LEFT CORNER, SLICE 400 IS IN THE LOWER RIGHT CORNER OF EACH INDIVIDUAL FIGURE. THE TOP FIGURE ARE 50 TIME SLICES IN THE RAW DATA BLOCK, THE MIDDLE FIGURE IS THE COLLECTION OF TIME SLICES IN THE 2D MIGRATED BLOCK AND THE LOWER FIGURE IS THE COLLECTION OF TIME SLICES IN THE 3D MIGRATED BLOCK. EACH FIGURE CONTAINS 50 SECTIONS OF 10 BY 10 METER, THE FIRST TEN SECTIONS ARE IN THE FIRST ROW, THE NEXT TEN IN THE SECOND ROW AND SO ON. IMPORTANT TO NOTICE BESIDES THE OBJECT IS THAT IN LAST SEVEN TIME SLICES OF THE 3D MIGRATED DATA THE REVERBERATION IS GONE AND THE OBJECT IS CLEAR. FURTHER ON, THE FOOTPRINT OF THE OBJECT IN THE LOWEST ROW OF FIGURES IN THE 3D MIGRATED DATA IS DISAPPEARED.

3.3.6 Deviations on spatial sample densities and positioning affect migration performance.

3.3.6.1 INTRODUCTION

In the previous examples migration was applied on fully documented datasets with exact recordings. In real life, data such as velocity information has to be retrieved from the dataset (Yilmaz 2001; Margrave 2003). Also the position of the receivers has to be estimated (Marsset, Henriot et al. 2001). The focusing with all parameters known was almost optimal. Instrument deviations and electronic noise always create unknowns in real data. How noise in the time signal affects migration algorithms is discussed in (Yilmaz 2001). Digital signal processing is very well understood, good references are (Oppenheim, Schafer et al. 1999; Mitra 2006). Filters and noise working in the time or frequency domain will not be covered here.

A good migration is desired but the possible inaccuracies leave us with open questions: What is the acceptable error interval on the positioning? Is there a link between position accuracy needed and the source frequency? A link with the bin sizes? Does spatial down sampling have an effect on the migration algorithm?

The positions and deviations on positions are processed but very often it is nothing more than applying offsets and applying a Kalman filter. Research and modeling on how exact positioning and how dense the spatial sampling has to be in VHRS, is rather limited to rules of thumb and positioning equipment available. The following section will give numbers and images on accuracy.

3.3.6.2 MIGRATION WITH EXACT POSITIONING AND SPATIAL DOWNSAMPLING

Figure 3-9 showed four details of time slices in a raw acoustic dataset. The observation was that the image starts to downgrade at 2.5 times the smallest bin size. A similar observation can be made in Figure 3-20. Figure 3-9 is not migrated so it does not have the same level of object distinction possibilities an inexperienced observer might think it has (meter scale) although it has the same image resolution. Migration transforms the time axis to a space axis (detection resolution sub meter scale). Figure 3-20 shows a real data volume with all dimensions in the space domain. The result is a volume matrix where a horizontal slice has been taken. Identical blurring of the image, as demonstrated in the unmigrated timeslices can be observed. There can be concluded that the resolution of the time slice has to be equal to or higher than the maximum theoretically achievable imaging resolution of the sonar.

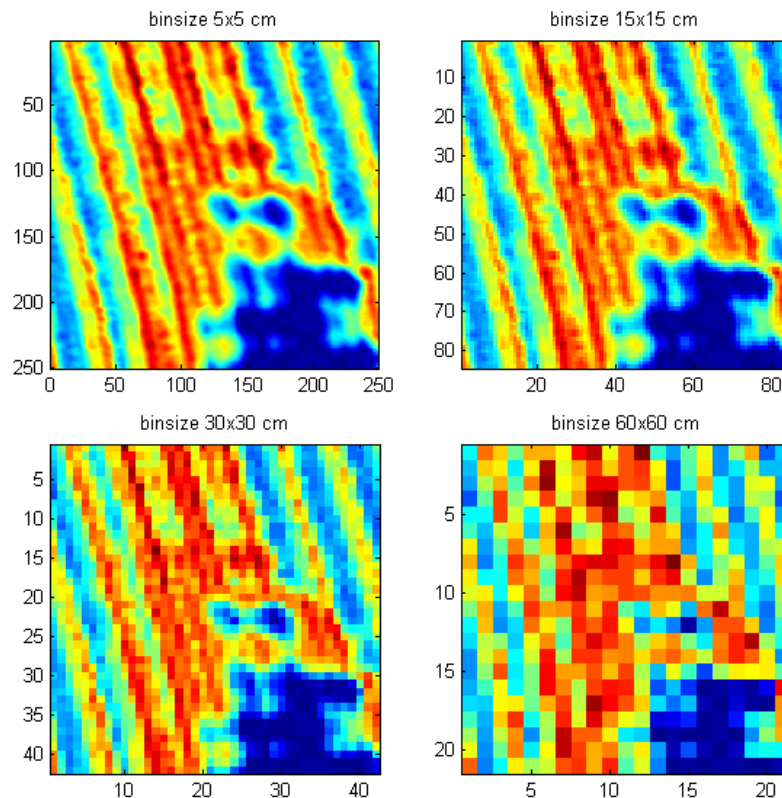


FIGURE 3-20: A DETAILED SECTION OF A 3D MIGRATED TIME SLICE AND THE EFFECT OF SPATIAL UNDER SAMPLING

3.3.6.2.1 MIGRATION WITHOUT SPATIAL DOWNSAMPLING AND WITH POSITION DEVIATIONS

The optimal bin size appears to be 12 by 12 cm. What measurement accuracy is needed for an optimal 3D migrated image? Because of memory optimizations the bin size used in the processing will be no longer 5 by 5 cm but 10 by 10 cm. Increasing the bin size to 10x10 cm, or reducing the resolution of the image, does not have any influence on the image because the resolution of the image is still higher than the maximum achievable imaging resolution of the sonar. In order to get 10 by 10 cm bins four 5 by 5 cm bins were stacked. Consider now that a recording system is used that has at least the capacity to locate each signal in the correct bin. In every bin the signal position can now vary maximum +/- 5 cm in cross line and inline direction. White noise will be summed with the position vectors. The pseudo-random white noise is uniformly distributed in the interval [-5, 5] cm or smaller. No noise on the vertical position is added, since we assume that a swell filter can correct accurately enough (Missiaen 2008). Figure 3-21 displays a detail of a seismic section before and after swell filtering. Since error in the vertical dimension will be the main problem in migration algorithms, it might however be a good test to add noise in the vertical dimension as well.

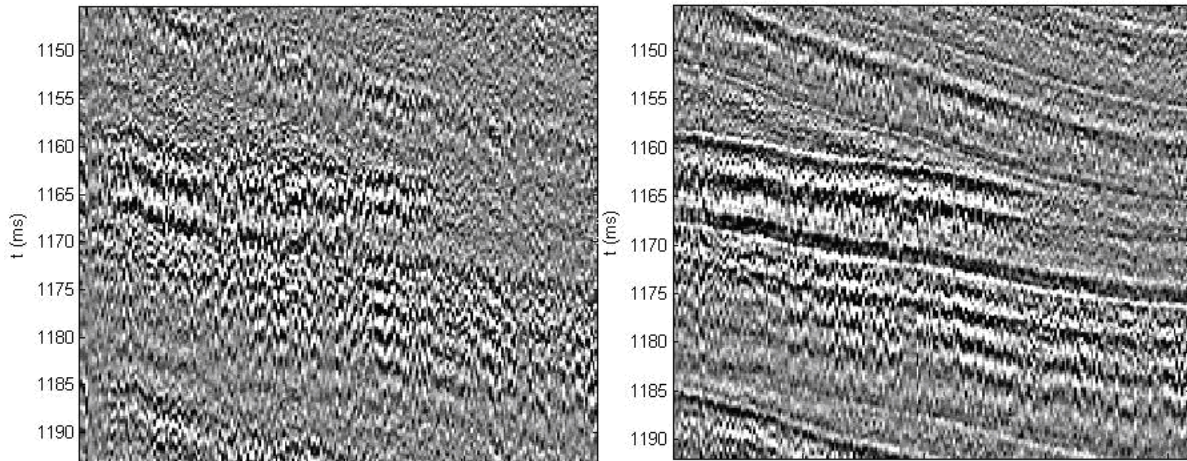


FIGURE 3-21: A DETAIL FROM A 2D HIGH RESOLUTION IMAGE BEFORE SWELL FILTERING (LEFT) AND AFTER SWELL FILTERING (RIGHT)

Figure 3-22 shows a series of time slices taken in the 3D migrated block. The top slice is the slice as it should be without positioning error on the traces. The next two slices are the equivalent slices of the top one but taken in a block with 1 and 2 cm variation on the position of each trace. Up till the 2 cm uniformly distributed noise the resulting image looks more or less acceptable. Distortion levels of 3 cm and 4 cm gives an unacceptable image. Figure 3-23 is a zoom on the object, the semi buried cylindrical mine, again the perfectly focused image clearly depicts the shape of the object, while on the 2 cm variation sections the object is visible but the shape is gone. The 4 cm position variation accuracy sections trough the object depict the object and shape in a much lower quality than the 0 and 2 cm blocks. Consider now that an acceptable image is created with 1 cm variation on the positioning of the traces. That would mean that the position variation can be maximum $1/36$ of the wavelength.

3.3.6.2.2 CONCLUSIONS

The bin grid for a 3D acoustic acquisition should have a length in X and Y direction of maximum one fourth of the wavelength of the source used (Yilmaz 2001). The migration result demonstrates a maximum error on the positioning should be maximum $1/18$ of the wavelength used and preferably lower than $1/36$ of the wavelength used. In practice a dataset recorded using a 3.5 kHz source should be binned in 12 x 12 cm bins and the variation on the grid positioning error of the traces should be lower than 2 cm. No offshore positioning system on a free floating platform is able to achieve that accuracy. A rigid matrix of receivers is the only option. Iteration algorithms and motion sensors mounted on the rigid frame have to be used to achieve a very high ping to ping positioning accuracy. In VHRS the only progress that has been made in this field is the swell filtering; making a ping to ping coherent image. But swell filtering does not correct on the x and y coordinates, moreover it corrects x y movements in the z direction. In the SAS research field, DPCA is trying to deal with this problem (Belletini and Pinto 2002). The question whether the DPCA algorithms work on bottom penetrating algorithms remains unanswered.

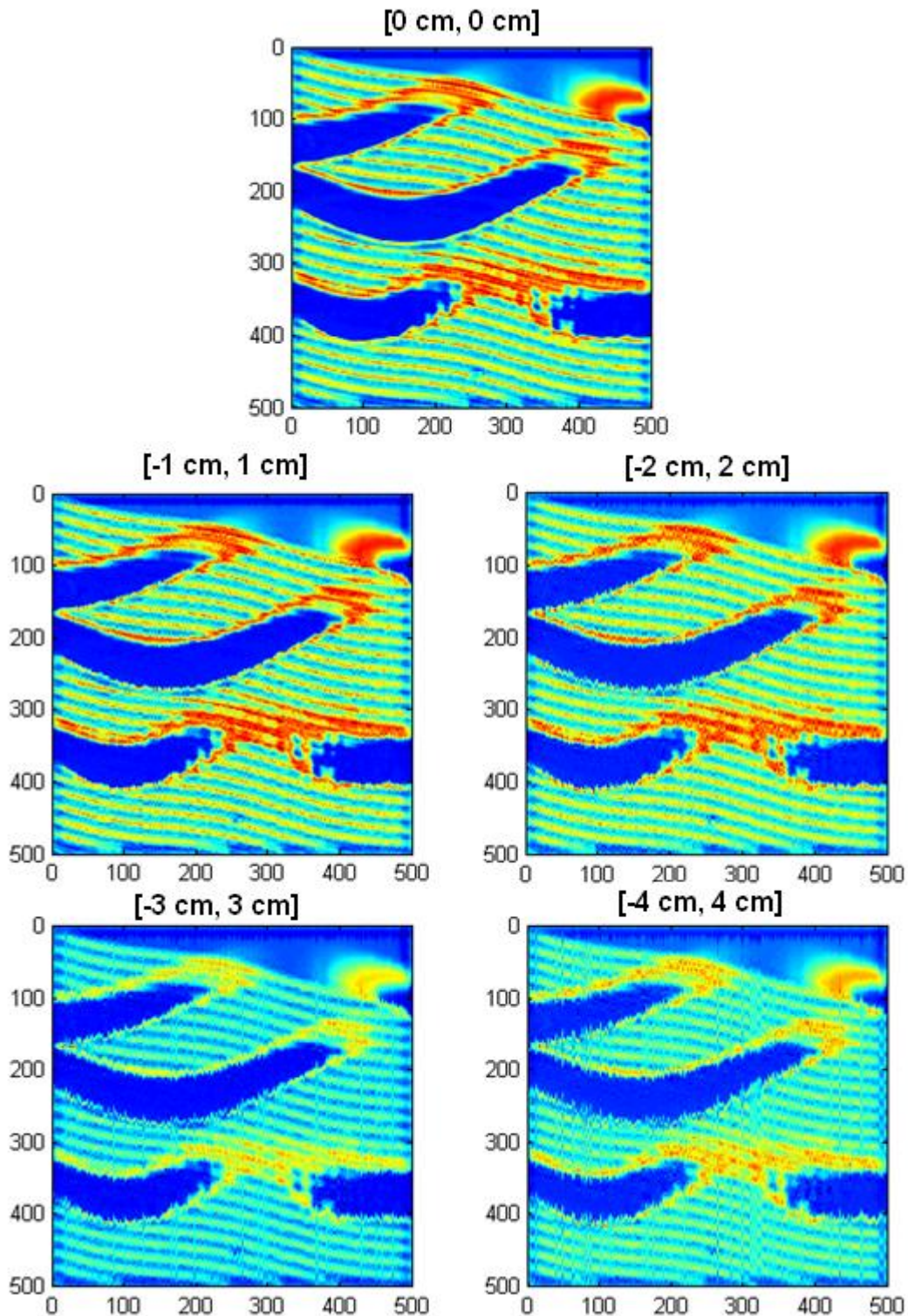


FIGURE 3-22: TIME SLICES IN A 3D MIGRATED ACOUSTIC DATASET. WHITE NOISE HAS BEEN ADDED TO THE POSITIONING. THE TOP FIGURE IS A 3D MIGRATED DATASET WITH EXACT POSITIONING OF EVERY SEISMIC TRACE. THE FOUR IMAGES IN THE CENTRE AND BOTTOM HAVE UNIFORMLY DISTRIBUTED WHITE NOISE ADDED TO THE POSITION COORDINATES OF EVERY TRACE WITH A DISTRIBUTION RANGING FROM 1 CM TO 4 CM.

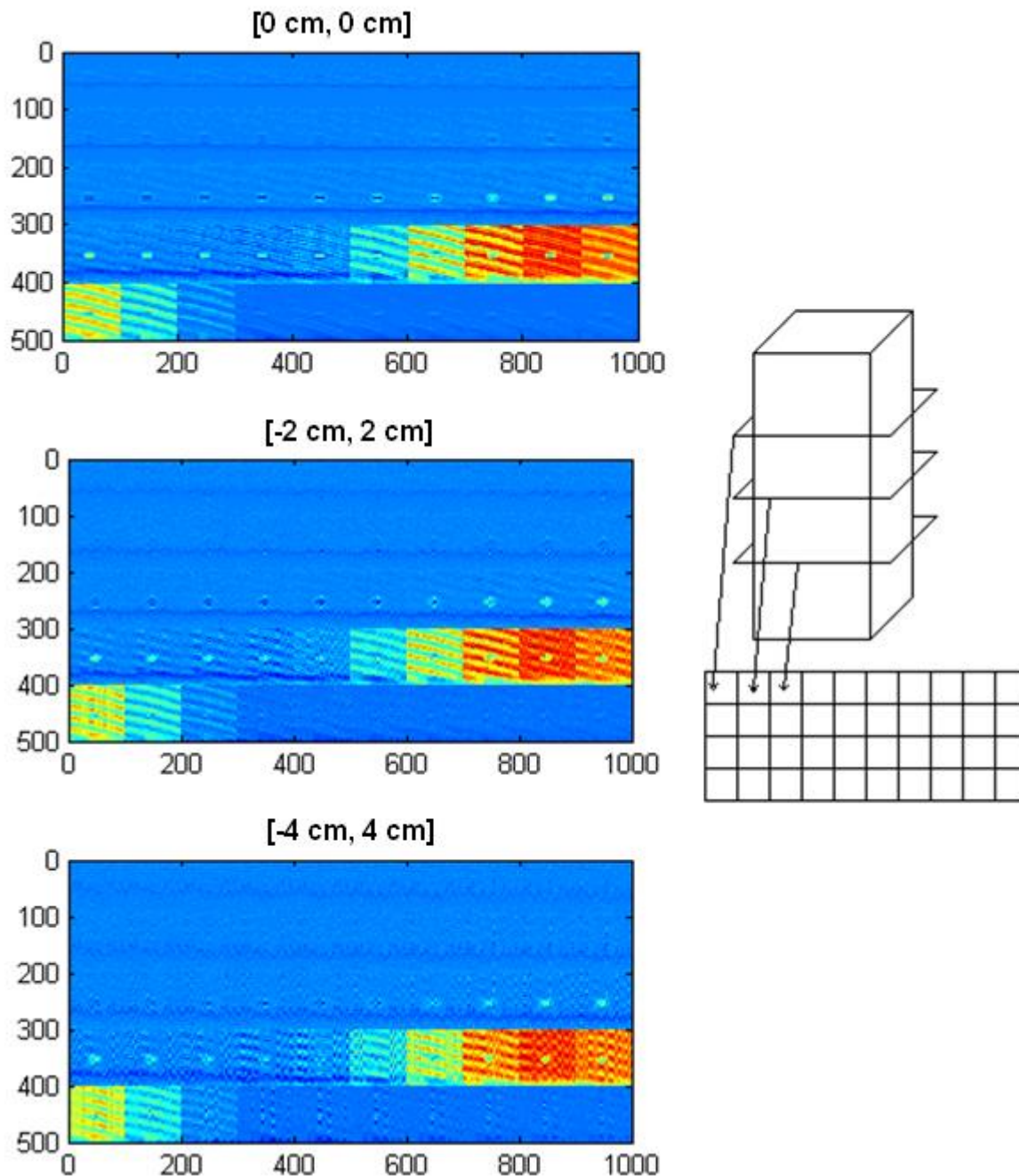


FIGURE 3-23: A VOLUME IS TAKEN OF 10 BY 10 BY 1.4 METER AND THEN HORIZONTALLY SLICED EVERY 3 CM, IN THE CENTRE OF THE VOLUME THERE IS THE OBJECT. TIME SLICES TAKEN IN THE ZONE WITH THE OBJECT AND TILED UP IN A FIGURE. SLICE 351 IS IN THE UPPER LEFT CORNER, SLICE 400 IS IN THE LOWER RIGHT CORNER OF EACH SEPARATE FIGURE. THE TOP FIGURE ARE TIME SLICES IN THE 3D MIGRATION OF THE ORIGINAL DATA, THE MIDDLE FIGURE ARE TIME SLICES ARE TAKEN FROM A BLOCK THAT HAS BEEN 3D MIGRATED WITH MAX 2 CM RANDOM VARIATION ON THE POSITION OF EACH TRACE AND THE LOWER FIGURE ARE TIME SLICES IN THE 3D MIGRATED BLOCK WITH MAX 4 CM RANDOM VARIATION ON THE POSITION OF EACH TRACE. EACH FIGURE CONTAINS 50 SECTIONS OF 10 BY 10 METER, THE FIRST TEN SECTIONS ARE IN THE FIRST ROW, THE NEXT TEN IN THE SECOND ROW AND SO ON.

3.4 CONCLUSIONS

- The model presented can contribute to evaluating acoustic processing algorithms.
- The model presented can help to recognize features on non-processed acoustic images.
- The model presented cannot be used to evaluate performances in multi-static environments with sources and receivers with certain beam patterns and wavelet functions.
- The model presented does not ray-trace so does not apply shadow and ray bending corrections.
- Network processing is easy to implement if the model has been specifically designed to operate in a network. Further developments will be made in function of network processing.
- Binning or spatial density of the 3D acoustic data is a function of the frequency components of the source wavelet.
- Binning the data into an under sampled acoustic volume does not dramatically affect the performance of the focusing or migration algorithms, but the resulting focused image is, just as the original image, of a lower quality. Spatial under sampling often occurs in industrial datasets, there are techniques similar to migration algorithms to reconstruct the missing traces.
- Spatial under sampling becomes extremely visible when it exceeds four times the required sampling rate.
- There can be concluded that the image resolution of the time slice has to be equal to or higher than the maximum theoretically achievable imaging resolution of the sonar.

4 TWO MAINSTREAM APPROACHES OF ACOUSTIC MODELING

4.1 BORIS 3D SSA (WAVENUMBER INTEGRATION)

BORIS 3D SSA is one of the most advanced underwater acoustic models for high resolution seismics and the study of reverberation caused by the boundary between two half spaces. The two half spaces used are the water column and the sediment volume. The model developed in the NATO Undersea Research Centre is used to study the effect of surface roughness on acoustic signals. Using the model for ping to ping coherence studies at first appeared to be a bridge too far (Pautet, Pouliquen et al. 2002; Pautet, Pouliquen et al. 2002; Pautet, McCloghrie et al. 2003). Pautet et al. concluded that no ping to ping coherence was observed in simulated datasets using the BORIS model. Ping to ping coherence is a fundament of micro navigation (Bellettini and Pinto 2002). Micro navigation is used to recalculate the exact position of the send and receive array of a SAS system. As demonstrated in chapter 3, near to exact knowledge of the position is crucial input for the migration algorithm. The objective laid down by Belletini and Pinto was to assess the BORIS model and to evaluate the earlier findings of Pautet et al. (Pautet, Pouliquen et al. 2002; Pautet, Pouliquen et al. 2002; Pautet, McCloghrie et al. 2003). First a demonstration with the Boris model is given about how the signal and the signal correlations should look like, secondly the model is made instable and tested on a perfectly flat horizontal seafloor using a mono static set-up. The perfectly flat seafloor acts as a mirror and should not return scatter to the receiver when the source and receiver are not insonifying the seafloor directly under the source-receiver pair (vertical incidence angle). Eventually the model appeared to be able to produce accurate signals that were able after (SAS)-reconstruction to match with the reconstruction performed on real data. The theory of micro navigation can contribute to the validation of signals generated with the BORIS model.

4.1.1 Introduction

3D VHRS recordings become more valuable when 3D migration is done (Yilmaz 2001). The previous chapter demonstrated that knowing the exact position of send and receive arrays is crucial to the performance of migration algorithms. Downscaling petroleum exploration techniques to very high resolution seismic systems has an effect on the binning and positioning strategy. Efforts had been made to correct the position of the recorded 3D VHRS traces by using a swell filter. The swell filter allows compensation for swell movement in the vertical direction but not the horizontal direction. A swell filter enhances a 2D image by time shifting seismic traces, but no corrections are made in the positioning matrix. It is a 2D seismic image enhancing technique. The research field of the synthetic aperture sonar developed parallel towards the same end product but advanced much more on the positioning problem.

Synthetic aperture sonar is a spin off from synthetic aperture radar (SAR). Initially the set-up was identical but under water. Not only has the hardware showed a lot of similarities but also the software did (Bruce 1992). The most used migration algorithm in this field was the f-k migration (ω -k algorithm) (Soumekh 1999). The f-k migration is the fastest migration but also the hardest one to apply under water, in non vertical incidence set ups. The f-k algorithm needs an environment preferably without lateral sound velocity changes (Yilmaz 2001; Margrave

2003). The SAR field predominantly used that algorithm to migrate data. SAS as well as SAR mostly applied the so called synthetic aperture (ω -k algorithm) on sonar. In the SAS field, the importance of a very precise positioning of the measurement was very well understood. There is the understanding that the instrument needed to be rigid and equipped with a very precise motion sensor, the phased arrays had to be denser than the 2m used in the 3D VHRS system used at the start of the research or in case of single channel recording the number of pings per meter have to be high. There was also understood that the smaller errors on the motion sensing could only be corrected using the acoustic signals (Bellettini and Pinto 2002).

However there were major contradictions between the field of modeling and the field of image reconstruction (Bellettini and Pinto 2002; Pautet, Pouliquen et al. 2002; Pautet, Pouliquen et al. 2002; Pautet, McCloghrie et al. 2003). The NURC modelers claimed, based on the wavenumber integration model BORIS SSA that the reconstruction algorithms based on micro navigation could not work, while the group of NURC migration specialists claimed it worked on real data. In what follows the tangle is straightened out. This research was a turning point in this PhD leading to the construction of a new acoustic model capable of dealing with very complex environments.

4.1.2 Preface: 2D and 3D acoustic models

The acoustic models can be subdivided into two groups: 2D models and 3D models. Expansions of 2D models to 3D environments also belong to the group of 2D models. 2D models might still be used for bottom penetrating sonar modeling, anti submarine warfare modeling and seismic modeling, where 3D models are still too heavy in terms of computability. The 2D models often go deeper into investigating physical phenomena such as ray bending, transmission loss etc. Some of the ASW models have been expanded to 3D but are not meant to be used for this type of research and as such they always introduce unacceptable limitations. In the 3D underwater acoustic models 2 groups can be found: models that solve a differential equation derived from the wave propagation equation and point scatter models. Point scatter models are the slowest models and by far the most archaic and memory consuming. Point scatter models are on the other hand reliable, flexible and accurate. For seismic migration researchers the use of wavenumber integration models versus the use of point scatterer models very much looks like the discussion between using the Stolt or f-k migration or the Kirchhoff migration. The use of a certain model depends upon the needs of the researcher. Mathematical models dealing with reverberation are under development since the seventies of the twentieth century. Some of the earliest are DOP (Marsh 1976), EIGEN/REVERB (Sienkiewicz, Boyd et al. 1975) and REVCEN (Princehouse 1977), they allow only monostatic approaches. Other models from the eighties and nineties of the twentieth century are in the monostatic field: PEREV (Smith, Tappert et al. 1993; Smith, Hodgkiss et al. 1996), REVMOD (Hodgkiss 1984), REVSIM (Chamberlain and Galli 1983), TENAR (Luby and Lytle 1987) and models allowing the bistatic mode are BAM (Bartberger 1985), BiKR (Fromm 1999), BiRASP (Fulford 1991), BISAPP (Pomerenk and Novick 1987), BISSM (Caruthers and Novarini 1993), OGOPOGO (Desharnais and Ellis 1997), RASP (Franchi, Griffin et al. 1984), RUMBLE (Bucker 1986), Under-Ice (Bishop, Ellison et al. 1987).

These models were not used because of the specific needs set previously. Freeware acoustic models are available at the Ocean Acoustics Library: <http://oalib.hlsresearch.com/>. A good systematic overview of these and other models is given by Etter (2003).

Some reference works collect most of the existing, mainly wavenumber integration based reverberation models: (Pace, Pouliquen et al. 1997; Jensen, Kuperman et al. 2000; Etter 2003). In ECUA conferences and proceedings (2004-2007) other more up to date acoustic models and models under construction are demonstrated. There are more models than just the ones described in the previous references. An intensively used model in the nineties and later on for example was SAFARI and the upgrade OASES (Schmidt and Glattetre 1985; Schmidt and Jensen 1985; Schmidt and Jensen 1985; Schmidt and G. 1986; Schmidt 1987; Schmidt 2004). *OASES is a general purpose computer code for modeling seismo-acoustic propagation in horizontally stratified waveguides using wavenumber integration in combination with the Direct Global Matrix solution technique. It is basically an upgraded version of SAFARI. Compared to SAFARI version 3.0 distributed by NURC, OASES provides improved numerical efficiency, and the global matrix mapping has been re-defined to ensure unconditional numerical stability in the few extreme cases where the original SAFARI has proved unstable*, (adapted from: <http://acoustics.mit.edu/faculty/henrik/oases.html>, the home website of OASES (Schmidt 2004)), OASES could not be used in this research because it is a 2D model. The model lost importance in high frequency acoustic modeling, but still has a significant importance in the modeling of bottom penetrating sonar systems. The move to 3D in high frequency acoustic modeling was only a matter of computation power. In the late nineties that move was made in NURC. A full 3D model designed by Eric Pouliquen, implemented by Gaetano Canepa, named BORIS 3D and the later upgrade BORIS 3D SSA was born (Canepa, Bergem et al. 1997; Bergem, Pouliquen et al. 1999; Pouliquen, Bergem et al. 1999). This thesis is not intended to be a literature study, hence a comparison of the models will not be done. Only one model will be fully investigated in this thesis (BORIS 3D SSA), not only to demonstrate a procedure of how to validate a model, it will also be a demonstration of what can go wrong if you do not fully control the model you are working with. Full control and understanding is not only understanding of the mathematics behind it but also understanding the limitations of the functions and simplifications the model uses.

4.1.3 Mathematics of BORIS 3D in a nutshell

The mathematical derivation of the model is discussed in (Pouliquen, Lyons et al. 1998). A summary of the applied formulae can be found in: The implementation of BORIS-3D: Bottom Response from Inhomogeneities and Surface Version 1.0 (Canepa, Bergem et al. 1997). The formulae concepts for surface scattering are relatively comprehensible. The signal is an integration of the acoustic response of elementary surface units. The response coming from these surface units where vector R from the source points to is a convolution of the directionality and mean sound speed, transmission level p_0 , the directionality patterns of source ($D_i(R)$) and receiver ($D_r(R)$), the acoustic impedance $\mathfrak{R}_{01}(R)$, the Green function and the source signal spectrum ($E(f)$). *The Green's function accounts for the propagation in the water column in the case of backscattering* (Canepa G., 1997).

$$dp_{(s)}(P, f) = +j \frac{\cos(\gamma(R))}{c_0} p_0 D_i(R) D_r(R) \mathfrak{R}_{01}(R) [fG(R)^2 E(f)] dS$$

And the inverse Fourier transform:

$$dp_{(s)}(P, t) = - \frac{\cos(\gamma(R))}{2\pi c_0 R_0^2} p_0 D_i D_r(R) \mathfrak{R}_{01}(R) e'(t - \frac{2R_0}{c_0}) dS$$

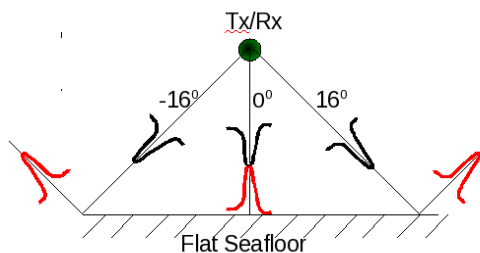
Integrating the previous expression gives the final result:

$$p_{(s)}(P, t) = \int_{(S)} dp_{(s)}(P, t)$$

An interesting note to add here is that this approximation can only be used in near to vertical angle of incidence with very narrow band signals with a relatively narrow lobe pattern (including side lobes) at a low frequency on a very rough seabed without abrupt changes of acoustic impedance (Pouliquen, Lyons et al. 1998).

4.1.4 Tuning of the BORIS 3D SSA model for side-scan simulation

The tuning of the BORIS model, in this thesis, is done on a perfectly flat seafloor, changing each time just one parameter in the model. Most of the tuning is done with the source receiver pair directed to the seafloor under small grazing angles. The source receiver pair does not insonify the area directly under, so only scatter and no reflection has to be taken into account. The model is not stable at that point, but this test is performed to get a feeling with possible instabilities of the model during normal use. It appears that fine tuning the model under unstable circumstances prevents possible errors during the stable applications. No volume calculations are made. All parameters used are given in this report in appendix 1. All steps can be reproduced. MATLAB® programs are given in the software book, while BORIS 3D SSA also has a MATLAB® toolbox coming with the package. BORIS 3D SSA can be acquired by contacting NURC.



4-1: THE SOURCE REVEIVER PAIR DIRECTED TO THE SEAFLOOR UNDER NON VERTICAL AND VERTICAL ANGLE OF INCIDENCE. VERTICAL ANGLE OF INCIDENCE WOULD CREATE A REFLECTION, NON VERTICAL ANGLE OF INCIDENCE AS SHOWN IN THE FIGURE, DIRECTS THE OUTGOING PING AWAY FROM THE SOURCE RECEIVER PAIR. THE BLACK BEAMS ARE THE INCOMMING PINGS, THE RED, THE OUTGOING.

4.1.4.1 GOALS

Before exploring the limitations of BORIS 3D SSA it is important to demonstrate what the result of the ping to ping coherence algorithm should be. These results were generated with both BORIS 3D SSA and verified with a point scatterer model (Staelens 2003). The sonar set up was chosen as described by Pautet et al. (Pautet, McCloghrie et al. 2003) and Figure 4-2.

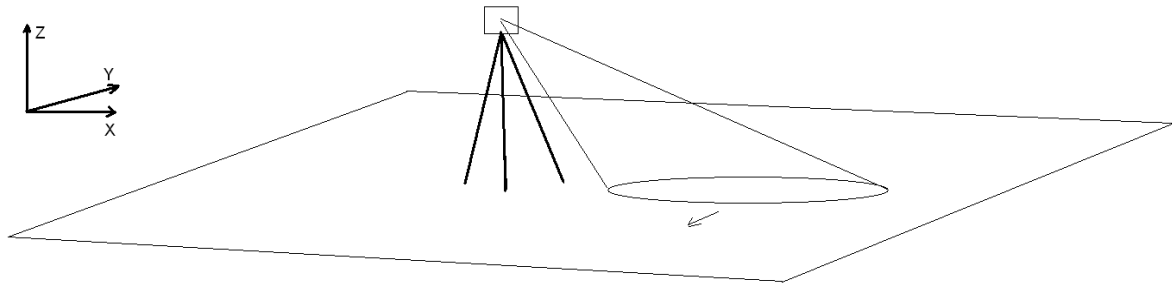


FIGURE 4-2: PURE YAW IS A ROTATION AROUND THE Z AXIS OF THE SONAR FACE. THE GRAZING ANGLE OF THE CENTRE OF THE BEAM IS 60° , THE SONAR IS POSITIONED 5 METER ABOVE THE SEAFLOOR.

The goal of the use of the BORIS 3D SSA model was to do a ping to ping coherence investigation of the acoustic response of the seafloor (Bellettini and Pinto 2002). According to the available literature there was no ping to ping coherence achieved on signals produced with the BORIS 3D SSA model (Pautet, Pouliquen et al. 2002; Pautet, Pouliquen et al. 2002; Pautet, McCloghrie et al. 2003). A mono static set-up is used and a parametric transducer with a circular Gaussian beam pattern such as the TOPAS. The transducer makes minor translation and rotation movements in between every ping. In this demonstration only the pure yaw (rotation around the vertical axis) situation is simulated. The area directly under the transceiver is not insonified.

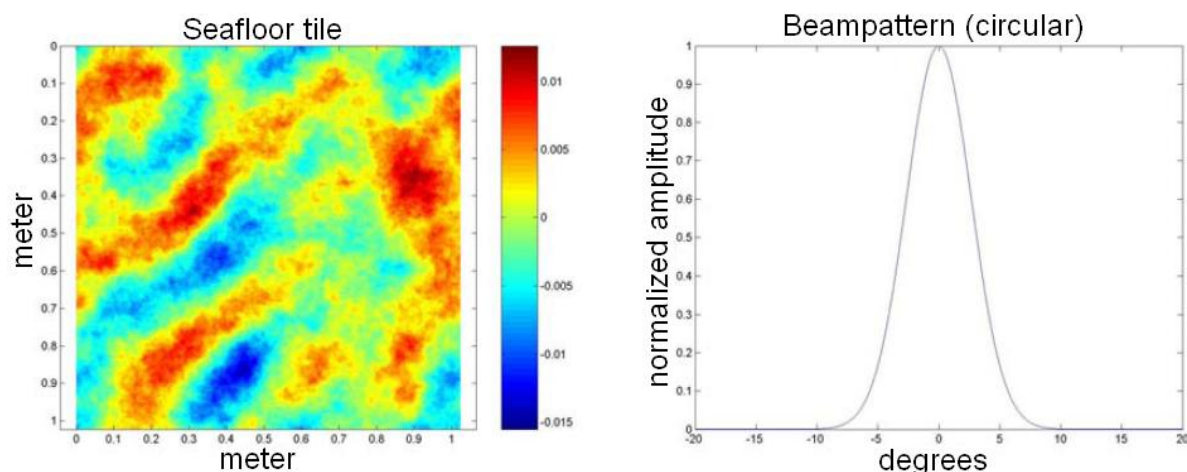


FIGURE 4-3: LEFT THE APPLIED SEAFLOOR TILE (BATHYMETRY) AND RIGHT THE BEAM PATTERN, THE COLOUR SCALE IS ALSO A METER SCALE RANGING FROM -0.15 TO +0.15.

The transducer makes a pure yaw movement while having a small angle of incidence with the seafloor and pings every 0.5 degrees. Lining up the acoustic data received at the transducer

delivers Figure 4-4. The horizontal lines in the image already suggest that there is a certain ping to ping correlation.

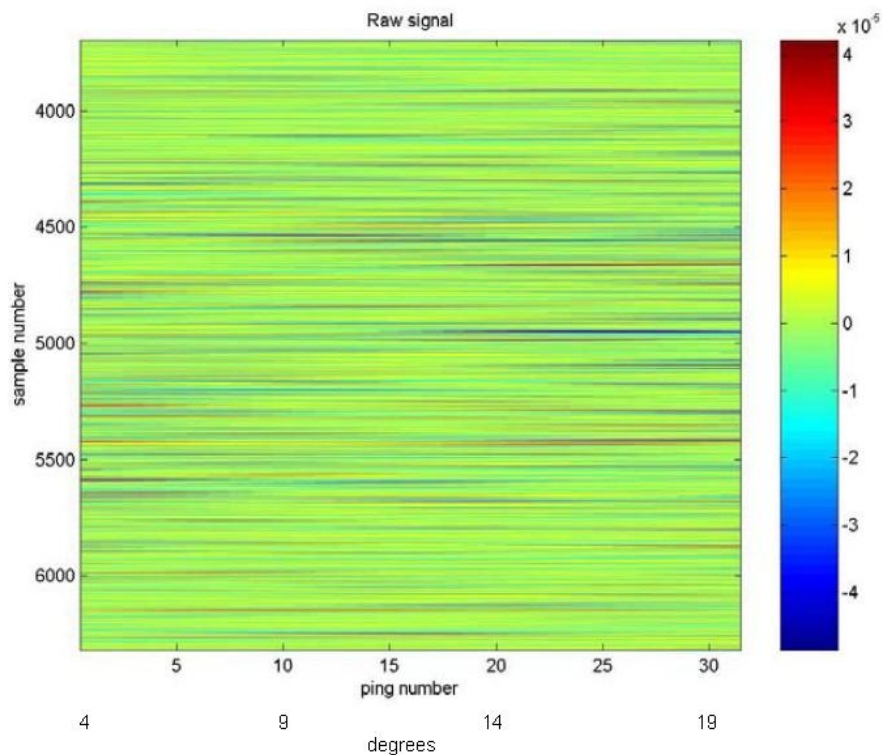


FIGURE 4-4: EVERY 0.5 DEGREES A PING IS SENT AND RECEIVED FROM THE SEAFLOOR. THESE PINGS ARE LINED UP IN THIS FIGURE. A PING TO PING RELATION IS CLEARLY VISIBLE (HORIZONTAL LINES IN THE IMAGE)

In order to find out whether there is a ping to ping correlation the pings are correlated with each other. When ping one is correlated with ping one an autocorrelation is the result (amplitude of the correlation = 1), when it is correlated with ping 2,3,...,31, 32 a certain correlation appears. The maximum value of the correlation has the same curve as the beam pattern of the transducer (Figure 4-5). When the same procedure is followed for every ping, and the correlation coefficient is calculated and drawn in a 2D matrix then Figure 4-6 appears. Because Figure 4-6 is an ideal test case to see if the BORIS 3D SSA model produces signals that follow the coherence laws in all circumstances, it can be used as a ping to ping test during the validation of the model.

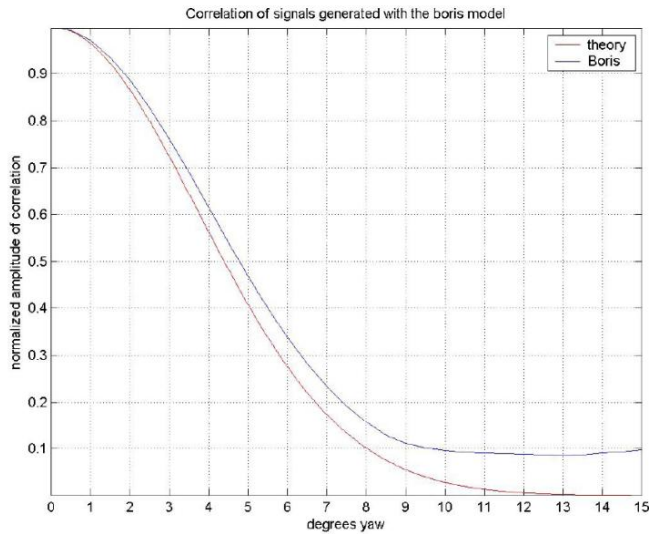


FIGURE 4-5: THE PATTERN OF THE CORRELATION IS SIMILAR TO THE BEAM PATTERN.

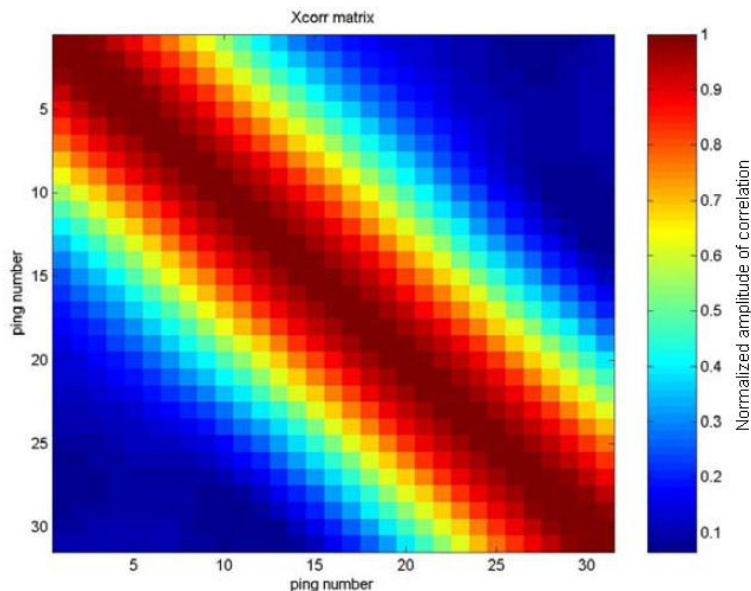


FIGURE 4-6: EVERY PING IS CORRELATED WITH ITSELF AND ALL THE OTHER PINGS IN THE SCAN. THE AUTOCORRELATION SHOWS UP IN THE DIAGONAL PATTERN (DARK RED LINE). THE COLOUR SCALE INDICATES FULL CORRELATION OR THE SIGNALS ARE EQUAL (DARK RED) TILL BLUE WHERE BLUE INDICATES THAT THE SIGNALS ARE COMPLETELY DIFFERENT AND THERE IS NO CORRELATION BETWEEN THE TWO SIGNALS.

4.1.4.2 IMPLEMENTATION STRATEGY PROPOSAL:

An important conclusion from the instability tests added in appendix is that the model when forced into instable behaviour (all nodes have a Z value zero) gives a wide spread of different acoustic responses. This phenomenon usually is non-random noise. This noise should be avoided at all cost. Non-random noise can have an effect on correlations. The amplitude of the noise can be very high, up till dominant if the model is not applied correctly. When applying signal processing algorithms on the produced signals, the amplitudes of the generated signal have to be minimum 20 dB above the noise amplitude. During a normal application of the model there is no way to see or know how high the amplitude of the noise is. The noise can be reduced

when using a certain implementation strategy. This section proposes the implementation strategy applied to get the correct signals. Other implementation strategies are possible but were not available at the time of doing this research.

STEP 1: Analyzing the influences of the beam pattern over/under sampling:

Under sampling the beam pattern generates severe instabilities of high amplitude. This parameter has no significant influence on calculation time, so oversampling is suggested.

STEP 2: Analyzing the influence of seafloor tile size and sampling

Changing the size of the seafloor tile only has an influence on the calculation time. Taking the tile as small as possible is suggested. Taking the tile too small may introduce unwanted effects due to the repetition of the tile in every direction.

STEP 3: Under and over sampling effects in the tile matrix

For a good result a serious over sampling is needed. The use of a 10kHz source indicates that a good sample rate is 1 cm, however 1 mm gives much better results but the calculation time increases.

STEP 4: Analyzing the influence of pulse sampling

The pulse is defined in a separate file and fed into the model. It is then convolved with the calculated impulse response. The pulse is defined in a line array, while the spacing between the samples is defined in the SAMPLING_FREQUENCY field in the model.ini file of the model. Changing the number of elements in the array by for example interpolation as such changes the central frequency of the pulse if the SAMPLING_FREQUENCY field in the model.ini file is not adapted.

STEP 5: Analyzing the influence of heading on a perfectly flat seafloor

It might be necessary to introduce 'forbidden angles' and to work only in angles that have a low noise response. The angles sensitive to the problem are symmetric and related to $\pi/2$ and $\pi/4$ angles. The spreading of the noise is bigger around $\pi/4$ angles but the amplitude of the noise is higher around the $\pi/2$ angles.

STEP 6: Analyzing the integration area, changing the integration area within the size of the beam pattern matrix

The integration has to be done, integrating the whole signal and not only the -3dB area. It is not necessary to integrate the whole zero padded part of the beam pattern. In order to decrease the calculation time it might be better to do this analysis earlier in this flow.

STEP 7: Analyzing the influence of the grazing angle

There is a dependency upon the grazing angle; further analysis should be done here. Pouliquen states that the model was originally designed to simulate signals pinged at near to vertical angle of incidence (Pouliquen E., 1998).

4.1.5 Encountered limitations of the BORIS_SSA model

Applying the BORIS 3D (SSA) model requires a strategy. After failure to work out a modeling cycle that allowed micro navigation processing (Pautet L. 2003) and a new attempt to do so, the conclusion was that micro navigation might contribute in the validation of the output of the BORIS model. The model did not have the necessary requirements needed to analyze sonar performance in object detection due to some restrictions. The use of the model in the perspective of this thesis was abandoned. The restrictive nature of the model is inherent to the approach of solving the wave equation through a 2D Fourier transform. Similar problems appear in migrations using 2D Fourier transforms. A number of features restrict the use in object detection modeling:

- **Tile and environment:** The environment in BORIS 3D SSA is defined as a flat tiled surface. The tiles are generated in such a way that top fits on bottom and left side on right side of the tile. The result is an infinite surface without any holes or gaps. Problematic is the flat surface and the same tile coming back constantly. This feature does not allow to test for example algorithms on slopes or on a topography. It also restricts the frequencies used and effects of bedforms.
- **Generation of the tile:** The generation of a seafloor tile is not based upon sediment dynamic models. In the case of a rippled surface, the model creates the correct pattern but not the correct shapes. The sand ripples generated with BORIS appear to be sinusoidal and very unrealistic. The same accounts for gravel.
- **4D options:** Using a 2D Fourier transform for the generation of the surfaces locks out options to work in 4D, with as fourth dimension time. A combination of dynamics and acoustics cannot be modeled.
- **Discrete beam:** The spatial pattern or beam pattern of the source is discrete. A function connected to a transducer array would be a lot easier and more correct. The discrete source pattern is problematic when modeling of small grazing angles is done or when the distribution of the frequency component of the wavelet is broad. The beam pattern is frequency invariable and that is not the case in real circumstances.
- **Wavelet:** As previously stated beam pattern and wavelet are not connected. In that case the use of minimum phase wavelets and other broadband wavelets is not recommended (remember chapter 1.7 where the variations of the source wavelet and beam pattern are discussed).
- **Multi-static:** bi-static approaches are allowed in BORIS 3D SSA but higher statics require to be split up in bi-static steps. That approach unnecessarily increases the calculation time because the first monostatic step is each time recalculated.
- **One Z coordinate per XY coordinate:** Probably one of the most restrictive features of the model is the construction of the environment. The environment consists of tiles (with a volume underneath). No other objects are allowed in the environmental model. Trying to introduce a mine shape in a tile implicates that the mine shape will be multiplied infinitely in the environment. Spherical shapes are impossible to introduce. Variation on scatter strength is impossible to introduce. The fixed position of every XY coordinate restricts the detail on the introduced object and the detail wanted restricts the environment because the tile has a maximum size.

- **Shadow:** The problems concerning the introduction of objects in the environment goes even deeper when the effect of shadowing is taken into account. BORIS 3D SSA does not trace the rays so it does not calculate shadows. Not calculating shadows is not only a problem with an object having a shadow on the seafloor or on another object. Not calculating the shadows also affects the shadowing of the seafloor features themselves on the seafloor. Every recording under small grazing angles has shadows. The shadows themselves are features which are used to detect and recognize ripples, objects, rocks,...
- **Small grazing angles:** the model appears to be not very stable when small grazing angles are used. Instabilities become dominant in the return. The model was not designed to be used in these circumstances.
- **Velocity profile:** BORIS 3D SSA does not support ray bending, a uniform medium is required. Sound velocity variations in the water column are a function of pressure, temperature and salinity. All three vary with depth, space and time. The resulting variations of sound velocity in the water column cause ray bending. Ray tracing is one option, and it is needed for the shadow calculations.
- **Doppler:** A receiver usually moves during recording, a moving receiver means that Doppler effects should be taken into account. BORIS 3D SSA does not take into account the Doppler effects. This is not unexpected since the mathematics behind the model already demonstrated that the final result of the model is a convolution of the impulse response of the environment with the wavelet.
- **Scatter strength:** there is no proper support of changes in scatter strength, other sediments, materials and so on all have more or less the same scatter strength. Major variations in acoustic impedance of the volume are not allowed. The model calculates the scatter strength from the volume properties.
- **Roughness:** one of the trickiest parts of the model and the main source of false signals is without any doubt the approach of roughness. The model is facet based, so the way facets are organized defines the roughness. Considering the rather limited tile size and number of facets that is a significant restriction. It would be better to use facets for calculations of shadows and to consider a surface with certain roughness properties.
- **The unreliability of volume calculations:** the volume calculations require an acoustic impedance volume with very low variability (Pouliquen E., 1998), but on the other hand a rough surface is needed. Both requirements contradict, personal communication with Gaetano Canepa, the implementer of the model, learned that the volume calculations are not reliable and should be considered outdated.
- **Directionality problems:** a DEM (see '4.2.5.2 Representation of the grid environment') is a digital terrain model with a constant spacing in at least 2 dimensions. That implies that the terrain model, that is in fact a matrix, has rows and columns. Rotating this matrix in front of a transceiver will regularly line up the facets in a geometrical order. That seems to generate increased noise levels in the BORIS 3D SSA model. This directionality problem has to be avoided at any cost.
- **Multi path:** The fourth order SSA introduces a limited multi-path calculation on a local scale (only surrounding facets take part in the calculation). Other options of multi-path calculations are not available and are very hard to implement.

- **Parallel processing:** One of the most powerful methods of modeling is parallel modeling. A central server distributes the calculations over a network to other slave computers. BORIS 3D SSA does not allow breaking up calculations into bits and parts. Enabling cluster computations would enable the step to larger seafloor tiles and more complex calculations.

4.2 3D MODEL SECOND EDITION (POINT-SCATTERING MODEL)

Modeling using discrete scatterers has never really been disbanded in underwater acoustics. It proved its value many times, but the search to less computation intensive algorithms pushed it to the background (Etter 2003). Often this method is used as a fast way to crosscheck more complex models. Point scatterer models usually are extremely memory consuming, and computationally inefficient. In some cases however, there is no way around this type of models. Recent advances in underwater acoustic imaging demonstrated the need for a well performing full 3D or 4D point scatterer model. Signals generated with models are used to test processing algorithms, but a good framework to generate these signals using a point scatterer model was not available. This type of model was developed and proved to be capable of containing almost every sand grain on the seafloor in a non repetitive virtually infinite environment. The model is not only able to deal with billions of data points, it is also able to ray trace shadows, calculate ray bending, to do multi-static measurements, do deal with objects, to calculate object-object shadowing, deal with multipath, do cluster computing,... The proposed model is in fact a toolbox allowing the modeler to generate extremely controllable signals in a very flexible and complex environment. It is to the modeler to adapt or add required algorithms where needed.

4.2.1 Introduction

Acoustic modeling and processing both are an extremely calculation intensive job. At the time of starting to think about writing an acoustic model (2003), there were no other fast development tools than MATLAB® to build up a model relatively fast. The disadvantage of MATLAB® is that it is not object oriented; on the other hand it enables to visualize results extremely fast. In 3D modeling, visualization of every step done is essential and therefore MATLAB® was the only option.

4.2.2 Specifications

Chapter 4.1.5 discussed the encountered problems in BORIS 3D SSA. Most of the described problematic limitations are connected to noise introduced by the algorithms applied in the f-k domain and the 2D Fourier transform back to the x-t domain (Pouliquen, Bergem et al. 1999). Fourier transforms need the sampling to be correct; in case of for example velocity variations the nodes of the facets would not be equidistant anymore so they should be resampled (Oppenheim, Schafer et al. 1999). F-k migration has the same problem, resampling the matrix to an equidistant matrix brings a reasonable solution, but resampling is never exact and will always introduce noise. (Yilmaz Ö., 2001) Resampling, with low residual noise generated in the transformations, is only possible if the velocity variations are very low (not in shallow water). Theoretically it might be possible to introduce some minimum ray bending in BORIS 3D SSA.

Shadows can never be introduced in BORIS 3D, the rigidity of the model simply does not allow shadow calculations. A second version of BORIS was published: BORIS 3D SSA. The SSA stands for small slope approximation. The small slope approximation corrects a bit for shadowing and multi path. The SSA correction works only for very small slopes, not for big ripples and objects. In other words the SSA algorithm works locally.

A new model with an old approach for impulse response calculation was the only option available (Princehouse 1977; Wilson and E. 1983; Palmese and Trucco 2006). A combined facet-point scatterer model might bring together most of the pros of both sides (point scatterer modeling and facet scatter modeling). Expanding it to a type of model that can contain a multi-beam echo sounder map dressed up with realistic seafloor tiles would make it even better than just a combination of the two types of model.

One of the main concerns and constraints with 3D and 4D point scatterer modeling on a large scale is the calculation time. Minimizing calculation time can be achieved by for example parallel computing.

Specifications were set for the new model, they are basically the sum of the specifications of the BORIS 3D SSA model minus the volume calculations and plus the solved list of shortcomings in 4.1.5.

TABLE 2: SUMMARY OF DIFFERENCES BETWEEN THE BORIS 3D SSA AND THE POINT SCATTERER MODEL.

	BORIS 3D SSA	Point Scatterer Model
reliable surface scatter signals	No	Yes
tile and environment	flat surface	LOD system, can contain a multi-beam map
Generation of the tile	function based, false shapes, no grain distribution	model based, grain and compaction modules, shapes and patterns realistic
4D options	No	Yes
Discrete beam	Yes	discrete and function approach possible (discrete = faster)
Wavelet	always the same (convolution)	can be a function, has angle dependencies
multi-static	Yes, but recalculates the first static each time	Yes, no recalculation of the first static
one Z-coordinate per XY-coordinate	Yes	no, an environment is facet built but the coordinates do not have to have fixed coordinates

Shadow	No, no ray tracing so no perfect shadow calculation	yes, ray tracing
Velocity profile	no, average velocity needed, no ray bending	Yes, and ray bending
Doppler	No	possible but not yet implemented
scatter strength	not directly controllable, uniform distribution	controllable through density and grain size distribution
Roughness	facet based	facet and scatter point based
Volume calculations unreliable	Yes	Implementation possible: use velocity volumes and floating scatter points. Not yet implemented
directionality problems	Yes	No
Multi path	in 4th order SSA but limited	possible but not yet implemented
parallel processing	No and not necessary	Possible and necessary

4.2.3 Point scatter versus facet scatter

The aim of the proposed model was to take the best of both types of models: facet scattering (Schmidt and Jensen 1985; Pouliquen, Lyons et al. 1998; Palmese and Trucco 2006) and point scattering (Wilson and E. 1983; George and Bahl 1995; Junfei, Hao et al. 2003; Lazarov and Minchev 2006; Gang and Nehorai 2007) and expand it to a type of model that can contain a swath bathymetry map dressed up with realistic seafloor tiles with information about roughness and acoustic impedances.

Point scatterer models were commonly used in the early eighties but have been pushed to the background for a long time until recently they seem to have gained new importance for solving complex problems. The higher performance of computers allows the simple, calculation intensive approach of point scatterer models to solve complex problems faced in for example sonar, GPR, SAR and ISAR research fields (Cooke 2003; Junfei, Hao et al. 2003; Lazarov and Minchev 2006; Palmese and Trucco 2006; Gang and Nehorai 2007; Shi and Nehorai 2007). The origin of the new boost and revival of point scatterer models lays in the combination of simplicity to implement with exact solution and low chance of generating errors. Moreover, point scatterer models do not make trade-offs and are extremely flexible in use. The drawback is the enormous calculation power needed for running point scatterer models.

Introducing calculation tricks reduces the calculation time significantly but has as a consequence (in the case of this proposed model) that the seafloor tiles and the objects have to be seen as two different entities in the modeling sequence. Facets with scatterers connected to the surface will be used for the tiled seafloor, while facet volumes with loose scatterers around the object facets

will be used to define the objects. The object vertex or facet matrices are not tiled meaning that every object is just two matrices: a facet matrix and a point scatterer matrix. A seafloor tile can be approached as an object but that increases the calculation time of the shadows severely. Therefore the option of scatterers connected to facets was chosen. That implicitly means that these facets contribute to roughness. In the case of complex seafloors (rocky bottom for example), it still is possible to approach some seafloor tiles as objects or to dress them up with semi buried objects.

Facets are to be used in ray tracing the shadows, while point scatterers will contribute to the actual signal or impulse response of the environment. The model is based upon a combined facet shadowing - point scattering algorithm. This approach enables the user to have almost unlimited modeling possibilities. The design is specifically aimed at modeling impulse responses of objects near to or on the boundary between two half spaces.

The proposed acoustic model is built up with several types of components each one optimized for their specific use. Three components can be distinguished: the seafloor, the objects and the source(s)/receiver(s).

- Seafloor: the seafloor is an environment built up with tiles. Tiling up a region is the only option when dealing with huge DTMs. The seafloor tile is a hybrid DEM-TIN (see 4.2.5.2 Representation of the grid environment). Scatterers are connected to facets. The scatterers define the roughness and impedance of the facet, while the facet function itself is used in the shadow calculations. This approach enabled a significant reduction in number of calculations for mapping out the shaded zones. Some obvious properties of sandy and muddy seafloors allowed major simplifications. These obvious properties were: a seafloor tile has no holes and has only one z coordinate per (x,y) coordinate.
- Object: the object consists of two relatively independent units: the scatterer matrix and the facet matrix. The facet matrix is used for ray tracing the shadow while the scatterer matrix is used for ray tracing the impulse response. Rays hitting a facet from the facet matrix before hitting a scatterer do not illuminate the scatterer. This is the standard approach in object scattering but it is extremely calculation intensive because it does not allow many simplifications since more than one facet should be taken into account. The advantage is that the solution is more exact, while in the seafloor processing the solution will be an approximation that is exact enough.
- Source/receiver: The source and receiver approach of the model is quite distinct. It leaves a lot of space for own initiatives. There is not really one outspoken module introduced. Depending on the wishes of the modeler concerning accuracy several options are open. These options include a continuous solution (function) a discrete solution or a combination of both. All functions should be subject to further research and development.

The main body of the model produces an impulse response matrix containing the following information:

- Scatter strength of scatterer (S_s)
- Spherical coordinates of every scatterer in a corrected uniform velocity medium. That means that ray tracing has been applied already, the distance

between two points has been measured taking into account the ray bending (R_t) and the outgoing theta (θ_{sr}) and phi (ϕ_{sr}) from ray going out/in the source/receiver has been taken.

- The resulting matrix $[\theta_{sr} \ \phi_{sr} \ R_t \ S_s]$ gives a re-projected environment with scatterer properties.

The final result is that any kind of source/receiver function can be used to calculate the resulting acoustic signal. The ideal would be a source/receiver defined as a function in continuous mathematics but that appears, at first sight, to be impossible. The complexity of the wavelet pattern forming does not make the implementation of continuous mathematics easy and a discrete solution is in terms of computation time slow, but in terms of programming very fast to make and easy to understand (see '1.7 A special case: chirp' where the angular variability of the wavelet pattern of a chirp array is described). Some solutions will be presented in '4.2.10 Discretisation of send and receive array versus array functions'.

4.2.4 Coordinate systems

The environment is constructed in the conventional Cartesian coordinate system, while the source and receiver patterns (when implemented) should be described using the spherical coordinate system used in the model. That means that the seafloor is somewhere on the negative Z axis.

Three coordinate systems are used in the modeling software. First of all the seafloor and objects are drawn in Cartesian coordinates, secondly all rotations around the X, Y or Z axis are done using cylindrical coordinates and the last system used in the ray tracing algorithm is a spherical coordinate system. For all transformations the preprogrammed functions in MATLAB® are used. Important to know is that in the model the transformations between the coordinate systems do not follow the standard implementations of MATLAB®. Avoiding pole singularities is essential to get the model working. Therefore the function `facet2sph.m` (see software book) has been developed. The standard transformation in MATLAB® is $[\text{THETA}, \text{PHI}, \text{R}] = \text{cart2sph}(X, Y, Z)$. The acoustic model uses $[\text{THETA}, \text{PHI}, \text{R}] = \text{cart2sph}(X, Z, -Y)$. Figure 4-7 shows how the transformation between Cartesian and spherical coordinates in the model works.

$$\text{THETA} = \text{atan2}(Z, X)$$

$$\text{PHI} = \text{atan2}(-Y, \sqrt{X^2 + Z^2})$$

$$\text{R} = \sqrt{X^2 + Z^2 + Y^2}$$

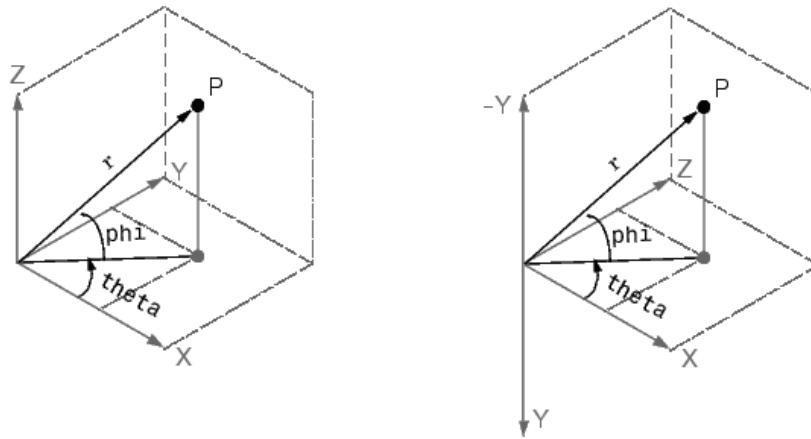


FIGURE 4-7: LEFT: THE STANDARD IMPLEMENTATION OF CARTESIAN TO SPHERICAL COORDINATE TRANSFORMATION IN MATLAB®. RIGHT: THE TRANSFORMATION USED IN THE ACOUSTIC MODEL. ADAPTED FROM THE MATLAB® HELP FILES.

The most annoying feature about this transformation and the reason why the standard transformation to spherical coordinates is not used to transform the environment is the 0° - 360° boundary in the field where the objects and seafloor are placed. The aim of the transformation used in the model is to have all objects and seafloor within the range 90° to 270° of ϕ and 180° to 360° for θ . **That means that only half a sphere is used in the model, so objects must not be put above the sonar without verifying the relative polar coordinates.** In each source or receiver position the axis will be generated with the source or receiver positioned in $(0,0,0)$. As a result it is important to remember that all features (seafloor and objects) should be on the negative Z axis of both sources and receivers. If there would be objects out of that area, one has to make sure they are not in a pole or a 0° - 360° boundary of the transformation. The model itself is protected against this error. The protection is situated in the ray tracing algorithm; it does not allow waves to diffract back up. This protection can be undone and should be changed in the file `vbloc.m` (see software book). The reason why these boundaries and poles are forbidden is because the ray tracing and shadowing algorithm is fed with spherical coordinates. When a facet contains a boundary or a pole, the algorithm will give erroneous results because the distance from 359° to 2° is extremely far for the algorithm, while in reality it is just 3° , with poles the situation is similar but more complex.

The cylindrical coordinate systems are only used in rotation of objects. Figure 4-8 depicts the connection between the Cartesian and the cylindrical coordinates used in the rotation of the objects around the X, Y and Z axis. This is all taken care off by the software, no precautions or limitations are to be taken into account.

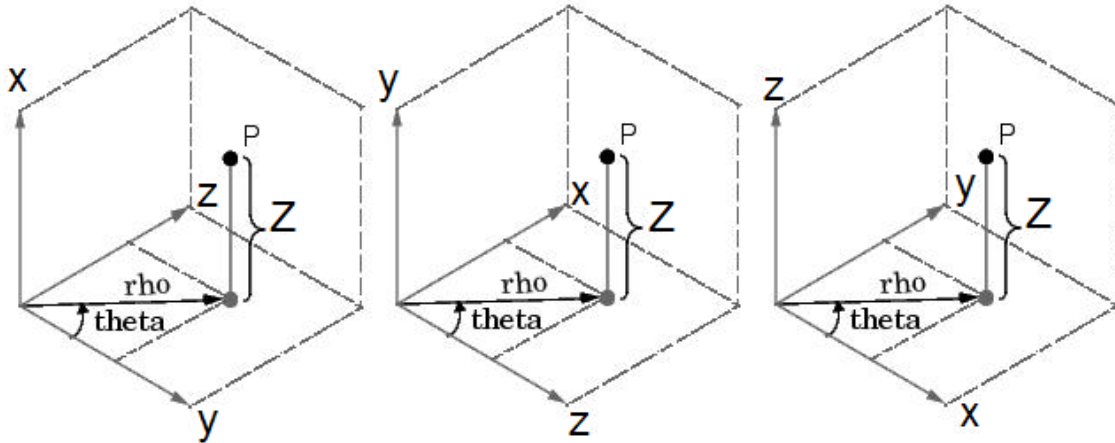


FIGURE 4-8: ADAPTED FROM THE MATLAB(R) HELP FILES. THIS FIGURE DEPICTS THE COORDINATE SYSTEM USED IN THE CARTESIAN - CYLINDRICAL TRANSFORMATION. THE CART2POL TRANSFORMATION IS USED IN THE ROTATION ALGORITHMS FOR THE OBJECTS.

4.2.5 Computer graphics in acoustic modeling

4.2.5.1 INTRODUCTION

It is not only the radar field that has much in common with underwater acoustics. Also the field of computer graphics and visualization in general has a common ground with underwater acoustics. Crossing over between different research fields always is an interesting and challenging job.

This chapter will highlight some aspects of computer graphics that might have a promising future in computational underwater acoustics. Some famous key algorithms such as rendering have counterparts in acoustics. But are all real-time (online) rendering or offline rendering algorithms applicable in underwater acoustics? The answer is: of course not. Visualization is as the word suggests: visualization. Correctness is not an issue as long as it looks correct. In underwater acoustics there is not the luck of having to deal with the limited sensors such as an eye or limited projectors such as a display with a certain pixel density or pixel matrix shape and size. Algorithms for real time rendering want to make things look correct up till a certain predefined zoom level. These algorithms appear not to be applicable. Other algorithms, based upon ray tracing that strive for a higher perfection or even the perfection (extremely high zoom levels), appear to be much more applicable, and might even have been derived from underwater acoustics. Algorithms to simplify the environment, ray trace shadows in a 3D model and rendering on a visualization matrix are only some which are also applicable in underwater acoustics. Probably there are many more algorithms that will demonstrate their value in computational underwater acoustics, but for now, only some essential algorithms have been successfully implemented. Also adapting some conceptual approaches from computer graphics, such as Level of Detail, will bring the acoustic models to a higher and more performing level.

Practitioners of computer graphics have always struggled with the trade-off between complexity and performance (Luebke, Reddy et al. 2003). Exactly the same struggle arises in 3D acoustic modeling. One of the first places to start to look for mathematical optimizations and ideas for 3D acoustic modeling should be the science of computer graphics or the GIS science (Burrough and McDonnell 1998). GIS is a science partly derived from computer graphics, hence some concepts

in this chapter will look familiar to GIS experts, other will not, therefore references will always be made to the computer graphics field and not the sometimes parallel GIS field. The visualization and rendering of 3D environments by computers might not offer complete solutions and complete clues for faster computations in 3D acoustic modeling (Luebke, Reddy et al. 2003). The least it can offer is for sure some basic approaches, concepts and methods on polygon processing. But maybe it can offer more, maybe it can offer concepts of computation time reduction. At first, a complete conceptual copy of discrete Level Of Detail (LOD) was considered (Clark 1976), later the concept appeared to be inapplicable in a non-modified version because directionalities of the triangles and not their sizes are the most important properties playing a role in the current acoustic model. The idea of Acoustic Level Of Detail (ALOD) might be a path that is abandoned at the moment because of lack of time and resources to adapt the model; it certainly is a path to be explored in the future versions of the model. The proposed acoustic model is based on a combined facet shadowing – scatterer point response approach. The ALOD should apply on at least one of the two components (scatterer point configuration and or facets). Applying LOD algorithms can be done on the facets if the scatterer point positions are no longer connected to the facet surface and positions. Introducing simplifications in scatter patterns derived from the scatter points might become another significant improvement.

In the interactive digital world, polygons are the building blocks of the environment. Every polygon can be subdivided into triangles. A triangle is the minimal unit to work with because it is both planar and convex. A polygon is convex if every line segment connecting two points on the boundary of the polygon is entirely contained (Luebke 1998). That is an important property when ray tracing is to be applied, because the algorithm to test whether the ray hits the polygon or not, is dramatically faster for planar convex polygons because it means that no 'holes' are to be found in the polygon. No risks on high computation times are taken and the standard procedure is to decompose the 3D environment into triangles.

LODs are not only used to simplify the rendering of 3D scenes, they are also used to make basic structures which might be bump-mapped or dressed up with surface tiles (Bloomenthal 1985; Onoue and Nishita 2003; Wikipedia 2007). That means that a LOD does not necessarily contain all available details. The LODs built for this acoustic model are based upon the fractal character of dunes and ripples (Tian-De, Qing-Song et al. 2001). The bump mapping in this model does not happen with a figure tile, it will happen with a higher detail DTM (DEM) and it can happen, as the fractal character suggests, till the desired level of detail has been reached with the same tile. This method is in LOD computer graphics known as the top down approach (Luebke, Reddy et al. 2003).

Once the triangularized 3D environment is built some other problems arise concerning shadowing in the environment. Rendering is the next process to deal with. Rendering is the process that generates an image from a 3D model. Rendering projects the 3D image in a 2D matrix or figure, that 2D matrix is defined by the pixel matrix of the display. Figure 4-9 displays a rendered photo realistic 3D model. The rendered figure has been ray traced; ray tracing included mirroring effects, transparency, shadowing,...

An acoustic impulse response should also be rendered, but the coordinate system to apply is angle based and not spatial and more important the matrix to render in has no pixel matrix to project data in, so it has no reductions.



FIGURE 4-9: A PHOTOREALISTIC RENDERED IMAGE CREATED BY USING POV-RAY. THIS IMAGE WAS CONSTRUCTED USING A 3D TRIANGULARIZED MODEL, A VIEWPOINT, TEXTURE, LIGHTING AND SHADING INFORMATION BEFORE BEING RENDERED. SOURCE: (WIKIPEDIA 2007)

For rendering, computer graphics offers several fast options (Wikipedia 2007) such as: scan line rendering (Schweitzer and Cobb 1982), rasterisation (Eker and Tucker 1989), ray casting (Hanrahan 1983) and radiosity (Cohen and Greenberg 1985), but the most exact, the slowest and the only true available option is ray tracing (Hanrahan 1983). Ray tracing in computer graphics is generally applied using a Monte Carlo technique, in the case of acoustic 3D modeling it will be applied with a line scanning technique. The Monte Carlo ray tracing techniques applied in computer graphics might be extremely promising for future 3D acoustic modeling. Here also further research is required.

No ray tracing algorithm is useful without rastering the triangles. The question whether a ray hits or passes next to a triangle is essential in shadow calculations, rastering methods are used to solve this unknown. Two rastering methods are used: edge walking and edge equations. Edge equations will be the only open option for 3D acoustic modeling.

There is one divergence between the acoustic modeling and computer graphics that always has to be taken into consideration. In computer graphics the result has to **look** correct, in acoustic modeling it has to **be** correct. In practice that means that real-time algorithms that have been developed to render complex models in a couple of milliseconds will not be useful because they are designed to make images look correct. Algorithms to render non-real-time images such as Figure 4-9 might be useful to a certain extent. It is the certain extent part that needs some further research (Garriga, Spa et al. 2005).

4.2.5.2 REPRESENTATION OF THE GRID ENVIRONMENT

The representation of the environment in computer graphics is a speciality on its own. Digital terrain models cannot only be found in computer gaming but also in scientific software such as GIS packages, terrain visualization and statistics packages, multibeam echo sounder online and

offline software, satellite imaging... Representing digital elevation models, digital terrain models and surface in general is fundamentally simpler than just a random 3D model of an object. It is simpler because a surface is considered as 2.5D and not full 3D, in other words the z coordinate is a function of the x and y coordinate. Since $z=f(x,y)$ and every z has only one possible value, 2.5D here also means that every z coordinate has a unique (x,y) coordinate. Further on the (x,y) coordinates are regularly spaced; it is a 2D plane with some bumps and pits in it. Moreover the 2.5D infinite surface has no holes, so no detection algorithms for holes have to be used.

4.2.5.2.1 FACET MODEL

Digital terrain model (DTM) representation using LOD algorithms can be done in two ways: regular gridded height fields or digital elevation models (DEMs) and triangulated irregular networks (TINs) (Heckbert and Garland 1999). Figure 4-10 demonstrates how fundamentally different the approaches are. Regular gridded systems are favoured over TIN for rendering. TINs have some significant disadvantages (Luebke, Reddy et al. 2003):

- In complex terrains three times the amount of data is needed to store the DTM. Because of the irregular spacing between the vertices (x,y,z) coordinates need to be stored, where a matrix of Z coordinates is sufficient for DEM.
- They are hard to integrate with raster databases
- Implementing of related functions is more complex because of the lack of simple overarching spatial organization.
- Runtime LOD is less efficient.

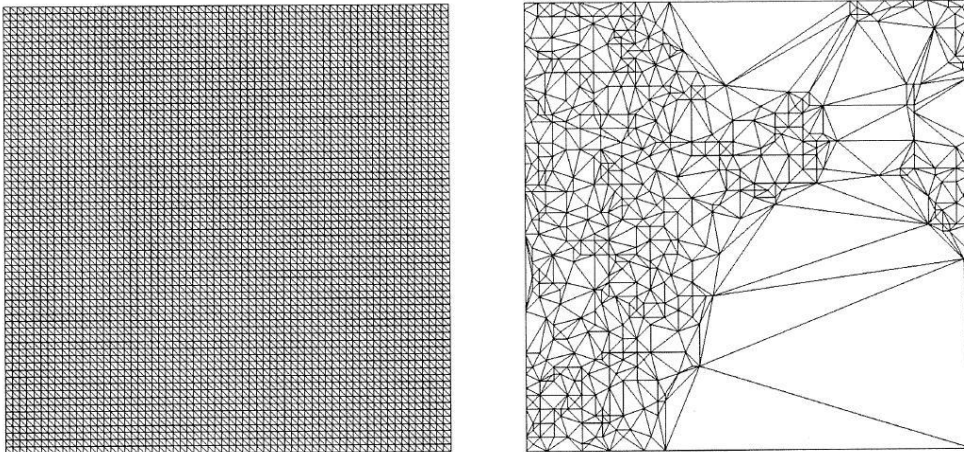


FIGURE 4-10: LEFT A REGULAR TERRAIN REPRESENTATION AS INITIALLY USED BY THE ACOUSTIC MODEL, AND RIGHT A TIN REPRESENTATION (GARLAND AND HECKBERT 1995). COPYRIGHT © 1995 CARNEGIE MELON UNIVERSITY.

Hybrid schemes exist and also this acoustic model is based upon a hybrid scheme. Hybrid schemes try to take the best of both worlds and combine it in one DTM. The original approach of the model was the DEM approach but after introducing the ray tracing and ray bending, introducing (x,y,z) coordinates instead of just a matrix of z coordinates became unavoidable. Re-gridding and interpolating would have been another option to bring the DEM-TIN hybrid back to a DEM but the interpolation would not have necessarily given, for every ray tracing from a different position, exactly the same DEM and as such it would have excluded multi static

modeling. In this first step of ray tracing the seafloor DTM is considered as too crucial to make approximations.

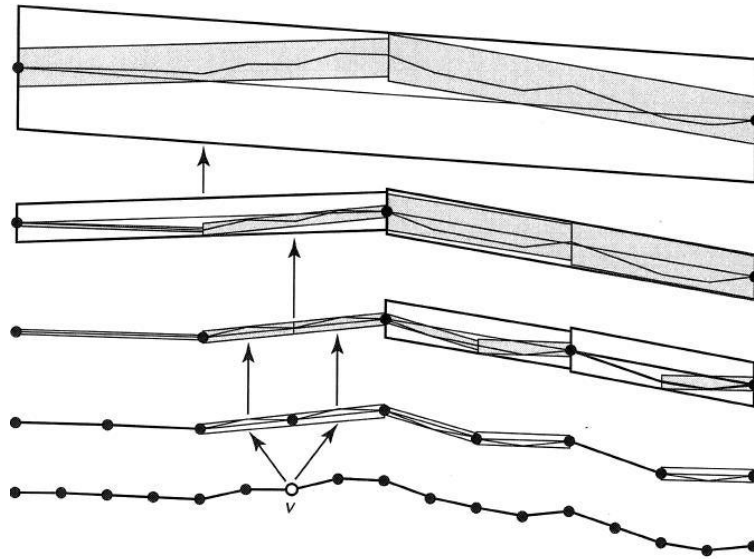


FIGURE 4-11: REDUCING THE NUMBER OF VERTICES OF A 1D SURFACE (DUCHAINEAU, WOLINSKY ET AL. 1997). COPYRIGHT © 1997 IEEE

The most commonly used bottom up simplifications of surface models were proposed by Duchaineau et al. (Duchaineau, Wolinsky et al. 1997). These algorithms might be useful in completely the opposite way they are used in computer graphics. In computer graphics they are used to simplify distant areas in the surface model, in under water acoustics it might have a future in near to vertical incidence angles or close to the source/receiver where small changes in facet configuration can have no influence on shadowing. These simplification schemes can only be applied on the shadow ray tracing algorithms and matrices. It is important to keep in mind that simplifications on the side of a tile will create holes or cracks due to the T junctions (Luebke, Reddy et al. 2003), so a retriangulation should be applied on the external tiles where the simplification has been applied. Several ways of dealing with the problems of eliminating cracks and T-junctions have been described (De Haemer and Zyda 1991; Leclerc and Lau 1994; Duchaineau, Wolinsky et al. 1997; Hoppe 1998; Rottger, Heidrich et al. 1998; Luebke, Reddy et al. 2003). It should be reminded that none of the simplifications may be done on the positions of the point scatterers, contributing to the impulse response. Further top down calculations dealing with splitting up of facets crossing a boundary between two water layers with a different sound velocity should be introduced.

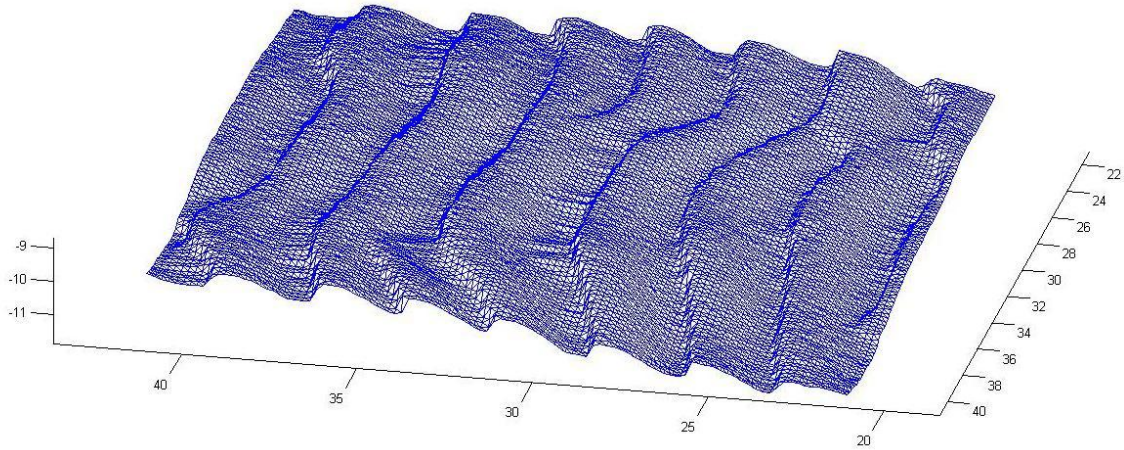


FIGURE 4-12: A HYBRID DTM, THE ORIGINAL DEM IS VISIBLE BUT THE SPATIAL SAMPLING IS NO LONGER UNIFORM. THIS IS AN EXAMPLE USED IN THE MODEL TESTING. THE SURFACE HAS BEEN GENERATED WITH THE MODEL PROPOSED IN 4.2.6.3.

Some technical considerations: facets are throughout the model flow stored in a 3D matrix or array. Each facet has three (X,Y,Z) or (φ,θ,R) coordinates. Two types of facet matrices are used: Cartesian and spherical coordinate matrices. Usually every Cartesian matrix contains pure (X,Y,Z) spatial coordinates, while spherical coordinates might contain both spatial coordinates and ray traced coordinates. Ray traced coordinates are coordinates relative to the source or receiver. The ray traced coordinates are the basis of the shadow calculation algorithm. Cartesian coordinates are only used on the user end of the model. Spherical coordinates might be introduced in the user end of the model, since they are easier to be used while defining a source/receiver aperture. Keep in mind that in this model the source/receiver aperture is not the -3dB opening angle of the source/receiver but depending on the required precision a -80dB or less area.

The facet coordinate 3D arrays are built as follows:

- Dimension 1: index is the facet number
- Dimension 2: 3 nodes
- Dimension 3: (X,Y,Z) or (φ,θ,R) of a facet node (1=X or φ , 2=Y or θ , 3=Z or R)

4.2.5.2.2 POINT SCATTERING MODEL

The point scatterer model connected to the seafloor tiles should not have directionalities in the resulting impulse response. The point scatterer positions are defined by a random function based upon an 'equal density of point scatterers in a facet' algorithm. That algorithm can easily be adapted if it would be not deliver satisfying results. Usually point scatterer matrices such as the one used in chapter 3.2 are based upon a DEM. DEM based matrices have the property that in both x and y direction they have a continuous sampling interval, while the Z coordinate defines the surface. Having in one plane a continuous sampling interval excludes an equal density per facet approach since all facets parallel to that plane will have more scatterers per unit of surface than non parallel facets, where facets perpendicular to the plane used to spread and project the scatterers might even have no scatterers at all. Moreover, equal spacing in sampling generates directionalities. Horizontal facets have the lowest 'visible' surface area, the surface area of a facet increases with increasing slope. The point scatterers are draped over the

original DEM and not over the hybrid DEM-TIN. First, the shadow matrix, generated in the facet calculations, will be implemented on the original DEM, then the point scatterers in the visible areas will be computed and ray traced. In order to generate each time the facets at the correct place, one should make sure that the feeds of the random algorithms are connected to the indices of the tiles and not to the relative position of each tile.

The first concern is to have a good performance of the algorithm. A good performance first of all means that the density of the scatterers is equal on every facet and there are no directionalities connected to the matrix in the impulse response. So it is important that the density of scatterers is much higher than the surface of the facet. When the density of scatterers is close to, or lower than 10 point scatterers per horizontal facet, an effect of directionalities appears as displayed in Figure 4-14. Adaptations in the code can be made to avoid this effect.

The algorithm to spread the point scatterers over the facet, delivered with the model, can be subject to change in the future. Currently the algorithm rotates the facet in a plane with equally spaced point scatterers (fixed dx and dy), after which a random algorithm with a certain feed (a fed random algorithm generates a pseudo random matrix) generates translation vectors added to the point scatterers. Using this method enables to give certain roughness parameters to the facets and to reduce directionality of scatter related to the DEM grid.

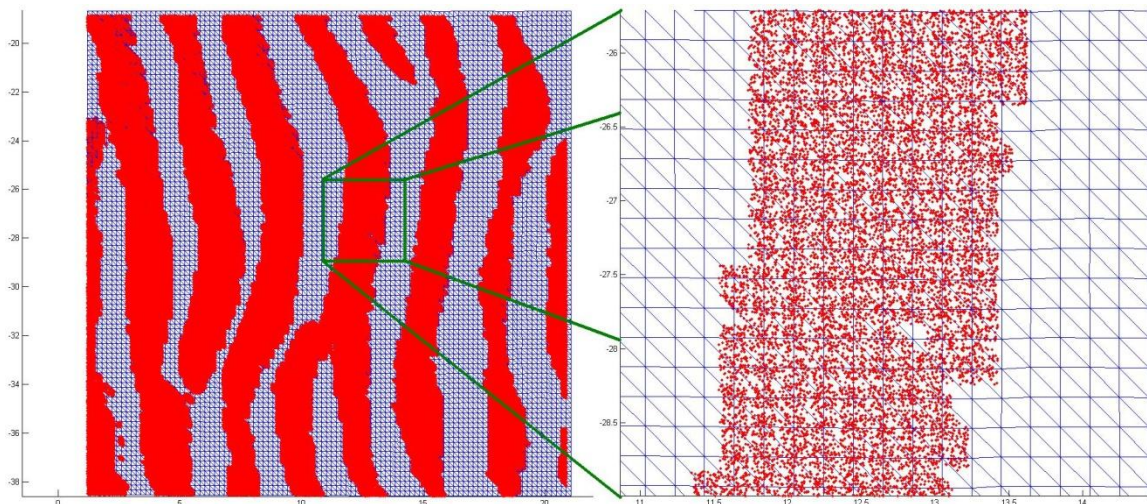


FIGURE 4-13: PRINCIPLE SKETCH OF THE POINT-SCATTERER POSITION ALGORITHM. LEFT: A TILE WITH ON TOP THE SCATTERERS (THE SCATTERER POSITION ALGORITHM HAS BEEN FED WITH THE SHADOW MATRIX, SO THE SCATTERERS ARE ONLY GENERATED IN THE, FOR THE SOURCE/RECEIVER, VISIBLE ZONES). RIGHT: A ZOOM IN ON ONE OF THE MEGA RIPPLES AND THE CORRESPONDING POINT SCATTERER MATRIX. THE FACETSIZE VERSUS SCATTERDENSITY IS TOO SMALL, DIRECTIONALITIES CAN BE OBSERVED.

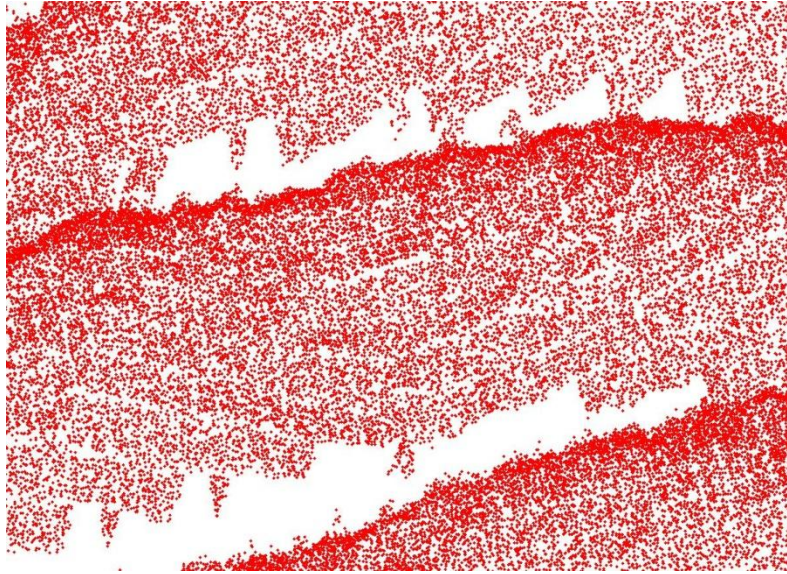


FIGURE 4-14: A CLOSER VIEW ON THE 3D IMAGE OF FIGURE 4-13. THE SAME DIRECTIONALITY PROBLEM IN THE POINT-SCATTERER MATRIX DUE A TOO LOW DENSITY CAN BE OBSERVED. THE FACET MATRIX IS VISUALIZED BY THE NEAR TO VERTICAL WHITE LINES RUNNING THROUGH THE IMAGE. A HIGHER DENSITY OF SCATTERERS REDUCES AND EVENTUALLY REMOVES THESE LINES.

The point scatterers are stored in a simple 2D matrix with in the first dimension the point scatterer index and in the second dimension the (X,Y,Z,S_s) with S_s defining the scattering strength or acoustic impedance. After ray tracing the impulse response array is formed with as stored coordinate system in the second dimension of the array: $(\varphi_s, \theta_s, R_s, \varphi_r, \theta_r, R_r, S_s)$. As Figure 4-13 demonstrates; only the point scatterers visible for both source and receiver are eventually re-generated, ray traced and stored in a file.

4.2.5.3 PROCESSING AND BUILDING 3D OBJECTS

Objects are, as the seafloor, constructed with triangular facets. The object does not have a raster approach and that makes them significantly different than the objects that could potentially be introduced in BORIS 3D SSA. The acoustic model currently has one module to construct four types of commonly used object shapes. The object contains a facet model and a point scatterer model. In order to preserve the shape properties, no point scatterers are connected to a facet. That means that a point scatterer model of a sphere is spherical while the facet model of a sphere, which will never be a perfect sphere, can be rather rough. The four essential objects are: a sphere, a cylinder, a tube and a manta or flattened cone shape (Figure 4-15).

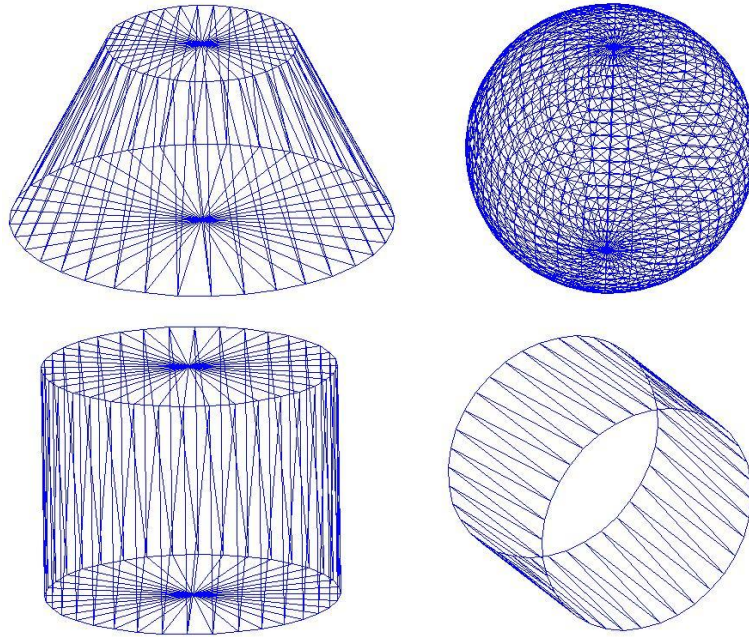


FIGURE 4-15: FOUR SHAPES OF OBJECTS. THESE SHAPES CAN BE GENERATED USING THE MINETYPE.M FILE DELIVERED WITH THE MODELING PACKAGE. TOP: MANTA (LEFT), SPHERE (RIGHT), BOTTOM: CYLINDER (LEFT), TUBE (RIGHT)

Users who would like to build their own objects can design them following the same strategy as demonstrated and documented in the `minetype.m` function in the software book of this thesis. Every object is composed out of sub-objects. These sub-objects are disks and tubes. For these objects two components are generated: facets and point scatterers. The final product is an array containing two matrices: a facet matrix and a point scatterer matrix.

Introducing a full 3D object in an environment is introducing complexity. Full 3D objects are not planar and might be concave (Luebke 1998). The possible concavity of the objects introduces the necessity to scan the complete object. The objects in the water column can float, but they can also be partly covered by the seafloor (Figure 4-16 and Figure 4-17). In the case of partial burial the ray tracing does not only need to scan the object but also part of the seafloor. The interaction between the object and the seafloor is an important ray tracing problem to solve. Another interesting situation is when an object throws a shadow on another object.

Processing possibly concave objects such as tubes and calculating the influence of the object on the environment is a significant part in the modeling software. Important to know is that when modeling a tube, no multi path calculations are done so no echo is generated.

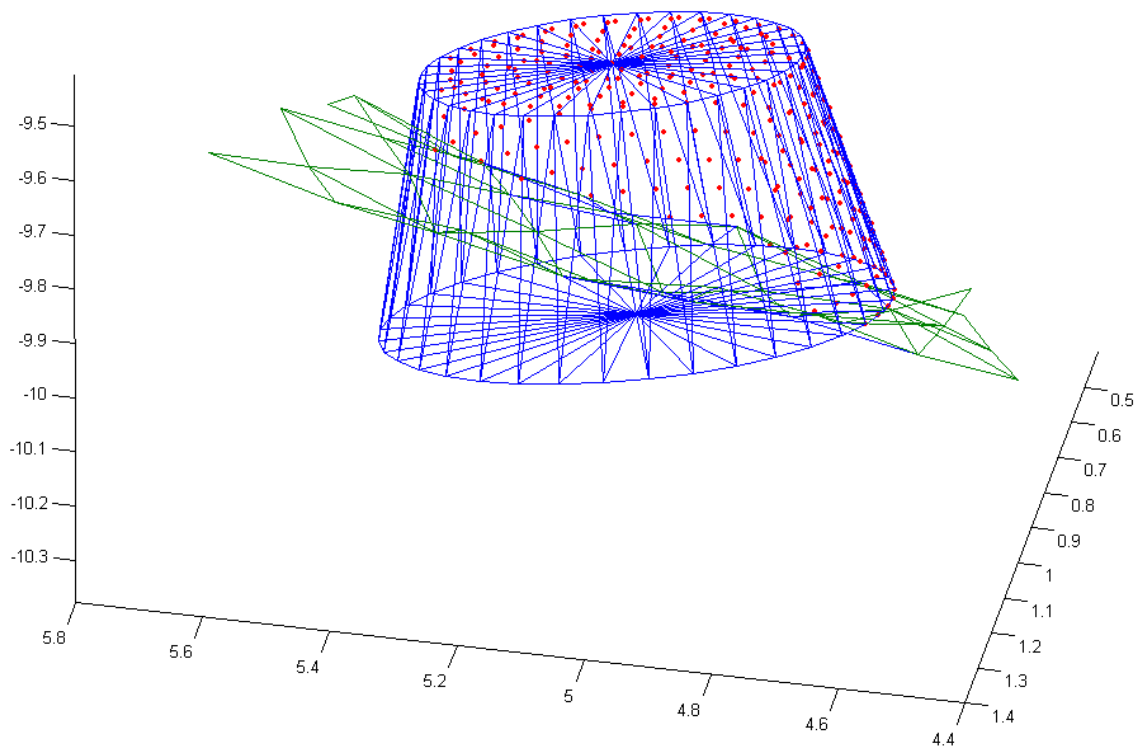


FIGURE 4-16: A PARTLY BURIED CONE SHAPED AS MANTA-LIKE OBJECT. THE BLUE FACET LINES ARE A SECTION OF THE SEAFLOOR AND THE OBJECT FACETS. THE RED DOTS ARE SOME RAY TRACED POINT SCATTERERS OF THE OBJECT, THE SOURCE TRANSDUCER COORDINATES ARE NOT MADE VISIBLE.

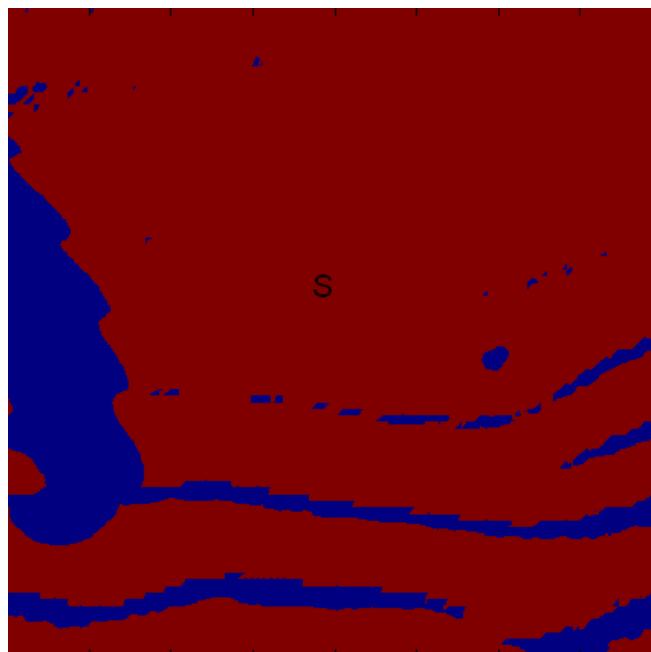


FIGURE 4-17: SHADOWS ON A TILE FROM A CYLINDER (LEFT) AND A SEMI BURIED MANTA MINE (CENTRE RIGHT) SEEN FROM A SOURCE S. THE CYLINDER IS CLOSE TO THE SOURCE AND THEREFORE HAS A HUGE SHADOW. THE RIPPLED SURFACE DETERMINES THE SHADOW SHAPE. THIS MATRIX IS FED INTO THE POINT SCATTERER MODELS. THE POINT OF VIEW IS IN THE CENTRE OF THE TILE.

4.2.5.4 ACOUSTIC LEVEL OF DETAIL (ALOD)

Acoustic level of detail or ALOD, is a new term and method proposal introduced in this thesis. So far no publications have been found on the topic. As previously mentioned in '4.2.1 Introduction' ALOD is derived from a term in computer graphics: Level Of Detail or LOD. The principle of LOD is that objects further away from the point of vision can be described with lower precision, higher simplification or less facets without the eye noticing it. This results in faster and more efficient rendering for the display, it also enhances performance of ray tracing and shadowing algorithms. With acoustics that is not the case. A rough surface, composed out of small facets will be more visible than a plane composed out of only two big facets. The plane will generate specular scatter in the acoustic response while the rough surface will generate scatter, even when the distance between sonar and facets of the rough surface is much longer than between the plane and the sonar. This principle together with reducing impedance differences is used in stealth weapons. Therefore it is not possible to simplify surfaces by retriangulation as used in graphic LOD. One might say that 'Size does not matter.' Is an important fact in underwater acoustic imaging. What is also very important is the incidence angle: Figure 4-17 shows that no shadow is forming under the source/receiver. The seafloor facet tile there could be replaced with a two facet per tile simplification. That principle opposes the graphic LOD system where objects close by have a lot of facets and objects far away have less facets. If within a radius around the source/receiver there are no facets with a negative incidence angle (ray hits the facet from underneath) no shadows are formed within that radius. How the ALOD principle has to be implemented and if it is an option at all is subject to further research.

4.2.5.5 SHADOWS, RASTERIZATION AND RENDERING

Rasterization is the process of turning a vector image into a raster image. Rasterizing is one of the essential processes used during rendering. In the case of computer graphics, the raster often is the display matrix. For underwater acoustics the raster is draped over the facet matrix. The raster will define the resolution of the solution. Important to note is that the raster is equally spaced along the x and y axis and not equally spaced if seen from the source/receiver.

Shadowing algorithms are extensively used in visualization of 3D and 2.5D models. Shadowing helps the brain to create a sense of 3D in a 2D image. Real time rendering of shadows is extremely calculation intensive, therefore the shadows are static or an operator is used. That operator estimates shadowing. A typical operator is based on taking the first derivative in a certain direction. In most applications that is more than enough. In acoustics however, an exact solution is a necessity. In computer graphics some applications, which are not necessarily shadowing algorithms, such as rasterization need an exact computation of triangle projection well (Luebke 1998). These algorithms may be used in the model for shadowing. A closer look to the two common strategies will learn that only one of the two will be applicable.

4.2.5.5.1 EDGE WALKING

Edge walking is an algorithm extensively used in rendering. This algorithm requires a fixed matrix such as a display matrix. Because it is based on a scan line approach it is optimal for image rendering directly on a display matrix. Figure 4-18 shows the basic idea of edge walking; one draws the edges vertically and fills in horizontal spans for each scan line. Since the scan line

is in the algorithm, and there is no scan line in the acoustic model, it makes it inapplicable in the acoustic model.

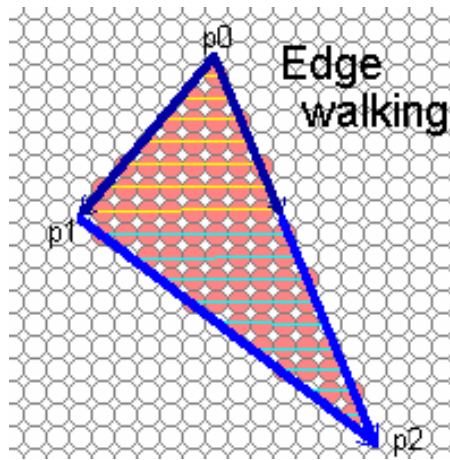


FIGURE 4-18: EDGE WALKING ALGORITHM VISUALIZED. DRAW THE EDGES VERTICALLY AND FILL IN HORIZONTAL SPANS FOR EACH SCAN LINE. ADAPTED FROM LUEBKE, 1998.

4.2.5.5.2 EDGE EQUATIONS

Digging into rendering and computer gaming algorithms brought the solution for the shadowing problem. Edge equations use the mathematical description of a line in a 2D plane in order to find out on what side of the line a pixel can be found. A triangle can be described using three line equations, and if the directions are correctly chosen, filling in the coordinates of a pixel in the equations will give a three times positive or three times negative solution. After ray tracing the facet is described in polar coordinates, or in other words a spherical raster around the source/receiver is used to project the facets on. If the facets are small enough, the facet can be seen as being projected on a 2D plane with a coordinate system based upon (φ_s, θ_s) . Substituting x and y in the equations enables us to find out if a pixel is inside or outside the triangle.

The line equations are:

$$A_1x + B_1y + C_1 = 0$$

$$A_2x + B_2y + C_2 = 0$$

$$A_3x + B_3y + C_3 = 0$$

Computing edge equations means solving A,B and C and filling in x and y . Only the resulting mathematical formulae will be described, more information can be found in the literature (Luebke 1998). Before starting the solution it is important to sort the vertices of the facet in ascending order of x and to give them the indices 1, 2 and 3. In the formulae x and y are replaced by φ and θ . The following formulae describe how the software is implemented.

$$A_1 = \theta_1 - \theta_2$$

$$B_1 = \varphi_1 - \varphi_2$$

$$C_1 = \varphi_1\theta_2 - \varphi_2\theta_1$$

$$A_2 = \theta_2 - \theta_3$$

$$B_2 = \varphi_2 - \varphi_3$$

$$C_2 = \varphi_2\theta_3 - \varphi_3\theta_2$$

$$A_3 = \theta_1 - \theta_3$$

$$B_3 = \varphi_1 - \varphi_3$$

$$C_3 = \varphi_1\theta_3 - \varphi_3\theta_1$$

$$r_1 = A_1\varphi + B_1\theta + C_1$$

$$r_2 = A_2\varphi + B_2\theta + C_2$$

$$r_3 = A_3\varphi + B_3\theta + C_3$$

When r_1, r_2 and r_3 have the same sign, the ray hits the facet.

Figure 4-19 demonstrates how the algorithm finds all the pixels inside the facet defined with three vertices. Although this algorithm was not designed for shadow calculation, but more for projection and colour interpolation, it appears to be very useful in the acoustic model.

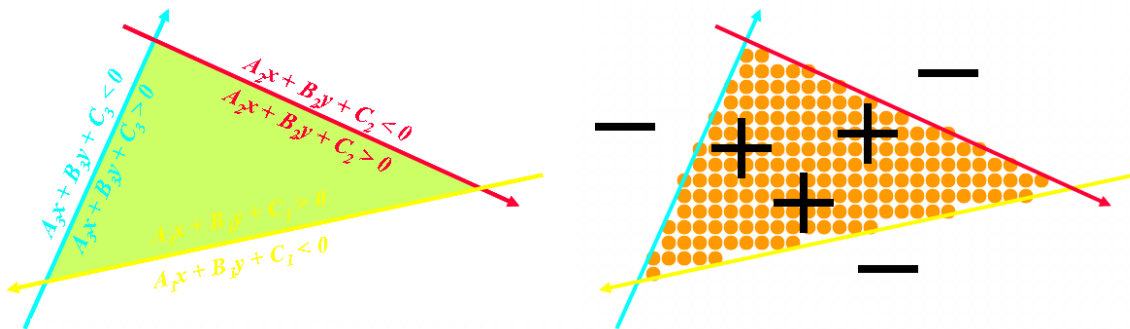


FIGURE 4-19: EDGE EQUATION ALGORITHM VISUALIZED. ADAPTED FROM LUEBKE, 1998.

4.2.5.6 CONCLUSION

Computer graphics is a fascinating science which might significantly contribute to the acoustic modeling science. Both sciences are young sciences that became more 'mature' stand-alone sciences less than two decades ago. Further research in this cross-over field is required.

The backbone of the model is based upon advances in the computer graphics field. Many applications in the computer graphics field cannot be copied blindly to an acoustic equivalent. Algorithms copied and applied into the acoustic model are sometimes used in the opposite way of the computer graphics application. An example of that phenomenon is the LOD system which needs more detail with distance and less when the tile comes close to the source/receiver. Another example is the rasterization algorithm that is used in a completely different situation. The rasterization algorithm could be copied without modifications.

The physics of light and sound have much in common. Also the softwares dealing with these phenomena appear to have much in common and have a huge potential of cross-fertilization.

4.2.6 Building the environment

4.2.6.1 INTRODUCTION

The environment is constructed by bump mapping a digital elevation model with high resolution geographical information tiles such as sand ripples tiles. The tiles in the model have three layers containing information about microbathymetry, absolute acoustic impedance of the top layer and the volume and grain size or roughness. The generation of these tiles is done using a sedimentological model. Since no existing sedimentological sand dynamic models were applicable in the acoustic model and no seafloor generating models from other acoustic models created a useful multilayer environment, a new sand dynamic model, specifically designed for the use in underwater acoustic modeling was created. Due to the fractal character of sand dynamics (Tian-De, Qing-Song et al. 2001), the sand dynamic model results can be used in several layers of the LOD bump mapping. The acoustic model also required the introduction of objects in the environment. The introduction of full 3D objects required major adaptations in the construction and design approach of the acoustic model.

Memory is the first concern of every model programmer. Using a 3D environment often leads to swapping in the memory segments of the computer. Swapping reduces the performance of the algorithm. Matrices containing DEM and object information have billions of vertices and that is impossible to handle for a standard PC. Breaking up or tiling up the environment is the only possible option. Tiling up an environment increases complexity in the model implementation but it also introduces some opportunities. The problems of tiling up are nested loops and boundary problems. The advantages are that the model can be used on a PC and even better the calculation can be solved on a network cluster of PC's.

4.2.6.2 TILING UP THE ENVIRONMENT

The environment used in the model is a tiled and bump mapped seafloor with some extra objects added to it. Basically that means that a top down LOD system has been progressively bump mapped with tiles containing higher detail DEM and geological information. Or in practice: the top level is a bathymetric map of a certain resolution and that bathymetric map is used to merge smaller tiles on of a higher detail. The merging of the bathymetric tiles can be done in layers (ex: bathymetry-dunes-mega ripples-sand ripples). Each three layered tile (bathymetry, grain size distribution, acoustic impedance) is bump mapped over the previous bump mapped LOD (Figure 4-21). Currently mostly the down level matrices, or highest detail matrices are used in the model. If the model is dealing with acoustic impedances and roughness, the bump mapping of the bathymetry has been applied during all initial tests.

Users of the BORIS 3D SSA model will recognize Figure 4-20 (Canepa, Bergem et al. 1997; Bergem, Pouliquen et al. 1999; Pouliquen, Bergem et al. 1999). The figure shows similarity with the figure published in the implementation report of Canepa, 1997. Basically the figure only demonstrates that one single tile generated with the proposed sand dynamic model can be tiled up with itself without leaving cracks or holes open. The major difference with the BORIS_SSA model is that here there are asymmetric sand ripples on the tile instead of sinusoidal (unnatural) sand ripples. Figure 4-21 demonstrates one of the fundamental differences with the BORIS_SSA model. The figure shows that the tiled environment can be draped over a multi-beam echo sounder map or a lower resolution version of the same tile. Note that the

visualization of a larger bump mapped area after ray tracing might look unnatural because refraction of the sound waves is implemented as bending the surface until an iso-velocity water volume has been generated, in the very beginning of the model flow.

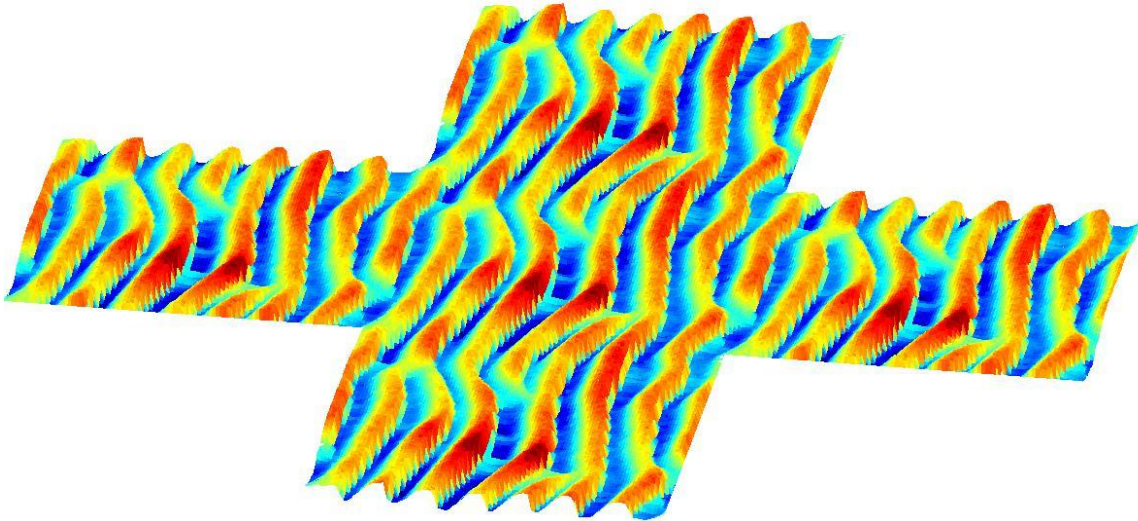


FIGURE 4-20: FIVE HIGH RESOLUTION SEAFLOOR TILES TILED UP. THIS FIGURE DEMONSTRATES THAT THE TILES LEAVE NO HOLES OPEN IN THE DEM, A PROPERTY REQUIRED FOR ACOUSTIC MODELING.

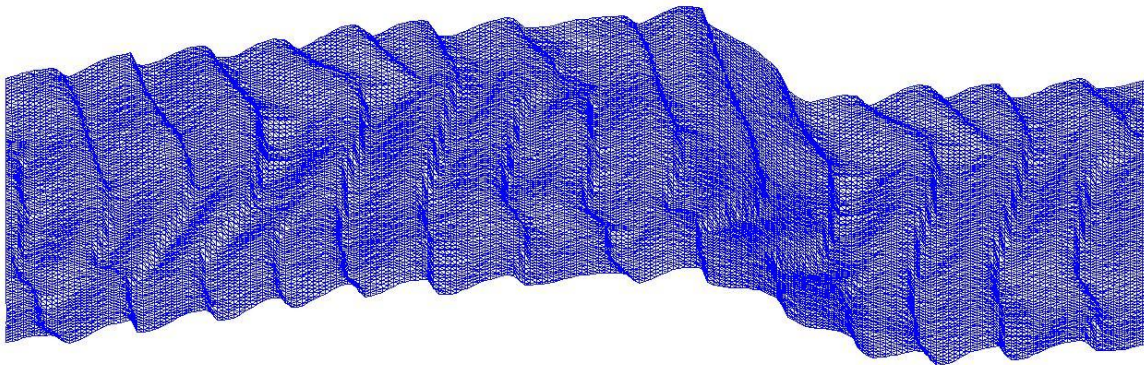


FIGURE 4-21: COMPLETELY PROCESSED TILES. BUMP MAPPING OF 2 SAND RIPPLE TILES ON A DUNE FIELD. THE BUMP MAPPING IS NOT DONE WITH A PICTURE AS IN COMPUTER GRAPHICS APPLICATIONS BUT WITH THE MICRO BATHYMETRY TILES DISPLAYED IN FIGURE 4-20.

4.2.6.3 GENERATING THE ENVIRONMENT: MODELING SAND DYNAMICS

This sub-chapter describes a simple approach to sub aqueous sand ripple, dune and other bedform pattern modeling. It focuses on the discrete multidimensional ripple generating computer algorithm, the adapted sedimentology rules and the comparison with wind blown ripple generating models or aeolian models. It has been specifically designed to be used in underwater acoustic research, but may also be used in sedimentological research and hydrodynamic engineering and modeling.

Military underwater acoustic research in shallow marine environments is extremely challenging. Models trying to predict mine hunting sonar performances in these environments very often generate unrealistic results. One of the reasons why models fail is because they simplify the

environment. These simplifications are valid in deep water or low acoustic frequencies but not in the shallow marine environments using high acoustic frequencies. A new generation of acoustic models is required. The first step to those new models is to redefine some of the major simplifications. One of those simplifications is the seafloor (Lyons, Fox et al. 2002). The main goal of this model is to create a realistic looking seafloor in a reasonable time, leaving out most complexities as vortices, which can be used as a starting point for acoustic modeling. For underwater acoustic modeling the grain distribution or roughness, the topography and the compaction is needed. The model will focus on these three parameters. The hydrodynamics too are essential, and the model is built to introduce that too, but detailed hydrodynamics are deliberately left out to decrease the calculation time. The following results and examples will all use extremely simplified hydrodynamics, and as such they will demonstrate that even with the rough assumptions, a realistic seafloor can be produced.

A sandy seafloor is covered with bedforms, the bedform dynamics themselves sorting and compacting the sediment (Soulsby 1997). Understanding the complex non-random sediment dynamics in general and the interaction with sea mines is essential to understand the resulting acoustic response of a sediment and semi buried or buried mines. Bedforms can be observed in any sandy environment where the shear stress caused by a current over a sand bed exceeds a certain threshold (Soulsby 1997). Once the threshold is exceeded, the granular medium reorganizes itself from a rough, relatively flat morphology into a ripple pattern. Sand ripples and dunes can be seen as self organizing patterns with a fractal character (Tian-De, Qing-Song et al. 2001). This property will prove to be useful in the acoustic models. Ripples and dunes may be generated by a sub aqueous current or by the wind (aeolian). Aeolian generated patterns have been described and modeled by Nishimori and Ouchi (Nishimori and Ouchi 1993), Anderson and Bunas (Anderson and Bunas 1993), Landry and Werner (Landry and Werner 1994), Yizhaq et al. (Yizhaq, Balmforth et al. 2004) gives a brief overview of some existing aeolian models and model approaches. Soulsby (Soulsby 1997) explains the sub aqueous transport mechanisms, but does not propose any model. The aeolian sediment transport processes and formulae as described (Anderson and Bunas 1993; Nishimori and Ouchi 1993; Landry and Werner 1994; Tian-De, Qing-Song et al. 2001; Zhang and Miao 2003; Yizhaq, Balmforth et al. 2004) do not apply in sub aqueous environments, but the resulting shapes and some patterns are similar. Therefore first existing aeolian models were evaluated and found to be inapplicable in underwater acoustic models. The models proved to be inapplicable because they were not designed to generate the parameters acousticians need and upgrading the models to an applicable level for acoustics appeared to be impossible. Nevertheless a lot can be learned from the methodological approach some of the authors have.

Four transport mechanisms are active in a sub aqueous system; avalanche, roll, saltation and creep. All mechanisms have been subject to extensive research (Soulsby 1997). In this model a combination of roll and saltation is the driving mechanism of sub aqueous sediment transport; a grain rolls or hops up the ripple following the least energy-consuming path to the crest where it may avalanche until it settles down in the main current shadow. In the literature the behaviour of sand and the threshold of movement of sand on a bedform is described mathematically (Dawson, Johns et al. 1983; Van Rijn 1984; Johns, Chesher et al. 1990; Johns, Soulsby et al. 1993; Soulsby 1997). If a pile of grains exceeds a certain stability angle, the pile will fail and grains will avalanche until that specific stability angle has been restored. The stability angle of sand in a non-energetic environment is about 32°-37°. Saltation is the most energy consuming way of

transport. Saltation means that grains are ejected from the sand bed, float in the water column and splash down downstream. Saltation is thought to be the driving mechanism for aeolian ripple formation (Anderson and Bunas 1993; Nishimori and Ouchi 1993; Landry and Werner 1994; Tian-De, Qing-Song et al. 2001; Yizhaq, Balmforth et al. 2004). There is a grey region between roll and saltation, therefore an artificial boundary is set; all grain movements influenced by more than one small scale feature of the sand bed during one discrete time increment (hopping) follow the roll equations. Basically that includes most of the bed load saltation. The fourth mechanism is the creep mechanism; some grains get enough energy to be destabilized, but do not get enough energy to roll up the ripple. These grains will modify their position on the ripple slope, they might move to an adjacent bin.

Starting with a simplified 2D approach of ripple formation, the model adopts the following sedimentological rules. Figure 4-22 shows a ripple and a coordinate system.

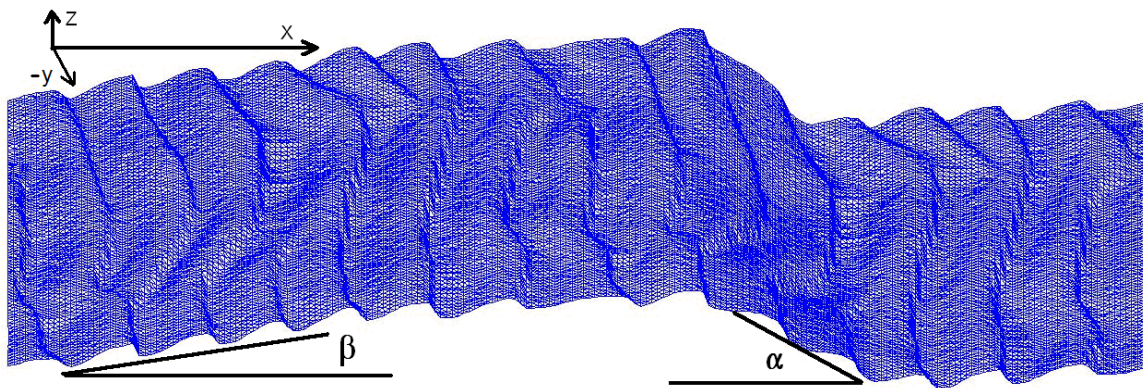


FIGURE 4-22: A 3D MODELED RIPPLE ON DUNE PATTERN (BUMP MAPPING AND TILING METHOD) WITH THE TWO STABILITY ANGLES THAT PLAY A ROLE IN 2D MODELING

The current flows in the positive X direction. The transport mechanisms can be subdivided in two groups: energy consuming mechanisms such as saltation, roll and creep and energy producing mechanisms as avalanching and sometimes creep. The system will get energy from the avalanching when a slope gradient in the system exceeds the stability angle, that angle is called α . The energy consuming mechanisms also have some stability angles. The angle β defines the maximum slope of the stoss side of the ripple. The stability angle γ for destabilized creeping grains will be related to the energy lost in friction and will be along the Y axis in the 3D model. The current shadow is defined as $h_x - h_{x-1} < 0$. Where h is the height of the considered bin, x and $x-1$, and the direction of the main current is along the positive X axis. Consider now one single spherical grain, with a diameter gd and a mass m . An increasing force is imposed on it, forcing it to move or roll. The grain will start rolling once the implied force is stronger than the friction force keeping the grain on its position. The model will use the integration of the force in the formulae. It will be referred to as energy. Per bin, per discrete unit of time t a grain can spend a maximum accumulated amount of energy: E_x . Exposed grains and grains positioned on a slope exceeding the stability angle β will be transported over a distance s during the time interval t . Time t is subdivided in elementary time units Δt . Typical to this model is that the length of t is not defined. It will be the spent energy and energy available in a bin who define the end of the time interval. The Δt units refer to the time needed per elementary movement s between two adjacent bins. $s = \sum \Delta s$ and $\Delta s = \sqrt{\Delta x^2 + (\Delta h + gd)^2}$ the elementary distance rolled between

two adjacent bins. The stoss side stability angle or β -function is not yet determined, β is set to an acceptable constant 7° , but is supposed to be related to the horizontal component of the water velocity vector on the sea floor, grain mass m and smallest current impact surface of a grain. A similar approach can be made for the β_2 -function related to vortices (Figure 4-23).

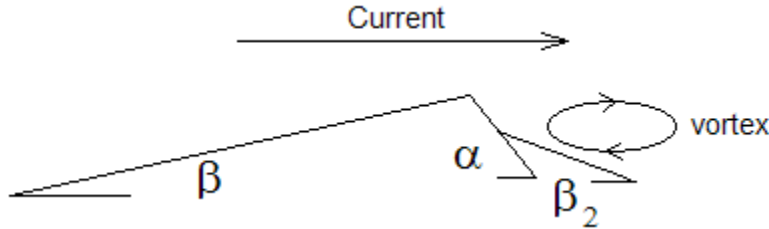


FIGURE 4-23: 2D SCHEMATIC REPRESENTATION OF A SAND RIPPLE WITH A VORTEX

A moving grain will spend an amount of energy within a time interval $t: E = \sum \Delta e$, with Δe defined as the energy used in one elementary movement between two adjacent bins (Δs in Δt). The grain will stop rolling as soon as the grain enters a bin where $E_x \leq E$, with E_x being the maximum energy in that bin calculated at the start of interval t and a function of the amount of energy a certain bin is imposed to due to the current. And the last rule of the roll movement is that all grains in a current shadow, $h_x - h_{x-1} < 0$, will not move at all. The α -function, or avalanche function is set to an acceptable constant: 32° . The summary of formulae for the energy consumption in roll, with a current in the positive X direction, is:

E_x is a function with a linear relationship to the hydrodynamics vector at that specific bin.

$$\begin{cases} E = \sum \Delta e \\ E \leq E_x \\ E_x = 0 \Leftrightarrow h_x - h_{x-1} < 0 \\ E_x = 0 \Leftrightarrow \begin{cases} h_x - h_{x-1} < h_{x+1} - h_x \\ \frac{h_x - h_{x+1}}{\Delta x} < \beta \end{cases} \end{cases}$$

With Δe defined as:

$$\Delta e = E_{friction}(m, \Delta s) + E_{gravity}(m, \Delta h)$$

The grain movement rules for roll and bed load saltation are:

$$\begin{cases} h_{x,\Delta t+1} = h_{x,\Delta t} - gd \\ h_{x+1,\Delta t+1} = h_{x+1,\Delta t} + gd \end{cases} \Leftrightarrow \Delta e > 0$$

And the grain movement rules for the avalanche:

$$\begin{cases} h_{x,\Delta t+1} = h_{x,\Delta t} - gd \\ h_{x+/-1,\Delta t+1} = h_{x+/-1,\Delta t} + gd \end{cases} \Leftrightarrow \frac{h_x - h_{x+/-1}}{\Delta x} > \alpha$$

This simple set of rules will give a 2D section of a ripple taken parallel to the current. $E_{gravity}$ is a function of the mass and the difference in height between two adjacent bins x and $x+1$. The avalanche mechanism is simplified, but demonstrates well the idea.

Expanding these rules to 3D makes the situation slightly more complex. We will again start with a two mechanism system and then expand to a three mechanism system. Imagine now that a number of 2D systems are set parallel to the current in a matrix. Using the above rules ripple shapes will appear in the matrix but no ripple pattern. A ripple pattern is formed because there is a communication between each 2D ripple shape. Here Δs as distance will be expanded to: $\Delta s = \sqrt{\Delta x^2 + \Delta y^2 + (\Delta h + gd)^2}$. As described in the sedimentation rules, a grain will follow the least energy consuming path, so in the roll movement there will be three options to roll to instead of one. The 3D expansion of the 2D rules for roll will be (assuming that roll is possible):

$$\Delta e_{optimal} = \min \begin{bmatrix} \Delta e_{x,y \rightarrow x+1,y-1} \\ \Delta e_{x,y \rightarrow x+1,y} \\ \Delta e_{x,y \rightarrow x+1,y+1} \end{bmatrix}$$

Avalanching will be expanded in the same way, instead of two avalanche directions there will now be eight directions of avalanche (diagonals are included).

The result of these expansions will be a 3D ripple like pattern (Figure 4-24). Users only interested in generating a ripple topography can, every time step, smooth the resulting matrix out in the Y direction. For users interested in acoustic impedances or dynamics, using this method in this step will generate false results because of compaction anomalies. Avoiding undesired effects related to the discretisation can be done using the creep method. This method allows a grain to move to one adjacent bin if the grain is exposed to the current and movement will not take energy out of the system. The rules for creep are:

$$\left\{ \begin{array}{l} h_{creep} = \min \begin{bmatrix} h_{x-1,y-1} \\ h_{x-1,y} \\ h_{x-1,y+1} \end{bmatrix} \leq h_{x,y} - gd - \gamma \Delta s \\ h_{optimal} = \min \begin{bmatrix} h_{x,y-1} \\ h_{x,y+1} \\ h_{x+1,y} \end{bmatrix} \leq h_{x,y} - gd - \gamma \Delta s \end{array} \right. \Leftrightarrow \begin{cases} h_{x,y,\Delta t+1} = h_{x,y,\Delta t} - gd \\ h_{optimal,\Delta t+1} = h_{optimal,\Delta t} + gd \end{cases}$$

The rules set and explained in the previous paragraph are very wide and open. Every user of the model can add extra restrictions or open up restrictions. Acousticians are also interested in acoustic impedances. The acoustic impedance of a sediment is the product of the sound speed through the sediment and the density of the sediment. Densely packed sand has a higher acoustic impedance than loosely packed sand (Jackson and Richardson 2007), mud has a lower acoustic impedance,... A complex mechanism as ripple progradation generates a sorted sediment with impedance changes. A simulation containing a compaction module generates Figure 4-25, the distribution of acoustic impedances in a ripple. The compaction module itself will not be

covered in this sub-chapter, at this point the module just gives an idea of the impedance distribution.

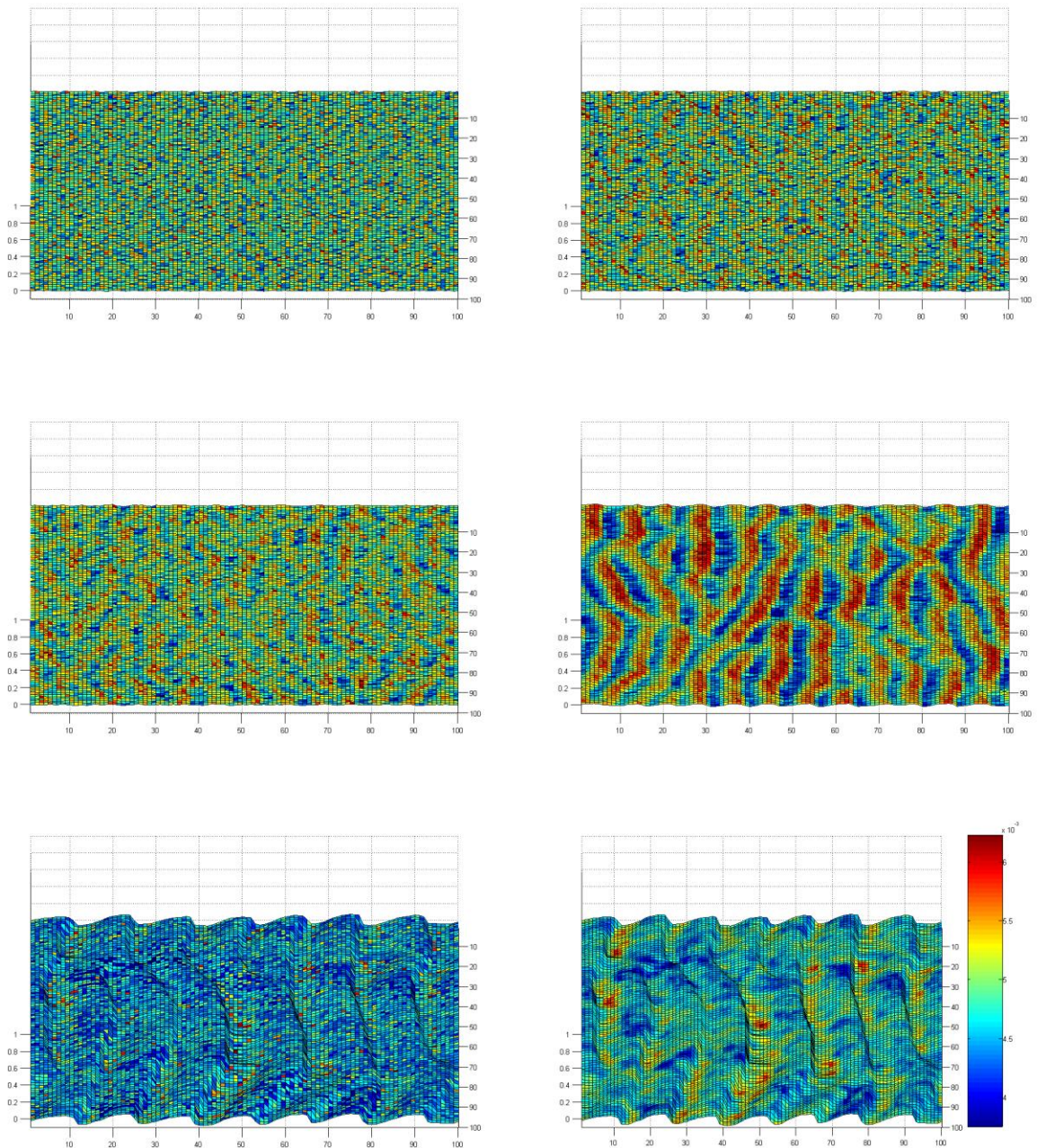


FIGURE 4-24: LEFT TOP: PHASE 3 OF THE RIPPLE FIELD EVOLUTION. RIGHT TOP: PHASE 8 OF THE RIPPLE FIELD EVOLUTION. LEFT CENTRE: PHASE 13 OF THE RIPPLE FIELD EVOLUTION. RIGHT CENTRE: PHASE 50 OF THE RIPPLE FIELD EVOLUTION. LEFT BOTTOM: PHASE 500 OF THE RIPPLE FIELD EVOLUTION BUMP MAPPED WITH THE GRAIN SIZE MATRIX. RIGHT BOTTOM: PHASE 500 OF THE RIPPLE FIELD EVOLUTION BUMP MAPPED WITH A VERSION OF THE GRAIN SIZE MATRIX PROCESSED WITH A MOVING AVERAGE FILTER OF 3 BY 3 BINS, GIVING EVERY BIN THE AVERAGE VALUE OF THE NEIGHBOURING BINS AND THE BIN ITSELF. IMPORTANT TO NOTICE ARE THE CONCENTRATIONS OF LARGER GRAINS (RED AND YELLOW SPOTS) IN THE RIPPLE TROUGHS.

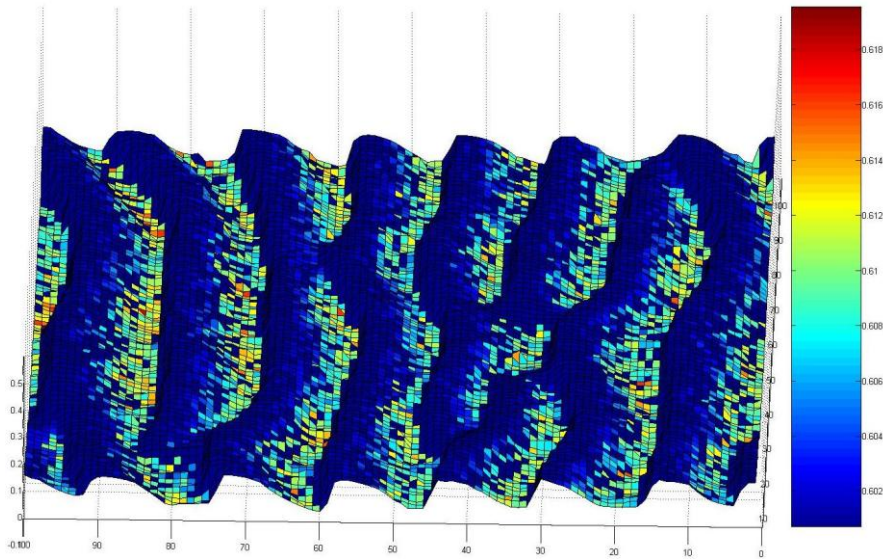


FIGURE 4-25: IMPEDANCE MAP PLOTTED ON TOP OF A TOPOGRAPHY TILE, THE HIGHEST IMPEDANCES CAN BE FOUND IN BETWEEN THE RIPPLES AND ON THE SIDE OF THE RIPPLES WHERE EROSION OCCURS.

To summarize, a new generation ripple and bedform model has been developed and the backbone has been presented in this sub-chapter. The model is not restricted to modeling only the topography but makes an opening to modeling the ripple and bedform dynamics as a whole. The model can be seen as a fundament from where each user can start building his own multidimensional model for his own purposes and apply his own simplifications and rules. The simplest model requires only four input parameters, next to a grain and height matrix: three stability angles and an input current velocity. A correlation between the stability angles and the input current is expected, this correlation would reduce the input parameters in the basic model to a function, friction and a current velocity. Due to the fact that each grain searches its optimal path no detailed hydrodynamics should be introduced in the model cycles.

4.2.6.4 AUTOMATED DETECTION OF SAND DUNE CRESTS

4.2.6.4.1 INTRODUCTION

Many paths have been explored in order to find a fast shadow calculation algorithm for 3D hybrid raster environments. Most of them were dead end streets. One of those dead end streets might not be a dead end street for the GIS operators because it swiftly converts raster based patterns to vector matrices. Computer graphics offered some solutions in shadow calculation: exact ray tracing solutions and the much faster approximate solutions. Ray tracing was the only true option, but maybe a third hybrid way out was available: detecting the crests of the sand waves and projecting them on the objects and surfaces. In a tiled fractal LOD system that would mean that the vectors could be reproduced infinitely and even bump mapped. Only the projection had to be redone for every tile. The solution did not prove to be very useful for underwater acoustic modeling. The algorithm does work fast enough to make a difference so it might serve other applications. The algorithm is able to detect the crests of sand waves on swath bathymetry raster maps and vectorize them.

One of the many paths towards fast shadow calculations and optimization of the algorithm was automatic detection of the dune crests in the tiles before the implementation in the LOD structure. The goal was to have vectors of the dune crests and to use them to project the shadows. Having the vectors enables the modeler to tile up not only the tiles but also the related vectors. Detection and generation of vectors was a success but the implementation appeared to be no optimization. Nevertheless, this algorithm goes further than the currently known and used algorithms in GIS because it makes vectors and is not just a raster representation. Using this algorithm on for example a multi-beam echo sounder map, a matrix with crest vectors enables easy calculations of for example current vectors. Therefore it is noteworthy to describe it.

4.2.6.4.2 THEORY

For the theoretical testing of the algorithm, a simulated seafloor tile is used. A simulated seafloor is the worst case scenario for testing because the surface has not been filtered or spline interpolated as is done with swath bathymetry maps. That means directionalities related to the algorithm that generated the tile might interfere with the crest detection algorithm. As soon as the algorithm performed well on the surface shown in Figure 4-26, it was tested on real bathymetric maps. The hardest sections to solve were chosen and used for further testing. The algorithm was expanded to real bathymetry and adapted, then it was again implemented on the modeled bathymetry,... this iteration was repeated until the algorithm performed well on both synthetic as real bathymetric data.

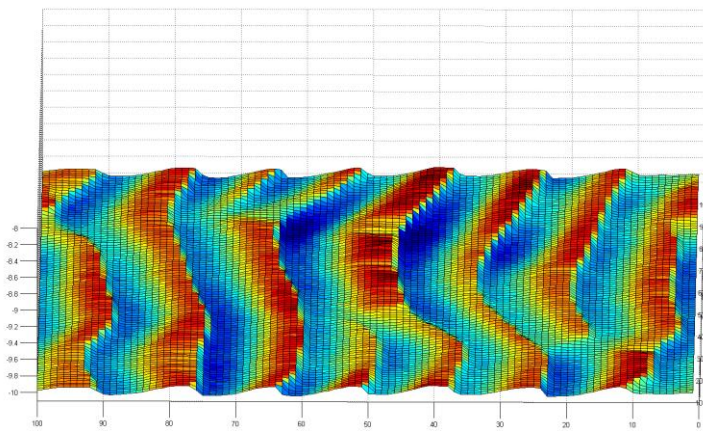


FIGURE 4-26: THE SEAFLOOR TILE USED IN THE ALGORITHM TESTING

Since the raster has no holes and exactly one z coordinate per (x,y) coordinate, the DTM surface in the algorithm is seen as a double-differentiable surface (Wood 1996). The algorithm itself differentiates in eight directions: along the X and the Y axis and the two diagonals each time in both positive and negative direction. Evans approximates a surface by a bivariate quadratic equation (Evans 1980; Wilson, O'Connell et al. 2007). A similar approach will be used throughout the algorithm. Many other algorithms for linear feature detection are proposed in the literature, most of them are algorithms applied on radar maps (Blondel, Sotin et al. 1992; Trinder and Wang 1998; Dillabaugh, Niemann et al. 2002; Quackenbush 2004; Hsu and Lai 2009; Sun and Vallotton 2009).

The algorithm consists of two main units: 1) the detection of the crests plus marking and cleaning of the detections in the raster. This method is based upon the Evans equation (Evans 1980) and generates Figure 4-27, displaying all the possible crests in a given raster, 2) the creation of vectors based upon the data displayed in Figure 4-27.

The detection of the crests starts with taking the first derivative of the surface. A convention for this section: when capitals are used and indices (i,j), we are working in discrete mathematics. Continuous mathematics is done with normal fonts and (x,y). This convention applies only in the following functions. F is the discrete surface grid with f as its analog counterpart.

$$g(x, y) = \frac{\partial f(x, y)}{\partial x} \text{ and a discrete counterpart } G(i, j) = F(i + 1, j) - F(i, j)$$

$$G'(i, j) = \begin{cases} G(i, j) \geq 0 \rightarrow G(i, j) = 1 \\ G(i, j) < 0 \rightarrow G(i, j) = 0 \end{cases} \text{ with as analog counterpart } g'(x, y)$$

That first derivative is then used to give each upcoming slope a '1' and all down going slopes a '0'. The G function can be expanded to all eight directions:

$$G(i, j)_h = F(i + 1, j) - F(i, j)$$

$$G(i, j)_{ht} = F(i, j) - F(i + 1, j)$$

$$G(i, j)_{d1} = F(i + 1, j + 1) - F(i, j)$$

$$G(i, j)_{d1t} = F(i, j) - F(i + 1, j + 1)$$

$$G(i, j)_v = F(i, j + 1) - F(i, j)$$

$$G(i, j)_{vt} = F(i, j) - F(i, j + 1)$$

$$G(i, j)_{d2} = F(i - 1, j + 1) - F(i, j)$$

$$G(i, j)_{d2t} = F(i, j) - F(i - 1, j + 1)$$

Differentiating another time the Boolean matrix G' is detecting the edges or the crests of the sand ripples.

$$g''(x, y) = \frac{\partial g'(x, y)}{\partial x} \text{ or discrete: } G'' \text{ with dimensions (Mg,Ng)}$$

The resulting matrix is then 2D cross correlated with the bathymetry matrix F with dimensions (Mf,Nf). The cross correlation is used to be sure that the crests are positioned on the correct place, if not the crest matrix G'' is shifted to the correct place.

$$C(i, j) = \sum_{m=1}^{Mg} \sum_{n=1}^{Ng} G''(m, n) \cdot \text{conj}(F(m + i, n + j))$$

The formula is adapted from the MATLAB® help files, m=1 and n=1 because MATLAB® does not start with index 0 in a matrix but with index 1.

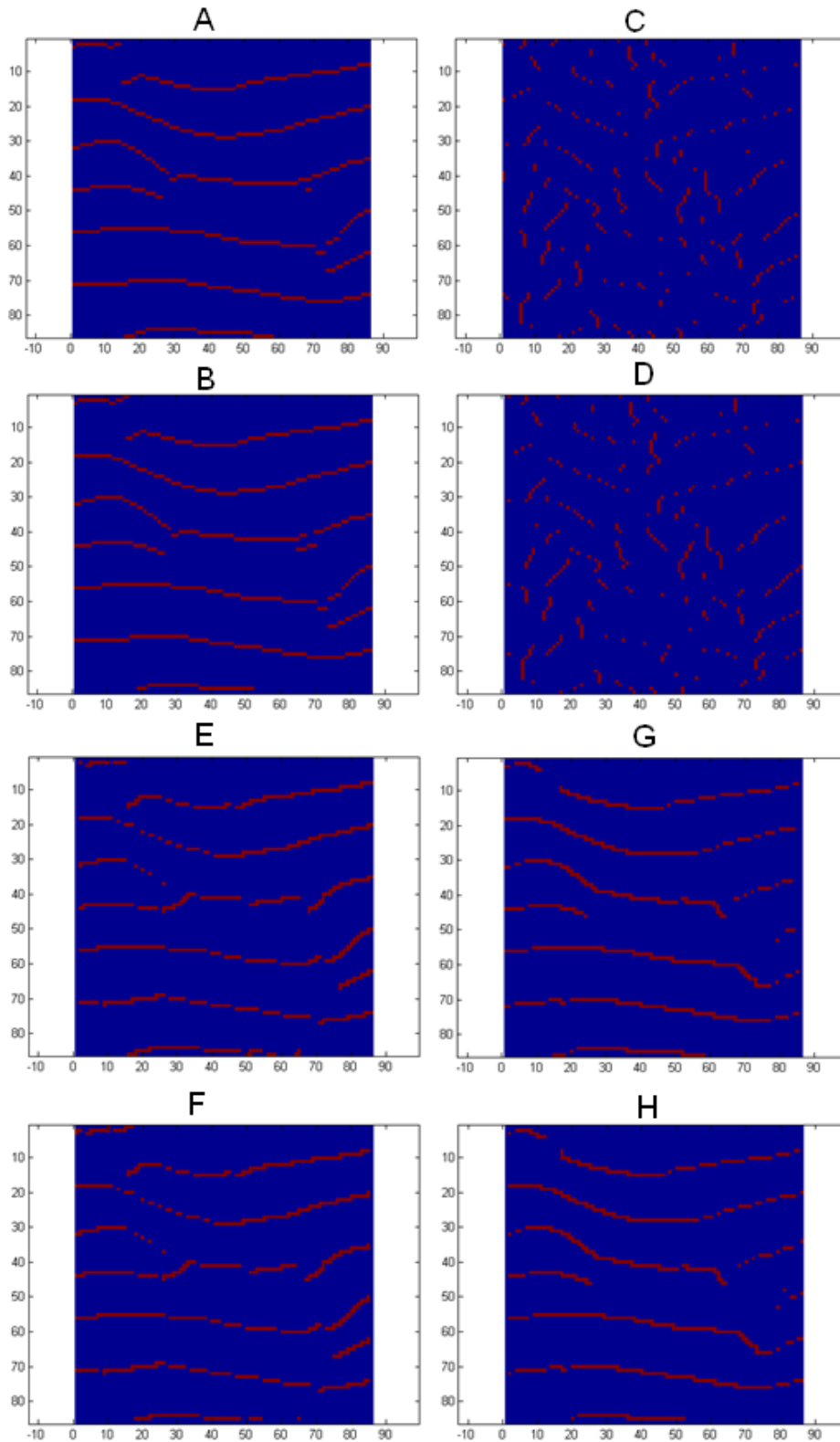


FIGURE 4-27: THE OUTPUT FROM THE CREST.M AND CRESTDIAG.M METHOD. A AND B DISPLAYS THE RESULT OF THE METHOD AFTER TAKING THE SECOND DERIVATIVE, TAKEN PERPENDICULAR TO THE SAND WAVES. C AND D: PARALLEL, E, F, G AND H: DIAGONAL. RED ARE THE DETECTIONS OF THE CRESTLINES. NOTE THAT HERE THE CRESTLINES HAVE NOT YET BEEN VECTORIZED.

After shifting the G'' raster on the correct place, the F' matrix is generated. The F' matrix is a smaller version of the F matrix because only the inner part of the F matrix can be processed; the outer ring of data in the raster is ignored. Two parameters are now calculated: mean amplitude ($mamp$) of the matrix crests and the standard deviation of the standard deviations along the rows and columns of the G'' matrix ($std2$)

$$mamp = \frac{\sum_{i=1}^{Mg} \sum_{j=1}^{Ng} G''(i, j) \cdot F(i, j)}{\max(\max(F)) \cdot \sum_{i=1}^{Mg} \sum_{j=1}^{Ng} G''(i, j)}$$

Two new vectors are created: the standard deviations along the rows and the columns of the G'' matrix $stdGr$, $stdGc$.

$$std = \sqrt{\frac{1}{n} \sum_{i=1}^n (x_i - \bar{x})^2}$$

$$std2 = 1 - \frac{std(stdGr)}{std(stdGc)} = 1 - \frac{std(std(G''))}{std(std(G''^T))}$$

Both parameters: $mamp$ and $std2$ will help to give an indication of respectively the best fit and the highest linearity. The best fit idea is relatively easy to understand: crests of sand waves are usually the highest points in the matrix, and the detections should be there too. The higher the amount of detections on the highest points, the better the fit. The standard deviation along one direction will give an indication of the spread of the data, if that spread along the rows is significantly different from the spread along the columns (another standard deviation) it gives an indication of the presence of a pattern, or in this case linearity. Both parameters are used in order to find the optimum solution of the two groups of four different matrix differentiations (normal differentiation and diagonal differentiation) and both solutions are given by the function searching the optimum solution to the main function.

A third matrix is returned, a statistics matrix S . The statistics matrix S contains information about the probability of the presence of a crest. The higher the number, the higher the probability.

$$S(i, j) = \sum_{n=1}^4 (mamp_n \cdot G''_n(i, j))$$

This results in Figure 4-28.

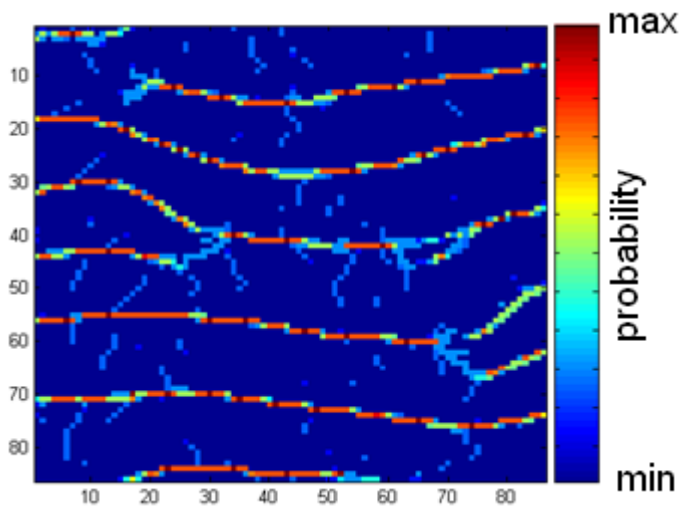


FIGURE 4-28: COMBINED OPTIMUM SOLUTIONS USED IN THE STATISTICS AND VECTOR CALCULATIONS. THE CREST LINES BECOME VISIBLE WITH DIFFERENT INTENSITIES. THIS MATRIX WILL BE USED TO CONNECT VECTORS BASED UPON THE DETECTIONS SHOWN AT FIGURE 4-27.

In the further processing, the best solution for the G'' matrix is chosen using `std2`. A function called `crestvectopt.m` is then called and the topography, the statistics matrix and the optimum G'' are the arguments given for further processing and generation of the vectors. Figure 4-29 summarizes the previously described raster operations.

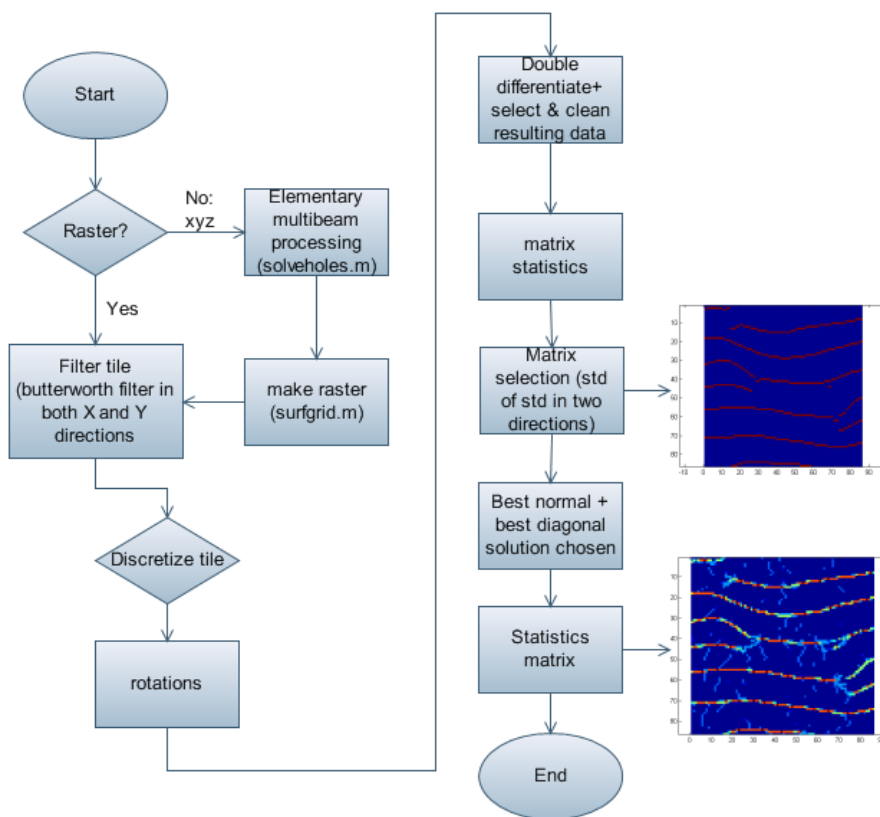


FIGURE 4-29: A SUMMARY OF THE RASTER OPERATIONS DONE AS A PREPARATION FOR THE VECTORISATION.

After focusing the raster to the crest lines and building a probability raster, the best G'' matrix is used as the basis for the vectorisation. The statistics matrix S is used to interconnect individual vectors to the maximum length vectors.

The vectorisation algorithm mainly consists of conditional statements. Putting them in a formula and detailed flow charts is meaningless. Therefore only a top level flow chart will be used to explain what happens. For more information I refer to the software book. The final result of the vectorisation is shown in Figure 4-31. In this case eleven vectors represent the crests of the surface. The final result is not 100% perfect but it is better than a hand picked vector. Moreover vectors allow easy manipulations, so finalizing the result by hand picking to almost perfection should now be a very fast procedure.

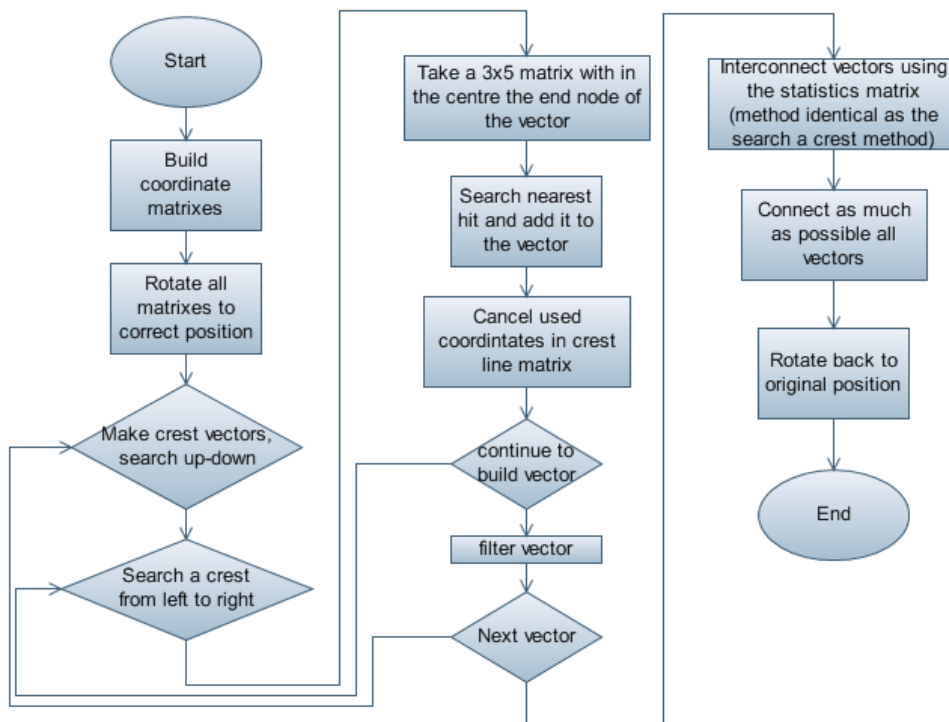


FIGURE 4-30: THE VECTORISATION FLOWCHART. FOR MORE INFORMATION SEE THE SOFTWARE BOOK. THE PROCEDURE THAT INTERCONNECTS VECTORS USING THE STATISTICS MATRIX IS A COMPLEX NON DIRECTIONAL PROCEDURE BASED UPON THE 'SEARCH A CREST' LOOP.

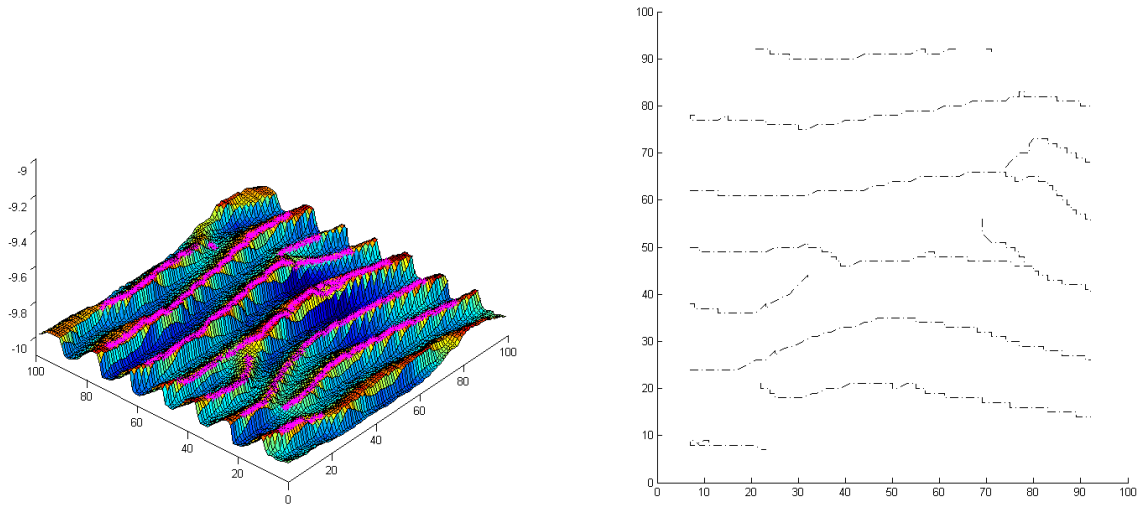


FIGURE 4-31: LEFT THE DIGITAL TERRAIN MODEL WITH THE VECTOR DETECTIONS (MAGENTA LINES) AND RIGHT THE ELEVEN CREST LINE VECTORS PLOTTED IN 2D.

4.2.6.4.3 PRACTICAL EXAMPLE

The practical example is a tile taken from a swath bathymetric map from a sand bank and has been specifically chosen to be ‘difficult to solve’ for the crest picking and vectorization algorithm. The difficulty lays in the varying directionalities of the sand wave pattern. The bathymetric image is shown in Figure 4-32.

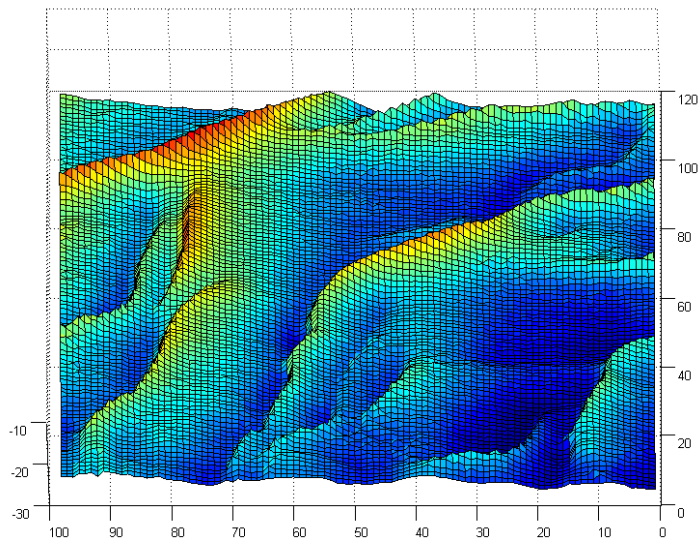


FIGURE 4-32: A PROCESSED SECTION OF A BATHYMETRY RASTER.

Detecting the crests and calculating the statistics gives Figure 4-33.

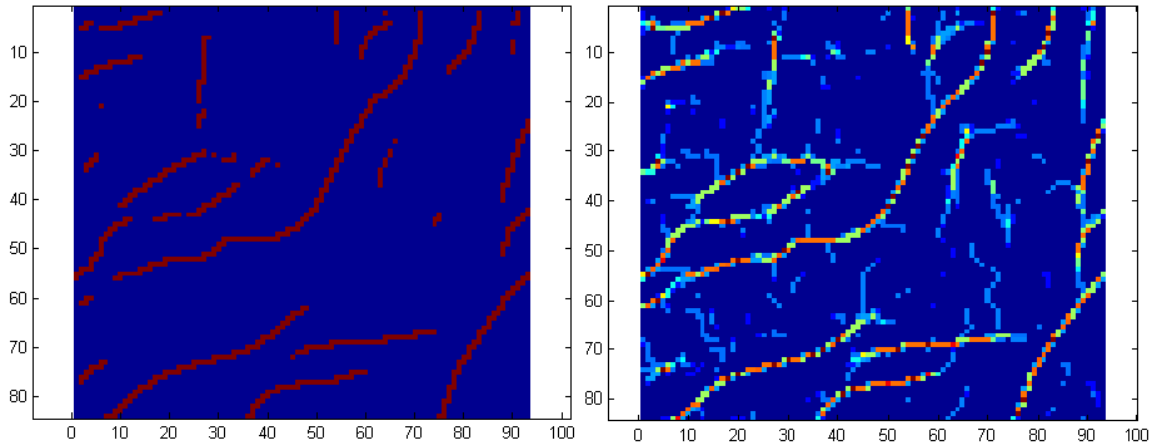


FIGURE 4-33: A DETECTION ALGORITHM AND THE STATISTICS MATRIX CALCULATED FROM THE OTHER DETECTION MATRICES

Deriving the vectors from Figure 4-33 gives Figure 4-34. Figure 4-34 displays the 22 vectors generated from the bathymetric map.

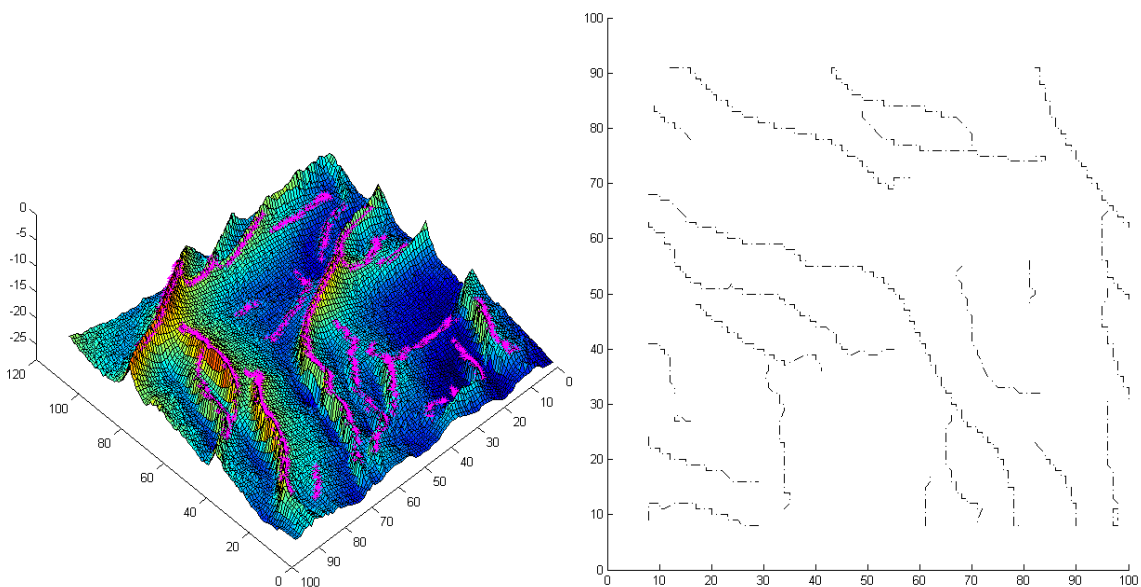


FIGURE 4-34: THE VECTORS DERIVED FROM THE CREST LINE MATRIX AND THE STATISTICS MATRIX

Also in the practical example the algorithm makes some minor mistakes. The number of mistakes in real bathymetric raster matrices is significantly lower than in the synthetic raster matrices used in the theory section. The reason for that is that errors are now not anymore related to a ripple generating algorithm that models a mathematical surface and the surface usually has been despiked and filtered. Difficult to filter systematic errors are no longer in the data. The algorithm proves to be better applicable on real data than on synthetic data. The algorithm currently only works on raster matrices without holes. For applications on complete real world datasets (swath bathymetry) the code will need some adaptations. An application has been made to deal with large raster matrices without holes based upon discretisation of the raster into smaller raster matrices.

4.2.6.4.4 CONCLUSIONS

- The algorithm to produce vectors from sand wave crests on both real and synthetic bathymetric maps performs best on real bathymetric maps.
- The resulting vectors are not a 100% perfect solution, but the solution is better and more accurate than hand picked solutions.
- Mixed and uniform directionalities are not problematic for the algorithm.
- The algorithm might be useful in GIS applications.
- This application demonstrates another useful application of modeled sand surfaces.

4.2.6.5 ROUGHNESS AND ACOUSTIC IMPEDANCES

Up to now only the bathymetric layer of the sand dynamic model has been used. Underwater acoustic modeling requires some more information about the seafloor in order to generate an acoustic response. The acoustic impedance is used to find out what portion of the energy is scattered around in the medium where the acoustic wave comes from and what portion of the energy is transmitted to the medium the acoustic wave was transmitted to. The acoustic impedance contrast at an interface is a function of the difference in velocity and density between two half spaces. In the case of sand volume the density and sound velocity are a function of the compaction of that volume. The compaction of a volume of sand however is not a random process as suggested in the BORIS_SSA model by introducing a random spread of acoustic impedances.

The sand dynamic model has an add-on that generates a non referenced and non calibrated impedance map. The impedance map is not referenced because it is a map of most probable internal compaction differences, the map has no absolute values and there is no scale on the minimum and maximum value of the map. Up till now, for modeling the values are made absolute and combined with the values of the underlying LOD structure. More research needs to be done on this topic in order to validate and calibrate the matrix. The generation of the impedance map is based upon the unique ability of the sand dynamic model to model a volume of sand and not just one sheet of sand. With every cycle in the calculation, the pressure on every grain induced by grains on top of it is calculated and recalculated to compaction through a function connecting existing compaction at that point combined with the pressure. Taking the pressure in the function instead of just the change in pressure induces also compaction in matrices, where nothing changes during a period of time, as happens in nature (subsidence). That compaction volume is stored until the next cycle and adapted again. Because sand is not elastic, the sand does not decompact, it only erodes. The final result is that the top layer of the volume or 3D matrix, as displayed in Figure 4-35, contains information about the relative difference in compaction or acoustic impedance. The compaction matrix given by the model is an index matrix. The indices refer to a compaction curve. Using this method gives a realistic acoustic impedance distribution, another dramatic improvement of the BORIS_SSA model.

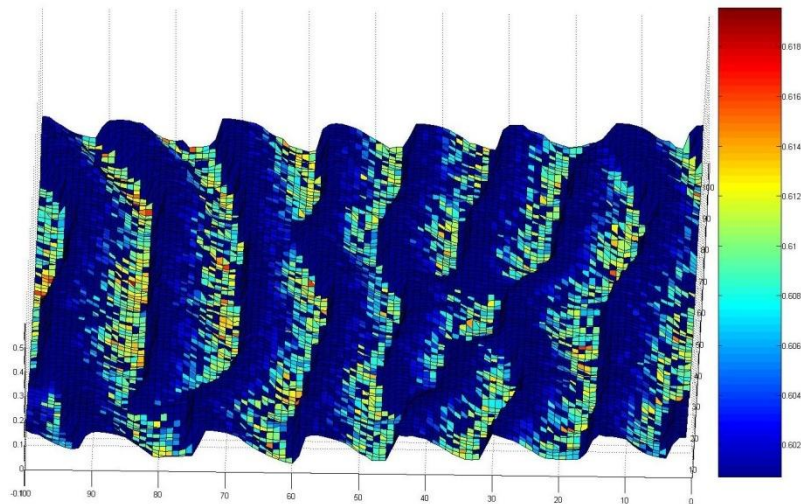


FIGURE 4-35: IMPEDANCE MAP PLOTTED ON TOP OF A TOPOGRAPHY TILE, THE HIGHEST IMPEDANCES CAN BE FOUND IN BETWEEN THE RIPPLES AND ON THE SIDE OF THE RIPPLES WHERE EROSION OCCURS.

Roughness has always been a point of misunderstanding between geologists and underwater acousticians. For underwater acousticians, roughness usually is a measure of surface variations in function of a frequency. Geologists sometimes abuse the term roughness as a direct link to grain size of sand. In this model, both can be adapted: grain sizes and the relative differences in height. The roughness acousticians usually refer to can be implemented in the LOD structure or can be implemented on smallest level or grain level of the model. The grain size distribution can be directly derived from the model itself. The model gives a dominant grain size per bin or raster point. Taking the neighbouring raster points into account gives an indication of the possible grain size spread. That spread function is then applied on the facet it applies to. The grain sizes themselves are implemented by giving more variation on relative positioning, while the scatter strength is calculated from the impedance. Other methods can easily be applied if necessary.

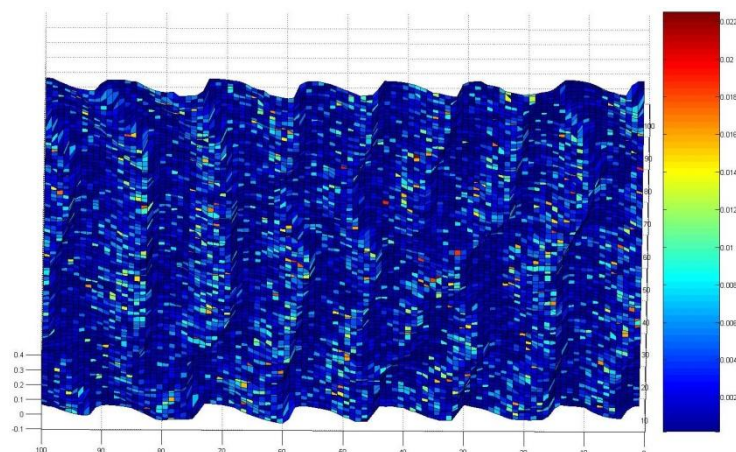


FIGURE 4-36: THE GRAIN SIZE DISTRIBUTION PLOTTED ON TOP OF THE BATHYMETRY TILE. THE DARKER HOMOGENEOUS REGIONS ARE LOCATED ON TOP OF THE CRESTS, WHILE THE PLACES WITH A HIGHER VARIATION IN GRAIN SIZES ARE LOCATED IN BETWEEN THE RIPPLE STRUCTURES. THIS PHENOMENON BECOMES MORE AND MORE APPARENT WITH DEVELOPMENT MATURITY OF THE SEAFLOOR (MORE CYCLES). ALSO SEE FIGURE 4-24 FOR A SIMILAR VERSION OF THIS FIGURE THAT HAS BEEN PROCESSED USING A 3X3 MOVING AVERAGE FILTER.

Splitting up the impedance and the grainsize and surface roughness enables a user to analyze the influences of impedance versus grainsize and surface roughness. It also enables to verify whether the black box models used in seafloor classification work correctly (by introducing acoustic data generated with these tiles as a feed).

4.2.6.6 MULTIPLE Z COORDINATES ON ONE XY COORDINATE

Allowing both raster topography and full 3D meshes makes the existence of a full 3D environment in the model possible. It is not possible to implement a full 3D option in the BORIS 3D SSA model, because it needs a raster as input. Meshes should be saved in a 3D matrix where each layer consists of three (x,y,z) coordinates. Mesh defined objects can have holes. The raster defined topography may never have holes. As in the raster topography, the roughness, grainsize and acoustic impedances are defined in the object model. The acoustic model calculates the acoustic impulse response from each object separately; this approach allows the possible introduction of more sophisticated acoustic models taking into account the internal structure of the object (Zampolli, Burnett et al. 2004). The external hull, defined with the mesh, is only used in the shadow calculations. More information about the 3D objects can be found in 4.2.5.3 Processing and building 3D objects.

4.2.7 Processing the environment: Refraction and ray tracing

After building the environment with a surface raster, embedded objects and submerged objects, it is time for some ray tracing and deformation of the environment. In a water column there is an acoustic velocity gradient. The acoustic velocity gradient is a function of the temperature gradient, salinity gradient and pressure gradient (Urick 1983). Acoustic velocity variations induce refraction of the acoustic waves. Ray bending can be calculated using Snell's law. Snell's law states that in a multilayered medium, which in each discrete layer has a constant velocity: c_1, c_2, c_3, \dots , and where an acoustic ray travels through the medium and hits each layer interface

with a grazing angle $\theta_1, \theta_2, \theta_3, \dots$ then $\frac{\cos \theta_1}{c_1} = \frac{\cos \theta_2}{c_2} = \frac{\cos \theta_3}{c_3} = \dots = \text{a constant for each ray.}$

Applying ray tracing to each vertex in the model gives information about the travel time of the bended ray from the source to the vertices and the exit angle from the source. An identical approach is taken for receivers. The model uses this information to project the environment in an iso-velocity environment (Figure 4-38). Practically that means that the sound velocity at the source is taken and used as the sound velocity for the complete environment. From that moment on all rays to any of the vertices are straight lines and are easy to put into an equation. These straight lines allow easy shadow calculations. The next step is re-projecting every vertex in that environment using the exit angle or a ray at the source or the incoming angle of a ray at the receiver. The `velblock.m` function generates the ray paths of source or receiver (Figure 4-37). These ray paths are in a later stadium used for interpolation. The spline interpolation appears to give a virtually exact solution in all regions where there are enough points to interpolate. Only at the very end (where the rays go horizontal) the interpolation deviates from the real value. Note that the rays do not refract up in this model.

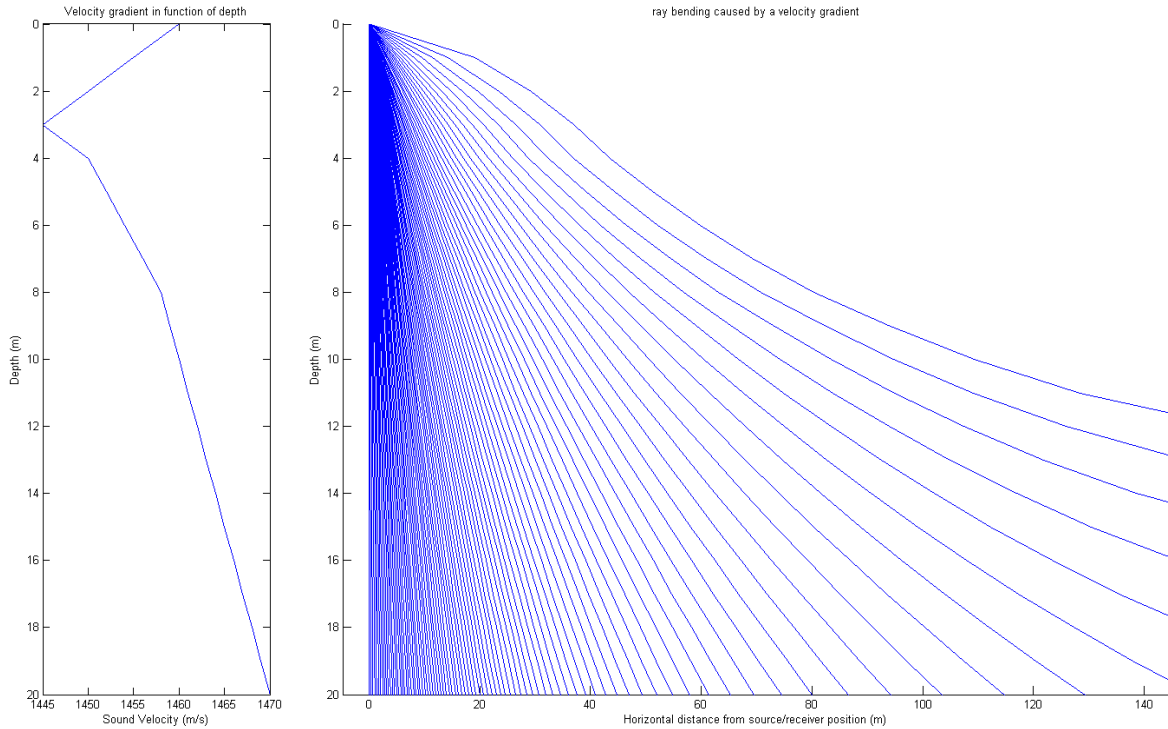


FIGURE 4-37: RAY BENDING IN A WATER COLUMN OF 20 METER CAUSED BY AN EXTREME ACOUSTIC VELOCITY GRADIENT. THE LEFT FIGURE DISPLAYS THE VELOCITY GRADIENT, THE RIGHT FIGURE DISPLAYS THE ACOUSTIC RAY PATHS THROUGH THE WATER COLUMN.

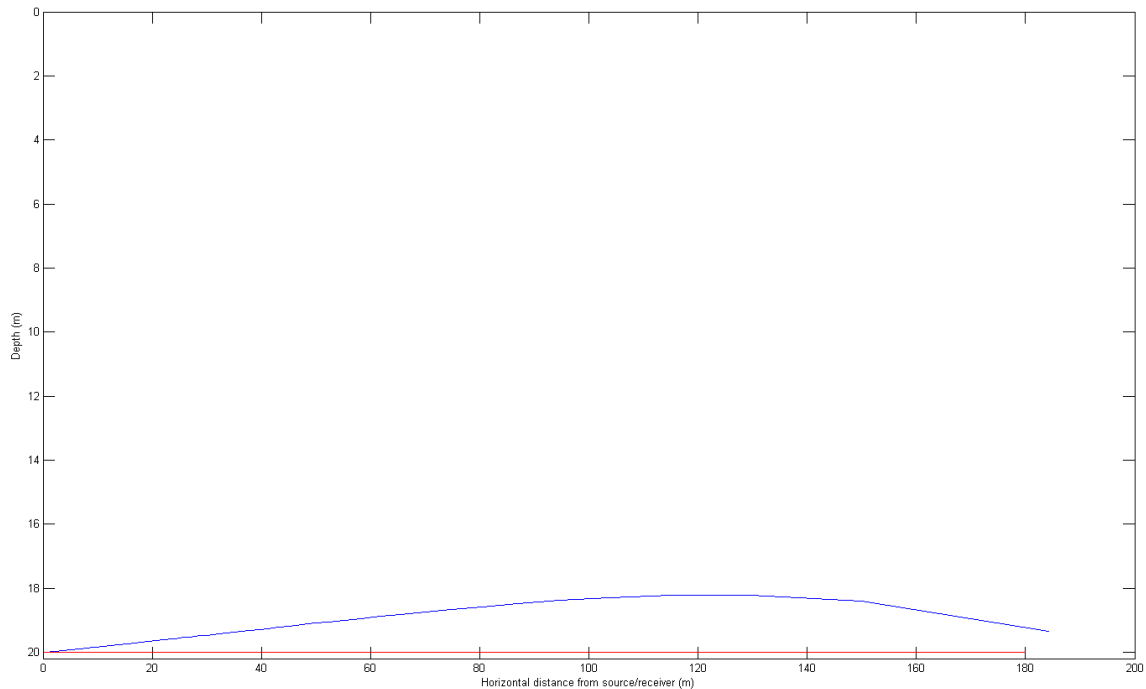


FIGURE 4-38: RELATIVE SURFACE DEFORMATION CAUSED BY THE RE-PROJECTING OF THE SURFACE IN AN ISO-VELOCITY MEDIUM. THE RED CURVE IS THE ORIGINAL SURFACE: A HORIZONTAL SURFACE AT 20 METRE OF FIGURE 4-37. AFTER PROJECTING THE ACOUSTIC TRAVEL DISTANCES IN A MEDIUM WITH A UNIFORM SOUND SPEED THE BLUE SURFACE APPEARS.

4.2.7.1 RAY TRACING VERTEX POINTS

After generating the velblock matrix, containing information about the ray paths in the water column, that matrix is used for interpolation. The `onewaytime.m` function provides the synthetic ray derived through a spline interpolation method from the velblock matrix. The `onewaytime.m` function also returns a matrix containing the information for the re-projection.

4.2.7.2 RAYTRACING FACETS

The facet ray tracing is only used in the shadow calculations. Basically the three vertices are traced. The ray traced facets are not used as backbone during the point scatterer ray tracing. Using the facet ray tracing results would, at first sight, dramatically increase the calculation time. The reason why the facet ray tracing is not used in the other modules is because these facets are considered as units and are not further discretized. A re-projected facet might not necessarily be a plane anymore (see Figure 4-38). When the facet appears not to be a plane anymore, interpolation of the point scatterers becomes a complex function to solve. So in order to approximate the new re-projected function, the facet should be further discretized. Further discretisation is not an option, so using the facets as a base plane to interpolate the point scatterers is not an option either. The approximation made by considering the facet as a flat plane has no significant influences on the shadow calculations.

4.2.7.3 RAY TRACING SCATTERERS

The scatter points are ray traced just as the vertex points are ray traced. This method is the most time consuming method in the whole model. Two different approaches are used throughout the model: a selective method and a brute force method. The first approach is that only the visible point scatterers are traced. In order to find the visible scatterers, the shadow matrix is combined with the scatterer matrix function. The second method is only used for the scatterers connected to the objects and does not consider shadows, it is a brute force method that ray traces the complete set of scatterers and meanwhile checks whether a facet blocks the ray or not. That facet can either be from the object itself or from the surface raster in case of embedded objects. Because of the complexity of some objects and the variable size of the facets (such as a tube), no better option was found.

4.2.7.4 RAY TRACING SHADOWS

The shadow calculation on the seafloor surface raster is an approximation. Every facet is subdivided into smaller facets. The vertices of these smaller facets are then ray traced as if they were point scatterers. When a facet has three invisible vertices, the whole facet is considered to be invisible. The key issue in this algorithm is to make enough subdivisions. Figure 4-39 demonstrates how the shadow changes with a changing sound velocity profile.

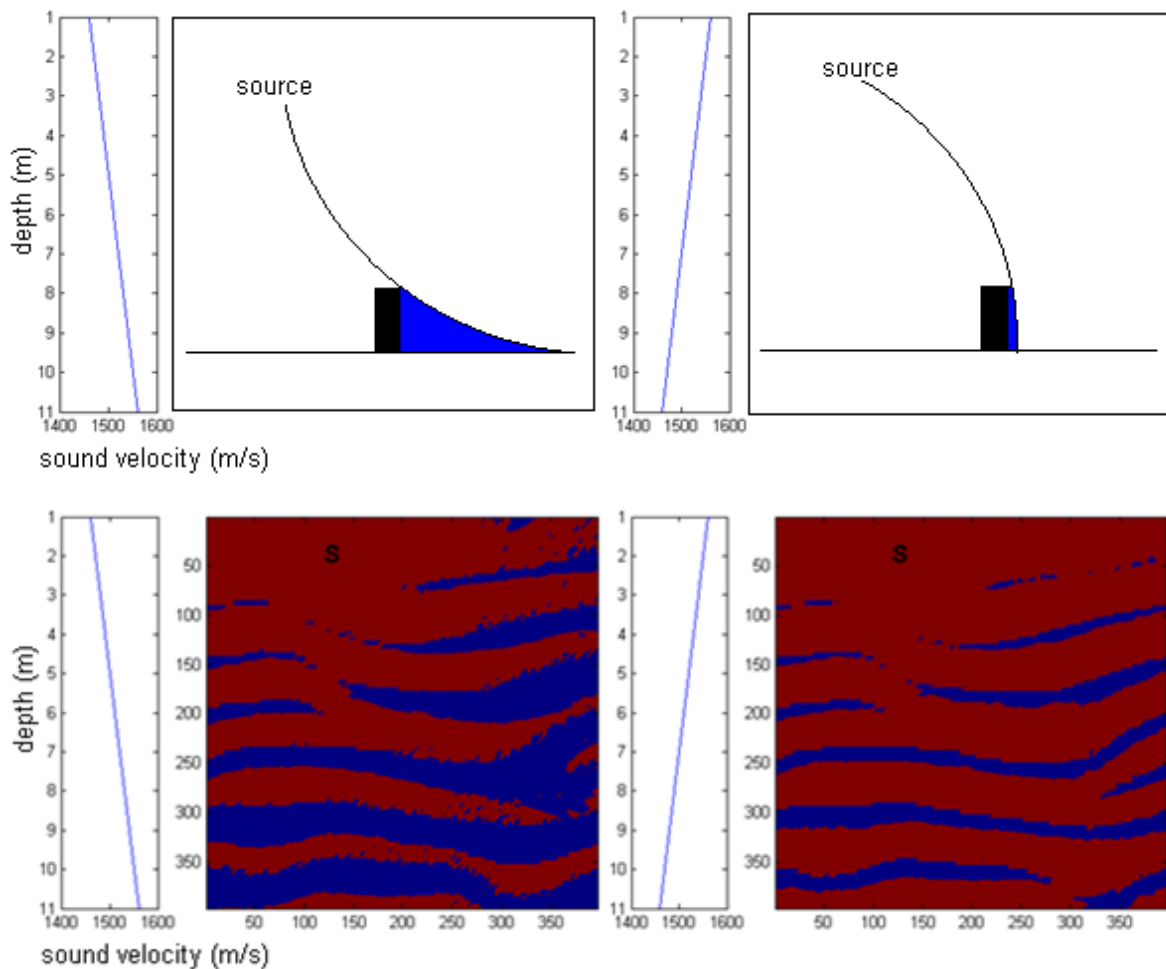


FIGURE 4-39: THE TOP TWO FIGURES DISPLAY THE PRINCIPLE OF RAY BENDING DUE TO A VELOCITY GRADIENT AND THE EFFECT ON THE SHADOW (BLUE). THE EQUIVALENT IN THE MODEL SAND DUNE FIELD IS A TRANSDUCER HELD APPROXIMATELY 10 METER ABOVE A SAND DUNE FIELD. LEFT THE WATER COLUMN HAS AN INCREASING LINEAR SOUND VELOCITY GRADIENT AND RIGHT WITH A LINEAR DECREASING SOUND VELOCITY GRADIENT. THE RESULTING SHADOW CALCULATION IS DISPLAYED (SHADOW = BLUE).

4.2.7.5 RETRIANGULATION AND EDGE EQUATIONS

A triangle collapse algorithm was tested (Hamann 1994; Gieng, Hamann et al. 1998) to reduce the amount of shadow data. The approach was implemented but later disbanded because of lack of time to adapt other methods. It might have some potential in calculation time reduction and reducing memory consumption.

The algorithm to define the visibility of a vertex works very simply: the function of a line is generated, with as input coordinates the position of the source/receiver and the vertex itself. This can be done because the environment can be considered as having no sound velocity gradient anymore. That line is then combined with a selection of facets that intersect the line using the edge equations, the distance to the vertex is compared with the distance to the intersection. When the distance to any intersection is smaller than the distance to the vertex, then the vertex is invisible. In order to reduce the calculation time, the edge equation is only

applied on a selection of facets made by some conditional statements using spherical coordinates.

4.2.7.6 TILING OF THE SHADOW RASTERS

Since the bathymetry is tiled up, also the shadow rasters are tiled up. Tiling up the shadow matrices has a small drawback in the algorithm of the shadow calculations: a boundary effect. That boundary effect can be seen in Figure 4-40. Because the tiles contain the same vertices at the boundary but these vertices have different indices the vertices become virtually invisible. Two solutions are possible: 1) coupling the identical vertices and the related non identical facets or 2) solving the problem afterwards with a fast algorithm. The last option was chosen because it appeared to be the most efficient one to implement.

4.2.8 Monostatic and multistatic approach

A monostatic set-up has both the receiver and the send array on the same position but not necessarily with the same beam pattern. An example could be a side scan sonar. A bistatic approach has send and receive array on two different positions. A multibeam echo sounder has both receive and send array close to each other but has a bistatic property in this model.

An interesting feature visualized on Figure 4-40 is the decrease of surface component with a bistatic set-up. When a well chosen bistatic set-up is used, the surface component in the acoustic signal might even be reduced to zero, at that moment the signal contains only volume component. This might be important in buried object detection.

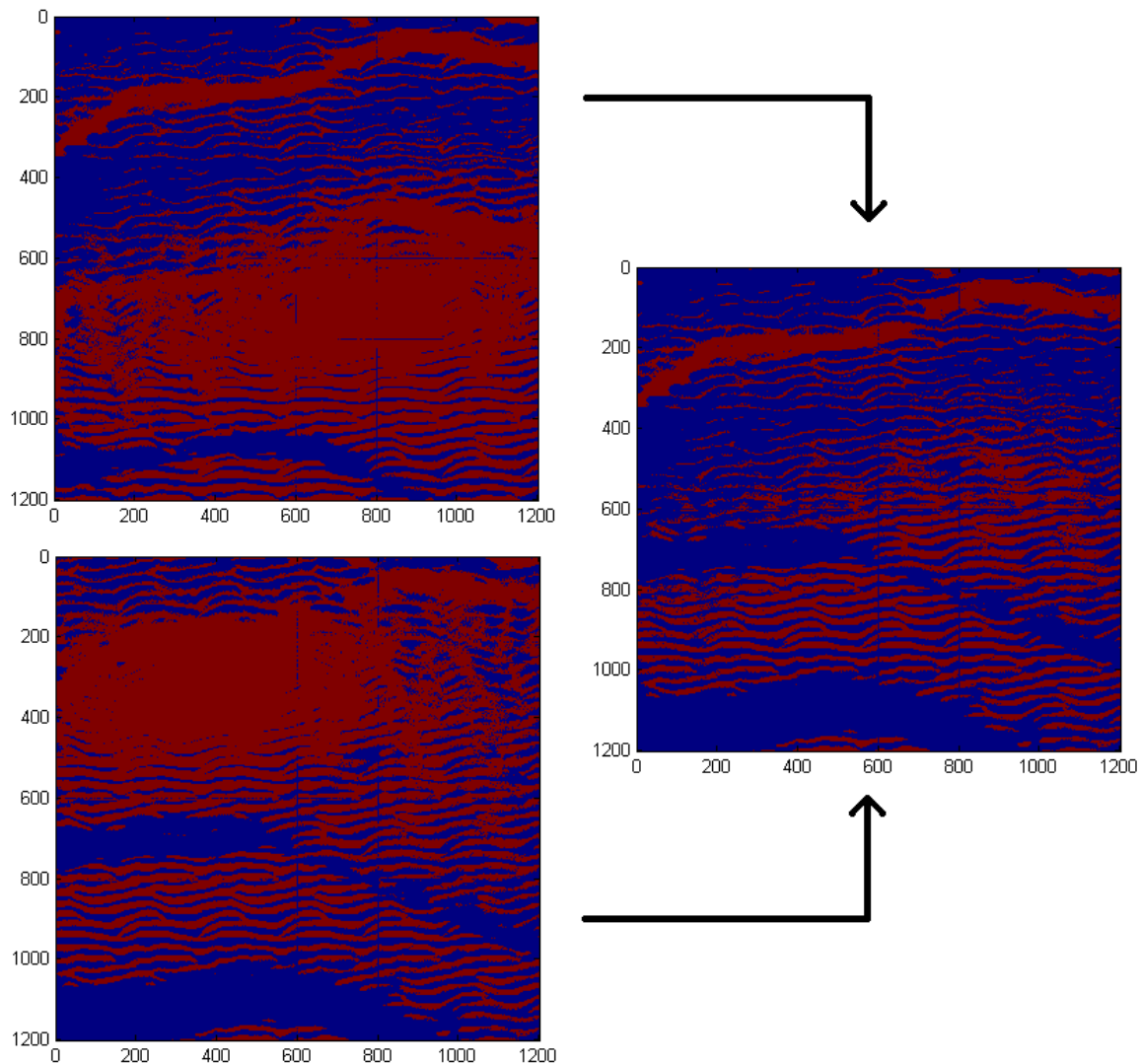


FIGURE 4-40: A MULTISTATIC APPROACH IS A COMBINATION OF BISTATIC APPROACHES. AND EVERY BISTATIC SET-UP IS A COMBINATION OF TWO MONOSTATIC APPROACHES. MULTIPLYING BOTH MONOSTATIC MATRICES (LEFT) GIVES THE BISTATIC MATRIX (RIGHT). SHADOW IS EQUAL TO ZERO, WHILE VISIBLE IS EQUAL TO ONE. NOW INTRODUCING BEAM PATTERNS ENABLES FAST CALCULATION OF THE ACOUSTIC RESPONSE.

4.2.9 Acoustic response and impulse response

Usually, in underwater acoustic and seismic modeling, the impulse response is calculated and then convolved with the source signal. This approach is one of the fundamental laws in reflection seismic modeling and inversion (Webster 1978; Yilmaz 2001) and is applied as such in almost every acoustic model. That approach can be applied with narrow band signals but not with sweeps and other broadband signals. The complexity of a real broadband wave field is often neglected in acoustic models. Therefore, in this model, the impulse response contains not only amplitude information but also angular information needed for ray tracing. As such the real wavelet sent to a specific point scatterer can be convolved. This process is described in '4.2.5.2.2 Point scattering model'. The chapter '1.7 A special case: chirp' demonstrated that processing broadband sources applying standard laws might be incorrect. Extra care was taken about acoustic source/receive patterns in this models' functionalities.

The resulting acoustic signal or trace S is calculated in a similar way as the model presented in the second chapter (French 1974). The distance from the source to a point scatterer and back to the receiver is measured after ray tracing, also the angles related to the in- and outgoing ray are stored to select the correct source signal or beam pattern attenuation and receiver pattern. This information is stored in a matrix R . The functions f_s and f_r describe the send and receive array in function of their position, dimensions, rotations, used frequency and phase spectrum, angle of incidence and a phase correction because of the discreteness of the signal. The f_s and f_r matrix will usually be implemented as a lookup table. It is to the modeler to make and feed the correct function of the source and receive arrays. The $TL(\omega)[R]$ or transmission loss array can be calculated in many ways (Kinsler, Frey et al. 1982; Urick 1982; Urick 1983; Yilmaz 2001; Katsnelson, Petnikov et al. 2002; Etter 2003) and includes the spreading and attenuation of the signal. The acoustic impedance per point scatterer is stored in the matrix S_s

$$S = f_s * f_r * TL(\omega)R * S_s$$

Transmission loss is usually applied on the impulse response matrix of the environment after which the impulse response is convolved with the source signal (Webster 1978). But often very important is the transmission loss in function of the frequency. Some models, mainly in the field of anti submarine warfare (ASW) correct for that (Marsh and Schulkin 1962; Rogers 1981; Jensen, Kuperman et al. 2000). Because of this frequency dependency which cannot be applied on the impulse response and not on the convolved acoustic signal, the transmission loss function should have a unique position in the acoustic model between the impulse response and the convolution. In fact it is the convolution algorithm that should be adapted. Although the importance of the frequency dependency is recognized, it has not yet been implemented in this model. A brief overview on available transmission loss functions is given in Etter 2003 and Jensen, Kuperman et al. 2000.

4.2.10 Discretisation of send and receive array versus array functions

The discreteness of a beam pattern and wavelets always introduces errors. The discreteness of the transducer arrays does not necessarily introduce similar errors. On the contrary, approaching the transducer as a discrete 2D array enables the modeler to come closer to reality. Consider the crystals or piezoelectric materials of a transducer so small compared to the wavelength they transmit or receive and they can be seen as point scatterers or point receivers with an omni directional beam pattern and a continuous wavelet. Putting these point scatterers in an array will introduce a beam pattern. That beam pattern can be described in continuous mathematics as has been demonstrated before but also introducing the change in wavelets in function of angle of incidence I was not able to do. At the end, when the source transmits or the receiver receives a sweep of frequencies and not just a narrow band it is not the beam pattern that is important, but it is the transmitted or received wavelet. Efforts have been done to combine both systems of discrete and continuous description of the wavelet properties but have been unsuccessful. In the model it is up to the user to decide what type of approach to use: either the user works with a narrow band signal and the source and receiver beam pattern can be described with a beam pattern and a sine burst that has its amplitude defined by the beam pattern or the user uses a broad or broader band signal where the beam pattern cannot be considered as being continuous throughout the transmission or reception and then the discrete

approach is the only option. In practice high frequency transducers such as side scan sonar transducers can be considered as very narrow band transducers.

All regular transducers, that includes the transducers described as a discrete array of point scatterers but no longer than a standard side scan sonar array, can be considered as short enough to use the same shadow matrix. In other words; they can be reduced to one single point scatterer with a beam pattern. A good rule of thumb is not to take an array longer than five times the shortest facet side length. When the array appears to be longer, it should be split up in two or more parts and the shadow matrix should be calculated for every respective part. That principle generates an array of two or more point scatterers with a certain beam pattern, that can be combined in the final result. Recalculating the shadow matrix for every single increment of the array would make the model impossible to use.

The best thing to do is to define your own source and receive functions and give the model what it needs during de construction of the signal.

4.2.11 Practical modeling workflow

An environment with three ripple fields and a bistatic test setup has been entered in the model, where source and receiver are both stationed 10 meter above the seafloor and have a horizontal distance from each other of 14 meter. The shadow matrix displays the environment and objects (Figure 4-41). There is a velocity gradient and three objects. Both source and receiver have a spherical beam pattern and the resulting signal is displayed in Figure 4-42. The complete modeling flow can be found in the software book. The flowchart is given in Figure 4-43. Shadow calculations are an important part in it and are split in three units: objects, receive array and send array. After calculating the shadows, the point scatterers are generated with fed pseudorandom algorithms. After generating the scatter positions, they are ray traced from both the send and receive array after which the beam patterns and wavelets can be applied and the resulting signal is generated.

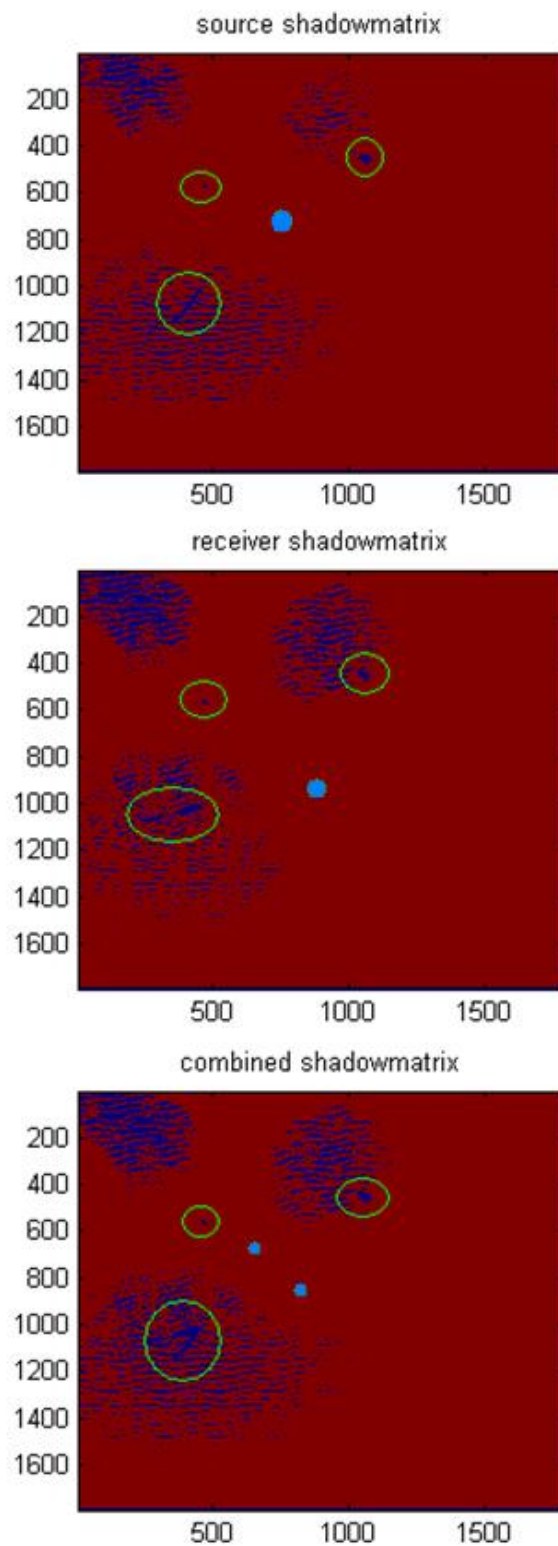


FIGURE 4-41: SHADOW MATRICES AND COMBINATION OF BOTH RECEIVER AND SOURCE MATRIX. THE GREEN AND BLUE DOTS ARE THE RECEIVER AND SEND ARRAY. THE GREEN CIRCLES ARE THREE OBJECTS INTRODUCED IN THE MODEL.

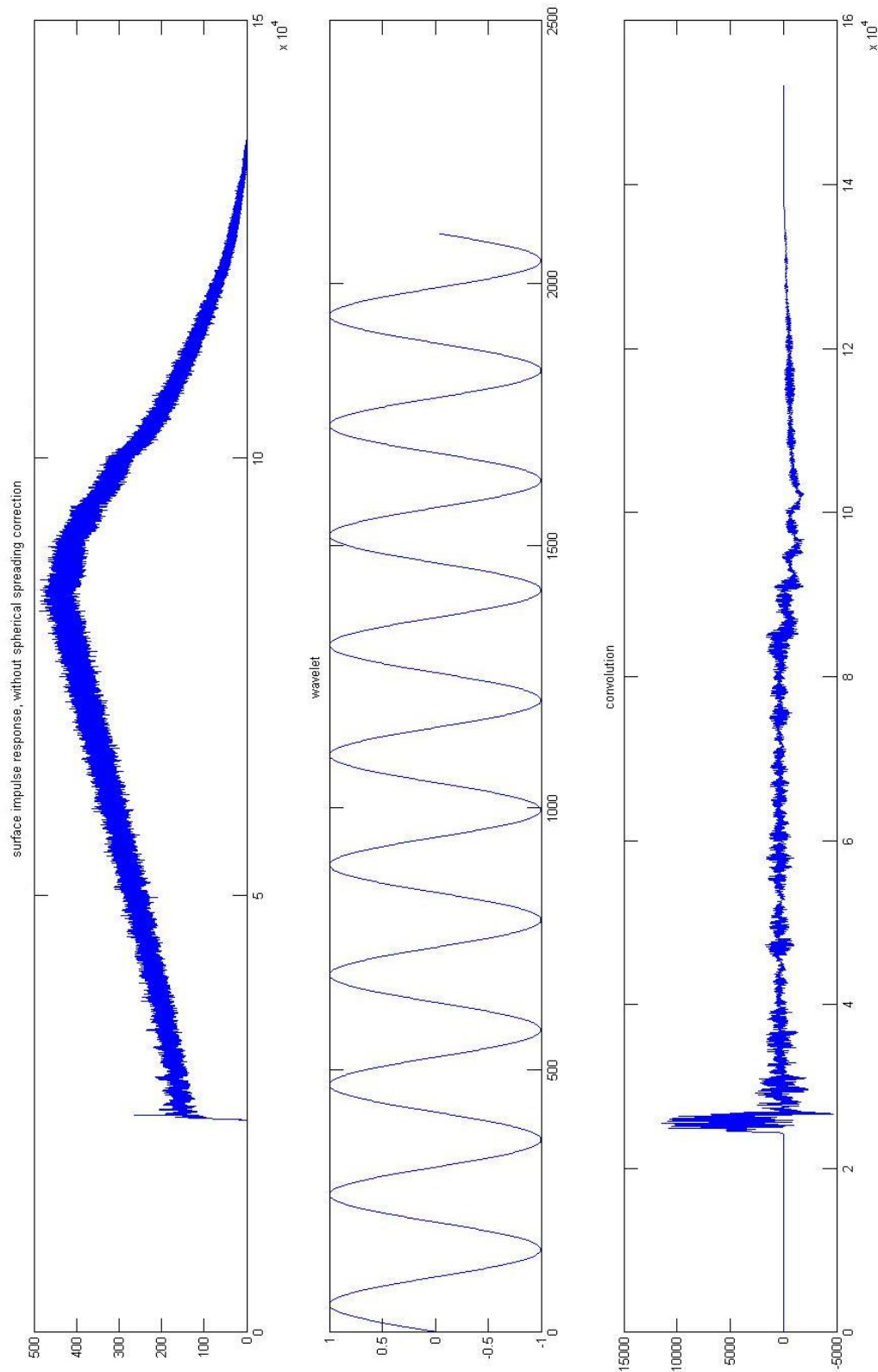


FIGURE 4-42: THE FINAL RESULT OF A MODELING CYCLE. THE TOP FIGURE IS THE IMPULSE RESPONSE OF THE ENVIRONMENT, THE CENTRE FIGURE IS A BURST USED IN THE CONVOLUTION (CONVOLUTION HAS BEEN TAKEN TO SIMPLIFY THE CALCULATION, NOTE THAT HERE ANY KIND OF ALGORITHM CAN BE USED.). THE BOTTOM FIGURE SHOWS THE RESULT OF A BISTATIC ACOUSTIC TEST, WHERE BOTH SOURCE AND RECEIVER HAVE A SPHERICAL POWER PATTERN.

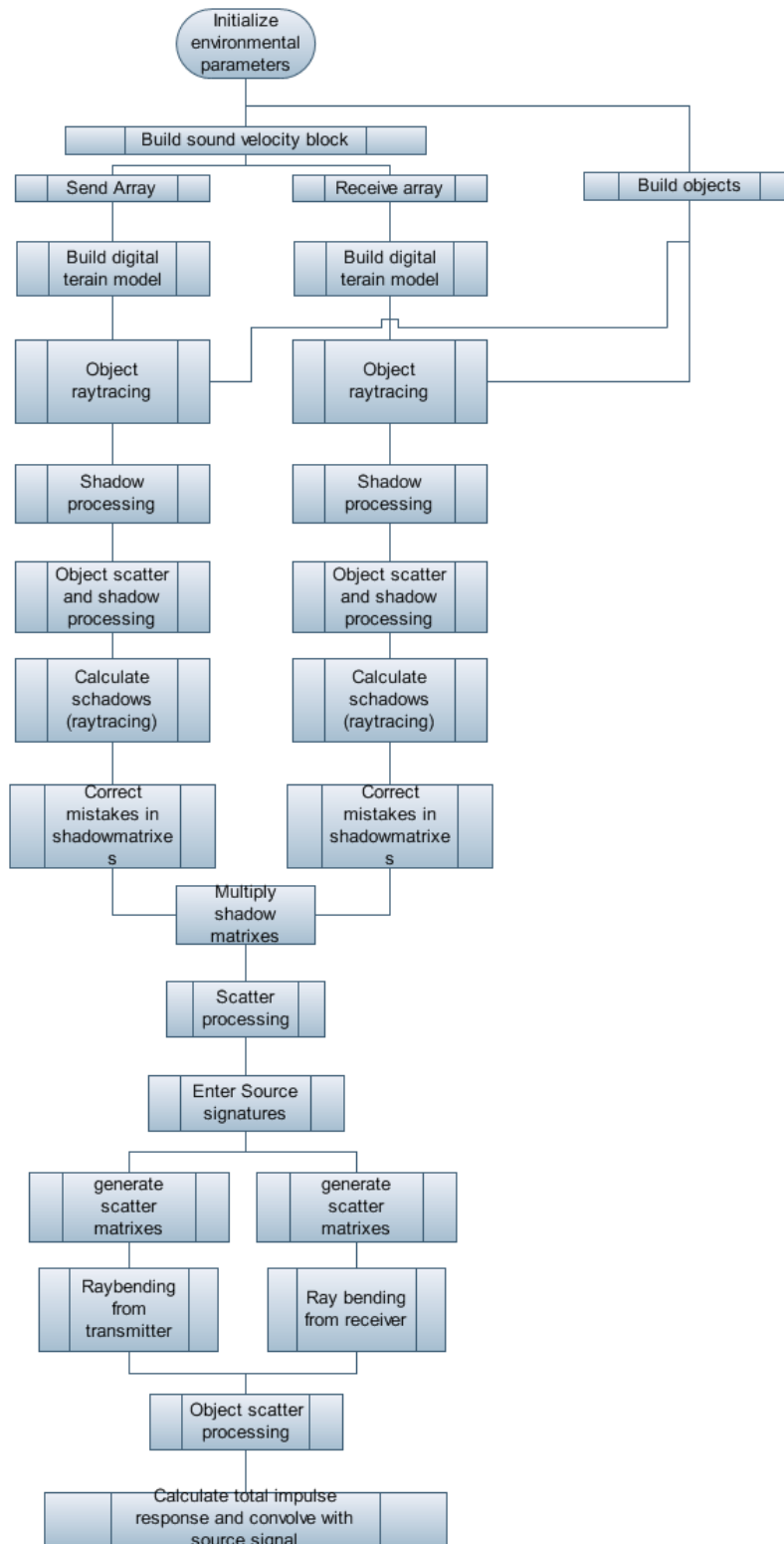


FIGURE 4-43: FLOWCHART OF THE COMPLETE MODELING FLOW. SHADOW CALCULATIONS ARE AN IMPORTANT PART IN IT AND ARE SPLIT UP IN THREE UNITS: OBJECTS, RECEIVE AND SEND ARRAY. AFTER CALCULATING THE SHADOWS, THE POINT SCATTERERS ARE GENERATED WITH FED PSEUDORANDOM ALGORITHMS. AFTER GENERATING THE SCATTER POSITIONS, THEY ARE RAY TRACED FROM BOTH THE SEND AND RECEIVE ARRAY AFTER WHICH THE BEAM PATTERNS AND WAVELETS CAN BE APPLIED

4.2.12 Conclusions

- The proposed model is slow but exact. Solving the model on a cluster of computers is a necessity.
- The model has been designed to run on a cluster of computers.
- The exactness of the model enables the use of the truly produced signals in signal processing algorithms
- The proposed model solves problems encountered in other 3D models, more specifically it changes:
 - Unrealistic environments by a LOD system bump mapped with bathymetry tiles and a grain and impedance matrix draped over.
 - Pseudo 3D environments by full 3D environments composed of a seafloor and objects. Objects can be part of the seafloor.
 - Uniform velocity in the water column by ray tracing.
 - Absence of shadows by using the ray tracing for shadow calculations.
 - Absence of impedance differences by introducing impedance differences.
 - No control over geologic roughness by introducing sand grain matrices at the level of sand grains.
 - Beam patterns only valid for narrow band systems by enabling the possibility to introduce wavelet patterns.

5 CONCLUSIONS AND OUTLOOK

Detailed conclusions can be found back at the end of every chapter. This chapter summarizes the most dominant lines in those conclusions.

5.1 OVERALL CONCLUSIONS

One of the most remarkable but not new overall conclusions is: 'Size does not matter.' An object can have a radius of a couple of centimeters and be visible on several pixels on a sonar image with a half a meter grid while other objects with meter range sizes are completely invisible. The direct visibility of an object or section of an object does not depend upon size, it depends upon three parameters: impedance differences, roughness and the presence of straight angles or acoustic retro reflectors. Size does matter in indirect visibility or shadow detection.

The 'size does not matter' observation accounts for underwater acoustics and detection of objects in the water column. But it accounts even more in the field of bottom penetrating sonars for the detection of buried objects. In buried object detection the signal to noise level is much lower, the source/receiver beam patterns are larger because of the low frequencies used and the reverberation and wave fronts are never fully migrated on a migrated image. These three problems are the origin of the absence of shadows for small objects on bottom penetrating images. Shadows can be observed on both migrated and non migrated low frequency acoustic images when for example shallow gas layers occur, but these are hundreds or thousands of times larger in size than a mine-like object and the acoustic impedance and roughness is much higher.

5.2 FIELD TESTS

Field tests were performed and acoustic instruments were tested in almost the full acoustic frequency band (0.5 kHz to 1.8 MHz). Most of the tests were done under fully controlled conditions. Observations done on experimental data are confirmed by observations done on modeled data. The connection between models and reality has been a very important issue throughout this research. The connection between models and reality has not been kept at the level of comparing db's but the parallel research has been done up till the level of signal analysis and signal processing.

5.2.1 Low frequency bottom penetrating tests (<15 kHz)

Two fundamentally different systems were used: linear acoustic systems and a non-linear acoustic system. The linear acoustic systems were: sparkers, a boomer, a chirp and a pinger. The non linear acoustic system was an Innomar parametric sonar.

Sparkers and boomers have a minimum phase broadband wavelet, while a pinger has a mixed phase 'narrowband' wavelet, and chirp has a broadband wavelet with a controlled phase. All three sources have a very big average main lobe. Proud object detection on raw images is possible with a boomer. Sparkers proved to be too low in frequency. With the pinger there were electronics problems. The chirp has not been specifically tested on object detection but is

probably not useful because processing of a chirp image might be much more complex than previously thought. If detection of a buried object would be possible with these systems, than it would certainly be after migrating the data. Migrating the experimental data proved to be impossible, the degradation of the image caused by the migration algorithm could be traced back to positioning inaccuracies and spatial aliasing. That migration with exact knowledge of the position and more traces in the spatial domain might enhance the image has been demonstrated by synthetic aperture sonar experiments on a rail.

Detecting a buried object using a parametric echo sounder has been demonstrated already a couple of times. The parametric field is only active in a very narrow beam or the main lobe of the two primary frequencies used. Every time the capacity of the sonar is demonstrated also the inapplicability of the system is demonstrated. The search time appears to be extremely high due to small footprint of the sonar and the platform carrying the sonar has to have an extreme stability and position accuracy.

Basically all the observations point in the same direction: the acoustic image has to be focused, that focusing can be done by the hardware (non-linear acoustics) or can be done by software (migration). Up till now, because of positioning accuracy problems, no software algorithm can migrate properly sonar images where other movements than translation happened. The tests leave the question on how accurate the positioning has to be open. Modeling will be used to put numbers on the accuracy question.

5.2.2 High frequency underwater acoustic tests (>15 kHz)

In high frequency acoustic processing, the received signal is seen as an AM signal. AM processing (enveloping) mirrors the transmitted high frequencies back into a very low frequency band. Because narrow band high frequency sonars are much more controllable in terms of beam pattern and transmitted wavelet, they were used to investigate the effects of beam pattern and platform stability on scatter properties. Also the causes of scatter have been thoroughly investigated

Platform stability is a key issue in underwater acoustic imaging. The tests demonstrated that an inferior side-scan sonar mounted on a more stable self-swimmng platform images better than a superior side-scan sonar mounted on a towed platform.

Because of beam pattern properties, rolling platforms cause severe image degradation. Rolling should be avoided at any cost.

A beam pattern with side lobes has to be avoided. Multipath of vertically oriented side lobes degrade the image. These multipath echoes are visible as bright lines in the acoustic data. These lines can be removed by processing but the data superimposed on it and later clipped by the electronics can never be restored, leaving a blind line of approximately one to two meters on the image.

The directionality properties of scatter have been clearly demonstrated by imaging an object from over ten different angles of incidence.

The imaging of a rough mine and a much bigger and much less visible fully cylindrical mine have demonstrated the effect of roughness on the acoustic image.

Tests with an acoustic retro reflector demonstrate that the side lobes of a side-scan sonar contribute significantly to the acoustic image.

The effect high impedance differences of for example gas bubbles and swim bladders of fishes on acoustic images have been demonstrated many times already by fish finding sonars (Naudts, Greinert et al. 2006). The results of these investigations were not discussed in this thesis.

5.3 THE MODELS

All models used proved their usefulness. One of the largest problems in the current acoustic models is the beam pattern. Beam patterns are based upon, and can only be introduced in narrow band systems. Broadband systems such as chirps and minimum phase explosion and implosion sources need wavelet patterns instead of beam patterns in the model.

Wavenumber integration models such as the BORIS 3D SSA model proved to be too rigid to do signal processing on the produced signals. Simple signal analysis is possible on the produced signals.

Point scatterer models proved to be the most flexible models to use and signal analysis-processing is possible. A very extreme edition, solving a whole set of problems including failing of previous and other models to deal with shadowing, wavelet pattern, ray bending, micro roughness, complete 3D and 4D environments and many more has been made and presented in this thesis. The model is currently able to deal with roughness and acoustic impedance in a realistic synthetic environment. Only multipath is not yet solved but can easily be solved.

Acoustic modeling is a necessary tool in acoustic image processing and building signal processing algorithms.

5.4 MIGRATION

Migration is a method used to focus an acoustic image. The method works fine on industrial seismic images, the application of these methods on much higher frequency images requires a full up-scaling of all requirements to those higher frequency levels.

Theoretical tests were performed to see how dense the spatial density of the acoustic signals should be. The spatial density varies linearly with the frequency used. One fourth of the wavelength used is a good rule of thumb.

Modeling indicated that a relative sub centimeter error on positioning is required to focus a 3.5 kHz image properly. That relative positioning can never be achieved with a combination of RTK and motion sensor. Signal processing is necessary to achieve that accuracy.

Knowing the size and dimensions of real world transducers, it is still a mystery how a real world system will ever be positioned on such accuracy.

5.5 OUTLOOK

The final model presented in this thesis might be a good tool to do further developments in the signal processing algorithms. It is clear that using real data to build signal processing algorithms is not always the good approach, since there are too many uncertainties on positioning. Having a model where all environmental settings are adjustable, realistic and known will increase the understanding of complex acoustic problems and might open opportunities in the field of signal processing.

The sediment dynamic model demonstrated might have an independent future in sedimentology. The model appears to be one of the most complete models available today. Tests with wave dynamics were successful, tests with barchan dunes were successful, tests with objects appeared to be promising but should be done with good hydrodynamic input.

6 REFERENCES

- Abelev, A. V., P. J. Valent, et al. (2003). Evaluation and quantification of randomness in free-fall trajectories of instrumented cylinders.
- Anderson, R. S. and K. L. Bunas (1993). "Grain-Size Segregation and Stratigraphy in Aeolian Ripples Modeled with a Cellular-Automaton." Nature **365**(6448): 740-743.
- Baccaert, J. and C. Baeteman (1980). Boring kb5d11w-B248. Brugge (Lissewege+Zeebrugge), Belgische Geologische Dienst: 3.
- Bartberger, C. L. (1985). The NADC bistatic active sonar model, Nav. Air. Devel. Ctr.
- Bellettini, A. and M. A. Pinto (2002). "Theoretical accuracy of synthetic aperture sonar micronavigation using a displaced phase-center antenna." Ieee Journal of Oceanic Engineering **27**(4): 780-789.
- Bergem, O., E. Pouliquen, et al. (1999). "Time evolution modeling of seafloor scatter. II. Numerical and experimental evaluation." J. Acoust. Soc. Am. **105**: 3142-3150.
- Best, A. I., D. J. Tuffin, et al. (2004). Acoustical behaviour of gas-bearing marine sediments. ECUA 2004, Delft.
- Beyer, R. T. (1960). "Parameter of Nonlinearity in Fluids." Journal of the Acoustical Society of America **32**(6): 719-721.
- Beyer, R. T. (1997). Nonlinear acoustics. Woodbury, NY, Acoustical Society of America.
- Bishop, G. C., W. T. Ellison, et al. (1987). "A Simulation-Model for High-Frequency under-Ice Reverberation." Journal of the Acoustical Society of America **82**(1): 275-286.
- Bjorno, L. (1977). "Parametric acoustic arrays." Proceedings of the NATO Advanced Study Institute of Signal Processing | Proceedings of the NATO Advanced Study Institute of Signal Processing: 33-59 | xxvi+400.
- Bjorno, L., J. Folsberg, et al. (1979). "Parametric Arrays in Shallow-Water." Journal De Physique **41**: 71-82.
- Blair, D. G. (2006). "Underwater acoustic imaging: image due to a specular reflector in the geometrical-acoustics limit." Journal of Marine Science and Technology **11**(2): 123-130.
- Blondel, P., N. G. Pace, et al. (2007). Buried Waste in the Seabed - Acoustic Imaging and Bio-toxicity (Results from the European SITAR project) Springer-Praxis.
- Blondel, P., C. Sotin, et al. (1992). "Adaptive Filtering and Structure-Tracking for Statistical-Analysis of Geological Features in Radar Images." Computers & Geosciences **18**(9): 1169-1184.
- Bloomenthal, J. (1985). "Modeling the mighty maple." Computer Graphics **19**(3): 305-311.
- Bruce, M. P. (1992). "A Processing Requirement and Resolution Capability Comparison of Side-scan and Synthetic-Aperture Sonars." IEEE Journal of oceanic engineering **17**(1): 12.

- Bucker, H. P. (1986). "Use of SALT tables for rapid calculation of sound angle, level and travel time." J. Acoust. Soc. Amer. **80**(suppl.1, S63 (abstract)).
- Bull, J. M., M. Gutowski, et al. (2005). "Design of a 3D Chirp sub-bottom imaging system." Marine Geophysical Researches **26**(2-4): 157-169.
- Burdic, W. S. (1991). Underwater acoustic system analysis, Second Edition, Prentice Hall.
- Burns, W. R. (1968). "A Statistically Optimized Deconvolution." Geophysics **33**(2): 255-&.
- Burrough, P. A. and R. A. McDonnell (1998). "Principles of Geographical Information Systems (Spatial Information Systems)." OXFORD UNIVERSITY PRESS.
- Canepa, G., O. Bergem, et al. (1997). The implementation of Boris-3D: Bottom response from inhomogeneities and surface version 1.0. Saclantcen special report: 147.
- Caruthers, J. W. and J. C. Novarini (1993). "Modeling Bistatic Bottom Scattering Strength Including a Forward Scatter Lobe." Ieee Journal of Oceanic Engineering **18**(2): 100-107.
- Chamberlain, S. G. and J. C. Galli (1983). "A Model for Numerical-Simulation of Nonstationary Sonar Reverberation Using Linear Spectral Prediction." Ieee Journal of Oceanic Engineering **8**(1): 21-36.
- Chun, J. H. and C. A. Jacewitz (1981). "Fundamentals of Frequency-Domain Migration." Geophysics **46**(5): 717-733.
- Clark, J. H. (1976). "Hierarchical Geometric Models for Visible Surface Algorithms." Communications of the Acm **19**(10): 547-554.
- Clarke, J. H., C. de Moustier, et al. (2005). Coastal Multibeam Sonar Training Course
- Cohen, L. (1995). Time-frequency analysis. Upper Saddle River, Prentice Hall.
- Cohen, M. F. and D. P. Greenberg (1985). "The hemi-cube: a radiosity solution for complex environments." Computer Graphics **19**(3): 31-40.
- Cooke, T. (2003). Scatterer labelling estimation for 3D model reconstruction from an ISAR image sequence. Proceedings of the International Conference on Radar. Adelaide, SA, Australia: 315-320.
- Dawson, G. P., B. Johns, et al. (1983). A numerical model of shallow-water flow over topography. Physical Oceanography of Coastal and Shelf Seas. B. Johns. Amsterdam, Elsevier.
- De Haemer, M. J. and M. J. Zyda (1991). "Simplifications of objects rendered by polygonal approximations." Computer & Graphics **15**(2): 175-184.
- Desharnais, F. and D. D. Ellis (1997). "Data-model comparisons of reverberation at three shallow-water sites." Ieee Journal of Oceanic Engineering **22**(2): 309-316.
- Dillabaugh, C. R., K. O. Niemann, et al. (2002). "Semi-automated extraction of rivers from digital imagery." Geoinformatica **6**(3): 263-284.

Dix, J. (2006). "Seismic Unix."

Duchaineau, M., M. Wolinsky, et al. (1997). ROAMing terrain: Real-time Optimally Adapting Meshes.

Ebbing, J. H. and C. Labban (1996). Geological history of the area off Walcheren and Zeewo-Vlaanderen (southwestern Netherlands), since the start of the Eemian, Mededelingen Rijks Geologische Dienst

Eker, S. M. and J. V. Tucker (1989). Tools for the formal development of rasterisation algorithms.

Etter, P. C. (2003). Underwater Acoustics Modelling and Simulation: Principles, Techniques and Applications, Spon Press.

Evans, I. S. (1980). "An integrated system of terrain analysis and slope mapping." Zeitschrift für Geomorphologic(36): 274-295.

Fawcett, J. A. (1998). Summary of object/waveguide scattering modelling at saclantcen. sacantcen report. La Spezia, Saclant undersea research centre: 66.

Fioravanti, S., M. Magueur, et al. (1997). A parametric synthetic aperture sonar for detection of proud and buried mines. sacantcen report. La Spezia, Saclant undersea Research Centre: 47.

Fox, W. L. J. and M. Magueur (1998). Detection of buried objects at low grazing angles: preliminary experimental results. Sacantcen report. La Spezia, Saclant Undersea Research Centre: 47.

Franchi, E. R., J. M. Griffin, et al. (1984). NRL reverberation model: a computer program for the prediction and analysis of medium-to-long-range boundary reverberation. , Nav. Res. Lab.

French, W. S. (1974). "2-Dimensional and 3-Dimensional Migration of Model-Experiment Reflection Profiles." Geophysics **39**(3): 265-277.

French, W. S. (1975). "Computer Migration of Oblique Seismic-Reflection Profiles." Geophysics **40**(6): 961-980.

Fried, N. W. (1992). An Investigation o a Large Step-Down Ratio Parametric Sonar and Its Use in Sub-Bottom Profiling. Engineering Science, Simon Fraser University. **Master of applied science**: 122.

Fromm, D. M. (1999). Multistatic active system performance modeling in littoral waters. 28th Meeting of the Technical Cooperation Program, Washington, DC., Nav. Res. Lab.

Fulford, J. K. (1991). Shallow water RASP upgrade, Nav. Oceanogr. Atmos. Res. Lab.

Gail, M. A. (1990). "Classification of Large-Scale Subaqueous Bedforms: A new look at an old problem." Journal of sedimentary Petrology **Vol 60**(1): 160-172.

Gang, S. and A. Nehorai (2007). "Cramer-Rao bound analysis on multiple scattering in multistatic point-scatterer estimation." IEEE Transactions on Signal Processing **55**(6): 2840-2850.

Gardner, G. H. F. (1985). Migration of seismic data. Tulsa, Society of Exploration Geophysicists.

- Gardner, G. H. F., W. S. French, et al. (1973). "Elements of Migration and Velocity Analysis." Geophysics **38**(6): 1200-1200.
- Gardner, G. H. F., W. S. French, et al. (1974). "Elements of Migration and Velocity Analysis." Geophysics **39**(6): 811-825.
- Garland, M. and P. S. Heckbert (1995). Fast Polygonal Approximation of Terrains and Height Fields. Technical Report CMU-CS-95-181 School of Computer Science, Carnegie Mellon University, Pittsburgh, PA.
- Garriga, A. A., C. Spa, et al. (2005). Computation of the complete acoustic field with finite-differences algorithms. Forum Acusticum Budapest 2005. 4th European Congress on Acoustics Budapest, Hungary: S31-S31.
- George, O. and R. Bahl (1995). "Simulation of Backscattering of High-Frequency Sound from Complex Objects and Sand Sea-Bottom." Ieee Journal of Oceanic Engineering **20**(2): 119-130.
- Gieng, T. S., B. Hamann, et al. (1998). "Constructing hierarchies for triangle meshes." Ieee Transactions on Visualization and Computer Graphics **4**(2): 145-161.
- Guðmundur, H. (2007). "Uboat.net." from <http://uboat.net/men/aces/top.htm>.
- Gutowski, M., J. Bull, et al. (2002). "Chirp sub-bottom profiler source signature design and field testing." Marine Geophysical Researches **23**(5-6): 481-492.
- Hamann, B. (1994). "A Data Reduction Scheme for Triangulated Surfaces." Computer Aided Geometric Design **11**(2): 197-214.
- Hamilton, M. F. and D. T. Blackstock (1998). Nonlinear acoustics. San Diego, Academic press.
- Hanrahan, P. (1983). "Ray tracing algebraic surfaces." Computer Graphics **17**(3): 83-90.
- Heckbert, P. S. and M. Garland (1999). "Optimal triangulation and quadric-based surface simplification." Computational Geometry-Theory and Applications **14**(1-3): 49-65.
- Herman, A. J., R. M. Anania, et al. (1982). "A Fast 3-Dimensional Modeling Technique and Fundamentals of 3-Dimensional Frequency-Domain Migration." Geophysics **47**(12): 1627-1644.
- Hodgkiss, W. S. (1984). "An Oceanic Reverberation Model." Ieee Journal of Oceanic Engineering **9**(2): 63-72.
- Hoppe, H. (1998). "Efficient implementation of progressive meshes." Computers & Graphics **22**(1): 27-36.
- Hsu, S. H. and J. Y. Lai (2009). "Extraction of geodesic and feature lines on triangular meshes." International Journal of Advanced Manufacturing Technology **42**(9-10): 940-954.
- Jackson, D. and M. Richardson (2007). High-Frequency Seafloor Acoustics. New York, Springer Science.
- Jensen, F. B., W. A. Kuperman, et al. (2000). Computational ocean acoustics, Springer-Verlag.

Johns, B., T. J. Chesher, et al. (1990). "The Modeling of Sandwave Evolution Resulting from Suspended and Bed-Load Transport of Sediment." Journal of Hydraulic Research **28**(3): 355-374.

Johns, B., R. L. Soulsby, et al. (1993). "A Comparison of Numerical-Model Experiments of Free-Surface Flow over Topography with Flume and Field Observations." Journal of Hydraulic Research **31**(2): 215-228.

Judson, D., J. Lin, et al. (1979). "Depth Migration after Stack." Geophysics **44**(3): 326-326.

Junfei, L., L. Hao, et al. (2003). "An algorithm to detect the presence of 3D target motion from ISAR data." Multidimensional Systems and Signal Processing **14**(1-3): 223-240.

Katsnelson, B. G., V. G. Petnikov, et al. (2002). "Shallow water acoustics." Journal of the Acoustical Society of America **112**(6): 2502-2504.

Kinsler, L. E., A. R. Frey, et al. (1982). Fundamentals of acoustics 3rd edition. New York, John Wiley & Sons.

Konrad, W. L. (1974). "Application of the parametric source to bottom and sub-bottom profiling." Proceedings of the 1973 Symposium on Finite-Amplitude Wave Effects in Fluids|Proceedings of the 1973 Symposium on Finite-Amplitude Wave Effects in Fluids: 180-3|282.

Kosloff, D. D. and E. Baysal (1983). "Migration with the Full Acoustic-Wave Equation." Geophysics **48**(6): 677-687.

Kuznetsov, P. V. (1971). "Equations of Nonlinear Acoustics." Soviet Physics Acoustics-Ussr **16**(4): 467-&.

Lambert, D. N., M. T. Kalcic, et al. (2002). "Variability in the acoustic response of shallow-water marine sediments determined by normal-incident 30-kHz and 50-kHz sound." Marine Geology **182**(1-2): 179-208.

Landry, W. and B. T. Werner (1994). "Computer-Simulations of Self-Organized Wind Ripple Patterns." Physica D **77**(1-3): 238-260.

Larner, K. L., L. Hatton, et al. (1981). "Depth Migration of Imaged Time Sections." Geophysics **46**(5): 734-750.

Lazarov, A. D. and C. N. Minchev (2006). ISAR signal modeling and image reconstruction with entropy minimization autofocussing. 2006 IEEE/AIAA 25th Digital Avionics Systems Conference.

Leclerc, Y. G. and S. Q. Lau (1994). Terra Vision: A terrain visualization system. Menlo Parc, CA, SRI International.

Lighthill, M. J. (1952). On Sound Generated Aerodynamically I. General Theory. Proc. Roy. Soc. , London.

Lighthill, M. J. (1952). On Sound Generated Aerodynamically II. Turbulence as a Source of Sound. Proc. Roy. Soc., London.

- Liu, J.-Y., P.-C. Hsueh, et al. (2002). "Coherent Reflection of Acoustic Plane Wave From a Rough Seabed With a Random Sediment Layer Overlying an Elastic Basement." Journal of Oceanic engineering **27**(4): 853-861.
- Luby, J. C. and D. W. Lytle (1987). "Autoregressive Modeling of Nonstationary Multibeam Sonar Reverberation." Ieee Journal of Oceanic Engineering **12**(1): 116-129.
- Luebke, D. P. (1998). "View-Dependent Polygonal Simplification." from www.cs.virginia.edu/~gfx/Courses/2005/Intro.Spring.05/lecture08.rasterization.ppt.
- Luebke, D. P., M. Reddy, et al. (2003). Level of detail for 3D graphics, Morgan Kaufmann publishers, an imprint of Elsevier Science.
- Lurton, X. (2002). An Introduction to Underwater Acoustics. Chichester, Praxis Publishing Ltd.
- Lyons, A. P. (2005). "The potential impact of shell fragment distributions on high-frequency seafloor backscatter." Ieee Journal of Oceanic Engineering **30**(4): 843-851.
- Lyons, A. P., W. L. J. Fox, et al. (2002). "Characterization of the two-dimensional roughness of wave-rippled sea floors using digital photogrammetry." IEEE Journal of Oceanic Engineering **27**(3): 515-524.
- Lyons, A. P. and E. Pouliquen (2004). "Advances in high-resolution seafloor characterization in support of high-frequency underwater acoustics studies: Techniques and examples." Measurement Science & Technology **15**(12): R59-R72.
- Malme, C. I. (1994). "Development of a High Target Strength Passive Acoustic Reflector for Low-Frequency Solar Applications." Ieee Journal of Oceanic Engineering **19**(3): 438-448.
- Margrave, G. F. (2001). Numerical Methods of Exploration Seismology with algorithms in Matlab (NMES). Calgary, CREWES.
- Margrave, G. F. (2003). Numerical Methods of Exploration Seismology with algorithms in Matlab (NMES). Calgary, CREWES.
- Marsh, H. W. and M. Schulkin (1962). "Shallow-water transmission." J. Acoust. Soc. Am. **33**: 334-340.
- Marsh, P. (1976). A computer program for studying the Doppler content of reverberation. Nav. Sea Syst. Command.
- Marsset, B., J.-P. Henriot, et al. (2001). VHR3D - Very high resolution 3D seismic method for detailed site investigation. MAST Project Final Technical Report: 258.
- Marsset, B., T. Missiaen, et al. (1998). "Very high resolution 3D marine seismic data processing for geotechnical applications." Geophysical Prospecting **46**(2): 105-120.
- McMechan, G. A. (1983). "Migration by Extrapolation of Time-Dependent Boundary-Values." Geophysical Prospecting **31**(3): 413-420.
- Missiaen, T. (2005). "VHR marine 3D seismics for shallow water investigations: Some practical guidelines." Marine Geophysical Researches **26**(2-4): 145-155.

- Missiaen, T. (2008). *Shallow Marine Acoustic Imaging in Environmental Investigations*. Ghent, Gent University. **PhD**: 164.
- Missiaen, T., N. Wardell, et al. (2005). "Subsurface imaging and sediment characterisation in shallow water environments - Introduction to the special volume." Marine Geophysical Researches **26**(2-4): 83-85.
- Mitra, S. K. (2006). Digital Signal Processing, A Computer-Based Approach, 3rd edition. Singapore, Mc Graw Hill.
- Moffett, M. B. and R. H. Mellen (1977). "Model for Parametric Acoustic Sources." Journal of the Acoustical Society of America **61**(2): 325-337.
- Moreaux, K. (2003). Geologische en geofysische analyse van hellingsinstabiliteiten in een kratermeer: Lac Pavin, Frankrijk. Department Geology and Earth Sciences. Gent, Ghent University. **MSc**: 117.
- Muir, T. G. and J. G. Willette (1972). "Parametric Acoustic Transmitting Arrays." Journal of the Acoustical Society of America **52**(5): 1481-&.
- Naudts, L., J. Greinert, et al. (2006). "Geological and morphological setting of 2778 methane seeps in the Dnepr paleo-delta, northwestern Black Sea." Marine Geology **227**(3-4): 177-199.
- Nishimori, H. and N. Ouchi (1993). "Formation of Ripple Patterns and Dunes by Wind-Blown Sand." Physical Review Letters **71**(17): 2841-2841.
- Onoue, K. and T. Nishita (2003). "A rendering method on desert scenes of dunes with wind-ripples." Transactions of the Institute of Electronics, Information and Communication Engineers D-II **J86D-II**(2): 282-289.
- Oppenheim, A. V., R. W. Schaffer, et al. (1999). Discrete-Time Signal Processing (2nd Edition). Upper Saddle River, NJ, Prentice-Hall, Inc.
- Pace, N. G., E. Pouliquen, et al. (1997). High frequency acoustics in shallow water, proceedings of a conference held in Lerici, Italy, 30 June to 4 July, 1997, organized and sponsored by the NATO SACLANT Undersea Research Centre. La Spezia, NATO SACLANT Undersea Research Centre.
- Palmese, M. and A. Trucco (2006). "Acoustic imaging of underwater embedded objects: Signal simulation for three-dimensional sonar instrumentation." Ieee Transactions on Instrumentation and Measurement **55**(4): 1339-1347.
- Pautet, L., P. McCloghrie, et al. (2003). Some aspects of the Impact of Environment on SAS performance. La Spezia, Italy, NATO Undersea Research Centre: 44.
- Pautet, L., E. Pouliquen, et al. (2002). A study of ping-to-ping coherence of the seabed response. Impact of Littoral Environmental Variability on Acoustic Predictions and Sonar Performance. N. G. Pace and F. B. Jensen, Kluwer Academic Publishers: 489-496.
- Pautet, L., E. Pouliquen, et al. (2002). Experimental study of fluctuations in coherent backscattering. European Conference on underwater acoustics, Gdansk, Poland.
- Pinto, M., A. Bellettini, et al. (2004). "A new synthetic aperture sonar design with multipath mitigation." AIP Conference Proceedings(728): 489-496.

Pomerenk, K. and A. Novick (1987). BISAPP user's manual, Mission Sci. Corp.

Pouliquen, E., O. Bergem, et al. (1999). "Time-evolution modeling of seafloor scatter. I. Concept." J. Acoust. Soc. Am. **105**: 3136-3141.

Pouliquen, E., G. Canepa, et al. (2004). Temporal variability of seafloor roughness and its impact on acoustic scattering. Seventh European Conference on Underwater Acoustics ECUA 2004, Delft, Netherlands, TU Delft.

Pouliquen, E. and A. P. Lyons (2002). "Backscattering from bioturbated sediments at very high frequency." Ieee Journal of Oceanic Engineering **27**(3): 388-402.

Pouliquen, E., A. P. Lyons, et al. (1998). "The Helmholtz-Kirchhoff approach to modeling penetration of acoustic waves into rough seabeds (A)." J. Acoust. Soc. Am. **104**(3).

Pouliquen, E., A. P. Lyons, et al. (1998). Penetration of acoustic waves into sandy seafloors at low grazing angles: the Helmholtz-Kirchhoff approach. Saclantcen report. La Spezia, Saclant undersea research centre: 43.

Princehouse, D. W. (1977). REVGGEN, a real-time reverberation generator. IEEE Int. Conf. Acoust. Speech Signal Process.

Princehouse, D. W. (1977). REVGGEN, a ream-time reverberation generator. IEEE Int. Conf. Acoust. Speech Signal Process.

Quackenbush, L. J. (2004). "A review of techniques for extracting linear features from imagery." Photogrammetric Engineering and Remote Sensing **70**(12): 1383-1392.

Richardson, M. D., G. R. Bower, et al. (2003). Mine burial by scour: preliminary results from the Gulf of Mexico.

Rogers, P. H. (1981). Onboard prediction of propagation loss in shallow water, NRL.

Rottger, S., W. Heidrich, et al. (1998). Real-time generation of continuous levels of detail for height fields.

Rydesäter, P. (2003, 2003). "TCP_UDP_IP - Network communication with other applic. & remote matlab control." Mathworks 2.0.5. from <http://www.mathworks.com/matlabcentral/fileexchange/loadFile.do?objectId=345&objectType=File>.

Schmidt, H. (1987). SAFARI: Seismo-acoustic fast field algorithm for range independent environments. La Spezia, Italy, SACLANT ASW Research Centre.

Schmidt, H. (2004). "OASES: Ocean Acoustics and Seismic Exploration Synthesis." from <http://acoustics.mit.edu/faculty/henrik/oases.html>.

Schmidt, H. and T. G. (1986). "Efficient global matrix approach to the computation of synthetic seismograms." Geophys. J. R. Astr. Soc **84**: 331-359.

- Schmidt, H. and J. Glattetre (1985). "A fast field model for three-dimensional wave propagation in stratified environments based on the global matrix method." J. Acoust. Soc. Am. **78**: 2105-2114.
- Schmidt, H. and F. B. Jensen (1985). "Efficient Numerical-Solution Technique for Wave-Propagation in Horizontally Stratified Environments." Computers & Mathematics with Applications **11**(7-8): 699-715.
- Schmidt, H. and F. B. Jensen (1985). "A full wave solution for propagation in multilayered viscoelastic media with application to Gaussian beam reflection at fluid-solid interfaces." J. Acoust. Soc. Am. **77**: 813-825.
- Schneider, W. A. (1978). "Integral Formulation for Migration in 2 and 3 Dimensions." Geophysics **43**(1): 49-76.
- Schultz, P. and J. Sherwood (1979). "Depth Migration before Stack." Geophysics **44**(3): 326-326.
- Schweitzer, D. and E. S. Cobb (1982). "Scanline rendering of parametric surfaces." Computer Graphics **16**(3): 265-271.
- Sheriff, R. E. (1984). Encyclopedic Dictionary of Exploration Geophysics. Tulsa, Society of Exploration Geophysics.
- Shi, G. and A. Nehorai (2007). "Cramer-Rao bound analysis on multiple scattering in multistatic point-scatterer estimation." Ieee Transactions on Signal Processing **55**(6): 2840-2850.
- Sienkiewicz, C. G., M. L. Boyd, et al. (1975). Computer-programmed models used at the University of Washington's Applied Physics Laboratory for evaluating torpedo sonar performance, Appl. Phys. Lab., Univ. Washington.
- Simpkin, P. G. and A. Davis (1993). "For seismic profiling in very shallow water, a novel receiver." Sea Technology.
- Smith, K. B., W. S. Hodgkiss, et al. (1996). "Propagation and analysis issues in the prediction of long-range reverberation." Journal of the Acoustical Society of America **99**(3): 1387-1404.
- Smith, K. B., F. D. Tappert, et al. (1993). "Comparison of UMPE/PEREV bistatic reverberation predictions with observations in the ARSRP natural lab." J. Acoust. Soc. Amer. **94**.
- Soulsby, R. (1997). Dynamics of marine sands, Thomas Telford Ltd.
- Soumekh, M. (1999). Synthetic Aperture Radar Signal Processing: with MATLAB Algorithms, John Wiley & Sons.
- Staelens, P. J. M. (2003). Correlation of backscatter simulated with the Boris model. La Spezia, NATO Undersea Research Centre: 7.
- Staelens, P. J. M. and A. Borghgraef (2006). Technical report of sonar and infrared tests in the harbour of Zeebrugge: detection of small floating or submerged objects. Brussels, Ministry of Defense.
- Stolt, R. H. (1978). "Migration by Fourier-Transform." Geophysics **43**(1): 23-48.

- Sun, C. and P. Vallotton (2009). "Fast linear feature detection using multiple directional non-maximum suppression." Journal of Microscopy-Oxford **234**(2): 147-157.
- Tian-De, M., M. Qing-Song, et al. (2001). "Computer simulation of aeolian sand ripples and dunes." Physics Letters A **288**(1): 16-22.
- Trauth, M. H., R. Gebbers, et al. (2007). MATLAB® Recipes for Earth Sciences, 2nd edition Berlin, Springer - Verlag.
- Trinder, J. C. and Y. D. Wang (1998). "Automatic road extraction from aerial images." Digital Signal Processing **8**(4): 215-224.
- Trorey, A. W. (1970). "A Simple Theory for Seismic Diffractions." Geophysics **35**(5): 762-&.
- Urlick, R. J. (1982). Sound propagation in the Sea, Peninsula Publishing.
- Urlick, R. J. (1983). Principles of underwater sound 3rd edition. Los Altos, California, Peninsula Publishing.
- Van Rijn, L. C. (1984). "Sediment transport: Part I: bed load transport; part II: suspended load transport; part III: bed forms and alluvial roughness." J. Hydrol. Div., Proc ASCE **110**.
- Vlaamse Hydrografie, A. K. (2007). "Sigurd Faulbaums." from <http://www.vlaamsehydrografie.be/wrakken/detail.aspx?id=84>.
- Webster, G. M. (1978). Deconvolution. Tulsa, Society of Exploration Geophysicists.
- Webster, G. M. (1978). Deconvolution. Tulsa, Society of Exploration Geophysicists.
- Westervelt, P. J. (1957). "Scattering of Sound by Sound." Journal of the Acoustical Society of America **29**(8): 934-935.
- Westervelt, P. J. (1957). "Scattering of Sound by Sound." Journal of the Acoustical Society of America **29**(2): 199-203.
- Westervelt, P. J. (1963). "Parametric Acoustic Array." Journal of the Acoustical Society of America **35**(4): 535-&.
- Wever, T. F. (2004). Final Report of the Specialist Team on Mine Burial Analysis (ST-MBA) NATO RESTRICTED. Kiel, NATO.
- Whaley, H. L. and L. Adler (1970). Model for the determination of the size and orientation of reflectors from ultrasonic frequency analysis.
- Wikipedia, B. m. (2007). "Bump mapping." from http://en.wikipedia.org/wiki/Bump_mapping.
- Wikipedia, R. c. g. (2007). "Rendering (computer graphics)." from [http://en.wikipedia.org/wiki/Rendering_\(computer_graphics\)#Techniques](http://en.wikipedia.org/wiki/Rendering_(computer_graphics)#Techniques).
- Wilson, G. R. and F. M. E. (1983). "Horizontal covariance of surface reverberation: Comparison of a point-scatterer model to experiment." J. Acoust. Soc. Am. **73**(3): 749-760.

- Wilson, M. F. J., B. O'Connell, et al. (2007). "Multiscale terrain analysis of multibeam bathymetry data for habitat mapping on the continental slope." Marine Geodesy **30**: 3-35.
- Wilson, O. (1988). Introduction to the Theory and Design of Sonar Transducers. Los Altos, CA, USA, Peninsula publishing.
- Wood, J. (1996). The Geomorphological characterisation of digital elevation models., University of Leicester. **Ph.D.**
- Yilmaz, Ö. (2001). Seismic data analysis: processing, inversion, and interpretation of seismic data. Tulsa, Society of Exploration Geophysicists.
- Yizhaq, H., N. J. Balmforth, et al. (2004). "Blown by wind: nonlinear dynamics of aeolian sand ripples." Physica D-Nonlinear Phenomena **195**(3-4): 207-228.
- Zabolotskaya, E. A. and R. V. Khokhlov (1969). "Quasi-Plane Waves in Nonlinear Acoustics of Confined Beams." Soviet Physics Acoustics-Ussr **15**(1): 35-&.
- Zampolli, M., D. S. Burnett, et al. (2004). "A finite-element tool for scattering from localized inhomogeneities and submerged elastic structures." AIP Conference Proceedings(728): 464-471.
- Zhang, Q. H. and T. D. Miao (2003). "Aeolian sand ripples around plants." Physical Review E **67**(5).

7 APPENDIX

Appendixes are added on the CD, they include the stresstest of BORIS 3D SSA and the software book + some animations and scripts.